III-V Semiconductor Nanostructures for Photoelectrochemical Water Splitting

A thesis is submitted for the degree of Doctor of Philosophy
of The Australian National University

Australian
National
University

Parvathala Reddy Narangari

November 2018

This thesis, to the best of my knowledge and belief, does not contain any results previously published by another person or submitted for a degree or diploma at any university except where due reference is made in the text.

N. Parvathala Reddy

Parvathala Reddy Narangari
Department of Electronic Materials Engineering
Research School of Physics and Engineering
The Australian National University
Canberra, ACT 2601
Australia
15 November 2018

Acknowledgements

I would like to take this opportunity to express my sincere gratitude to the many people who supported me either directly or indirectly in the marathon innings of my PhD.

Firstly, I would like to thank my research supervisory panel including Prof. H. H. Tan, Prof. Chennupati Jagadish, Dr. Siva Karuturi, Dr. Sudha Mokkapati, Dr. Shaguftha Naureen, Assoc. Prof. Jennifer Wong-Leung and Assoc. Prof. Fu Lan for their valuable contributions and support. It was a great opportunity for me to be a part of Prof. Chennupati Jagadish's group, who is a pioneering and eminent scientist in nanotechnology and semiconductor optoelectronics. I am bowled over by his down-to-earth demeanor and treatment of students as colleagues despite being one of the most prominent scientists on the globe. He always supported, encouraged and gave me valuable insights and advice throughout my PhD. I am thankful to him for giving his time in reading my thesis even though he was on sabbatical leave and busy with many of his commitments. Special thanks to Prof. H. H. Tan for being the chair of my supervisory panel and providing me with timely and constructive criticism, intriguing research meetings and friendly PhD supervision. I appreciate his encouragement and support when I changed my research directions due to unavoidable circumstances. I will never forget his way of handling complex and delicate situations without hurting others and the way he bailed me out from very tough and sensitive situations.

I am extremely thankful to Dr. Siva Kaurturi for his exceptional mentorship, constant encouragement and invaluable support at each and every step of my PhD since I started working with him. I am glad to have had a principle supervisor like Siva, who has a great pool of ideas, likes to take up new challenges, explores new collaborations and shows enthusiasm to broaden research skills. I believe that Siva's arrival to the group was a significant turning point in my PhD. His involvement made my PhD a pleasant and joyful ride. He not only introduced me to the filed the photocatalysis but also spent time on experiments and gave significant inputs and suggestions in designing projects and writing papers, research reports and research presentations. He even gave unprecedented inputs and advice in job hunting, including preparing for job applications and interviews. He has always been friendly, cared for me like a family member and is prepared to help on both professional and personal fronts. I am thankful to Dr. Sudha Mokkapati for her support in simulations and optical experiments

especially during my first project and caring for me like a family member. I also thank Dr. Shaguftha Naureen, who introduced me to top-down fabrication techniques, trained me on various instruments and helped me during the first two years of my PhD. My thanks also go to Dr. Fan Wang for his help in teaching and training on micro-photoluminescence. I would like to extend thanks to Dr. Sanjoy Nandi and Dr. Dinesh Venkatachalam for their help in electrical characterizations and Dr. Ziyuan Li for training on photoluminescence measurements.

I would like to acknowledge the Australian National Fabrication Facility-ACT Node and its technical support team without whom I could not accomplish my device fabrications. I owe thanks to Dr. Fouad Karouta for sharing knowledge, suggestions and inputs in top-down fabrication and forwarding the valuable job advertisement links that he come across. Special thanks to Dr. Kaushal Vora, who is friendly, supportive and possesses all-round knowledge in fabrication. He was always the first person for me to contact if I faced problems with any of the instruments and to discuss with him if I faced failure in any device fabrication. I thank Dr. Mykhaylo Lysevych for growing epitaxial films using MOCVD for me. I also thank Dr. Naeem Shahid, Dr. Li Li and Dr. Mark Lockrey for their support and training on EBL, FIB and CL systems respectively. My thanks also go to the ANFF technical support team and EME technical staff including Mr. Dane Kelly, Mr. Chris Kafer and Mr. Joshua Carr for their friendly discussions and efforts to keep ANFF and EME equipment running smoothly.

The support offered by the Research School of Physics and Engineering admin staff is long lasting. I sincerely thank EME department administrator Mrs. Julie Arnold and HDR admin staff Liudmila Mangos and Karen Nulty for their smooth handling of all the administrative matters which allowed me to focus on my research with a free mind. I would like to acknowledge National Computational Infrastructure for providing access to the computational facility. I greatly appreciate the financial support from the Australian Research Council (ARC), Australian National University and Australian Nanotechnology Network (ANN).

I would like to thank all my past and present student colleagues for their help, support, encouragement and making my PhD life joyful. I express special thanks to Mr. Joshua Butson for being the first reader of my thesis, providing English corrections and a helping hand in experiments. My thanks also go to Mr. Naiyin Wang, Ms. Rowena Yew, Mr. Yesaya C. Wenas, Ms. Bijun Zhao, Mr. Dipankar Chugh, Dr. Tuan Tran, Mr. Faijun Li, Dr. Kun Peng, Dr. Qian Gao, Dr. Xiamong Yuan, Dr. Shuai (Jack) Li, Dr. Tim Burgess, Dr. Dhruv Saxena, Dr. Aruni Fonseka, Dr. Amira Amerduddin,, Mr. Inseok Yang, Ms. Zahra Azimi, Mr. Vidur Raj Singh, Mr. Ahmed Alabadla, Mr. Sonachand Adhikari, Mr. Fanlu Zhang, Ms. Andrea Hadley, Mr.

Mohammad Rashidi, Ms. Aswani Gopakumar and Ms. Nikita Gagrani for their help and keeping me company during the good and bad times of my PhD journey. I would like to acknowledge Mr. Sudhakar Joseph for his assistance in finding accommodation and settling down in Canberra when I arrived. I also thank friends from all parts of my life including Sukantha Debbarma, Mr. Ch. Bapanyanna, Dr. Sreekanth Mandati, Dr. Sandhya Rani Punugupati, Dr. Nagarjuna Neella, Mr. Lokesh and Mr. Sreenivasula Reddy Yellappagi for their moral support and helping hands in needy times.

I express the deepest gratitude to my family for their never-ending love, support and encouragement. I am always indebted to my parents as they have supported and allowed me to pursue my dreams even though they are illiterate and going through hardships. I cannot ask them for more than what they have done for me. My elder brother, Samba Siva Reddy, is the one who believed in me more than myself and encouraged me to aim for greater heights in my studies. Moreover, he made me free of all family tensions by handling family responsibilities after he started working. I can still remember how my eldest brother, Rama Sudhakar Reddy, used take care of me during school holidays. The support and love of my grandparents Late Sagili Malla Reddy and Sagili Bayamma towards me is invaluable. I am fortunate to find Naveena as a life partner in the midst of my PhD, who is very responsible, understanding, encouraging and supportive. Simple thanks is not enough for her understanding of my PhD commitment and managing the pregnancy and baby by herself in my absence. I would like to acknowledge the support provided by my sister-in-law Shobha Rani since she became part of our family. Last but not least, thanks to the latest entrants and little stars of our family Gautham, Prayag and Ruthvik for making me feel relaxed during hard times through their beautiful smiles and funny activities.

Abstract

The research interest in hydrogen generation via photoelectrochemical (PEC) water splitting is ever growing owing to its potential to generate clean and portable form of energy. In PEC water splitting, semiconductor harvests sunlight and splits water into hydrogen and oxygen to produce hydrogen fuel. However, the lack of a single robust and low energy band gap semiconductor material that can straddle both water redox potentials is the main barrier to achieve efficient water splitting. III-V semiconductors can make ideal photocatalytic materials for PEC water splitting due to their outstanding optoelectronic properties including tunable band gaps to cover the entire solar spectrum, band edges straddling water redox potentials, high absorption coefficients and high crystalline quality. Among the III-V semiconductors, GaN and InP based materials have been shown to have great potential as efficient photoelectrodes for water splitting and can also form an effective combination for high efficiency tandem PEC cells with complementary band gaps. In addition, photoelectrodes based on one-dimensional nanostructures are shown to greatly enhance the PEC performance from improved light absorption, increased semiconductor/electrolyte interface area and reduced carrier diffusion length over their planar counterparts. This thesis presents an investigation of GaN, InGaN quantum wells and InP nanopillars (NPs), fabricated using top-down methods, as photoelectrodes for PEC water splitting applications.

Fabrication of GaN and InP NPs were carried out using inductively coupled plasma (ICP) etching of pre-masked epitaxial wafers, towards investigation of their PEC performance. Electron beam lithography (EBL) and self-assembled random mask techniques were employed to produce etch masks for ICP fabrication of ordered and random NPs, respectively. Ordered GaN NPs, fabricated using ICP etching of an EBL-patterned GaN epilayer, showed that the morphology and optical properties of the NPs are influenced by the NP dimensions. The photoluminescence (PL) intensity of the NP array increased with decreasing pitch while the side wall angle of the NPs decreased with decreasing pitch. Four-fold enhancement in PL intensity was observed for NP arrays with 400 nm pitch and 100 nm diameter compared to their planar counterpart. Finite-difference time-domain (FDTD) simulations revealed that the antireflection and enhanced emission properties of NPs compared to the epilayer contribute to

the enhanced PL intensity of GaN NP arrays. Further, quantum efficiency of the NPs, evaluated using power dependent PL and FDTD simulations, was found to be comparable to that of the epilayer.

The cost-effective and scalable fabrication of high density random GaN and InP NPs with controlled dimensions was demonstrated using ICP etching and self-assembled random mask techniques for PEC water splitting. GaN and InP NPs exhibited drastic enhancement in absorption properties below their band gap compared to the respective planar structures, mainly due to reduced reflection losses. The PEC performance of random GaN NPs photoanodes was tested in 1 M NaOH under simulated one sun illumination. NPs generated the highest ever reported photocurrent density for GaN photoanodes due to exceptional absorption by the NPs, and increased depletion layer area and semiconductor/electrolyte interface area. Moreover, the PEC performance of NPs was found to be strongly influenced by carrier concentration and NP dimensions. While NP diameter resulted in an anodic shift of the onset potential, increasing the carrier concentration led to an increase in onset potential and overpotential of GaN photoanodes. We further engineered the band gap of GaN NPs by incorporating InGaN/GaN multiple quantum wells (MQWs) to further improve the PEC performance of GaN NPs. PL and diffuse reflectance measurements confirmed that the introduction of InGaN/GaN MQWs into GaN extended the optical absorption by the NPs into the visible part of the solar spectrum, thereby contributing to the substantial improvement in photocurrent density for InGaN/GaN MQW NPs. Furthermore, GaN NP photoanodes were found to exhibit improved photostability after being decorated with co-catalysts such as NiO and Co_3O_4. The accumulation of photogenerated charge carriers at semiconductor surface trigger the self-oxidation of GaN photoanode during water oxidation reaction and results in photocorossion of GaN photoanodes. Deposition of co-catalyst significantly reduced the self-oxidation of GaN photoanode by extracting the photogenerated carriers out of photoanode and participate in water oxidation reaction.

InP NP photocathodes were fabricated by developing a Au-based random mask and were investigated for their PEC performance in 1 M HCl electrolyte. It was found that the PEC performance of as-fabricated InP NPs was adversely affected by the plasma damage caused by the top-down fabrication process. After removing the plasma damaged surface with controlled wet etching in sulfur contained oleylamine (S-OA) solution, InP NP photocathodes exhibited exceptional PEC performance, with photocurrents of NPs reaching close to the theoretical maximum achievable limit for InP. Time-resolved photoluminescence (TRPL) measurements revealed that the S-OA treatment not only removed the plasma damage but also passivated the

NP surface through the formation of a sulfide layer around the NPs. Moreover, in addition to the improved PEC performance, S-OA improved the stability of the InP NP photocathodes against photocorrosion.

In summary, cost-effective and scalable fabrication of GaN and InP NP photoelectrodes using top-down fabrication is demonstrated in this dissertation for efficient PEC water splitting. The highest ever reported current density is achieved for both the photoelectrodes owing to enhanced light absorption and semiconductor/electrolyte interface area. Co-catalyst deposition and S-OA treatment were investigated to improve the photostability of GaN and InP photoelectrodes, respectively. The simple and scalable top-down fabrication of NPs developed in this work can be adapted for a wide variety of materials with a broad range of applications.

List of Publications

1. **Parvathala Reddy Narangari**, Siva Krishna Karuturi, Yiliang Wu, Jennifer Wong-Leung, Kaushal Vora, Mykhaylo Lysevych, Yimao Wan, H. H. Tan, C. Jagadish, and S. Mokkapati "Ultrathin Ta_2O_5 Electron-Selective Contacts for High Efficiency InP Solar Cells" ***Nanoscale 11**, 7497(2019)*
2. Joshua Butson, **Parvathala Reddy Narangari**, Siva Krishna Karuturi, Rowena Yew, Mykhaylo Lysevych, Hark Hoe Tan, and Chennupati Jagadish, "Photoelectrochemical Properties of InGaN/GaN MQW Nanopillars", ***Nanotechnology*** **29**, 045403 (2018). (Equal contributing first author and corresponding author).
3. Siva Krishna Karuturi, Heping Shen, Rowena Yew, **Parvathala Reddy Narangari**, Jennifer Wong-Leung, Hark Hoe Tan, and Chennupati Jagadish, "An Integrated Perovskite-TiO_2/CdS Tandem Photoelectrode for Unassisted Solar Hydrogen Generation", ***ACS Applied Materials & Interfaces*** **10**, 23766 (2018).
4. Siva Krishna Karuturi, Rowena Yew, **Parvathala Reddy Narangari**, Jennifer Wong-Leung, Li Li, Kaushal Vora, Hark Hoe Tan, and Chennupati Jagadish, "CdS/TiO_2 Photoanodes via Solution Ion Transfer Method for Highly Efficient Hydrogen Generation", ***Nano Futures*** **2**, 015004 (2018).
5. Yimao Wan, Siva Krishna Karuturi, Chris Samundsett, James Bullock, Mark Hettick, Di Yan, Jun Peng, **Parvathala Reddy Narangari**, Sudha Mokkapati, Hark Hoe Tan, Chennupati Jagadish, Ali Javey, and Andres Cuevas, "Tantalum Oxide Passivated Electron Heterocontacts for Silicon Photovoltaics and Photoelectrochemical Water Reduction", ***ACS Energy Letters*** **3**, 125 (2018)
6. **Parvathala Reddy Narangari**, Siva Krishna Karuturi, Mykhaylo Lysevych, Hark Hoe Tan, and Chennupati Jagadish, "Improved Photoelectrochemical Performance of GaN Nanopillar Photoanodes" ***Nanotechnology*** **28**, 154001(2017).
7. **N. Parvathala Reddy**, Shagufta Naureen, Sudha Mokkapati, Kaushal Vora, Naeem Shahid, Fouad Karouta, Hark Hoe Tan, and Chennupati Jagadish, "Enhanced

luminescence from GaN nanopillar arrays fabricated using a top-down process", ***Nanotechnology*** **27**, 065304 (2016).

8. Guanyu Liu, Siva Krishna Karuturi, Alexandr N. Simonov, Monika Fekete, Hongjun Chen, Noushin Nasiri, Nhien H. Le, **Parvathala Reddy Narangari**, Mykhaylo Lysevych, Thomas R. Gengenbach, Adrian Lowe, Hark Hoe Tan, Chennupati Jagadish, Leone Spicciac and Antonio Tricoli, "Robust Sub-Monolayers of Co_3O_4 Nano-Islands: a Highly Transparent Morphology for Efficient Water Oxidation Catalysis", **Advanced Energy Materials 6,** 1600697 (2016)

Submitted/In preparation

9. Joshua D. Butson, **Parvathala Reddy Narangari**, Mykhaylo Lysevych, Jennifer Wong-Leung, Yimao Wan, Siva Krishna Karuturi, Hark Hoe Tan and Chennupati Jagadish, "InGaAsP as a Promising Narrow Band Gap Semiconductor for Photoelectrochemical Water Splitting" ***ACS Applied Materials & Interfaces*** (Submitted)
10. **Parvathala Reddy Narangari** et al., "Surface Modification of InP Nanostructures using Sulfur Contained Oleylamine for Stable and Efficient Water Splitting" (in preparation)
11. Siva Krishna Karuturi et al., "Perovskite-Silicon Tandem Absorbers for High Efficiency Unbiased Solar Hydrogen Generation" (in preparation) (co-author)

Conference Papers

1. **N Parvathala Reddy**, Shagufta Naureen, Fan Wang, Kaushal Vora, Naeem Shahid, Fouad Karouta, Hark Hoe Tan, and Chennupati Jagadish," Fabrication and Photoluminescence Studies of GaN Nanopillars", Conference on Optoelectronic and Microelectronic Materials and Devices (COMMAD) 2014, 133-136

Acronyms and Symbols

A.M	air mass filter
ABPE	applied bias-to-current conversion efficiency
CCD	charge coupled device
EBL	electron beam lithography
FDTD	finite-difference time-domain
ICP	inductively coupled plasma
IPCE	incident photon-current-conversion efficiency
MOCVD	metal organic chemical vapour deposition
MQW	multi quantum well
SHE	standard hydrogen electrode
NP	nanopillars
PEC	photoelectrochemical
PECVD	plasma enhanced chemical vapor deposition
PL	photoluminescence
QE	quantum efficiency
RF	radio-frequency
RHE	reversible hydrogen electrode
RIE	reactive ion etcher
RTA	rapid thermal annealing
SEM	scanning electron microscope
S-OA	sulfur dissolved oleylamine
TEGa	triethylgallium
TMGa	trimethylgallium
TRPL	time-resolved photoluminescence
TMIn	trimethylindium
UV-Vis	ultraviolet-visible

Contents

Acknowledgements .... ***iv***

Abstract .... ***vii***

List of Publications .... ***x***

Acronyms and Symbols .... ***xii***

Contents .... ***xiii***

List of Figures .... ***xviii***

List of Tables .... ***xxiv***

Chapter 1 Introduction ***1***

1.1. Background and motivation 1

1.2. Renewable hydrogen production methods 4

1.2.1. Solar thermal water splitting 4

1.2.2. Electrolysis 6

1.3. Photocatalytic water splitting 8

1.3.1. Working principle 8

1.3.2. Photochemical water splitting 10

1.3.3. Photoelectrochemical water splitting 11

1.4. Photocatalytic semiconductor materials 12

1.5. Aim of this thesis 15

1.6. Literature Review 18

1.6.1. GaN-based ternary alloys 18

1.6.2. Indium phosphide 24

1.7. Outlook for hydrogen economy 26

1.8. Key challenges and objectives of this thesis 27

1.9. Organization of this thesis 28

1.10. References ... 29

Chapter 2 Experimental Methods ... 41

2.1. Epitaxial growth of GaN based alloys ... 41

2.2. Design of etch mask ... 43

2.2.1. Plasma enhanced chemical vapor deposition ... 43

2.2.2. Electron beam lithography ... 44

2.2.3. Rapid thermal annealing ... 45

2.3. Plasma etching ... 46

2.3.1. Reactive ion etching ... 46

2.3.2. Inductively coupled plasma etching ... 47

2.4. Characterization of NPs ... 49

2.4.1. Scanning electron microscopy ... 49

2.4.2. Photoluminescence ... 50

2.4.2.1. Micro-photoluminescence ... 50

2.4.2.2. Time-resolved photoluminescence ... 51

2.4.3. UV-Vis spectrophotometry ... 52

2.5. Finite-Difference Time-Domain Simulations ... 53

2.6. Photoelectrochemical testing station ... 54

2.7. Summary ... 57

2.8. References ... 57

Chapter 3 Fabrication of Ordered GaN Nanopillars Using Top-down Approach ... 59

3.1. Introduction ... 59

3.2. Fabrication of ordered GaN NPs ... 60

3.3. Morphology of GaN NPs ... 61

3.4. Optical characterization ... 62

3.4.1. Room temperature photoluminescence ... 63

3.4.2. Power dependent photoluminescence ... 64

3.5. FDTD simulations of optical properties ... 65

3.5.1. Absorption characteristics ... 65

3.5.2. Emission characteristics 66
3.5.3. Quantum efficiency of GaN nanopillars 68
3.6. Summary 70
3.7. References 71
Chapter 4 Fabrication and Photoelectrochemical Studies of Random GaN Nanopillar Photoanodes 75
4.1. Introduction 75
4.2. Fabrication of random GaN nanopillars 76
4.3. Fabrication of GaN photoanodes 78
4.4. Morphology of the GaN NPs 79
4.5. Optical properties of NPs 81
4.6. Depletion layer in n-GaN 81
4.7. Photoelectrochemical performance of GaN photoanodes 83
4.7.1. Influence of carrier concentration on PEC performance 84
4.7.1.1. Planar photoanodes 84
4.7.1.2. GaN NP photoanodes 85
4.7.1.3. Applied Bias Photon-to-Current Conversion efficiency 86
4.7.2. Influence of NP dimensions on the PEC performance 87
4.7.2.1. Influence of NP diameter 87
4.7.2.2. Influence of length 89
4.8. Electrochemical impedance spectroscopy 90
4.9. Conclusions 91
4.10. References 91
Chapter 5 Band Gap Engineering and Photostability of GaN Photoanodes 95
5.1. Introduction 95
5.2. Design and fabrication of InGaN/GaN MQW NP photoanodes 96
5.3. Optical properties of InGaN/GaN MQWs 97
5.3.1. Optical reflectivity of InGaN/GaN MQWs 97

5.3.2. Photoluminescence of InGaN/GaN MQWs 98

5.4. PEC performance of InGaN/GaN MQW photoanodes 100

5.4.1. PEC performance of planar photoanodes 100

5.4.2. PEC performance of NP photoanodes 101

5.5. Incident photon-to-current conversion efficiency 103

5.6. Applied Bias Photon-to-Current Conversion efficiency 104

5.7. Stability of GaN photoanodes 105

5.7.1. Transition metal oxide co-catalysts for stability of NP photoanodes 106

5.7.2. NiO co-catalyst for the stabilization of NP photoanodes 106

5.7.3. Co_3O_4 co-catalyst for the stabilization of NP photoanodes 108

5.7.4. Electrochemical impedance spectroscopy 110

5.8. Summary 111

5.9. References 112

Chapter 6 Fabrication and Photoelectrochemical Studies of InP Nanopillars 115

6.1. Introduction 115

6.2. Fabrication of InP NPs 117

6.3. Plasma surface damage removal 118

6.3.1. Morphology of NPs 118

6.3.2. Optical characterization of NPs 120

6.4. Absorption properties of NPs 122

6.5. PEC studies of InP photocathodes 123

6.5.1. Fabrication of InP photocathodes 123

6.5.2. PEC performance of NP photocathodes 123

6.5.3. Influence of S-OA treatment on PEC performance of NP photocathodes 125

6.6. Electrochemical impedance of NP photocathodes 126

6.7. Stability of NP photocathodes 128

6.8. Conclusions 129

6.9. References 130

Chapter 7 Conclusions and Future Scope ***133***

7.1. Conclusions 133

7.2. Future scope 135

7.2.1. Improving the PEC performance of InGaN/GaN MQW photoanodes 136

7.2.2. Engineering the onset potential of InP photocathodes 136

7.2.3. Cost effective strategies for III-V semiconductor photoelectrodes 138

7.3. References 139

List of Figures

Figure 1.1: History and prediction of (a) the global energy consumption in quad units, (b) the consumption pattern of resources for producing energy and (c) the energy related carbon dioxide emissions. 2

Figure 1.2: Schematic of two-step thermal water splitting 5

Figure 1.3: Schematic illustration of electrolyzer for electrolytic water splitting. 7

Figure 1.4: Schematic of hydrogen production through electrolysis of water using electricity generated by renewable technologies [13]. 8

Figure 1.5: Schematic of the energy band diagram for photocatalytic water splitting for hydrogen generation. 8

Figure 1.6: Schematic illustration of the photocatalytic water splitting principle [19] 10

Figure 1.7: Schematic of a photochemical system for water splitting [24, 25]. 11

Figure 1.8: Schematic illustration of photocatalytic water splitting [15]. 11

Figure 1.9: Schematic illustration of a photoelectrochemical system for solar water splitting [18]. 12

Figure 1.10: Chemical elements that are involved in the formation of photocatalysts [24]. ... 13

Figure 1.11: The calculated oxidation (red bars) and reduction potentials (black bars) relative to the NHE and vacuum level for a series of semiconductors in solution at pH=0, the ambient temperature 298.15 K, and pressure 1 bar. Also plotted are the water reduction (H^+/H_2) and oxidation (O_2/H_2O) potentials (dashed lines), and valence (green columns) and conduction (blue columns) band edge positions at pH=0 [33]. 13

Figure 1.12: Band edge positions of various semiconductors against the water redox potentials [24]. 14

Figure 1.13: (a) Schematic of a PEC set up under tandem illumination and (b) band edge potentials of various nitride materials against water redox potentials (green dotted lines) and band edge positions of $In_xGa_{1-x}N$ (red-dotted lines) with increasing x from left to right (0 to1) [40]. 15

Figure 2.1: Photograph of the AIXTRON MOCVD reactor used in this work for growth of GaN and InGaN/GaN MQW structures. 42

Figure 2.2: Schematic illustration of processing steps involved in EBL patterning of Cr mask...44

Figure 2.3: Schematic illustration of the reactive ion etching system used in this work.........47

Figure 2.4: Schematic illustration of typical inductively coupled plasma reactive ion etching system..48

Figure 2.5: Schematic illustration of electron-material interactions and consequent outcomes. 49

Figure 2.6: Schematic representation of micro-PL system used for optical characterization of GaN and InGaN/GaN samples [12]. 51

Figure 2.7: Schematic optical design of TRPL set-up used for photoluminescence and minority carrier lifetime measurement of InP [13]. 51

Figure 2.8: Schematic representations of (a) light-matter interactions, (b) specular reflectance on smooth surfaces and (c) diffuse reflectance on rough surfaces. 52

Figure 2.9: (a) A picture of the PEC measurement set-up, (b) schematic of the three electrode PEC cell and photographs of (c) the quartz cubic cell, (d) three electrodes, (e) cell lid mounted with the three electrodes and (f) InP and GaN photoelectrodes used in this dissertation. 55

Figure 2.10: Schematic of electrochemical impedance spectroscopy measurement set-up…………………………………………………………………………………..57

Figure 3.1: Flow chart of the processing steps involved in top-down fabrication of GaN NPs using ICP etching of EBL-patterned GaN epilayer. 61

Figure 3.2: SEM images of GaN NP arrays with 100 nm diameter and a pitch of (a) 400 nm (b) 600 nm and (c) 800 nm taken at a 52° tilt angle. 61

Figure 3.3: (a) NP dimensions used for calculating the sidewall angle, α and (b) variation of NP sidewall angle as a function of array pitch. 62

Figure 3.4: (a) Room temperature PL spectra from NP arrays with different pitch and (b) normalized peak intensity and full width at half maximum of the PL

emission as a function of array pitch. Data for the GaN epilayer in (b) is also shown for comparison at pitch = 0. 63

Figure 3.5: Power dependent PL of GaN epilayer and NP array with 400 nm pitch measured at room temperature using μ-PL. 64

Figure 3.6: Electric field distribution of incident radiation in (a) epilayer, (b) NPs and (c) influence of array pitch on reflection, transmission and absorption properties calculated using FDTD simulations. The color bars on the right sides of figures (a) and (b) represent the normalized intensity of the electric field distribution of incident radiation from 0 to 1. 65

Figure 3.7: Far field emission patterns from (a) epilayer, (b) NPs in xy-plane and the influence of array pitch on (c) collection efficiency and (d) light extraction efficiency. 67

Figure 3.8: Dependence of quantum efficiency on photo-excited carrier concentration. The points are experimental data and the line is a fit to experimental data following the approach of Yoo et. al [21]. 70

Figure 4.1: Illustration of the processing steps involved in the fabrication of random GaN NPs using a top-down approach. 77

Figure 4.2: SEM images of (a) the Ni random mask formed by RTA annealing of 5 nm Ni at 900 ^{0}C in an Ar atmosphere, (b) the SiO_2/Ni random mask from the top and (c) the SiO_2/Ni hard mask taken at a 52^0 angle. 78

Figure 4.3: Photographs of (a) a NP photoanode with Ni/Au contacts and (b) a NP photoanode painted with nail polish to avoid carrier leakage into the electrolyte. 79

Figure 4.4: SEM images of (a) to (c) GaN NPs (images taken at a 30^0 tilt angle) with increasing lengths obtained from 5 nm Ni masked GaN sample by varying the ICP etch times from 60 to 120 s and (d) to (f) GaN NPs with increasing diameter (images taken at a 52^0 tilt angle) achieved by 120 s ICP etching of 5, 10 and 15 nm Ni masked GaN epilayers. 79

Figure 4.5: Diameter distribution of GaN NPs fabricated from ICP etching of (a) 5, (b) 10 and (c) 15 nm Ni masked GaN samples. 80

Figure 4.6: Diffuse reflectance spectra of planar and NP samples fabricated using 5, 10 and 15 nm thick Ni film mask. 81

Figure 4.7: Schematic illustration of band bending in n-doped semiconductors NPs............82

Figure 4.8: Linear sweep voltammetry of GaN planar and NP photoanodes measured in 1 M NaOH electrolyte using a three electrode configuration PEC setup under dark and sunlight illumination...83

Figure 4.9: Linear sweep voltammetry of planar n-GaN photoanodes with varying carrier concentration. 85

Figure 4.10: Linear sweep voltammetry of GaN NP photoanodes of fixed diameter and length with varying carrier concentration. 86

Figure 4.11: ABPE of (a) planar and (b) NP GaN photoanodes with varying carrier concentration...86

Figure 4.12: Linear sweep voltammetry of GaN NP photoanodes of varying diameter fabricated using ICP etching of 5, 10, 15 nm Ni film masked Sample 2 for 120 s. D1, D2 and D3 in the figure legend represent the NP samples fabricated using 5, 10 and 15 nm Ni film masks respectively...88

Figure 4.13: Linear sweep voltammetry of GaN NP photoanodes of varying lengths, where the ICP etching time was set to 30, 60 and 120 s to vary the length of NPs formed using the 5 nm Ni masked Sample 2. L1, L2 and L3 in the figure legend refers to the NP samples etched for 30, 60 and 120 s respectively. 89

Figure 4.14: Nyquist plots of GaN planar photoanodes with varying carrier concentration and NPs fabricated from S2 using 5 nm Ni etch mask and 120 s ICP etching time. 90

Figure 5.1. (a) Schematic of InGaN/GaN MQW epilayer structure and (b) SEM image of InGaN/GaN MQW NPs...96

Figure 5.2. Diffuse reflectance spectra of (a) planar and (b) NP InGaN/GaN MQWs with varying In concentration. Ref, 20, 30 and 50% In legend indicate the InGaN/GaN samples with 0, 20, 30 and 50% In content in InGaN respectively. 97

Figure 5.3. Room temperature photoluminescence spectra of InGaN/GaN MQW (a) planar and (b) NP samples. Ref, 20, 30 and 50% In in the legend represent the 0, 20, 30 and 50% In content in the InGaN/GaN samples respectively..................................99

Figure 5.4: J-V characteristics of InGaN/GaN MQW planar photoanodes measured under dark and sunlight illumination using a three terminal PEC set up..............................101

Figure 5.5. J-V characteristics of InGaN/GaN MQW NP photoanodes measured under dark and sunlight illumination using a three terminal PEC set up..............................102

Figure 5.6. Incident photon-to-current efficiency (IPCE) of the reference and 30% In planar and NP photoanodes measured at zero applied potential versus the Ag/AgCl reference electrode. 104

Figure 5.7: ABPE of InGaN/GaN MQW (a) planar and (b) NP photoanodes with different In content in InGaN layers. 105

Figure 5.8. (a) Photostability of planar and NP GaN reference photoanodes under AM1.5 light illumination at 0 V vs. Ag/AgCl in 1 M NaOH electrolyte and (b) schematic energy band diagram of GaN/co-catalyst/electrolyte and electron and hole transfer at the material interfaces (CB: conduction band, VB: valence band and E_f: Fermi level)..106

Figure 5.9. SEM image of GaN NPs decorated with a NiO co-catalyst taken at a 52° tilt angle...107

Figure 5.10: (a) Current density-time plots of NP photoanodes with the NiO co-catalyst, (b) long term photostability of NiO-coated NP photoanodes under AM1.5 light illumination at 0 V vs. Ag/AgCl in 1 M NaOH electrolyte and (c) variation of photocurrent density with applied bias for GaN NP photoanodes with and without NiO co-catalyst. 108

Figure 5.11: (a) SEM image of GaN NPs coated with Co_3O_4 nanoparticles using flame spray synthesis, (b) linear sweep voltammetry of NP photoanodes with and without Co_3O_4 under one sun illumination and (c) photostability of the NP photoanodes in 1 M NaOH electrolyte with and without Co_3O_4. 109

Figure 5.12: (a) Nyquist plots of bare (open squares) and Co_3O_4-decorated GaN NP photoanodes (solid squares) fitted with an equivalent circuit impedance and (b) the equivalent circuit used to model the photoelectrode/electrolyte interface. In figure (a), the solid black line is the fitted curve from the equivalent circuit model. 110

Figure 6.1: SEM image of InP NPs fabricated using ICP etching of self-organised randomly masked p-InP wafers. The image was taken at a 52° tilt angle and the scale bar is 500 nm. 117

Figure 6.2: SEM images of (a) as-fabricated large area InP NPs and S-OA trim etched NPs for (b) 60 min and (c) 90 min. SEM images were taken at a 52° tilt angle and scale the bar is 500 nm. 119

Figure 6.3: (a) TRPL decay curves and (b) PL spectra of the InP wafer and NPs with and without wet treatment in S-OA solution measured by exciting the samples with a green laser. 120

Figure 6.4: Diffuse reflectance spectra of InP planar and NPs before and after S-OA wet etching. 122

Figure 6.5: Linear-sweep voltammetry of planar and as-fabricated InP NP photocathodes under one sun illumination in 1 M HCl electrolyte. 124

Figure 6.6: Influence of wet treatment on (a) PEC performance and (b) ABPE of NPs tested in 1 M HCl electrolyte. 125

Figure 6.7: (a) Nyquist plots of NP photocathodes measured before and after S-OA treatment and fitted to the Randles circuit and (b) Equivalent electrical circuit. 127

Figure 6.8: Amperometric J-t curves of the InP NP photocathodes at 0 V vs. RHE under simulated one sun illumination in 1 M HCl electrolyte with and without S-OA treatment. The inset shows the transient J-t plots of InP NP photocathodes. 128

Figure 7.1: Schematic of the semiconductor/electrolyte interface energetics in electrolyte for (a) p and (b) n^+-p InP photocathodes [4]. 137

List of Tables

Table 1.1: Commonly used metal oxide redox cycles in a two-step thermal water splitting for hydrogen generation[9]. 5

Table 4.1: Sample numbers and the corresponding n-type carrier concentrations. 77

Table 4.2: Estimated depletion layer width for different carrier concentrations in n-GaN epilayers. 82

Table 5.1. Fill factor calculated for PEC performance of planar and NP photoanodes. 103

Table 6.1: Minority carrier lifetime of the InP wafer and NPs with and without S-OA treatment extracted by fitting the TRPL decay curves with exponential decay functions. 121

Chapter 1

Introduction

1.1. Background and motivation

The development of renewable energy technologies is of utmost importance to sustain the civilization of human kind, with major environmental concerns arising from fossil fuel usage for energy generation. According to the International Energy Outlook 2017, the U.S. Energy Information Administration (EIA) predicts that global energy consumption is expected to rise by 28% from the year 2015 to 2040 (Figure 1.1(a)) [1]. The escalating energy demands emerge from countries outside of the Organization for Economic Cooperation and Development (OECD) to meet their strong and long-term economic growth and fast-growing populations. Although renewable energy is the fastest growing form of energy, fossil fuels such as coal, natural gas and petroleum are still expected to continue as the dominant energy resources to meet the global energy demands (Figure 1.1(b)). Fossil fuels are predicted to be exhausted in the next 50 to 100 years if they are consumed at the present rate. Moreover, the increased combustion of fossil fuels over the next few decades is expected to raise the carbon dioxide (CO_2) levels in the atmosphere by 16% from the year 2015 to 2040 (Figure 1.1(c)). Non-OECD nations will become the main sources of increased CO_2 emissions as they continue to rely heavily on fossil fuels to meet the growth in energy demand. In the case of non-OECD nations, CO_2 emissions will increase by 25% in 2040 compared to the 2015 level, while the emissions from OECD nations will remain at the same level for the projected period of time. The fast-growing CO_2 emissions into the atmosphere can become a serious threat to the global environment and ecological systems due to global warming, which causes the rise of sea levels, frequent and intense heat waves, severe droughts, increased floods due to heavy rainfall and powerful hurricanes.

To prevent global warming threats, 197 countries agreed to take the initiative to keep this century's global temperature rise below 2 ^{O}C above pre-industrial levels in the 2015 Paris Agreement that came into effect on 4 November 2016. Nuclear technology has proven to be one of the most successful commercial carbon free technologies for generating electricity. At present, several countries rely on nuclear technology for energy generation, which is expected

to grow at an average rate of 1.5% per year from 2015 to 2040 as shown in Figure 1.1(b). However, the safety, storage and maintenance of radioactive waste is always a cause of concern for nuclear power generation. Severe disasters such as massive death tolls and long-lasting diseases have taken place in history due to system faults and natural disasters. Moreover, nuclear fuel is a non-renewable energy resource like fossil fuels.

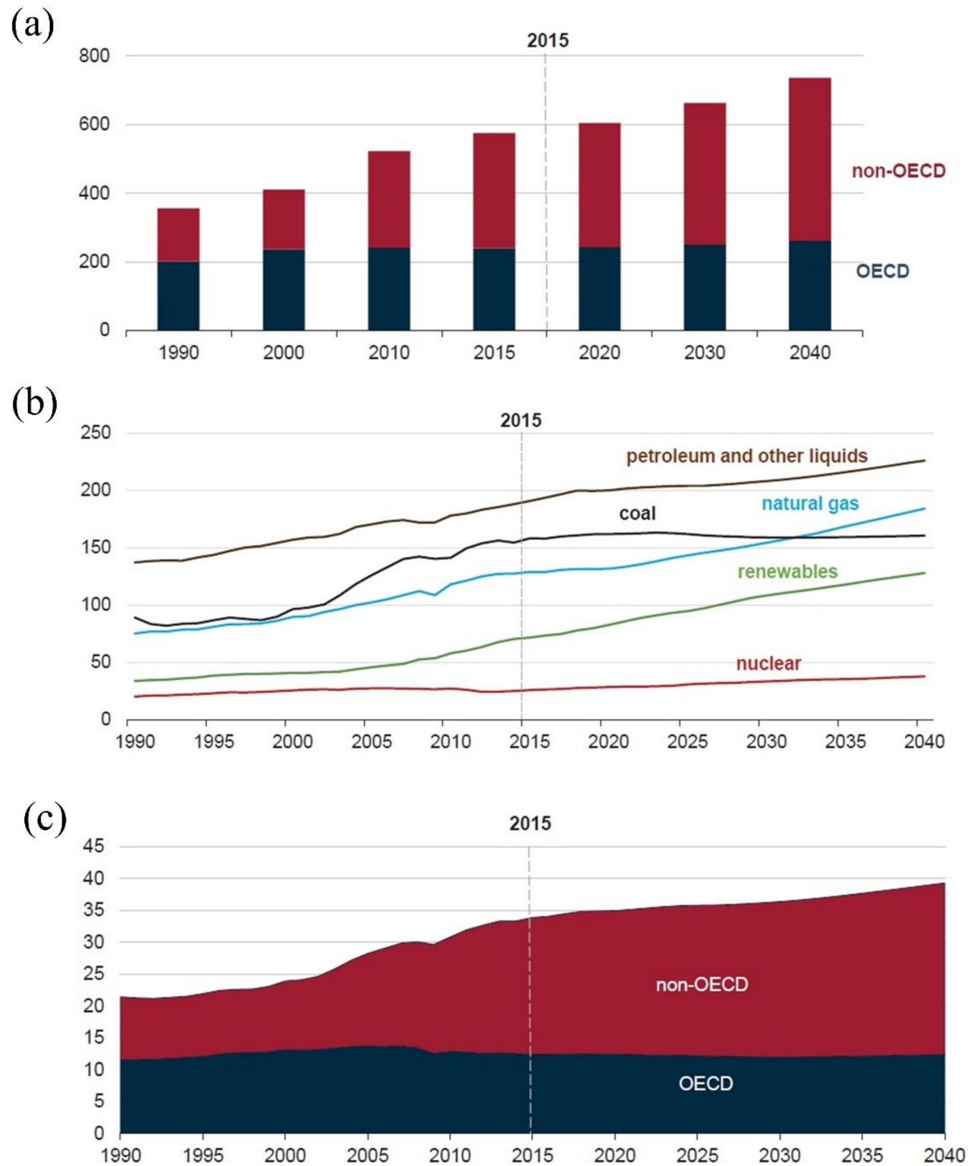

Figure 1.1: History and prediction of (a) the global energy consumption in quad units, (b) the consumption pattern of resources for producing energy and (c) the energy related carbon dioxide emissions.

Therefore, the development of renewable energy technologies is crucial for generating carbon free electricity to meet sustainable global energy needs. At present, renewable energy

contributes 17% of the total electricity generated by all the available energy resources and is expected to reach 27% by 2040 at an average annual growth rate of 2.8%. Solar energy has great potential to become the leading renewable energy resource among all the existing renewable sources such as hydropower, wind, tidal, biomass and geothermal in terms of extractable energy and may even overcome the predicted renewable electricity generation [2]. Earth receives three orders of magnitude higher solar energy than the present global energy requirement (18.3 terawatt-year per annum in 2014). Therefore, the development of efficient and cost-effective solar energy technologies to harness solar energy could position solar energy as the mainstream energy resource for surplus carbon free electricity generation. Solar cells, which convert sunlight directly into electricity, are leading the renewable energy technologies at present [3]. However, the intermittent nature of the output energy and transportation losses are the biggest hurdle for solar cells to meet the future goals of fully renewable energy sources [4-6]. Unpredictable weather and seasonal changes result in huge fluctuations in energy production that can result in frequent breakdowns of power grids connected to solar cell plants, which supply electricity to the consumers. Solar cells also require ultra-high capacity energy storage devices for storing electricity generated during the day to meet the night time needs.

The conversion of sunlight to chemical energy can be a promising alternative approach to meet the energy demands of future generations because chemical fuels can be stored either in gaseous or liquid form and used when required. Further, the transport of chemical fuels using pipelines or freight reduces the energy transportation losses significantly compared to the electricity losses generated by other resources. The solar-to-chemical energy conversion can be best achieved by artificial photosynthesis using artificial materials. Research interest in photocatalytic water splitting is growing strong compared to other artificial photosynthesis processes as this technique produces clean, storable and high energy density hydrogen as a fuel. This technique uses sunlight to generate hydrogen by splitting water into hydrogen and oxygen. The hydrogen can be used as a fuel to generate electricity using fuel cells and to drive motor vehicles by burning hydrogen in internal combustion engines [7]. The combustion of hydrogen, in turn, produces environmentally friendly water as a reaction by-product. In order to capture these advantages, the development of cost effective, highly efficient and stable renewable technologies should be realised to produce hydrogen in a sustainable and economic manner. The US Department of Energy (DoE) estimates that hydrogen will be cost competitive with fossil fuels when the production cost for hydrogen reaches to \$2 to \$4 kg^{-1}, including production, delivery and dispensing [8]. However, at present, the cost of any hydrogen production technology is far away from this target. Although photocatalytic hydrogen

generation is still at research stage, it is a green technology and has the potential to become cost competitive among the existing technologies to produce hydrogen. In this context, this dissertation is an extensive study on robust and highly efficient photocatalytic water splitting for the production of hydrogen using sunlight using semiconductor photoelectrodes.

1.2. Renewable hydrogen production methods

Hydrogen can be produced via water splitting using three main processes such as thermolysis, electrolysis and photolysis by harvesting solar energy in either a direct or an indirect way. The hydrogen production cost should be reduced to

1.2.1. Solar thermal water splitting

Water is a stable substance and it is an abundant source of hydrogen. The generation of hydrogen fuel using solar thermal water splitting involves a series of thermochemical reactions at very high temperatures. Such high temperatures can be realized using solar energy concentrators to achieve solar thermal splitting of water into its constituent elements. Very high temperatures, greater than 2500 K, are mandatory for direct thermal decomposition of water into hydrogen and oxygen. Further, the production of oxygen and hydrogen in a single step may lead to the explosive accidents. Recently, multi-step chemical reactions were developed to avoid these risks by generating hydrogen and oxygen at different stages of the reaction. Moreover, reaction temperatures are reduced by developing suitable chemical reactions and catalysts after numerous studies. Currently, thermochemical water decomposition can be achieved at around 1000 ^{O}C, which can easily be achieved using solar light concentrators. In a typical two-step solar thermal water splitting (Figure 1.2), the first step involves the production of oxygen via metal oxide reduction at elevated temperature, generated using concentrated sunlight. In the second step, the metal oxide is recovered to the original oxidation state through an oxidation process under water exposure, releasing hydrogen. Generally, the oxidation of metal oxides takes place at a relatively lower temperature compared to the reduction process. Only a few metal oxides operate in two-step solar thermal water splitting, while the majority of metal oxides operate in three or more steps. The commonly used two-step thermochemical redox cycles for thermal water splitting are shown in Table 1.1. In general, two-step thermochemical redox cycles can be subdivided into two categories; volatile and non-volatile. Metal oxides used in volatile cycles undergo solid to gas phase transitions, whereas the metal oxides used in non-volatile redox cycles remain in the solid phase during thermodynamic chemical reactions. The non-volatile redox cycles can be further divided into stoichiometric

and non-stoichiometric cycles. Stoichiometric metal oxides form solid solutions during the reduction cycle and the metal oxide is partially reduced. In contrast, metal oxides used in non-stoichiometric cycles remain crystallographically stable while the lattice accommodates changes in anion or cation vacancy concentrations.

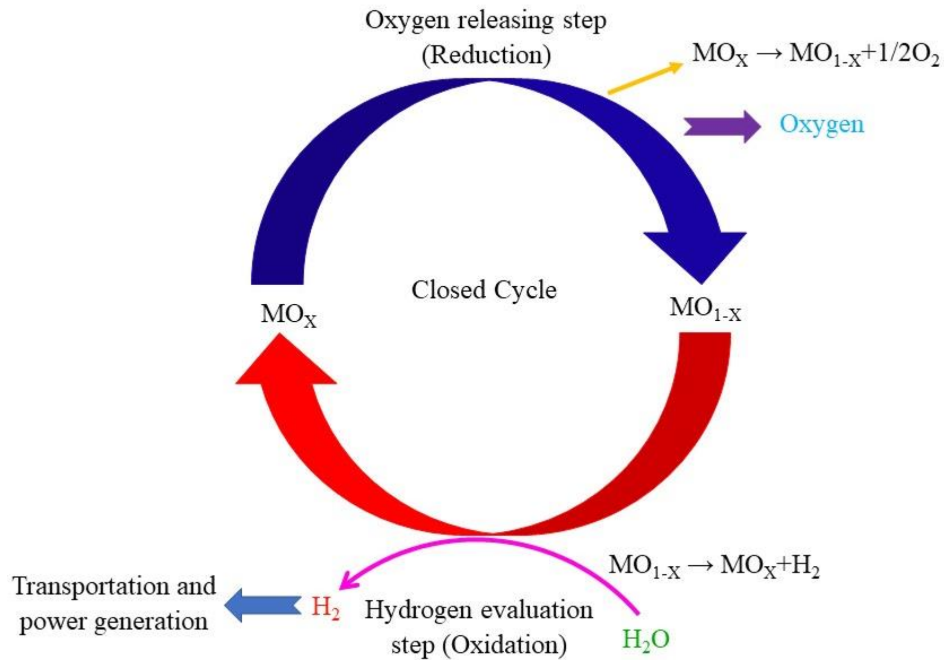

Figure 1.2: Schematic of two-step thermal water splitting

Table 1.1: Commonly used metal oxide redox cycles in a two-step thermal water splitting for hydrogen generation[9].

Category	Cycle name	Simplified reduction reactions
Volatile	Zinc oxide Tin oxide	$ZnO(s) \rightarrow Zn(g)$ $SnO_2 \rightarrow SnO(g)$
Non-volatile (Stoichiometric)	Iron Oxide Ferrite Hercynite	$Fe_2O_3 \rightarrow FeO$ $M_xFe_{3-x}O_4 \rightarrow xMO + (3-x)FeO$ $Fe_3O_4 + 3Al_2O_3 \rightarrow 3FeAl_2O_4$ $M_xFe_{3-x}O_4 + 3Al_2O_3 \rightarrow (3-x) FeAl_2O_{4-x} + xMAl_2O_4$
Non-volatile (non-stoichiometric)	Ceria Doped ceria Perovskite	$CeO_2 \rightarrow CeO_{2-\delta}$ $M_xCe_{1-x}O_2 \rightarrow M_xCe_{1-x}O_{2-\delta}$ $ABO_3 \rightarrow ABO_{3-\delta}$

Volatile and non-volatile stoichiometric redox cycles are proven to have high hydrogen production capacity. However, handling issues are the main hindrance for use in practical applications. Volatile metal oxides require a rapid thermal quenching step to prevent material loss due to the gas phase deposition of material on the reactor surfaces. Non-volatile stoichiometric redox cycles have the possibility to sinter or slag phase after the reduction step. Among the thermochemical redox pairs in Table 1.1, perovskites are promising candidates as the reduction process takes place at lower temperature and can produce significant quantities of hydrogen at relatively high reaction rates. The lack of optimum metal oxides and suitable reactor designs are preventing solar thermal water splitting from becoming commercially viable technology for hydrogen generation, although significant efforts have been made.

1.2.2. Electrolysis

In electrolytic processes, electricity is passed through water to split it into hydrogen and oxygen. A device used for water electrolysis is called an electrolyzer and the schematic of a typical electrolyzer is shown in Figure 1.3. The use of electricity generated from fossil fuels for electrolytic processes again produces greenhouse gases. The use of renewable technologies to supply the electricity for running the electrolyzer makes it a renewable and clean energy technology for generating hydrogen fuel. The combination of renewable energy and electrolyzer is an industrially developed technology and it has potential to be a major hydrogen producer. The electricity generated from solar cells and wind mills is used for the electrolysis of water (Figure 1.4). The oxidation reaction occurs at the anode and produces oxygen, while the reduction reaction occurs at the cathode and generates hydrogen. The chemical reactions involved in electrolysis are as follows

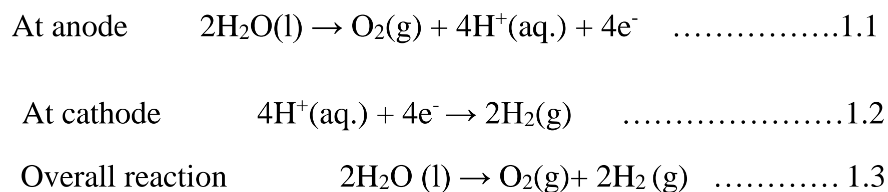

At anode $2H_2O(l) \rightarrow O_2(g) + 4H^+(aq.) + 4e^-$ ……………1.1

At cathode $4H^+(aq.) + 4e^- \rightarrow 2H_2(g)$ …………………1.2

Overall reaction $2H_2O\ (l) \rightarrow O_2(g) + 2H_2\ (g)$ ………… 1.3

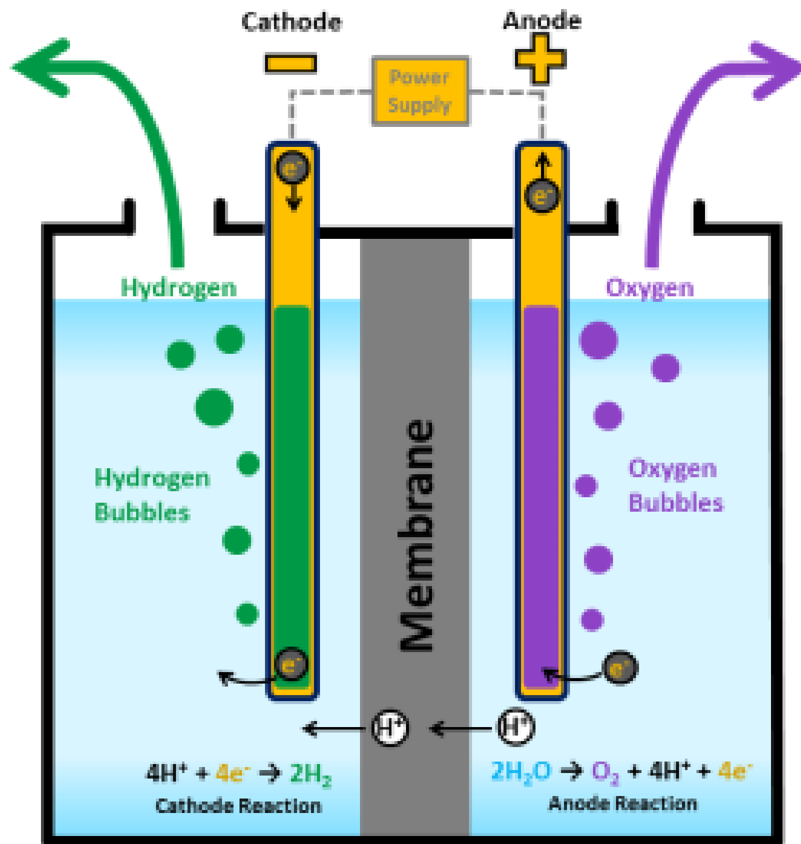

Figure 1.3: Schematic illustration of electrolyzer for electrolytic water splitting.

The gas generation rate in electrolysis is proportional to the current passed through the electrodes and the quantity of hydrogen is ideally twice that of oxygen. In an ideal case, a potential difference of at least 1.23 eV between the cathode and anode is required to split water into hydrogen and oxygen in electrolysis. However, in practice, a potential energy of 1.6 – 2.0 eV is needed for the electrolysis of water due to resistive voltage drops and other electrolyzer losses. The difference between the potential energy for practical and ideal water splitting is called the overpotential. Overpotentials can be minimized by loading oxygen and hydrogen evaluation catalysts onto their respective anode and cathode, which in turn improve the efficiency of the electrolysis process. At present, electrolyzers with a conversion efficiency of 56-73% are commercially available in the market depending on the electrolysis technology [10, 11] . Various studies are still in progress to further improve electrolyzer efficiencies to 85% [11, 12]. Despite highly efficient electrolyzers, high costs are involved in the generation of hydrogen using the renewable sources and electrolyzer combination. The high cost of electricity from renewable resources and energy losses including current conversions (DC-AC) and grid transmissions contribute to the high prices of hydrogen fuel (Figure 1.4). The cost reduction of electricity using renewables is critical to reach the targeted DOE cost goals of $2 - $4 kg^{-1} of hydrogen for renewable electrolysis of water.

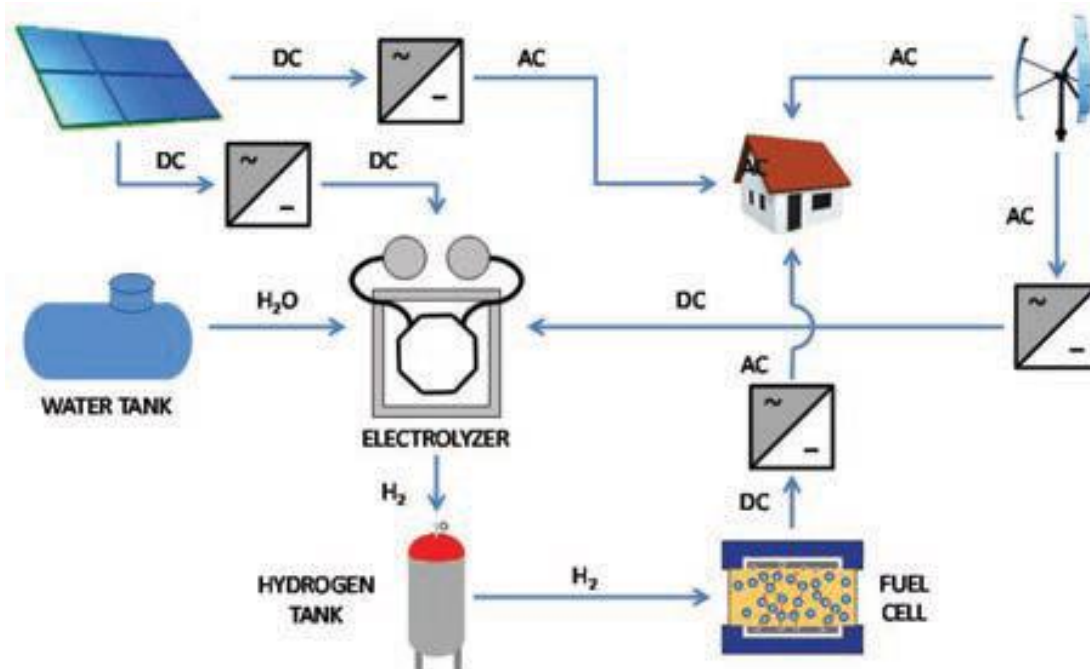

Figure 1.4: Schematic of hydrogen production through electrolysis of water using electricity generated by renewable technologies [13].

1.3. Photocatalytic water splitting

Photocatalytic water splitting is an alternative approach for renewable electrolysis for hydrogen generation. Unlike renewable electrolysis, sunlight is harvested by the electrodes themselves and used directly for water splitting in photocatalysis. The direct use of sunlight in photocatalysis eliminates energy losses due to multiple energy conversions and transmission losses, thereby have the potential to reduce the cost of hydrogen fuel. Further, the photocatalysis of water is a simple process unlike other solar hydrogen generation technologies that involve much complexity.

1.3.1. Working principle

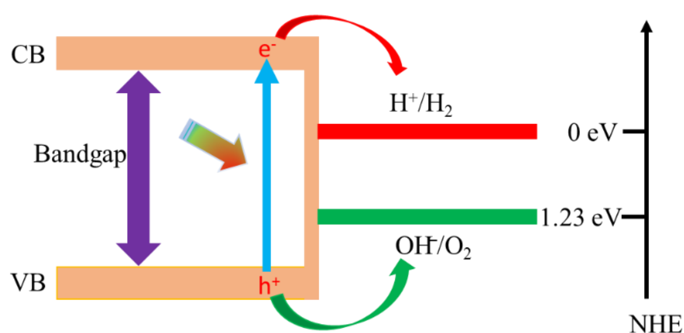

Figure 1.5: Schematic of the energy band diagram for photocatalytic water splitting for hydrogen generation.

The photocatalysis of water has attained enormous research interest for generating hydrogen since the first report on water splitting using TiO_2 by Fujishima and Honda [14]. Photocatalytic water splitting is a three-step process and its principle mechanism is shown in Figure 1.5. The illumination of a semiconductor with photons of greater energy than the semiconductor band gap excites electrons into the conduction band and generates electron and hole pairs in the material. The excited electrons in the conduction band and holes in the valence band migrate to the electrode surface. Holes in the valence band cause water oxidation at semiconductor surface to generate oxygen while electrons in the conduction band result in water reduction to produce hydrogen. The reduction and oxidation potentials of water lie at 0 and 1.23 V versus Normal Hydrogen Electrode (NHE), respectively. Notably, additional energies are required to overcome the energy barriers of the oxygen evolution reaction (OER) and hydrogen evolution reaction (HER), and to improve the charge transfer kinetics at the solid-liquid interface. Consequently, the ideal semiconductor band gap for photocatalytic water splitting lies between 1.6 to 2.0 eV [15]. Moreover, the conduction band must be more negative than the water reduction potential and the valence band must be more positive than the water oxidation potential for photocatalysts to split the water into its constituent elements. The overall water splitting reaction of photocatalytic water splitting is as follows:

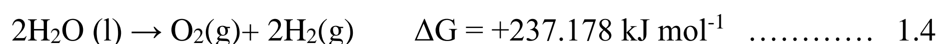

$$2H_2O\,(l) \rightarrow O_2(g) + 2H_2(g) \qquad \Delta G = +237.178 \text{ kJ mol}^{-1} \quad \ldots\ldots\ldots\ldots \quad 1.4$$

Figure 1.6 shows a schematic of photogenerated carriers that undergo different processes. After photoexcitation, in an ideal case, photogenerated carriers migrate to surface reaction sites and participate in water redox reactions. However, in reality, some of the photogenerated carriers are lost due to bulk and surface recombination. Defects in the materials act as traps for photogenerated carriers and become deactivation centers for water splitting. These deactivation centers are detrimental to solar-to-hydrogen (STH) conversion efficiency. A reduction in photocatalyst size can mitigate bulk recombination due to the reduced carrier transfer length to the surface. Further, a reduction in photocatalyst size enhances the catalytic sites for water splitting due to the increased surface area of the photocatalyst. However, photocatalyst size should not fall into the regime of surface recombination domination regime. These two factors can help to improve the STH conversion efficiency of the photocatalyst. Photocatalysis can be classified into two types: photochemical water splitting and photoelectrochemical water splitting [16-18].

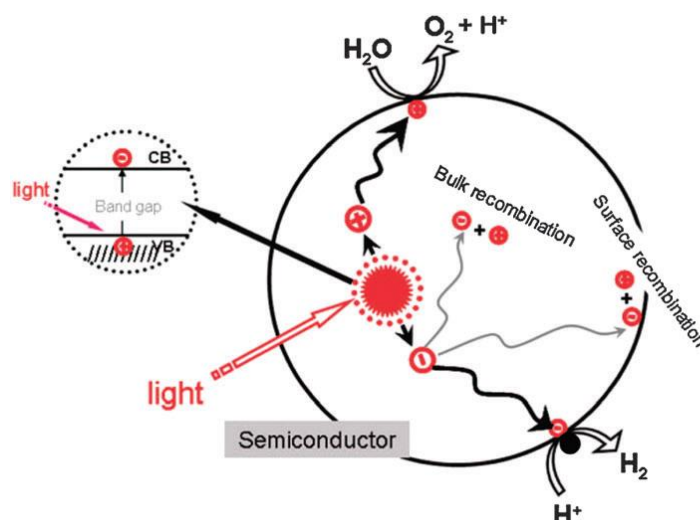

Figure 1.6: Schematic illustration of the photocatalytic water splitting principle [19]

1.3.2. Photochemical water splitting

In photochemical water splitting, the water redox reactions take place at the same semiconductor surface. An example of a photochemical water splitting system is illustrated in Figure 1.7. The semiconductor photocatalysts are suspended as nanoparticles in the electrolyte. In order to generate hydrogen using photochemical reactions, the band edges of the semiconductor materials must straddle the water redox potentials. A wide variety of oxide and sulfide materials have been developed for photochemical water splitting applications under UV and visible illumination since the first demonstration on TiO_2 by Fujishima and Honda in 1972. Nitrides and oxynitrides such as Ta_3N_5, TaON and $LaTiO_2N$ have also been demonstrated for photochemical hydrogen fuel generation [20]. However, photochemical water splitting suffers due to the lack of robust materials with optimum band gaps for efficient water splitting. The loss of photogenerated carriers due to recombination is another challenging issue in photochemical systems. The loading of co-catalysts can minimize the recombination of photogenerated carriers at the surface by facilitating charge transfer, thereby enhancing the conversion efficiency (Figure 1.8). K. Maed et al. demonstrated an improvement in water splitting efficiency using co-catalysts by decorating GaN:ZnO solid solution with Mn_3O_4 and Rh/Cr_2O_3 as O_2 and H_2 evolution promoters, respectively [21]. Recently, a solar -to-hydrogen (STH) conversion efficiency of 1.8% under concentrated sunlight was reported by M. G. Kibria et al. for a Rh/Cr_2O_3 co-catalyst deposited on double band GaN/InGaN nanowires [22] for visible light driven water splitting. Over 130 inorganic semiconductors including oxides, sulfides, phosphides, nitrides and oxynitrides are known to catalyze the photochemical water splitting reaction or either water oxidation or reduction in the presence of sacrificial agents

[23]. Although a wide variety of photocatalysts have been developed, the detailed mechanisms of water reduction and oxidation on semiconductor surfaces are not yet well understood at the molecular level. Many questions about charge transfer between semiconductors and co-catalysts, and its dependence on the structural and electronic features of the interface are still open [23].

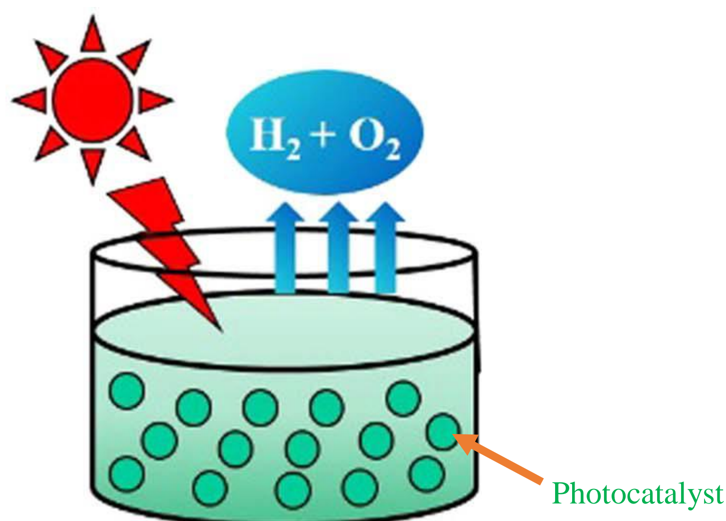

Figure 1.7: Schematic of a photochemical system for water splitting [24, 25].

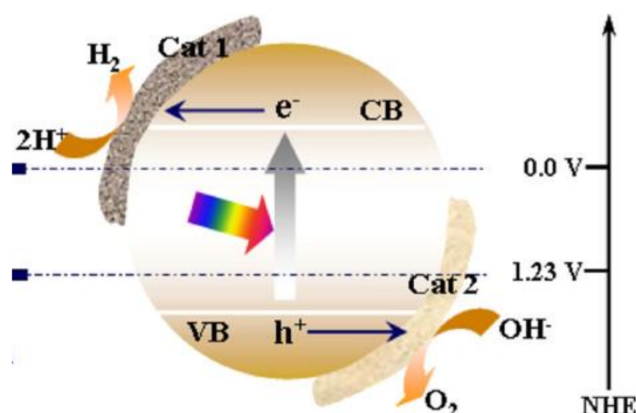

Figure 1.8: Schematic illustration of photocatalytic water splitting [15].

1.3.3. Photoelectrochemical water splitting

A schematic illustration of a typical photoelectrochemical (PEC) water splitting system is shown in Figure 1.9. The PEC system comprises a working electrode and a counter electrode dipped in electrolyte. The working electrode can work either as a photoanode or photocathode depending on the type of photoactive material. The minority carriers drift to the photoelectrode surface after sunlight illumination and participate in the half water redox reaction at the surface.

The majority carriers are transferred to the counter electrode through the external circuit/bias and perform the remaining half water redox reaction at the counter electrode. In PEC water splitting, hydrogen and oxygen are generated separately. This facilitates the collection of ultrapure hydrogen after vapor removal. Contrary to the photochemical process, this system does not require an external gas unit to separate the hydrogen and oxygen. Analogous to the photochemical system, catalyst loading and nanostructuring of the photoelectrode play a crucial role in improving the water splitting efficiency of the PEC system [26]. Over 18% STH conversion efficiency was reported for photoelectrode consisting GaInP and GaInAs subcells on a GaAs by W. H. Cheng et. al. using PEC water splitting [27]. However, these photoanodes suffer from high materials cost and photodegradation [27, 28]. The economic viability and stability of the photoelectrodes are crucial while achieving the targeted 10% STH conversion efficiency for the commercialization of this technology [29, 30].

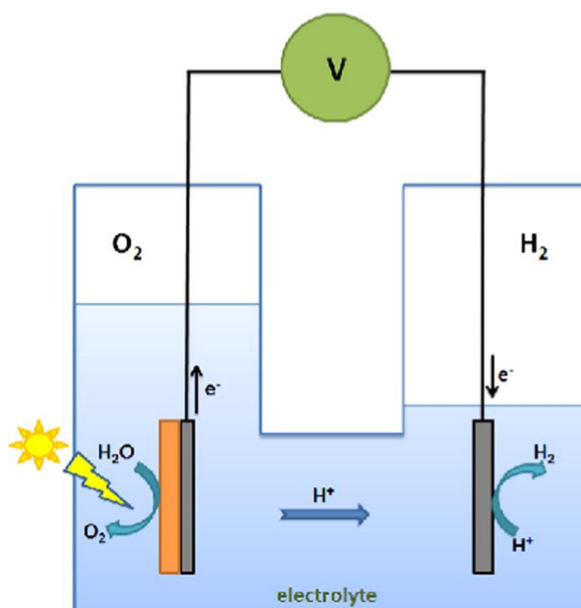

Figure 1.9: Schematic illustration of a photoelectrochemical system for solar water splitting [18].

1.4. Photocatalytic semiconductor materials

A broad range of semiconductors have been investigated extensively for the photocatalysis of water, since the first demonstration of the photocatalytic performance of TiO_2 in the 1970s [14, 16, 31, 32]. The photocatalysts are composed of the chemical elements which are listed in Figure 1.10 [24]. Oxides, nitrides and sulfides are widely studied materials among the various photoelectrode materials for water splitting applications. The valence band of the photoelectrode is typically composed of the 2p orbitals of oxygen, 2p of nitrogen or 3p of sulfur

elements. The conduction band of the material is formed either by the d or sp orbitals of the metal cation, having a typical electronic configuration of d^0 or d^{10}.

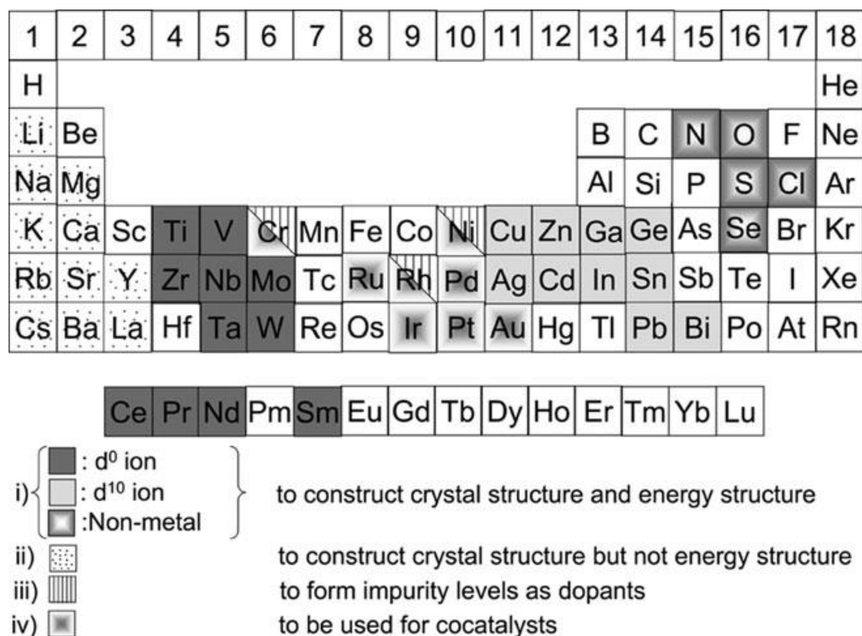

Figure 1.10: Chemical elements that are involved in the formation of photocatalysts [24].

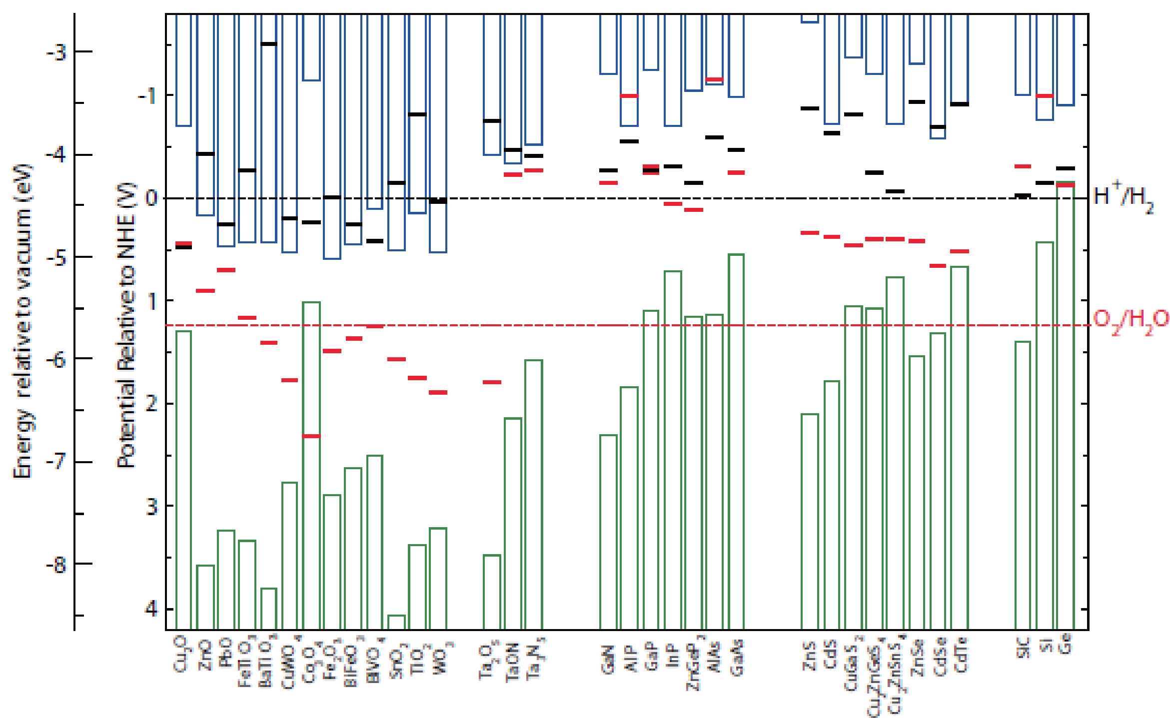

Figure 1.11: The calculated oxidation (red bars) and reduction potentials (black bars) relative to the NHE and vacuum level for a series of semiconductors in solution at pH=0, the ambient temperature 298.15 K, and pressure 1 bar. Also plotted are the water reduction (H^+/H_2) and oxidation (O_2/H_2O) potentials (dashed lines), and valence (green columns) and conduction (blue columns) band edge positions at pH=0 [33].

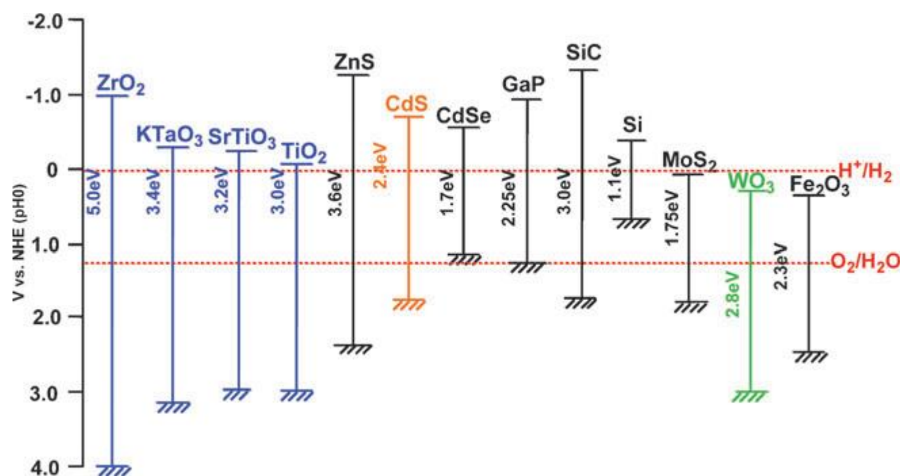

Figure 1.12: Band edge positions of various semiconductors against the water redox potentials [24].

Figure 1.11 and Figure 1.12 presents the conduction and valence band positions of various photocatalytic materials against the water redox potential at pH=0 calculated using ab initio simulations [33]. There is a considerably limited number of photocatalytic materials such as ZrO_2, $KTaO_3$, $SrTiO_3$, TiO_2, Cu_2O, Ta_2O_5, TaON, ZnS, CdSe, ZnSe, GaN and SiC that can perform overall water splitting without external energy as their energy band edges straddle both the water reduction and oxidation potentials. However, due to the wide band gaps of these materials, the STH conversion is limited to low values. The STH conversion efficiency, in theory, is highly dependent on the band gap of the material. Therefore, several band gap engineering approaches are proposed to minimize the band gap of the photoelectrode material. The introduction of foreign elements into conventional materials is the most commonly used strategy for band gap engineering of the materials. The incorporation of impurities introduces either donor or acceptor levels depending on the impurity type. As a result, low energy photons can be absorbed through donor level-CB or VB-acceptor level transitions and then contribute to the improved STH conversion efficiency. T. Umebayashi et al. showed the formation of localized occupied levels within the band gap or valence band with 3d transition metal doping of TiO_2 using ab initio band calculations, with a shift to lower energies with increasing dopant atomic number [34].

The nitridation of some metal oxides can engineer the band gap of the photoelectrode material. The relatively low positive orbital potential of the N 2p orbital compared to the O 3p can lead to a lower band gap after nitridation. The valence bands of these photoelectrodes are modified after the compound formation which is formed by the hybridization of the O 3p and N 2p orbitals and become less positive. TaON [20] and $LaTiO_2N$ are a few examples of band

gap engineering through the nitridation of metal oxides. The formation of solid solutions from materials having similar valence band potentials is one more approach to engineer the band gap of the photoelectrodes. GaN:ZnO is one of the most successful compounds with this strategy. The solid solution has a smaller band gap than that of its separate components, GaN (3.4 eV) and ZnO (3.2 eV), and exhibits a similar wurtzite crystal structure like that of its individual components. The repulsion between the Zn 3d and N 2p orbitals raises the valence band to more negative values which results in the reduced band gap of the solid solution. By following this approach, a GaN:ZnO solid solution with a band gap of 2.38 eV has been experimentally demonstrated with the composition $Ga_{0.38}N_{0.33}Zn_{0.13}O_{0.16}$ [35, 36]. Semiconductors, which cannot meet the energy criteria, can still be used for self-driven photocatalysis once a heterostructure is formed with materials of appropriate band gaps.

1.5. Aim of this thesis

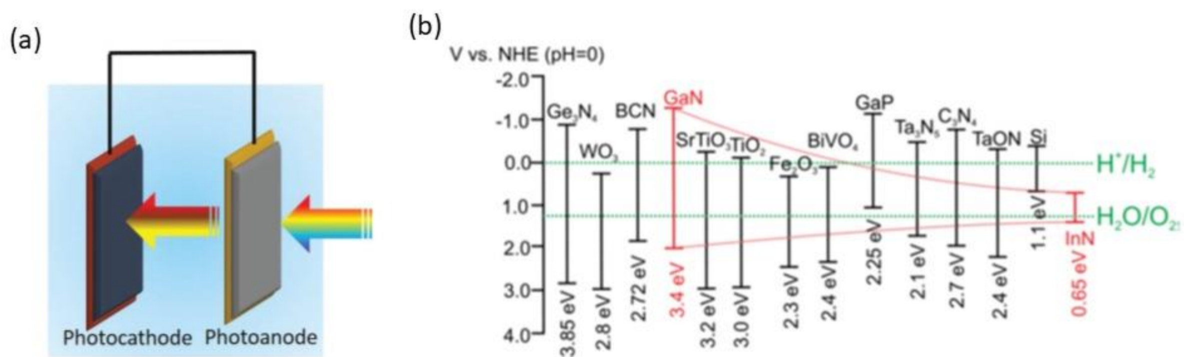

Figure 1.13: (a) Schematic of a PEC set up under tandem illumination and (b) band edge potentials of various nitride materials against water redox potentials (green dotted lines) and band edge positions of $In_xGa_{1-x}N$ (red-dotted lines) with increasing x from left to right (0 to1) [40].

The development of efficient and economically viable photocatalytic materials is essential for hydrogen generation at the price of \$2-3 kg^{-1} set by the U.S. Department of Energy to compete with conventional energy resources [8]. A wide variety of materials such as metal oxides, sulphides, nitrides and many other semiconductor materials have been investigated for photocatalytic water splitting over four decades [37, 38]. However, to date, the reported STH conversion of photocatalytic materials is low due to poor carrier mobility, inefficient absorption and insufficient redox potentials. Inefficient absorption due to large band gaps in excess of 3 eV and poor hole mobility are the main drawbacks preventing oxides from being efficient

photoelectrodes [38, 39]. On the other hand, sulphides and oxynitrides require sacrificial reagents for hydrogen generation, although they have optimum band gaps and favourable energy band positions against water redox potentials, which is not ideal for hydrogen generation. There is a lack of single robust materials that can meet the ideal photocatalytic material requirements such as suitable band gap, high carrier mobility, stability and band edge positions for efficient photocatalytic water splitting.

The PEC tandem cell (Z scheme), consisting of photoactive- anode and cathode components with complementary energy band gaps, has been perceived to be an ideal and alternative approach for unassisted water splitting. A schematic of a PEC tandem cell for overall water splitting is shown in Figure 1.13(a). The simultaneous excitation of the photoelectrodes eliminates the basic requirement of favourable band edge potentials for a single material for overall water splitting as the reduction and oxidation reactions occur at different semiconductor surfaces. Moreover, the two semiconductors can have smaller band gaps because each needs to support only half reactions. Consequently, light absorption by the photoelectrodes can be extended into the visible region of the solar spectrum. However, for overall water splitting using PEC tandem cells to occur, the band edge potentials of the photocathode and photoanode must straddle the water reduction and oxidation potentials, respectively. Also, part of the sunlight should be transmitted from the front to the rear photoelectrode. Most importantly, the photoexcited photoanode and photocathode must provide sufficient photovoltage to oxidize and reduce water at the semiconductor/electrolyte interfaces without electrical energy from an external source. The combination of InGaN as a larger band gap front electrode and InP as a small band gap rear electrode as the photoanode and photocathode, respectively, can make an excellent PEC tandem cell to achieve outstanding STH conversion efficiency. The band gap of InGaN can be tuned by changing the In content in such a way that it can make an ideal tandem device with InP. The efficiency of a PEC tandem cell depends on the performances of the individual photoelectrodes and their half-cell conversion efficiencies. Therefore, the development of efficient GaN-based and InP photoelectrodes could enable high efficiency PEC tandem systems for overall water splitting.

The GaN-based ternary alloy InGaN is a promising material for photoelectrodes owing to its variable band gap, band edges that straddle the H_2 and O_2 redox potentials, larger carrier mobility and high chemical stability [41]. The band gap of InGaN can be varied from 0.7 (InN) to 3.4 eV (GaN) by varying the In concentration, which allows its light absorption to be tuned from the UV to far IR regions [42]. Moreover, up to an In content of 50%, the valence and conduction band edges of InGaN straddle both the hydrogen and oxygen evolution reaction

(HER and OER) potentials, which means that it can drive unassisted water splitting (Figure 1.13(b)) and also be used either as a photoanode or photocathode [22, 40, 43]. Due to its highly crystalline nature and strong ionic bonds, InGaN exhibits high carrier transport and chemical stability. On the other hand, InP possesses several attractive attributes such as a well-matched band gap of 1.35 eV to the solar spectrum, a favourably aligned conduction band for the water reduction reaction and low surface recombination velocity. The conduction band of InP lies above the water reduction potential to facilitate electron transfer for hydrogen generation, which makes it an optimum material for photocathodes. Further, the low surface recombination velocity of InP is an important characteristic for non-planar materials, specifically, nanostructured materials for photocatalytic water splitting to raise the photoconversion efficiency.

Further, nanostructures offer great potential for solar water splitting over their planar counterparts. Nanostructures possess several essential attributes towards achieving efficient water splitting such as enhanced light absorption, reduced carrier transfer lengths, large surface area to facilitate efficient charge transfer at the semiconductor/electrolyte interface and enlarged depletion area at the nanostructured surface that drives charge separation efficiently. In the case of GaN alloys, nanostructures have the potential to accommodate higher In concentrations while maintaining good quality InGaN layers given that nanostructures can be made stress-free [22, 44]. Nanostructures can be synthesized either using bottom-up or top-down approaches. Out of these two approaches, the top-down method is an ideal approach for the formation of nanostructures with controlled morphology and uniform doping as it allows for the use of high quality GaN epilayers grown using well-matured planar growth technology wherein the doping concentration can be precisely controlled. The morphology of the nanostructures can be controlled by well-established lithography techniques or random masking techniques. On the other hand, bottom-up approaches suffer from a lack of control over the morphology of nanostructures and doping of NPs [45, 46]. Therefore, a top-down approach provides the opportunity to analyse the influence of nanostructure parameters on their PEC performance.

This thesis is devoted to developing highly stable and efficient GaN-based and InP nanopillar (NP) photoelectrodes using a top-down approach for PEC water splitting applications by making use of the outstanding photocatalytic properties of GaN-based alloys and InP and the advantages of a top-down approach. We investigated the influence of carrier concentration, NP dimensions and band gap engineering of the nanostructures on the PEC performance to achieve optimum photoconversion efficiency. Several characterization

techniques were employed to elucidate the PEC results of NP photoelectrodes. We also carried out photostability tests for these photoelectrodes.

1.6. Literature Review

1.6.1. GaN-based ternary alloys

GaN-based alloys have attracted considerable research interest over the past decade for solar water splitting applications. The advancement of epitaxial techniques in the growth of high crystalline quality GaN epilayers in the early 90's, to meet the requirements of high performance LEDs, [47] opened the opportunity for GaN in solar water splitting applications [48-52]. An early demonstration of GaN as a viable photoelectrode material for PEC water splitting was reported in the year 1995 by Kocha et al. [53]. Following this first report, several investigations on the PEC properties of GaN photoelectrodes revealed that the band edges not only straddle both the water oxidation and reduction potentials but also overcome the overpotentials, which makes it an ideal material for photocatalysis without any external bias [53-57]. Lin et al. investigated the influence of Ga- and N-polar surfaces of n-GaN systems on their PEC properties [58]. They demonstrated that the onset potentials of Ga-polar surfaces are more negative than N-polar surfaces. However, N-polar surfaces yielded much higher photocurrents compared to Ga-polar surfaces at higher positive applied voltages. Ono et al. studied the dependence of the PEC properties of n-GaN photoanodes on the carrier concentration and found that the optimum carrier concentration to obtain the maximum photocurrent was 1.7×10^{17} cm^{-3} [59]. In another study, Maeda et al. found that the photocatalytic performance of GaN is strongly dependent on crystalline quality and the type of co-catalyst employed [60]. They revealed that the GaN surface on its own acts as an inherent OER catalyst for water oxidation reaction, while HER co-catalyst is critical for the water reduction reaction. They achieved stable and stoichiometric evolution of hydrogen and oxygen by coating GaN with a $Rh_{2-y}Cr_yO_3$ HER co-catalyst.

The large band gap of GaN limits its STH conversion efficiency as it can only capture about 5% of the solar spectrum. Therefore, engineering the band gap of GaN is essential to improve the STH conversion efficiency of GaN photoelectrodes. Several strategies have been employed to engineer the band gap of GaN to extend the absorption of GaN into visible region of the solar spectrum. Fuji et al. reported that the presence of alcohol in NaOH improved the hydrogen evolution rate by nearly two times and reduced the photocorrosion of the GaN caused by self-oxidation [61]. The enhanced hydrogen generation activity was attributed to the

relatively easier oxidation of alcohol compared to water. Arai et al. reported that doping with divalent-metal-ions (Zn^{2+} or Mg^{2+}) improved the efficiency of GaN photoelectrodes coated with RuO_2 as a HER promoter [62]. Researchers also employed the elimination of current crowding and surface area enhancement techniques to boost the efficiency of GaN photoelectrodes. Waki et al. employed photolithographically patterned metal strips and n-GaN ridges to achieve higher photocurrents for n-GaN photoelectrodes [63] as they eradicate current crowding and increase the effective surface area due to ridges. In another study, immersed finger-type indium tin oxide ohmic contacts were used on top of p-GaN and n-GaN to minimize current crowding at the semiconductor surface and improve the photoresponse and hydrogen generation rate of the GaN photoelectrodes [64, 65]. Nakamura et al. achieved a remarkably stable and relatively high photocathode current using polarization engineered photoelectrodes compared to p-GaN [66]. The proposed photoelectrode of u-GaN/AlN/n-GaN as a photocathode without p-GaN exhibited several times improvements in photocathode currents compared to that of p-GaN.

The extension of photocatalytic activity into the visible part of the solar spectrum is key to improving the GaN photoelectrode performance drastically. Liu et al. adopted defect-engineering strategy to demonstrate the visible region PEC activity of GaN photoelectrodes [67]. The introduction of Mn impurities into GaN reduced the band gap of GaN due to the formation of an intermediate band within the band gap of GaN, related to the Mn impurity. As a result, Mn-doped GaN photoelectrodes exhibited photoresponse characteristics in visible spectrum (400 to 600 nm) with an incident photon-to-current conversion efficiency (IPCE) of 61% at 450 nm. However, these photoelectrodes are prone to photocorrosion due to the presence of structural defects in GaN, formed by the introduction of Mn.

GaN can form a low band gap ternary alloy (InGaN) with the incorporation of In into GaN and the band gap of InGaN can be tuned from the UV to near infrared regions by varying the In content. Further, as discussed in Section 1.5 (Figure 1.13 (b)), the InGaN band edges can straddle both water redox potentials up to 50% In content in InGaN, which indicates that the photocatalysis of water can be possibly realized up to red and even near infrared spectral regions of the solar spectrum. Therefore, the incorporation of In into GaN is the most reliable band gap engineering strategy to improve the PEC conversion efficiency by capturing a large portion of the solar spectrum. Fuji et al. demonstrated the improved photocatalytic activity for an $In_{0.02}Ga_{0.98}N$ photoelectrode in 1 M HCl electrolyte compared to a GaN photoelectrode at 1 V_{CE} [68]. Li et al. investigated the influence of In content in InGaN on the PEC properties of 200 nm thick InGaN photoelectrodes grown using MOCVD [69]. The marked enhancement in

PEC performance and hydrogen generation rate was reported with increasing In concentration from 20% to 40%. However, the onset potential for the InGaN photoelectrodes was shifted towards positive potentials and increased with increasing In content from 0% to 20% [51]. The maximum photoresponse and IPCE of 9% at 400-430 nm with good photostability was observed for InGaN photoelectrodes with 20% In in HBr electrolyte [51]. In another study, Aryal et al. reported excellent photostability and much higher conversion efficiency for p-InGaN compared to p-GaN [50]. The stability was attributed to the p-type conductivity of the electrode because it participates in reduction reaction and hence prevents the photocorrosion of p-InGaN photoelectrodes. Li et al. applied surface treatment to $In_{0.3}Ga_{0.7}N$ in H_2SO_4 to obtain higher photocurrents and IPCE of 58% under 400-430 nm for $In_{0.3}Ga_{0.7}N$ photoelectrodes [70]. The In-rich InGaN phases, formed by In segregation on the surface, acted as surface recombination centers for photogenerated carriers and hence reduced the photocurrent. The H_2SO_4 treatment suppressed surface recombination centers by removing the In-rich InGaN phases, which resulted in improved photocurrents for H_2SO_4 treated samples compared to the untreated samples [71]. The growth of thick InGaN with high In concentration has been extremely challenging for a number of reasons such as lattice mismatch and formation enthalpy between GaN and InN [71-74]. These factors create a large number of non-radiative recombination centers and strong carrier localization, which limits the photoresponse of InGaN materials. Further, the growth of thick layer with high In concentration in InGaN/GaN generates misfit dislocations if they are grown beyond a certain critical thickness. This critical thickness of the InGaN layer falls drastically with increasing In concentration [75]. Therefore, the growth of high quality crystalline InGaN materials with high In content and sufficient thickness is extremely challenging.

The development of nanostructured materials can provide a solution to mitigate the bulk defects due to reduced foot print size and reduced carrier transfer lengths. In addition, nanostructures offer enhanced absorption and surface area for substantial improvement in conversion efficiency of photoelectrodes [76-80]. Further, nanostructures can accommodate higher In concentrations into InGaN due to strain relaxation which can help to capture a large portion of the solar spectrum. GaN-based nanostructures can be synthesized via bottom-up or top-down approaches. In the bottom-up approach, nanostructures are grown either by selective area epitaxial growth or vapour-liquid-solid growth [81-83]. Metal Organic Chemical Vapour Deposition (MOCVD) and Molecular Beam Epitaxy (MBE) are the most commonly used growth techniques for growing nanostructures using bottom-up approaches. A considerably good number of studies were carried out on GaN-based nanowires (NWs) grown using bottom-

up methods for water splitting applications [22, 44, 84-90]. Alotaibi et al. demonstrated high efficiency PEC water splitting and hydrogen generation using Plasma Assisted MBE (PAMBE) grown Si-doped and undoped nanowires (NWs) in HBr and KBr electrolytes. The maximum IPCE of ~15% and 18% were reported for undoped and Si-doped GaN nanowire photoelectrodes under 350 nm light illumination, respectively. Varadhan et al. demonstrated that surface passivation of GaN NWs in 1,2-ethane dithiol (EDT) improved the PEC performance and photostability of NW photoelectrodes substantially [91]. The IPCE of NWs was improved to 18.3% after EDT treatment compared to the IPCE of 8.1% obtained prior to the treatment. The PEC enhancement was attributed to several factors, including improved charge separation via the change in flat-band potential and band edge potentials and the enhanced carrier lifetime after the EDT passivation of the NWs.

To improve the photoconversion efficiency of the NW photoelectrodes, InGaN was grown either as InGaN NWs itself or as InGaN/GaN multiple quantum well (MQW) NWs as they extend absorption into visible region. Caccamo et al. demonstrated visible light driven water splitting using MOCVD grown GaN/InGaN core/shell NW structures with 30% In [89]. The GaN/InGaN core/shell NWs were synthesized using selective area MOCVD by growing InGaN around GaN NWs. The core/shell NWs exhibited 10-fold higher photocurrents compared to the GaN NWs and improved photoresponse compared to planar InGaN. Ebaid et al. reported 0.21% STH conversion efficiency for GaN/InGaN core/shell photoelectrodes [84]. The InGaN/GaN NWs were formed by epitaxial deposition of InGaN/GaN MQWs around GaN NWs in a core/shell structure using MOCVD. With careful optimization of In content and number of QWs, they achieved a maximum IPCE of 8.6% at 350 nm at 1 $V_{cathode}$ and an applied bias photon-to-current conversion efficiency (ABPE) of 0.21% at 0.4 $V_{cathode}$ in HCl electrolyte. In another work, the authors investigated the role of carrier dynamics in InGaN/GaN MQW core/shell NWs to understand their impact on the PEC properties of photoanodes [92]. The InGaN/GaN MQW photoelectrodes with QW thickness up to 3 nm exhibited higher onset potentials and lower photocurrent density due to strong localization effects and defect induced recombination in the QWs. The increase of QW thickness minimized the localization effects and exhibited strong band-to-band transitions. The authors achieved a high efficiency of 15% at 350 nm and 1 $V_{cathode}$ and high photocurrent at zero bias by careful engineering of the InGaN QW thickness. Kamimura et al. reported the growth of n- and p-InGaN NWs without GaN using PAMBE and employed them for PEC water splitting using *in situ* electrochemical mass spectroscopy. They achieved 60 min photostability and a maximum IPCE of ~40% at -0.5 V vs NHE in the entire visible region for the p-InGaN photoelectrode.

Rodriguez et al. obtained two times improvement in the PEC performance of InGaN photoelectrodes after the decoration of InGaN with InN quantum dots [93]. They demonstrated a maximum IPCE of 56% at 600 nm at 0 V *vs* Ag/AgCl and 10 h of photostability in H_2SO_4. In another study, Rajaambal et al. reported highly stable and efficient visible light PEC properties for ZnO photoelectrodes decorated with InGaN quantum dots [94].

InGaN NWs grown on Si were also used for water splitting applications. The growth of NWs on Si reduces materials cost and can supply an external bias if integrated with solar cells for overall water splitting. Hwang et al. synthesized three-dimensional hierarchical nanostructures of InGaN NWs on Si wire arrays to enhance the effective surface area for PEC water splitting [95]. The single phase InGaN NWs were grown by halide chemical vapour deposition vertically on the sidewalls of the Si wires. The hierarchical photoanodes achieved nearly five-fold improvement in photocurrents compared to InGaN NWs grown on a planar substrate. However, the measured photocurrent for hierarchical photoanodes was very low, which could be due to the fast carrier recombination and inefficient charge transfer resistance at the semiconductor/electrolyte interface. In another study, Alotaibi et al. demonstrated highly stable, efficient and scalable $In_{0.3}Ga_{0.7}N$/GaN core/shell double band NW photoanodes grown by PAMBE on a Si substrate for water splitting [96]. The core/shell double band NWs provided efficient light absorption and stable PEC reactions in HBr electrolyte. A maximum IPCE of 27.6% was measured at 350 nm at 1 V vs Ag/AgCl in HBr electrolyte. Recently, Chu et al. realized the growth of InGaN nanowires with a band gap of 1.7 eV (50%) on Si using PAMBE for solar water oxidation [97]. The InGaN NW photoanode loaded with an IrO_2 co-catalyst produced a low onset potential of 0.1 V vs RHE and a record half-cell solar energy conversion efficiency of 3.6%.

The integration of solar cell devices with InGaN photoelectrodes has been developed to supplement the external bias required for efficient overall PEC water splitting. A photoconversion efficiency of 0.18-0.23% was achieved using an n-InGaN photoelectrode biased by GaAs solar cells [98]. Dahal et al. realized a monolithic solar-PEC device with 1.5% STH conversion efficiency based on an InGaN/GaN MQW solar cell [99]. The monolithic device demonstrated excellent chemical stability for a prolonged time period (7 days). In another work, Fan et al. achieved a monolithic solar-PEC device for water splitting by growing a dual absorber photocathode, consisting of p-InGaN/tunnel junction/n-GaN NW arrays, on Si solar cells [100]. The monolithically integrated photocathode exhibited stable photoactivity for 3 hrs and an ABPE of 8.7% at 0.33 V_{NHE}, nearly unity faradic efficiency for hydrogen generation. Alotaibi et al. developed a dual-photoelectrode device, consisting of a photoanode

and a photocathode with complementary energy band gaps for unassisted solar-driven water splitting [101]. Both electrodes were illuminated in parallel by splitting the solar spectrum spatially and spectrally. They reported nearly 20-fold enhancement in the power conversion efficiency under visible light (400-600 nm) using a dual-photoelectrode device consisting of a GaN NW photoanode and an InGaN photocathode compared to the individual photoelectrodes in HBr electrolyte. In the same work, they further demonstrated the dual-photoelectrode consisting of GaN and InGaN photoanodes connected in parallel and a Si/InGaN photocathode for unassisted water splitting with a STH conversion efficiency of 1.5% [101]. Recently, notable work on GaN-based photocatalytic materials was carried out for the generation of hydrogen fuels using photochemical water splitting [22, 40, 90, 102-109]. So far, a stable STH conversion efficiency of ~1.8% was reached using photochemical water splitting for double-band GaN/InGaN NW structures in seawater under concentrated sunlight illumination [22].

Almost all GaN-based nanostructured materials used for PEC studies were grown using a bottom-up approach either with MOCVD or MBE. On the other hand, GaN-based nanopillars (NPs) fabricated using a top-down approach used for PEC water splitting are rarely reported. In a top down approach, nanostructures are fabricated via plasma or chemical etching of pre-patterned epitaxial grown wafers. Benton et al. [110] reported significant enhancement of photocurrent and hydrogen generation for n-GaN/MQW (InGaN/GaN)/p-GaN NPs, fabricated using a top-down process, compared with their planar counterparts. The hydrogen evolution rate was increased from 0.1 to 0.73 ml h^{-1} cm^{-2} and STH conversion efficiency enhanced from 0.1 to 0.73% using NP arrays. Tseng et al. investigated the influence of length of the NPs and surface damage to NPs that occurred during the dry etching on the PEC performance of NP photoanodes, however, the photocurrents were significantly low [111, 112]. Also, nanoporous GaN-based materials developed using photoelectrochemical and anodic etching were also employed for PEC studies and exhibited improved photocurrents compared to the planar photoelectrodes [113-115].

So far, irrespective of growth method, research has been mainly focused on improving the PEC performance of InGaN/GaN photoelectrodes by incorporating higher In concentrations into InGaN nanostructures. However, the systematic investigation of the effect of NP parameters on PEC performance is still missing. Understanding the influence of nanostructure dimensions, carrier concentration and In content in InGaN with controlled nanostructure dimensions on PEC performance can build a strong foundation to design highly efficient nanostructured photoelectrodes by optimizing the nanostructure properties. The NPs formed with a top-down approach can provide the best platform for understanding the

dependence of PEC performance on NP parameters as they are derived from highly crystalline and uniformly doped epitaxial wafers with well controlled mask pattern techniques. On the other hand, the bottom-up growth of GaN NWs has not yet reached state-of-the-art material quality level [116]. Therefore, the top-down approach is an ideal method for fabricating NPs to investigate the influence of carrier concentration, NP dimensions and In concentration on the PEC performance of NP photoanodes.

1.6.2. Indium phosphide

Lately, indium phosphide (InP) has attained considerable research interest as a photocathode for PEC solar water splitting owing to its direct band gap nature, well matched band gap (1.35 eV) to the solar spectrum, favourable conduction band position with respect to the water reduction potential and low surface recombination velocity. Moreover, InP can make a well matched low band gap material for tandem photoelectrodes to generate hydrogen fuel with a high photoconversion efficiency. So far, Gao et al. have achieved the highest stable photocathodic conversion efficiency for InP-based photocathodes. They reported 15.8% cathodic conversion efficiency for a buried junction p-n^+ InP photoelectrode with periodic array of NPs at the surface in $HClO_4$ electrolyte under one sun illumination [117]. The onset potential of the photoelectrode was controlled by the buried junction instead of the semiconductor/electrolyte interface which resulted in very high onset potential for the photocathode. The periodic array of NPs at the top of photoelectrode, fabricated by nanoimprint lithography and plasma etching, improved the photocurrent due to enhanced absorption. These two factors contributed to achieve the highest photo conversion efficiency of 15.8 % for InP-based photoelectrodes. In the same work, the author’s group demonstrated six hours stability of the InP photocathode by depositing a thin TiO_2 layer using atomic layer deposition (ALD) [117].

Heller and Vadimsky were the first to demonstrate p-InP as a photoelectrode for PEC water splitting in 1981. They demonstrated 12% conversion efficiency and 28 mA/cm^2 photocurrent density in HCl electrolyte under one sun illumination for a p-InP photocathode coated with a rhodium catalyst [118]. Munoz et al. improved the light-to-chemical conversion efficiency to 14.5% by photoelectrochemical treatment of homoepitaxial p-InP (100), grown by MOCVD, followed by Rh deposition [119]. The increased surface activation of the InP contributed to the improved photoconversion efficiency of the photocathode. The surface activation occurred due to the increased electron affinity of the semiconductor by 0.44 eV after photoelectrochemical treatment in 1 M HCl because of the formation of In-Cl interfacial

dipoles. Lee et al. demonstrated the photostability of InP photoelectrodes in $HClO_4$ electrolyte by depositing a TiO_2 film as a protective layer on top of the InP [120]. Lin et al. reported that the TiO_2 not only stabilized the InP photocathode but also improved the onset potential [121]. The surface recombination of the InP was reduced after TiO_2 deposition due to favourable band-bending at the InP/TiO_2 interface for selectively collecting minority electrons while repelling the holes. As a result, the onset potential of the InP photoelectrode was improved from 0.63 V vs RHE for bare p-InP to 0.81 V vs RHE for the TiO_2-coated p-InP photocathode in $HClO_4$ electrolyte under one sun illumination [121]. In another study, a remarkable improvement in solar hydrogen generation was demonstrated by Li et al. for a p-InP photocathode by modifying the surface with a thin layer of Ti and amorphous MoS_x nanoparticles [122]. The PEC enhancement was attributed to the excellent electro-catalytic activity of amorphous MoS_x nanomaterials and high photovoltage resulted from the favourable band alignments at the InP/Ti interface.

The growth of InP films and NWs on relatively cheaper substrates such as Si have been developed to reduce the cost of photoelectrode materials as they consume less material and use cheap substrates. In addition, nanostructures offer enhanced surface area, absorption and reduced carrier transfer length to further boost the PEC performance of photoelectrodes. Hettick et al. demonstrated non-epitaxial InP films, grown using thin-film vapour-liquid-solid (TF-VLS), as excellent photocathodes for PEC water splitting with a power conversion efficiency of 11.6% in 1 M $HClO_4$ electrolyte [123]. An excellent photocurrent of 29.4 mA/cm^2 was achieved for non-epitaxial InP films, which is comparable to that of epitaxial films and a very reasonable onset potential of 630 mV under a solar simulator with an AM 1.5 filter. Gao et al. demonstrated vapour-liquid-solid (VLS) grown InP NWs on InP wafers as a photocathode for PEC water splitting [124]. The InP NWs were grown using MOCVD with MoS_3 deposited on top as a catalyst. A photocathodic efficiency of 6.4% was reported for the MoS_3-coated InP NW photocathode with only 3% of the substrate area covered by NWs (filling fraction) under one sun illumination. In another study, Kornienko et al. reported 4% light-to-hydrogen efficiency in a half-cell configuration for an InP NW photocathode grown on Si using MOCVD. They also demonstrated 0.5% overall water splitting efficiency by integrating the InP NW photocathode with a nanoporous $BiVO_4$ photoanode in a tandem system.

The formation of nanostructures using a top-down approach is scalable and possesses control over the nanostructure dimensions and carrier concentration. The top-down fabrication of InP NP photocathodes for PEC water splitting was reported in 2012 by Lee et al. [120]. So far, to the best of our knowledge, this is the only work which has reported on the PEC propertied

of InP NPs. They achieved ~14% conversion efficiency for a p-InP NP photocathode, fabricated by a simple self-masking RIE process, tested in 1 M $HClO_4$ electrolyte under a solar simulator fitted with an AM 1.5G filter. In another study, Li et al. manifested PEC hydrogen generation using a nanoporous InP photocathode formed by an electrochemical anodization process [125]. The nanoporous InP photocathode exhibited 8.9 times improvement in photocurrent density compared to their planar photoanodes. However, the photocurrents of nanoporous InP photoanodes (3 mA/cm^2) were very low compared to the photocurrent density (29.2 mA/cm^2) obtained for top-down NP photocathodes demonstrated by Lee et al. [120]. The PEC properties of nanostructured InP photocathodes have not yet been exploited to their full extent and further studies are still needed. Specifically, InP NPs formed by a top-down approach have a high chance to reach benchmark efficiencies for InP photocathodes as the top-down approach is a well matured technique compared to the bottom-up approaches for synthesis of nanostructures, where the NPs are fabricated from high quality wafers or epitaxial layers. Once the benchmark efficiencies are established with the help of top-down fabricated photocathodes, the NP platform can be transformed to the bottom-up growth methods to replicate the NP parameters obtained using the top-down approach eventually to meet the low-cost materials requirements for the economically viable solar water splitting.

1.7. Outlook for hydrogen economy

The US Department of Energy (DoE) projected that the hydrogen will be cost-competitive with fossil fuels when the production cost for hydrogen reaches \$2 to \$4 kg^{-1}, including production, delivery and dispensing [8]. However, at present, the cost of any hydrogen production technology is far away from this target. Generation of hydrogen through electrolysis using a combination of renewable energy and electrolyzer is an industrially developed technology that has the potential to be a major hydrogen producer. At present, electrolyzers with a conversion efficiency of 56-73% are commercially available in the market depending on the electrolysis technology [10-12]. Despite highly efficient electrolyzers, this technology faces high prices of hydrogen fuel due to the combination of electricity cost from renewable resources and energy losses including current conversions (DC-AC) and grid transmissions. On the other hand, unfortunately, hydrogen production using photocatalysis is still in the research stage and much work needs to be done for commercialization. To commercialize photocatalysis technology, the photoelectrodes should exhibit a stable STH conversion efficiency of 10% [29, 30]. Although over 18% STH conversion efficiency has been reported for III-V semiconductor photoelectrodes, they suffer from photodegradation and

exorbitant prices of materials and processing [27]. Stability over 20 years is required for photoelectrodes (including both light absorbers and catalysts) to make the hydrogen fuel generated using photocatalysis cost competitive with other renewable energy technologies.

1.8. Key challenges and objectives of this thesis

The development of photoelectrodes with suitable band gap materials to maximize sunlight absorption and the ability to drive overall water splitting is critical to realize reliable and efficient tandem illumination PEC devices. III-V semiconductor materials have the capability to meet the requirements to become superior tandem photoelectrodes to achieve highly efficient tandem devices. Nanostructured photoelectrodes of these materials further improves the PEC performance of the photoelectrodes due to the enhanced absorption and increased electrolyte/semiconductor interface area, as well as reducing the materials cost due to low usage of materials. However, there are several key challenges that needs to be addressed to make use of III-V semiconductor nanostructures as highly reliable photoelectrodes.

- So far, most of the nanostructures used for solar water splitting are grown using bottom-up methods. However, bottom-up growth methods still suffer from a lack of reproducibility of high-density and large area nanostructures using catalyst-free growth methods to minimize the metal contamination of nanostructures, which is crucial for the PEC performance of the photoelectrodes.
- The impact of doping concentration and dimensions of the nanostructures on PEC performance are not explored to the full extent even though optimised parameters are crucial to achieve ideal PEC performance for photoelectrodes.
- A detailed investigation on band gap engineering of PEC photoelectrodes is required to capture the maximum portion of the solar spectrum and thereby improve the PEC performance of photoelectrodes.
- The long-term stability of photoelectrodes against photocorrosion is of utmost important and it has not yet been achieved to the level of implementing them in commercial technologies.

The main objective of this thesis is to demonstrate highly efficient photoelectrodes for PEC water splitting by exploring nanostructures fabricated using a top-down approach, band gap engineering and optical engineering of photoelectrodes. The following research plans are designed in this thesis to achieve this objective

- Develop cost-effective mask production techniques to fabricate highly reliable large area III-V nanostructures with high density, controlled dimensions and optimum doping concentration.
- Fabricate and study III-V semiconductor planar and nanostructured photoelectrodes for PEC water splitting.
- Investigate and explore the light/matter interactions to maximise light absorption in photoelectrodes.
- Establish the key parameters of nanostructures for achieving highly efficient III-V semiconductor photoelectrodes by systematically investigating the influence of carrier concentration and nanostructure dimensions on the PEC performance of photoelectrodes.
- Explore band gap engineering approaches to extend the III-V semiconductor absorption into the visible part of the solar spectrum there by improve the PEC performance of photoelectrodes.
- Explore transition metal oxide catalysts to stabilize the III-V photoelectrodes against photocorrosion.
- Develop chemical processing methods that can simultaneously remove the surface damage of nanostructures, fabricated using top-down approach, and protect them from photocorrosion.

1.9. Organization of this thesis

This thesis is organized into seven chapters.

Chapter 1 presents a brief introduction of renewable hydrogen generation technologies using solar energy and a literature review on GaN and InP photoelectrodes for photoelectrochemical water splitting. This chapter is also aimed at finding the shortcomings in these research areas and set the motivation for this thesis.

Chapter 2 presents the experimental techniques used to fabricate high quality and large area GaN and InP nanopillar photoelectrodes and to study their PEC properties. This chapter discusses the fabrication tools used for etching the GaN and InP planar and NP photoelectrodes, structural and optical techniques used for characterization of the photoelectrode materials and the PEC testing station.

Chapter 3 discusses the optimization of GaN NP fabrication using inductively coupled plasma etching (ICP) for the top-down approach and the influence of NP array pitch on the

morphology and optical properties of the NPs. It also discusses the optical quality of the NPs measured using photoluminescence and optical absorption and extraction calculated using FDTD simulations.

Chapter 4 presents the fabrication of large area random GaN NPs using a top-down approach, wherein self-assembled random mask techniques are employed for ICP etch mask preparation. This chapter is also focused on PEC studies of GaN planar and NP photoanodes and the influence of carrier concentration and nanopillar dimensions such as length and diameter of the NPs on the photoelectrochemical properties of the NP photoanodes. Optical and electrochemical impedance spectroscopy characterisations are also presented to explain the PEC properties of the photoanodes.

Chapter 5 deals with the band gap engineering of GaN NPs and their PEC performance. InGaN MQWs are introduced into GaN epilayers to reduce the band gap so that absorption by the photoanodes can be extended into the visible spectrum. The influence of In content on the PEC properties of the InGaN/GaN MQWs is also investigated in this chapter. This chapter is also focused on the stabilization of GaN photoanodes by deposition of NiO and Cr_3O_4 co-catalysts.

Chapter 6 introduces the fabrication of large area random InP NPs using ICP and examines their PEC properties. The wet etching methods of InP nanopillars to remove plasma etch damage is also presented in this chapter. This chapter also focuses on the stabilization of InP NP photocathodes by conformal deposition of TiO_2 using atomic layer deposition.

Chapter 7 provides a summary of the thesis and potential research extension for this thesis.

1.10. References

[1] U. S Energy Information Administration 2017 International Energy Outlook 2017. https://www.eia.gov/outlooks/ieo/pdf/0484(2017).pdf

[2] Perez R a M P 2009 A Fundamental Look at Supply Side Energy Reserves for the Planet *The IEA SHC Solar Update* **50** 2

[3] Green M A, Hishikawa Y, Dunlop E D, Levi D H, Hohl-Ebinger J and Ho-Baillie A W Y 2018 Solar cell efficiency tables (version 51) *Progress in Photovoltaics: Research and Applications* **26** 3-12

[4] Chen H, Cong T N, Yang W, Tan C, Li Y and Ding Y 2009 Progress in electrical energy storage system: A critical review *Progress in Natural Science* **19** 291-312

[5] Alotto P, Guarnieri M and Moro F 2014 Redox flow batteries for the storage of renewable energy: A review *Renewable and Sustainable Energy Reviews* **29** 325-35

[6] Lund H 2007 Renewable energy strategies for sustainable development *Energy* **32** 912-9

[7] Schlapbach L and Züttel A 2001 Hydrogen-storage materials for mobile applications *Nature* **414** 353

[8] U. S. Department of Energy 2006 Hydrogen, Fuel Cells and Infrastructure Technologies Program, Multi-Year Research, Development and Demonstration Plan. https://www.nrel.gov/docs/fy05osti/34289.pdf

[9] Scheffe J R and Steinfeld A 2014 Oxygen exchange materials for solar thermochemical splitting of H_2O and CO_2: a review *Materials Today* **17** 341-8

[10] Turner J, Sverdrup G, Mann M K, Maness P C, Kroposki B, Ghirardi M, Evans R J and Blake D 2008 Renewable hydrogen production *International Journal of Energy Research* **32** 379-407

[11] Holladay J D, Hu J, King D L and Wang Y 2009 An overview of hydrogen production technologies *Catalysis Today* **139** 244-60

[12] Grigoriev S, Porembsky V and Fateev V 2006 Pure hydrogen production by PEM electrolysis for hydrogen energy *International Journal of Hydrogen Energy* **31** 171-5

[13] Marino C, Nucara A and Pietrafesa M 2015 Electrolytic Hydrogen Production From Renewable Source, Storage and Reconversion in Fuel Cells: The System of the "Mediterranea" University of Reggio Calabria *Energy Procedia* **78** 818-23

[14] Fujishima A and Honda K 1972 Electrochemical Photolysis of Water at a Semiconductor Electrode *Nature* **238** 37-8

[15] Jang J S, Kim H G and Lee J S 2012 Heterojunction semiconductors: A strategy to develop efficient photocatalytic materials for visible light water splitting *Catalysis Today* **185** 270-7

[16] Chen X, Shen S, Guo L and Mao S S 2010 Semiconductor-based Photocatalytic Hydrogen Generation *Chemical Reviews* **110** 6503-70

[17] Walter M G, Warren E L, McKone J R, Boettcher S W, Mi Q, Santori E A and Lewis N S 2010 Solar Water Splitting Cells *Chemical Reviews* **110** 6446-73

[18] Ahmad H, Kamarudin S K, Minggu L J and Kassim M 2015 Hydrogen from photo-catalytic water splitting process: A review *Renewable and Sustainable Energy Reviews* **43** 599-610

[19] Chen X, Li C, Gratzel M, Kostecki R and Mao S S 2012 Nanomaterials for renewable energy production and storage *Chemical Society Reviews* **41** 7909-37

[20] Maeda K, Lu D and Domen K 2013 Direct Water Splitting into Hydrogen and Oxygen under Visible Light by using Modified TaON Photocatalysts with d0 Electronic Configuration *Chemistry – A European Journal* **19** 4986-91

[21] Maeda K, Xiong A, Yoshinaga T, Ikeda T, Sakamoto N, Hisatomi T, Takashima M, Lu D, Kanehara M, Setoyama T, Teranishi T and Domen K 2010 Photocatalytic Overall Water Splitting Promoted by Two Different Cocatalysts for Hydrogen and Oxygen Evolution under Visible Light *Angewandte Chemie International Edition* **49** 4096-9

[22] Kibria M G, Chowdhury F A, Zhao S, AlOtaibi B, Trudeau M L, Guo H and Mi Z 2015 Visible light-driven efficient overall water splitting using p-type metal-nitride nanowire arrays *Nat Commun* **6** 6797

[23] Osterloh F E 2008 Inorganic Materials as Catalysts for Photochemical Splitting of Water *Chemistry of Materials* **20** 35-54

[24] Kudo A and Miseki Y 2009 Heterogeneous photocatalyst materials for water splitting *Chemical Society Reviews* **38** 253-78

[25] Sheng C, Wei L, Yanfa Y, Thomas H, Ishiang S, Dunwei W and Zetian M 2017 Roadmap on solar water splitting: current status and future prospects *Nano Futures* **1** 022001

[26] Tilley S D, Cornuz M, Sivula K and Grätzel M 2010 Light-Induced Water Splitting with Hematite: Improved Nanostructure and Iridium Oxide Catalysis *Angewandte Chemie International Edition* **49** 6405-8

[27] Cheng W-H, Richter M H, May M M, Ohlmann J, Lackner D, Dimroth F, Hannappel T, Atwater H A and Lewerenz H-J 2018 Monolithic Photoelectrochemical Device for Direct Water Splitting with 19% Efficiency *ACS Energy Letters* **3** 1795-800

[28] Khaselev O and Turner J A 1998 A Monolithic Photovoltaic-Photoelectrochemical Device for Hydrogen Production via Water Splitting *Science* **280** 425-7

[29] Cox C R, Lee J Z, Nocera D G and Buonassisi T 2014 Ten-percent solar-to-fuel conversion with nonprecious materials *Proceedings of the National Academy of Sciences* **111** 14057-61

[30] Nocera D G 2012 The Artificial Leaf *Accounts of Chemical Research* **45** 767-76

[31] Kitano M and Hara M 2010 Heterogeneous photocatalytic cleavage of water *Journal of Materials Chemistry* **20** 627-41

[32] M. N Y R, Consuelo Á G M, F. d V, A. V d l M J and G. F J L 2009 Water Splitting on Semiconductor Catalysts under Visible-Light Irradiation *ChemSusChem* **2** 471-85

[33] Chen S and Wang L-W 2012 Thermodynamic Oxidation and Reduction Potentials of Photocatalytic Semiconductors in Aqueous Solution *Chemistry of Materials* **24** 3659-66

[34] Umebayashi T, Yamaki T, Itoh H and Asai K 2002 Analysis of electronic structures of 3d transition metal-doped TiO2 based on band calculations *Journal of Physics and Chemistry of Solids* **63** 1909-20

[35] Maeda K, Teramura K, Takata T, Hara M, Saito N, Toda K, Inoue Y, Kobayashi H and Domen K 2005 Overall Water Splitting on $(Ga_{1-x}Zn_x)(N_{1-x}O_x)$ Solid Solution Photocatalyst: Relationship between Physical Properties and Photocatalytic Activity *The Journal of Physical Chemistry B* **109** 20504-10

[36] Maeda K, Takata T, Hara M, Saito N, Inoue Y, Kobayashi H and Domen K 2005 GaN:ZnO Solid Solution as a Photocatalyst for Visible-Light-Driven Overall Water Splitting *Journal of the American Chemical Society* **127** 8286-7

[37] Li Y and Zhang J Z 2010 Hydrogen generation from photoelectrochemical water splitting based on nanomaterials *Laser & Photonics Reviews* **4** 517-28

[38] Ariffin S N, Lim H N, Talib Z A, Pandikumar A and Huang N M 2015 Aerosol-assisted chemical vapor deposition of metal oxide thin films for photoelectrochemical water splitting *International Journal of Hydrogen Energy* **40** 2115-31

[39] Yu X, Marks T J and Facchetti A 2016 Metal oxides for optoelectronic applications *Nat Mater* **15** 383-96

[40] Kibria M G and Mi Z 2016 Artificial photosynthesis using metal/nonmetal-nitride semiconductors: current status, prospects, and challenges *Journal of Materials Chemistry A* **4** 2801-20

[41] Maruska H P and Tietjen J J 1969 The preparation and properties of vapor-deposited single-crystal-line GaN *Applied Physics Letters* **15** 327-9

[42] Morkoc H 2013 *Nitride Semiconductor Devices: Fundamentals and Applications*: Wiley-VCH Verlag GmbH & Co. KGaA)

[43] Parameshwaran V, Gallinat C, Enck R W, Sampath A V, Shen P H, Kuykendall T, Aloni S, Wraback M and Clemens B M 2012 III-V nitride semiconductors for solar hydrogen production. In: *SPIE Defense, Security, and Sensing*: SPIE) p 7

[44] Pendyala C, Jasinski J B, Kim J H, Vendra V K, Lisenkov S, Menon M and Sunkara M K 2012 Nanowires as semi-rigid substrates for growth of thick, $In_xGa_{1-x}N$ ($x > 0.4$) epi-

layers without phase segregation for photoelectrochemical water splitting *Nanoscale* **4** 6269-75

[45] Tessarek C, Heilmann M, Butzen E, Haab A, Hardtdegen H, Dieker C, Spiecker E and Christiansen S 2014 The Role of Si during the Growth of GaN Micro- and Nanorods *Crystal Growth & Design* **14** 1486-92

[46] Zhu J, Wang L, Zhang S, Wang H, Zhao D, Zhu J, Liu Z, Jiang D and Yang H 2010 The fabrication of GaN-based nanopillar light-emitting diodes *Journal of Applied Physics* **108** 074302

[47] Nanishi Y 2014 The birth of the blue LED *Nature Photonics* **8** 884

[48] Theuwis A, Strubbe K, Depestel L M and Gomes W P 2002 A Photoelectrochemical Study of $In_xGa_{1-x}N$ Films *Journal of The Electrochemical Society* **149** E173

[49] Fujii K, Kusakabe K and Ohkawa K 2005 Photoelectrochemical Properties of InGaN for H_2 Generation from Aqueous Water *Japanese Journal of Applied Physics* **44** 7433-5

[50] Aryal K, Pantha B N, Li J, Lin J Y and Jiang H X 2010 Hydrogen generation by solar water splitting using p-InGaN photoelectrochemical cells *Applied Physics Letters* **96** 052110

[51] Luo W, Liu B, Li Z, Xie Z, Chen D, Zou Z and Zhang R 2008 Stable response to visible light of InGaN photoelectrodes *Applied Physics Letters* **92** 262110

[52] Fujii K, Nakamura S, Yokojima S, Goto T, Yao T, Sugiyama M and Nakano Y 2011 Photoelectrochemical Properties of $In_xGa_{1-x}N$/GaN Multiquantum Well Structures in Depletion Layers *The Journal of Physical Chemistry C* **115** 25165-9

[53] Shyam S. Kochaa M W P, Douglas J. Arenta, Joan M. Redwingb, Michael A. Tischlerb and John A. Turnera 1995 Electrochemical Investigation of the Gallium Nitride-Aqueous Electrolyte Interface *The Journal of The Electrochemical Society* **142**

[54] Beach J D, Collins R T and Turner J A 2003 Band-edge Potentials of n-type and p-type GaN *J Electrochem Soc* **150** A899-A904

[55] Katsushi F, Takeshi K and Kazuhiro O 2005 Hydrogen Gas Generation by Splitting Aqueous Water Using n-Type GaN Photoelectrode with Anodic Oxidation *Japanese Journal of Applied Physics* **44** L543

[56] Katsushi F and Kazuhiro O 2005 Photoelectrochemical Properties of p-Type GaN in Comparison with n-Type GaN *Japanese Journal of Applied Physics* **44** L909

[57] Ohkawa K F a K 2006 Bias-Assisted H2 Gas Generation in HCl and KOH Solutions Using n-Type GaN Photoelectrode *The Electrochemical Society* **153** A468

[58] Kikawa S, Kobayashi N, Yamamoto J, Ban Y and Matsumoto K 2009 Flat-Band Potentials of Ga-face and N-face in Free-Standing n-GaN Electrode and Their Effects on Water Electrolysis *e-Journal of Surface Science and Nanotechnology* **7** 847-50

[59] Ono M, Fujii K, Ito T, Iwaki Y, Hirako A, Yao T and Ohkawa K 2007 Photoelectrochemical reaction and H_2 generation at zero bias optimized by carrier concentration of n-type GaN *The Journal of Chemical Physics* **126** 054708

[60] Kazuhiko M, Kentaro T, Nobuo S, Yasunobu I and Kazunari D 2007 Photocatalytic Overall Water Splitting on Gallium Nitride Powder *Bulletin of the Chemical Society of Japan* **80** 1004-10

[61] Katsushi F, Hitoshi N, Keiichi S, Takashi K, Meoung-Whan C and Takafumi Y 2008 Improvement of hydrogen generation efficiency using GaN photoelectrochemical reaction in electrolytes with alcohol *physica status solidi c* **5** 2333-5

[62] Arai N, Saito N, Nishiyama H, Inoue Y, Domen K and Sato K 2006 Overall Water Splitting by RuO_2-dispersed Divalent-ion-doped GaN Photocatalysts with d10 Electronic Configuration *Chemistry Letters* **35** 796-7

[63] Waki I, Cohen D, Lal R, Mishra U, DenBaars S P and Nakamura S 2007 Direct water photoelectrolysis with patterned n-GaN *Applied Physics Letters* **91** 093519

[64] Liu S-Y, Lin Y-C, Ye J-C, Tu S J, Huang F W, Lee M L, Lai W C and Sheu J K 2011 Hydrogen gas generation using n-GaN photoelectrodes with immersed Indium Tin Oxide ohmic contacts *Opt. Express* **19** A1196-A201

[65] Liu S-Y, Sheu J K, Lee M L, Lin Y-C, Tu S J, Huang F W and Lai W C 2012 Immersed finger-type indium tin oxide ohmic contacts on p-GaN photoelectrodes for photoelectrochemical hydrogen generation *Opt. Express* **20** A190-A6

[66] Nakamura A, Fujii K, Sugiyama M and Nakano Y 2014 A nitride based polarization-engineered photocathode for water splitting without a p-type semiconductor *Physical Chemistry Chemical Physics* **16** 15326-30

[67] Liu S-Y, Sheu J K, Lin Y-C, Tu S J, Huang F W, Lee M L and Lai W C 2012 Mn-doped GaN as photoelectrodes for the photoelectrolysis of water under visible light *Opt. Express* **20** A678-A83

[68] Katsushi F, Kazuhide K and Kazuhiro O 2005 Photoelectrochemical Properties of InGaN for H 2 Generation from Aqueous Water *Japanese Journal of Applied Physics* **44** 7433

[69] Pantha B N, Sedhain A, Li J, Lin J Y and Jiang H X 2009 Electrical and optical properties of p-type InGaN *Applied Physics Letters* **95** 261904

[70] Li M, Luo W, Liu Q, Zhuang Z, Li Z, Liu B, Chen D, Zhang R, Yu T and Zou Z 2013 An efficient $In_{0.30}Ga_{0.70}N$ photoelectrode by decreasing the surface recombination centres in a H_2SO_4 aqueous solution *Journal of Physics D: Applied Physics* **46** 345103-10

[71] Li M, Luo W, Liu B, Zhao X, Li Z, Chen D, Yu T, Xie Z, Zhang R and Zou Z 2011 Remarkable enhancement in photocurrent of $In_{0.20}Ga_{0.80}N$ photoanode by using an electrochemical surface treatment *Applied Physics Letters* **99** 112108

[72] Stoica T and Calarco R 2011 Doping of III-Nitride Nanowires Grown by Molecular Beam Epitaxy *IEEE Journal of Selected Topics in Quantum Electronics* **17** 859-68

[73] Yam F K and Hassan Z 2008 InGaN: An overview of the growth kinetics, physical properties and emission mechanisms *Superlattices and Microstructures* **43** 1-23

[74] Ho I h and Stringfellow G B 1996 Solid phase immiscibility in GaInN *Applied Physics Letters* **69** 2701-3

[75] Holec D, Zhang Y, Rao D V S, Kappers M J, McAleese C and Humphreys C J 2008 Equilibrium critical thickness for misfit dislocations in III-nitrides *Journal of Applied Physics* **104** 123514-20

[76] Spurgeon J M, Atwater H A and Lewis N S 2008 A Comparison Between the Behavior of Nanorod Array and Planar Cd(Se, Te) Photoelectrodes *The Journal of Physical Chemistry C* **112** 6186-93

[77] Xiao F X, Miao J, Tao Hua B, Hung S F, Wang H Y, Yang Hong B, Chen J, Chen R and Liu B 2015 One-Dimensional Hybrid Nanostructures for Heterogeneous Photocatalysis and Photoelectrocatalysis *Small* **11** 2115-31

[78] Chen H M, Chen C K, Liu R-S, Zhang L, Zhang J and Wilkinson D P 2012 Nano-architecture and material designs for water splitting photoelectrodes *Chemical Society Reviews* **41** 5654-71

[79] Jung H S, Hong Y J, Li Y, Cho J, Kim Y-J and Yi G-C 2008 Photocatalysis Using GaN Nanowires *ACS Nano* **2** 637-42

[80] Kato H, Asakura K and Kudo A 2003 Highly Efficient Water Splitting into H_2 and O_2 over Lanthanum-Doped $NaTaO_3$ Photocatalysts with High Crystallinity and Surface Nanostructure *Journal of the American Chemical Society* **125** 3082-9

[81] Hersee S D, Sun X and Wang X 2006 The Controlled Growth of GaN Nanowires *Nano Letters* **6** 1808-11

[82] Lin Y T, Yeh T W, Nakajima Y and Dapkus P D 2014 Catalyst-Free GaN Nanorods Synthesized by Selective Area Growth *Advanced Functional Materials* **24** 3162-71

[83] Qian F, Li Y, Gradečak S, Park H-G, Dong Y, Ding Y, Wang Z L and Lieber C M 2008 Multi-quantum-well nanowire heterostructures for wavelength-controlled lasers *Nature Materials* **7** 701

[84] Ebaid M, Kang J-H, Lim S-H, Ha J-S, Lee J K, Cho Y-H and Ryu S-W 2015 Enhanced solar hydrogen generation of high density, high aspect ratio, coaxial InGaN/GaN multi-quantum well nanowires *Nano Energy* **12** 215-23

[85] Kibria M G, Zhao S, Chowdhury F A, Wang Q, Nguyen H P, Trudeau M L, Guo H and Mi Z 2014 Tuning the surface Fermi level on p-type gallium nitride nanowires for efficient overall water splitting *Nature communications* **5** 3825

[86] Kamimura J, Bogdanoff P, Lahnemann J, Hauswald C, Geelhaar L, Fiechter S and Riechert H 2013 Photoelectrochemical properties of (In,Ga)N nanowires for water splitting investigated by in situ electrochemical mass spectroscopy *J Am Chem Soc* **135** 10242-5

[87] Fan S, AlOtaibi B, Woo S Y, Wang Y, Botton G A and Mi Z 2015 High efficiency solar-to-hydrogen conversion on a monolithically integrated InGaN/GaN/Si adaptive tunnel junction photocathode *Nano letters* **15** 2721-6

[88] AlOtaibi B, Nguyen H P, Zhao S, Kibria M G, Fan S and Mi Z 2013 Highly stable photoelectrochemical water splitting and hydrogen generation using a double-band InGaN/GaN core/shell nanowire photoanode *Nano letters* **13** 4356-61

[89] Caccamo L, Hartmann J, Fabrega C, Estrade S, Lilienkamp G, Prades J D, Hoffmann M W, Ledig J, Wagner A, Wang X, Lopez-Conesa L, Peiro F, Rebled J M, Wehmann H H, Daum W, Shen H and Waag A 2014 Band engineered epitaxial 3D GaN-InGaN core-shell rod arrays as an advanced photoanode for visible-light-driven water splitting *ACS applied materials & interfaces* **6** 2235-40

[90] Kibria M G, Nguyen H P T, Cui K, Zhao S, Liu D, Guo H, Trudeau M L, Paradis S, Hakima A-R and Mi Z 2013 One-Step Overall Water Splitting under Visible Light Using Multiband InGaN/GaN Nanowire Heterostructures *ACS Nano* **7** 7886-93

[91] Varadhan P, Fu H C, Priante D, Retamal J R, Zhao C, Ebaid M, Ng T K, Ajia I, Mitra S, Roqan I S, Ooi B S and He J H 2017 Surface Passivation of GaN Nanowires for Enhanced Photoelectrochemical Water-Splitting *Nano Lett* **17** 1520-8

[92] Ebaid M, Kang J-H, Lim S-H, Cho Y-H and Ryu S-W 2015 Towards highly efficient photoanodes: the role of carrier dynamics on the photoelectrochemical performance of InGaN/GaN multiple quantum well coaxial nanowires *RSC Advances* **5** 23303-10

[93] Alvi N u H, Soto Rodriguez P E D, Aseev P, Gómez V J, Alvi A u H, Hassan W u, Willander M and Nötzel R 2015 InN/InGaN quantum dot photoelectrode: Efficient hydrogen generation by water splitting at zero voltage *Nano Energy* **13** 291-7

[94] Rajaambal S, Mapa M and Gopinath C S 2014 $In_{1-x}Ga_xN$@ZnO: a rationally designed and quantum dot integrated material for water splitting and solar harvesting applications *Dalton Transactions* **43** 12546-54

[95] Hwang Y J, Wu C H, Hahn C, Jeong H E and Yang P 2012 Si/InGaN Core/Shell Hierarchical Nanowire Arrays and their Photoelectrochemical Properties *Nano Letters* **12** 1678-82

[96] AlOtaibi B, Nguyen H P T, Zhao S, Kibria M G, Fan S and Mi Z 2013 Highly Stable Photoelectrochemical Water Splitting and Hydrogen Generation Using a Double-Band InGaN/GaN Core/Shell Nanowire Photoanode *Nano Letters* **13** 4356-61

[97] Chu S, Vanka S, Wang Y, Gim J, Wang Y, Ra Y-H, Hovden R, Guo H, Shih I and Mi Z 2018 Solar Water Oxidation by an InGaN Nanowire Photoanode with a Bandgap of 1.7 eV *ACS Energy Letters* **3** 307-14

[98] Liu S-Y, Sheu J K, Lin Y-C, Chen Y-T, Tu S J, Lee M L and Lai W C 2013 InGaN working electrodes with assisted bias generated from GaAs solar cells for efficient water splitting *Opt. Express* **21** A991-A6

[99] Dahal R, Pantha B N, Li J, Lin J Y and Jiang H X 2014 Realizing InGaN monolithic solar-photoelectrochemical cells for artificial photosynthesis *Applied Physics Letters* **104** 143901

[100] Fan S, AlOtaibi B, Woo S Y, Wang Y, Botton G A and Mi Z 2015 High Efficiency Solar-to-Hydrogen Conversion on a Monolithically Integrated InGaN/GaN/Si Adaptive Tunnel Junction Photocathode *Nano Letters* **15** 2721-6

[101] AlOtaibi B, Fan S, Vanka S, Kibria M G and Mi Z 2015 A Metal-Nitride Nanowire Dual-Photoelectrode Device for Unassisted Solar-to-Hydrogen Conversion under Parallel Illumination *Nano Letters* **15** 6821-8

[102] Fan S, Shih I and Mi Z 2017 A Monolithically Integrated InGaN Nanowire/Si Tandem Photoanode Approaching the Ideal Bandgap Configuration of 1.75/1.13 eV *Advanced Energy Materials* **7** 1600952

[103] Kibria Md G, Qiao R, Yang W, Boukahil I, Kong X, Chowdhury Faqrul A, Trudeau Michel L, Ji W, Guo H, Himpsel F J, Vayssieres L and Mi Z 2016 Atomic-Scale Origin of Long-Term Stability and High Performance of p-GaN Nanowire Arrays for Photocatalytic Overall Pure Water Splitting *Advanced Materials* **28** 8388-97

[104] Kibria M G, Chowdhury F A, Zhao S, Trudeau M L, Guo H and Mi Z 2015 Defect-engineered GaN:Mg nanowire arrays for overall water splitting under violet light *Applied Physics Letters* **106** 5

[105] Mi Z and Zhao S 2015 Extending group-III nitrides to the infrared: Recent advances in InN *physica status solidi (b)* **252** 845-1204

[106] Kibria M G, Chowdhury F A, Trudeau M L, Guo H and Mi Z 2015 Dye-sensitized InGaN nanowire arrays for efficient hydrogen production under visible light irradiation *Nanotechnology* **26** 285401

[107] Kibria M G, Chowdhury F A, Zhao S, AlOtaibi B, Trudeau M L, Guo H and Mi Z 2015 Visible light-driven efficient overall water splitting using p-type metal-nitride nanowire arrays *Nature Communications* **6** 6797

[108] Kibria M G, Zhao S, Chowdhury F A, Wang Q, Nguyen H P T, Trudeau M L, Guo H and Mi Z 2014 Tuning the surface Fermi level on p-type gallium nitride nanowires for efficient overall water splitting *Nature Communications* **5** 3825

[109] Guan X, Chowdhury F A, Pant N, Guo L, Vayssieres L and Mi Z 2018 Efficient Unassisted Overall Photocatalytic Seawater Splitting on GaN-Based Nanowire Arrays *The Journal of Physical Chemistry C* **122** 13797-802

[110] Benton J, Bai J and Wang T 2013 Significantly enhanced performance of an InGaN/GaN nanostructure based photo-electrode for solar power hydrogen generation *Applied Physics Letters* **103** 133904

[111] Tseng W J, van Dorp D H, Lieten R R, Mehta B, Vereecken P M and Borghs G 2013 Enhanced Photocatalytic Activity of Nanoroughened GaN by Dry Etching *ECS Electrochemistry Letters* **2** H51-H3

[112] Tseng W-J, van Dorp D H, Lieten R R, Vereecken P M, Langer R and Borghs G 2014 Impact of Plasma-Induced Surface Damage on the Photoelectrochemical Properties of GaN Pillars Fabricated by Dry Etching *The Journal of Physical Chemistry C* **118** 11261-6

[113] Benton J, Bai J and Wang T 2014 Utilisation of GaN and InGaN/GaN with nanoporous structures for water splitting *Applied Physics Letters* **105** 223902

[114] Basilio A M, Hsu Y-K, Tu W-H, Yen C-H, Hsu G-M, Chyan O, Chyan Y, Hwang J-S, Chen Y-T, Chen L-C and Chen K-H 2010 Enhancement of the energy photoconversion efficiency through crystallographic etching of a c-plane GaN thin film *Journal of Materials Chemistry* **20** 8118-25

[115] Ryu S-W, Zhang Y, Leung B, Yerino C and Han J 2012 Improved photoelectrochemical water splitting efficiency of nanoporous GaN photoanode *Semiconductor Science and Technology* **27** 015014-8

[116] Bergbauer W, Strassburg M, Kölper C, Linder N, Roder C, Lähnemann J, Trampert A, Fündling S, Li S F, Wehmann H H and Waag A 2011 N-face GaN nanorods: Continuous-flux MOVPE growth and morphological properties *Journal of Crystal Growth* **315** 164-7

[117] Gao L, Cui Y, Vervuurt R H J, van Dam D, van Veldhoven R P J, Hofmann J P, Bol A A, Haverkort J E M, Notten P H L, Bakkers E P A M and Hensen E J M 2016 High-Efficiency InP-Based Photocathode for Hydrogen Production by Interface Energetics Design and Photon Management *Advanced Functional Materials* **26** 679-86

[118] Heller A and Vadimsky R G 1981 Efficient Solar to Chemical Conversion: 12% Efficient Photoassisted Electrolysis in the [p-type InP(Ru)]/HCl-KCl/Pt(Rh) Cell *Physical Review Letters* **46** 1153-6

[119] Munoz A G, Heine C, Lublow M, Klemm H W, Szabo N, Hannappel T and Lewerenz H J 2013 Photoelectrochemical Conditioning of MOVPE p-InP Films for Light-Induced Hydrogen Evolution: Chemical, Electronic and Optical Properties *ECS Journal of Solid State Science and Technology* **2** Q51-Q8

[120] Lee M H, Takei K, Zhang J, Kapadia R, Zheng M, Chen Y Z, Nah J, Matthews T S, Chueh Y L, Ager J W and Javey A 2012 p-Type InP nanopillar photocathodes for efficient solar-driven hydrogen production *Angew Chem Int Ed Engl* **51** 10760-4

[121] Lin Y, Kapadia R, Yang J, Zheng M, Chen K, Hettick M, Yin X, Battaglia C, Sharp I D, Ager J W and Javey A 2015 Role of TiO2Surface Passivation on Improving the Performance of p-InP Photocathodes *The Journal of Physical Chemistry C* **119** 2308-13

[122] Li Q, Zheng M, Zhong M, Ma L, Wang F, Ma L and Shen W 2016 Engineering MoS_x/Ti/InP Hybrid Photocathode for Improved Solar Hydrogen Production *Scientific Reports* **6** 29738

[123] Hettick M, Zheng M, Lin Y, Sutter-Fella C M, Ager J W and Javey A 2015 Nonepitaxial Thin-Film InP for Scalable and Efficient Photocathodes *J Phys Chem Lett* **6** 2177-82

[124] Gao L, Cui Y, Wang J, Cavalli A, Standing A, Vu T T, Verheijen M A, Haverkort J E, Bakkers E P and Notten P H 2014 Photoelectrochemical hydrogen production on InP nanowire arrays with molybdenum sulfide electrocatalysts *Nano Lett* **14** 3715-9

[125] Li Q, Zheng M, Zhang B, Zhu C, Wang F, Song J, Zhong M, Ma L and Shen W 2016 InP nanopore arrays for photoelectrochemical hydrogen generation *Nanotechnology* **27** 075704.

Chapter 2

Experimental Methods

This chapter presents the experimental methodologies used to accomplish this dissertation. The experimental techniques employed starting from growth of epitaxial layers to testing the photoelectrodes for hydrogen generation performance are described. This work made use of MOCVD for the growth of GaN and InGaN/GaN multi quantum well (MQW) epitaxial films, electron beam lithography (EBL) and self-organized random mask techniques for designing the etch mask, reactive ion etching (RIE) and inductively coupled plasma (ICP) for the etching of SiO_2 and top-down fabrication of GaN and InP nanopillars (NPs), scanning electron microscopy (SEM) for microstructural characterization, photoluminescence measurements and UV-Vis spectrophotometry for optical characterization and photoelectrochemical testing station to test the photoelectrochemical performance of GaN, InGaN/GaN MQW and InP materials. In addition, Finite-Difference Time-Domain (FDTD) method was also used to simulate light-matter interactions to design the NP structures.

2.1. Epitaxial growth of GaN based alloys

The crystalline quality of the materials is critical for solar water splitting applications. Metal-organic chemical vapor deposition (MOCVD) is an industrially adopted sophisticated technique used to grow high crystalline quality III-V semiconductor epitaxial films. The principle of MOCVD involves the pyrolysis of metal-organic precursors at high temperature followed by chemical reactions on the substrate surface, which leads to the nucleation and growth of epitaxial thin films on single crystal substrates. Typically, either methyl or ethyl metal-organic precursors are used as sources of group III elements while hydrides are used as sources of group V elements for MOCVD growth of III-V semiconductors. The overall reaction that occurs during MOCVD growth is as follows.

$$(III)R_3 + (V)H_3 \rightarrow III\text{-}V + 3RH \quad \ldots\ldots\ldots\ldots\ldots 2.1$$

where R_3 refer to the organic alkyl group. All n-GaN and n-GaN/(InGaN/GaN MQWs)/n-GaN structures used in this dissertation were grown on c-axis sapphire wafers (α-Al_2O_3) using an AIXTRON closed-coupled shower head MOCVD reactor (Figure 2.1). Unlike

the horizontal flow MOCVD reactor, the gases are introduced through gas channels in the shower head ceiling. The system is capable of growing three two-inch wafers at a time. The susceptor of the reactor is made of graphite and coated with graphite to sustain very high temperatures (up to 1300 ^{O}C). Further, the susceptor is rotated at a constant speed to obtain uniform epitaxial films.

Figure 2.1: Photograph of the AIXTRON MOCVD reactor used in this work for growth of GaN and InGaN/GaN MQW structures.

In this work, trimethylgallium (TMGa), triethylgallium (TEGa), ammonia (NH_3), trimethylindium (TMIn) and silane (SiH_4) were used as sources of gallium (Ga), nitrogen (N), indium (In) and n-type dopant, respectively, for the growth of two sets of samples: (i) n-GaN and (ii) n-GaN/(InGaN/GaN MQWs)/n-GaN epitaxial films. The epitaxial growth of n-GaN layers, n-GaN layers in MQW structures and InGaN/GaN MQW layers were carried out at chamber pressures of 200, 133 and 400 mbar, respectively. Hydrogen was used as a carrier gas for the growth of n-GaN wafers and n-layers in MQW structures and switched from hydrogen to nitrogen while growing InGaN/GaN MQW layers. TMGa, NH_3 and SiH_4 sources were simultaneously injected into the MOCVD reactor, maintained at a temperature of 1060 ^{O}C, to grow the n-GaN layers. The carrier concentration of n-GaN was adjusted by varying the flow rate of SiH_4. GaN barrier and InGaN quantum well layers in InGaN/GaN MQWs were grown at temperatures of 820 and 730 ^{O}C, respectively. TEGa and NH_3 were used for growth of GaN barriers, while TEGa, TMIn and NH_3 were used as precursors for growth of InGaN QW layers. The flow rate of TMIn was controlled to tune the In concentration in the QWs for reducing the

band gap of GaN. Prior to the growth of epitaxial films, the sapphire substrate was baked at 1050 ^{O}C under hydrogen flow for 5 mins to decontaminate the surface. In subsequent steps, nitridation of the substrate was carried out at 550 ^{O}C by injection of NH_3 into the MOCVD reactor followed by the formation of a GaN nucleation layer through TMGa injection. Then, a thick undoped GaN buffer layer was grown at a higher temperature of 1040 ^{O}C to minimize defect density for the subsequent layers of interest.

2.2. Design of etch mask

Top-down approaches use either dry (plasma) etching or chemical (solution) etching for the formation of nanopillars (NPs). The NPs used in this thesis were fabricated using ICP etching which is a dry etching process. The design of a suitable mask for the top-down fabrication of NPs is crucial as the etch mask determines the dimensions of the NPs. We used a bilayer metal/SiO_2 as an etch mask for the fabrication of NPs, where the metal is either Cr, Ni or Au. The type of metal used for the etching mask was chosen based on the materials to be etched. Two techniques were employed for the creation of the etch mask, namely EBL and rapid thermal annealing (RTA). EBL was utilised for the creation of small area ordered mask patterns, while RTA was used to produce large area random masks.

2.2.1. Plasma enhanced chemical vapor deposition

Plasma enhanced chemical vapor deposition (PECVD) is widely used in industries for the deposition of device quality thin films at low temperatures. It is a cost-effective technique for the deposition of dielectric thin films with high deposition rates. In PECVD, the chemical reactions involving radio frequency excited gaseous reactants (plasma) results in the reaction product being deposited as a film on a substrate. The deposition of dielectric films at low temperature is critical for compound semiconductors because some of them are unstable at temperatures greater than 400 ^{O}C. The plasma in PECVD enables the chemical reactions at lower temperatures compared to thermal CVD, which facilitates PECVD for low temperature deposition of thin films compared to traditional CVD. To create the metal/SiO_2 mask in this work, an Oxford Plasmalab 100 PECVD system with a load lock chamber was used to deposit 500 nm of SiO_2 film on GaN, InGaN/GaN MQWs and InP wafers. The top electrode of the PECVD system was connected to dual frequency power generators (13.56 MHz and 50-450 kHz) through a matching network while the bottom electrode was connected to the ground, which also features the heat source [1, 2]. The SiO_2 deposition was carried out at a temperature of 300 ^{O}C and 20 W RF power. SiH_4/N_2O/N_2 gases were introduced into the PECVD chamber

at flow rates of 9/710/161 sccm through the gas channels in the top-electrode. The PECVD chamber pressure was maintained at 650 mTorr while depositing SiO_2 film.

2.2.2. Electron beam lithography

Electron beam lithography (EBL) is a versatile nanofabrication technique used to draw custom shapes with very high precision [3]. EBL involves scanning a focused beam of electrons on a surface coated with an electron sensitive resist followed by immersion of the sample in a solvent called a developer. The electron beam exposed part of the resist is selectively removed in the case of positive tone resist and vice versa in case of negative tone resist when immersed in the developer. This is because the focused electron beam changes the solubility of the resist upon exposure. EBL can be used to produce nanofeatures of sub-10 nm size due to the shorter wavelength of the electron beam. Furthermore, EBL is a mask-free technique, unlike UV photolithography, which enables it to draw the patterns of desired shapes. However, due to 'serial' nature of electron beam writing, the throughput of EBL is very low. In this thesis, a RAITH 150 EBL was employed to design the chromium (Cr) etch mask for plasma etching of SiO_2 followed by GaN-based NPs.

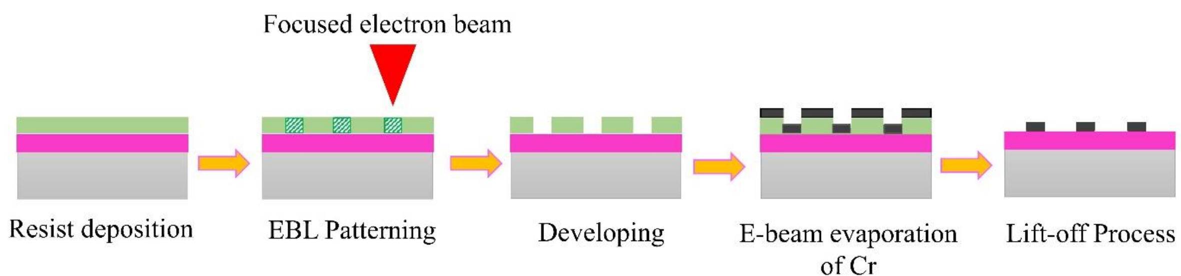

Figure 2.2: Schematic illustration of processing steps involved in EBL patterning of Cr mask.

Figure 2.2 shows a flow chart of the processing steps involved in the preparation of the etch mask using EBL. Double layers consisting of high dissolution rate PMMA 495 A2 and low dissolution rate PMMA 950 A4 as top and bottom electron sensitive resists, respectively, were used to design the EBL mask. The solubility difference between the two layers in the developer generates an undercut profile in the resist. These undercut profiles improve the metal lift-off process. The EBL process began by spin coating the first layer on SiO_2 deposited on GaN wafers at 500 RPM for 5 s followed by 1200 RPM for 45 s. The samples were then soft baked at 180 ^{O}C using a hot plate for 3 mins to get rid of solvents in the resist. The second layer PMMA 950 A4 resist was spin-coated at 3000 RPM speed for 45 s followed by 3 min soft baking at 180 ^{O}C. After electron beam resist coating, samples were exposed with a focused

electron beam, accelerated by a 20 kV source and using a 10 μm aperture, to write the desired square array pattern of holes. The resist was subjected to a 500 $\mu C/cm^2$ dose at a 4 μm step size. EBL exposed samples were then immersed in MIBK:IPA (1:3) for selective removal of the electron beam exposed area of the resist to create an array of nano-holes. Next, the samples were loaded into a barrel etcher to remove the residues of the resist using oxygen plasma at room temperature. The oxygen plasma was created in the barrel etcher at 0.3 bar pressure with an O_2 flow rate of 300 sccm and power of 100 W. In subsequent steps, the Cr film was deposited onto the EBL patterned samples using electron beam evaporation (e-beam evaporation). The metal lift-off process in acetone during the final step produced the square array pattern of Cr nano-discs.

2.2.3. Rapid thermal annealing

Rapid thermal annealing is a process used to heat semiconductor wafers to very high temperatures in a few seconds and anneal them at higher temperatures for a short duration of time. This technique is widely used in semiconductor device fabrication for changing the electrical properties of the wafers, activation of the dopants, improving the density of the films, removing ion implantation damage and changing interfaces of films [4]. RTA uses either lamp-based heating, a hot chuck, or a hot plate that a wafer is brought near to so as to heat the samples. Due to the short annealing times, the throughput of RTA is very high. However, only one wafer can be processed at a time using RTA. Recently, RTA was explored for the creation of nanoscale metal dots to fabricate quantum confined Si nanodots for resonant plasma-wave generator for biphotonic sensing applications [5-9]. Due to self-segregation at high temperature, RTA converts metal films into nano-islands. These metal nano-islands were used in this work as an etch mask for the plasma etching of SiO_2 and subsequent GaN, InGaN/GaN MQWs and InP etching. We used a Qualiflow JetFirst 100 RTA to create the self-organized random Ni and Au masks through the self-segregation of metal films for fabrication of large area random GaN-based and InP NPs, respectively. The RTA uses halogen lamps to heat the samples from the top and SiC wafers were used as carrier wafers to load the samples into the RTA. Au film converts into nano-islands at lower temperatures compared to Ni films. For this reason, Au was used as an etch mask for the fabrication of InP NPs, given that InP dissociates if annealed at high temperatures. To make the self-organized random etch masks, thin layers of Ni and Au were deposited on top of SiO_2 coated GaN and InP wafers, respectively, using e-beam evaporation under high vacuum. The Ni coated and Au coated samples were then loaded into the RTA. The temperatures of the samples were raised to 900 ^{o}C for Ni and 500 ^{o}C for Au

in 10 s and maintained at those temperatures for one minute. The temperature was monitored using a thermocouple placed underneath the SiC carrier wafer. Ar gas was introduced into the RTA chamber to maintain an inert atmosphere during the annealing process. More details about the Ni and Au self-organized etch masks are presented in Chapters 4, 5 and 6.

2.3. Plasma etching

Plasma etching techniques in this work were employed to etch SiO_2 to form the metal/SiO_2 mask and subsequent fabrication of GaN, InGaN/GaN MQW and InP NPs. Plasma etching is a dry etch process and involves the selective removal of materials through the formation of volatile products with the reactive plasma species. The reactive plasma is generated at low pressure by applying an electrical potential to the appropriate reactive gas mixture [10]. The plasma is a mixture of charged particles (electrons and positive ions) and radicals. The reactive plasma attacks the material and reacts with it to form volatile products. Unlike wet etching, plasma etching is an isotropic etching process and possesses very high throughput with excellent uniformity and reproducibility. Reactive ion etching (RIE) and inductively coupled plasma (ICP) etching reactors are the two most commonly used plasma reactors among the many varieties of plasma reactors for plasma etching processes. In this work we used RIE for SiO_2 etching and ICP for the fabrication GaN-based alloy and InP NPs.

2.3.1. Reactive ion etching

An Oxford PlasmaLab 80 Plus RIE system was used for etching SiO_2 in this work. A schematic illustration of the RIE system is shown in Figure 2.3. Gas inlets are located at the top of the RIE reactor that introduce the gases into the reactor chamber. A 13.56 MHz frequency power generator is connected to the bottom electrode while the top electrode is grounded and the RIE system operates in capacitively charge coupled plasma mode. The application of radio frequency high voltage between the electrodes ionizes and dissociates the gases entering from the gas inlet at low chamber pressures. Due to their light weight, electrons move rapidly compared to the ions in the plasma and hence further participate in ionization events on a course to reach the bottom electrode. Moreover, the electrons arrive at the bottom electrode in a relatively short time compared to the ions and create a negative charge on the bottom electrode. This negative bias voltage is often referred to as a direct current (DC) bias or self-bias V_b. The negative bias of the electrode accelerates the positive ions in the plasma towards the bottom electrode and the resultant build-up of kinetic energy of the positive ions is proportional to the ion charge and the DC bias of the electrode. The ion energy is strongly

influenced by the RF power among the other plasma process parameters such as reactor pressure and gas flow because the DC bias is mainly controlled by the RF power. The energy of the ions is transferred to the sample when they hit the surface and initiate the etching process which is called physical etching or ion-driven etching. The ions bombard the sample surface together with the reactive ions and neutral radicals, created in the plasma, and participate in physical and chemical etching of the sample.

Generally, fluorine-based gas chemistry is used for etching SiO_2 where the volatile etching product is SiF_4 [11]. In this work, RIE etching was employed to etch the SiO_2 around the metal masks (Cr, Ni and Au) generated using RTA as described in Section 2.2.3 to produce the metal/SiO_2 mask for the fabrication of InP NPs. SiO_2 etching was carried out at room temperature using a CHF_3 plasma, generated at 200 W RF power. The CHF_3 gas was injected into the reactor at a flow rate of 25 sccm and a reactor pressure of 30 mTorr. The etch rate of SiO_2 measured using ellipsometry was 31 nm/min. The etching of SiO_2 resulted in the formation of a metal/SiO_2 mask with vertical and smooth side walls.

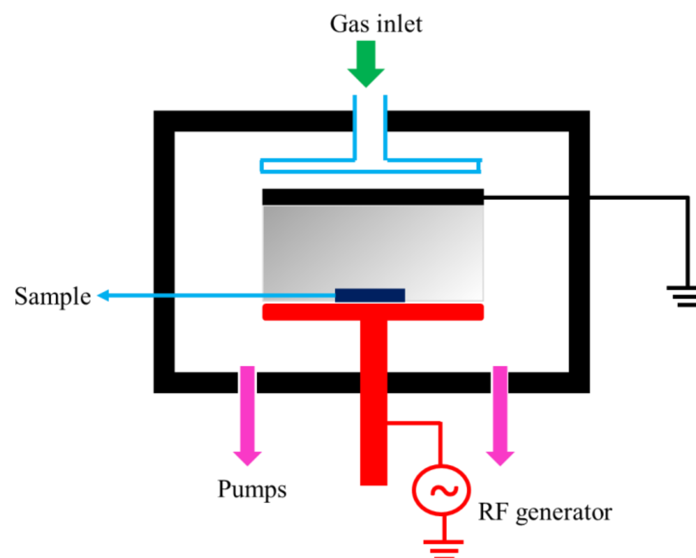

Figure 2.3: Schematic illustration of the reactive ion etching system used in this work

2.3.2. Inductively coupled plasma etching

ICP features two RF power generators for isolating plasma generation and ion acceleration, unlike single RF power for both functions in RIE. Figure 2.4 shows a schematic illustration of a typical ICP system used for plasma etching. The coil RF power around the chamber ignites the plasma at a remote location whereas the RF power coupled to the lower electrode induces the DC bias for accelerating the ions. This permits the independent control over the plasma density and DC bias by varying the RF powers. For instance, a higher plasma

density can be achieved at lower ion energy by increasing the ICP power and keeping the bottom electrode RF power small. Samples subjected to low ion energy endure less plasma etching damage compared to high energy plasma etching. Further, due to high plasma density, a higher anisotropic etching rate can be achieved for ICP compared to RIE. Moreover, ICP plasma processes occur at lower pressures compared to RIE.

In this work, a Versaline LL ICP system was used for the fabrication of GaN and InGaN/GaN MQW NPs, while an SAMCO ICP system was employed for the fabrication of InP NPs. The ICP reactors consist of a 2 MHz RF power generator for igniting the plasma and a 13.56 MHz RF power generator for controlling the energy and directionality of the ions. Si carrier wafers were used to load the samples into the ICP reactors. The ICP reactors feature a load-lock system and helium back side cooling to maintain constant wafer temperature during etching. The pre-patterned masks, prepared in Sections 2.2.2, 2.2.3 and 2.3.1, were mounted on Si carrier wafers to load into the reactors. Silver heat sink paste was applied at the backside of each sample to transfer the heat to the carrier wafer. $Cl_2/Ar/H_2$ and gas chemistries was used for etching the GaN, InGaN/GaN MQW and Cl_2/Ar was used for etching InP NPs. The GaN and InGaN/GaN MQWs, grown using MOCVD as described in Section 2.1, were used for the formation of their NPs. For InP NPs, p-type wafers were purchased from vendor (AXT, Inc). Details of the ICP etching of GaN and InGaN/GaN NPs are discussed in Chapters 3, 4 and 5, while InP etching details are presented in Chapter 6 of this thesis.

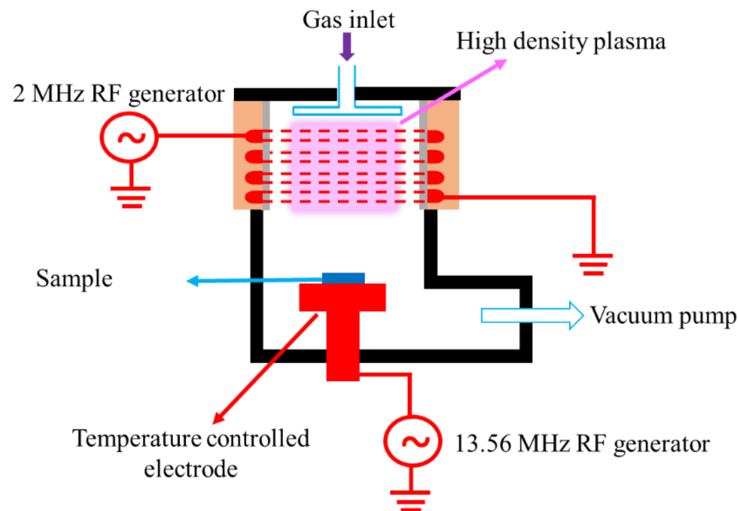

Figure 2.4: Schematic illustration of typical inductively coupled plasma reactive ion etching system.

2.4. Characterization of NPs

The characterization of materials is critical before using them in any applications. We used scanning electron microscopy for structural characterization, photoluminescence and time-resolved photoluminescence for testing the optical quality of the NPs and UV-Vis spectrometry to study the optical properties of GaN, InGaN/GaN MQWs epitaxial wafers, InP bulk wafers and NPs.

2.4.1. Scanning electron microscopy

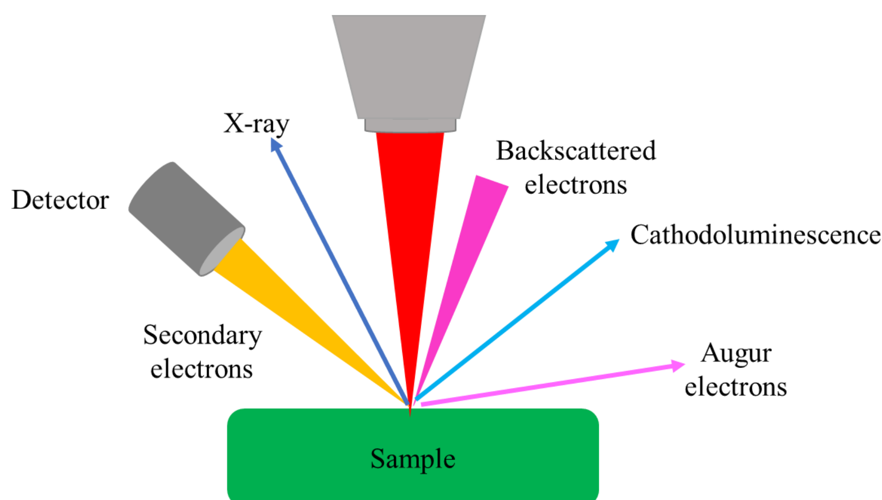

Figure 2.5: Schematic illustration of electron-material interactions and consequent outcomes.

The basic working function of SEM involves the scanning of a sample surface with a focused electron beam to produce an image. As shown in Figure 2.5, the electron-sample interactions generate diverse signals, where each of it carries discrete and valuable information about the sample. Among the various signals, backscattered electrons and secondary electrons retain information about sample topology. Capturing these electrons through appropriate detectors reveals the sample surface morphology at nanoscale resolution. Electrons knocked out from the outermost orbitals of the atoms because of inelastic scattering interactions between the electron beam and the sample are referred as secondary electrons and they possess very low energy (<50 eV). As a result, most of the electrons ejected from deep inside of the samples are easily trapped by the surrounding materials and only those electrons generated near the surface can escape from the material to contribute to the image. This helps to get highly surface sensitive information as only electrons originating from the top few nanometers of the sample surface contribute to the image. On the other hand, backscattered electrons originate from elastic interactions between electrons and the sample. The yield of backscattered electrons is proportional to the atomic number of the surface atoms. This facilitates SEM to determine

chemical composition based on the variation in the intensity of the backscattered electrons with the atomic size, if they are made of different atomic compositions. We used an FEI Helios 600 NanoLab SEM for structural characterization of the samples in this thesis. The SEM is capable of capturing images with a very high resolution (0.9 nm) and also features a focused ion beam. The SEM, operated in secondary electron mode, was used for optimization of EBL processing to pattern the etch mask, self-organized random etch mask and morphological studies of the NPs used in this work.

2.4.2. Photoluminescence

Photoluminescence (PL) is a process in which the photoexcited carriers recombine radiatively to emit light. The illumination of a sample with a laser of energy greater than that of the semiconductor band gap excites the electrons into the conduction band, thus generating electron and hole pairs. The excited electrons immediately reach the minimum of the conduction band through thermal relaxation and recombine radiatively with the holes at top of the valence band to emit light. The energy of the emitted photon is equivalent to the band gap of the excited semiconductor. PL is typically used for determination of the semiconductor band gap, material quality, recombination mechanisms and detection of impurity levels and defects. We used micro-PL and time-resolved photoluminescence (TRPL) systems for the optical characterization of GaN and InP, respectively.

2.4.2.1. Micro-photoluminescence

The design of the micro-PL (μ-PL) system used for optical characterization of GaN and InGaN/GaN MQW wafers and their NPs is shown in Figure 2.6. A 325 nm wavelength ultraviolet (UV) He-Cd gas laser was used for the photoexcitation of each sample at room temperature. The laser beam reached the sample after passing through power filters and a beam splitter. The laser beam was focused onto the sample using a microscope equipped with a UV light compatible objective lens. The emitted light from the sample was collected through the same objective lens and directed to the monochromator. The processed signal from the monochromator was then detected using a Si charge-coupled device (CCD). A band-pass filter was placed in front of the monochromator to block the reflected laser light from the sample surface. In this work, the μ-PL system was used to study the photoluminescence of planar and NP GaN and InGaN/GaN MQWs. It was also used to investigate the optical quality of the GaN NPs, fabricated using a top-down approach, by measuring the power dependent PL. This

measurement was enabled by fixing a neutral density (ND) power wheel filter in the laser path between the laser and the optical microscope, which changes the power of the laser light at the sample illumination.

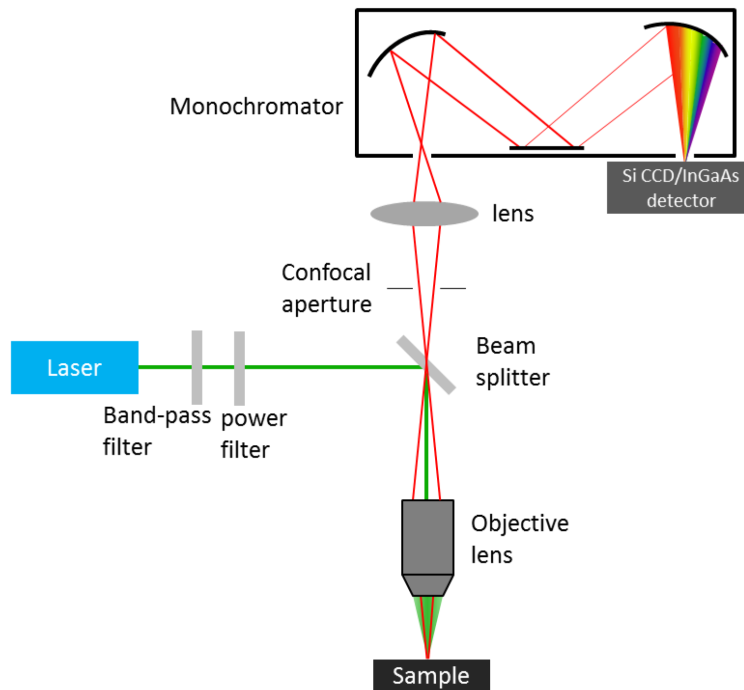

Figure 2.6: Schematic representation of micro-PL system used for optical characterization of GaN and InGaN/GaN samples [12].

2.4.2.2. Time-resolved photoluminescence

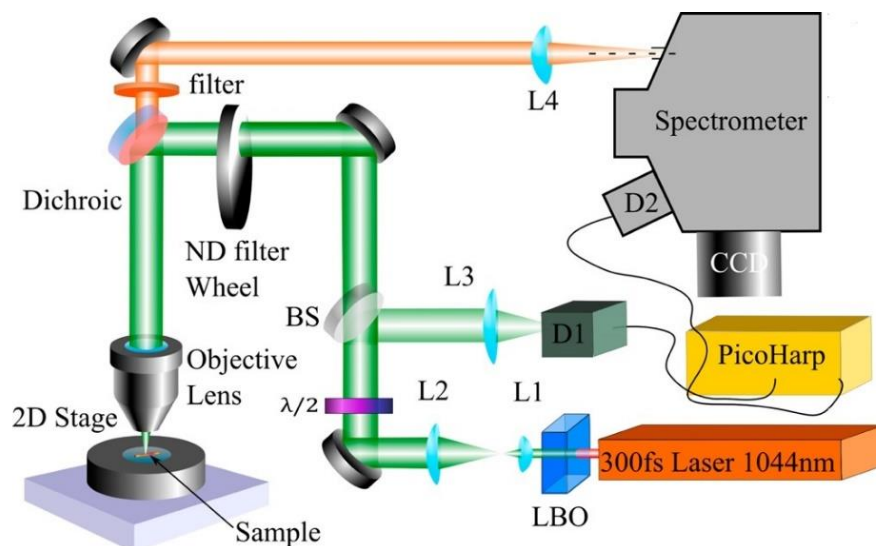

Figure 2.7: Schematic optical design of TRPL set-up used for photoluminescence and minority carrier lifetime measurement of InP [13].

The optical design of the TRPL system used for our work is shown in Figure 2.7. The samples were excited using a 522 nm wavelength pulsed laser, which was generated by the frequency doubling of an Yb:YAG laser when passed through a LBO crystal. The excitation pulse had a duration of 300 fs and a repetition rate of 20.8 MHz. The laser beam was focused on the sample through a 10x (Nikon LU Plan, NA 0.75) microscope objective lens and the emitted light from the sample was also collected through the same lens. For lifetime measurements, the collected light from the objective lens was transferred to a Si single photon avalanche diode, which was connected to a Picoharp 300 time-correlated single photon counting (TCSPC) system. The TRPL system, in this work, was used for PL and minority carrier lifetime measurements of InP samples at room temperature. These measurements were used to analyse the influence of plasma etching damage on the optical quality of InP.

2.4.3. UV-Vis spectrophotometry

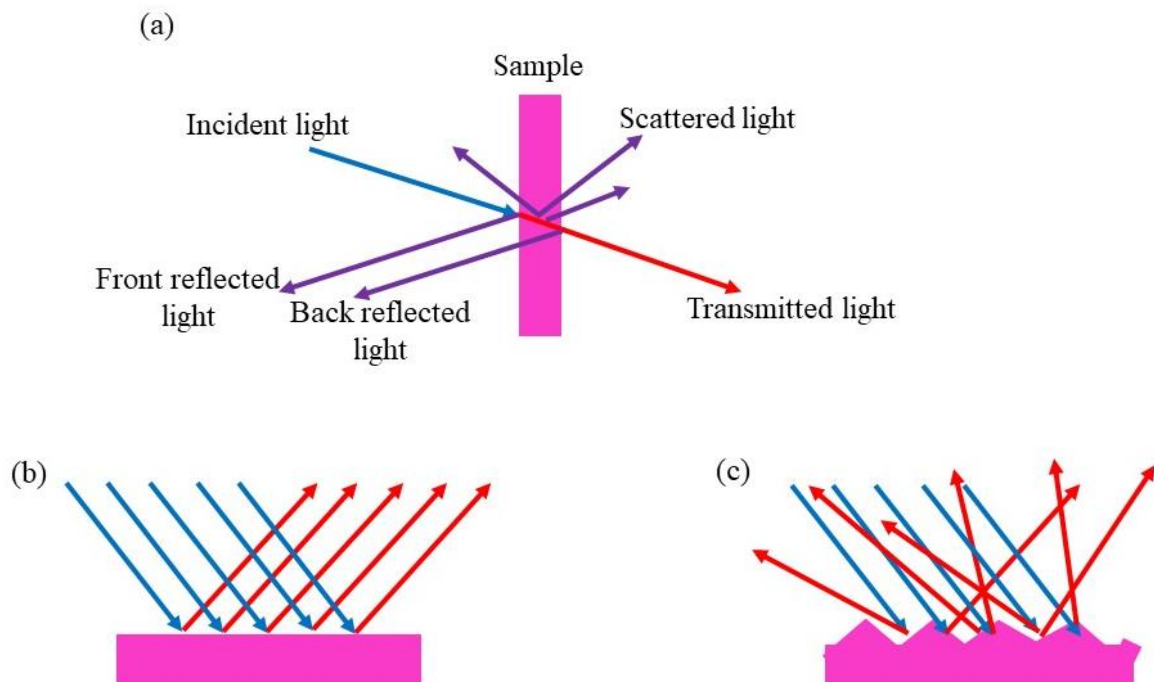

Figure 2.8: Schematic representations of (a) light-matter interactions, (b) specular reflectance on smooth surfaces and (c) diffuse reflectance on rough surfaces.

Light-matter interactions, as shown in Figure2.8(a), produce various outcomes such as reflection, transmission, absorption, scattering, refraction and polarization. UV-Vis spectrophotometry can be used to measure the absorption, transmission and reflectance properties of materials. Reflections are classified into two types called specular reflectance (Figure 2.8(b)) and diffuse reflectance (Figure 2.8 (c)). Specular reflectance is often described

as mirror-like reflection where light is reflected in single direction when incident on a smooth surface by following reflection laws. In the case of diffuse reflectance, light is reflected in all directions rather than a single angle like specular reflectance. This indicates that diffuse reflectance contains specular reflectance as well. Diffuse reflectance often occurs due to the nanostructured materials surface. The Lambda 950 (Perkin Elmer) spectrophotometer equipped with an integrating sphere was employed to measure the diffuse reflectance of planar and NP GaN and InP in this thesis. The light absorption of the samples is calculated by subtracting diffuse reflection and transmission from the incident light intensity. Transmission losses can be neglected for thick direct band gap materials because they possess very high absorption coefficients. This indicates that the absorption properties of direct band gap semiconductors solely depends on the reflectance and hence decreases in reflection losses increases the absorption.

2.5. Finite-Difference Time-Domain Simulations

Finite-Difference Time-Domain (FDTD) simulation is a versatile numerical analysis technique to solve Maxwell's equations in the time domain. FDTD simulations have been successfully used to model and solve electromagnetic wave and material interactions for over two decades. The FDTD simulation package is user friendly and relatively easy to use and interpret simulation results compared to other numerical simulation methods. The biggest advantage of FDTD is that it can obtain broadband frequency calculations with a single simulation, being a time domain simulation method. Further, FDTD simulations can provide animated displays of changes in the electromagnetic field in the model since they evolve with time. This feature allows the user to follow the progress of the simulation with time and perceive if any shortcomings occur on a course of completion of the simulation.

The commercially available Lumerical, Inc FDTD simulation package was used in this thesis to calculate the light absorption and extraction efficiencies of GaN NP arrays. 3D CAD environment was used to design and define the physical dimensions of the GaN NPs. Then, the plane wave source and monitors were added to the simulation region to generate the electromagnetic waves and collect the electromagnetic fields, respectively. Well-matched boundary conditions, simulation dimensions and mesh size were defined to obtain reliable and accurate results. Further details of the simulation set-up and their outcomes are discussed in Chapter 3.

2.6. Photoelectrochemical testing station

The measurement of hydrogen is an important parameter in assessing the PEC performance of photoelectrodes. However, the hydrogen measurements are considered critical if the photoelectrodes can run the water splitting without external bias in a two electrode PEC system. For other photoelectrodes assessed under bias conditions in a three-electrode setup, linear sweep voltammetry, incident photon-to-current current conversion efficiency (IPCE), applied bias photon-to-current conversion efficiency (ABPE), and electrochemical impedance measurements are commonly used as metrics to study the PEC performance of photoelectrodes [1, 2]. According to the solar-to-hydrogen conversion (STH) efficiency definition, the amount of hydrogen produced from water splitting is proportional to the photocurrent generated by the photoelectrode. The STH efficiency is determined using the following equation

$$STH = \frac{1.23[V] \times J_{ph}[mA/cm^2] \times \eta_F}{P_{incident}[mW/cm^2]} \times 100\% \qquad \ldots\ldots\ldots\ldots\ldots..2.2$$

where J_{ph} is the photocurrent density of the photoelectrode, $P_{incident}$ is the power of illuminating light and η_F is the Faradic coefficient. From Equation 2.2, the STH efficiency is linearly dependent on photocurrents generated by photoelectrodes. Therefore, measurement of J-V characteristics can be used as a measure to study the PEC performance of the photoelectrodes which are not suitable for overall water splitting. As a result, in this thesis, we used J-V characteristics to test the PEC performance of photoelectrodes. I also investigated the ABPE, IPCE and electrochemical impedance of photoelectrodes in this work to give further insights into the materials developed.

Figure 2.9(a) shows the PEC measurement set-up used in this work for the investigation of the PEC performance of GaN, InGaN/GaN MQWs and InP photoelectrodes. The PEC testing station consists of a PEC measurement cell, potentiostat and solar simulator. PEC measurements were carried out at room temperature in a three electrode PEC cell as shown in schematic Figure 2.9(b). Figure 2.9(c) and (d) show photographs of the PEC cell and the photoelectrodes used in our work. The PEC cell was a cubic shape and made of high-quality transparent quartz (Figure 2.9(c)). The PEC set-up comprised of three electrodes: working electrode, counter electrode and reference electrode (Figure 2.9(d)). The electrodes were mounted through rigid holes in a lid made of Teflon, which covered the top of the PEC cell, to avoid the dependence of photocurrent on the positioning of the photoelectrodes. As shown in Figure 2.9(e), the electrodes were placed at the corners of a right-angle triangle design, where the working electrode and counter electrode were separated equally by 1.3 cm from the

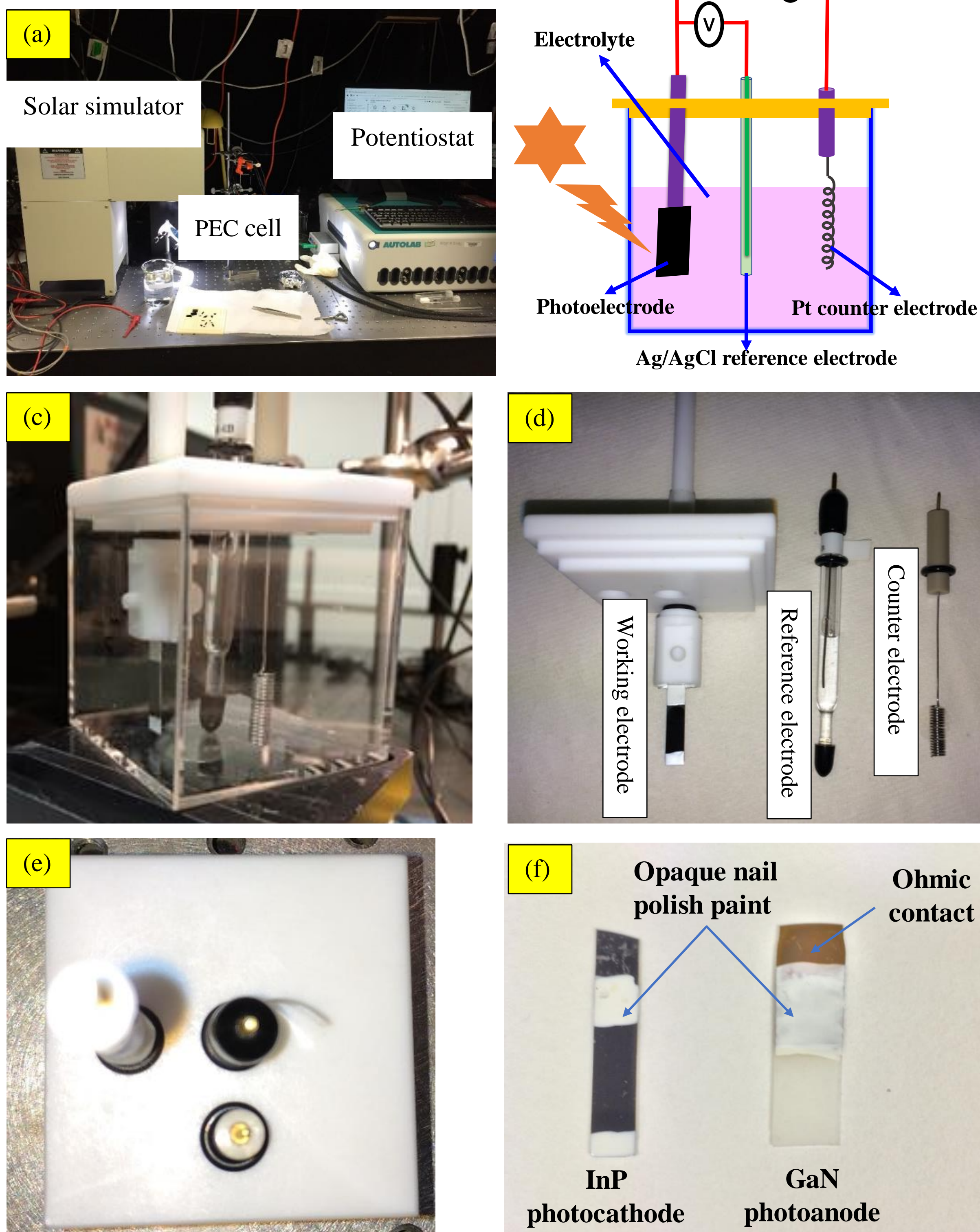

Figure 2.9: (a) A picture of the PEC measurement set-up, (b) schematic of the three electrode PEC cell and photographs of (c) the quartz cubic cell, (d) three electrodes, (e) cell lid mounted with the three electrodes and (f) InP and GaN photoelectrodes used in this dissertation.

reference electrode. A coiled platinum wire auxiliary electrode with dimensions of 23 cm in length and 0.5 mm in diameter and an RE-1B model Ag/AgCl reference electrode with 3 M NaCl internal solution were used as the counter electrode and reference electrode, respectively (Figure 2.9(d)). Both were supplied by BAS Inc. The reference potential of the Ag/AgCl electrode was 0.195 V versus reversible hydrogen electrode measured at 25 ^{O}C. A Class A Newport solar simulator consisting of a 150 W Xenon lamp fitted with an air mass 1.5 (AM 1.5) filter was used to illuminate the working electrode. The output power of the solar simulator was calibrated using a solar power meter provided by Newport. The solar light intensity at the working photoelectrode was adjusted to 100 mW/cm^2 or one sun light intensity by adjusting the lamp power. All electrolyte chemicals used in this work were purchased from Sigma-Aldrich. The electrolyte was filled in the PEC cell such that the active area of each photoelectrode was completely immersed in the electrolyte. The planar and NP GaN, InGaN/GaN MQWs and InP were used as working electrodes to test their PEC performance. Figure 2.9(f) show photographs of GaN and InP photoelectrodes used in this work. Crocodile clips were used to connect the electrodes to the electrical measurement control system. White nail polish was used to protect the contacts and prevent absorption in the contact regions and also to define the area of the photoelectrodes. The active photoelectrode area was calculated by using digital photographs and Microsoft PowerPoint tools. The Autolab potentiostat (Autolab, PGSTAT302N) from Metrohm was used as a measurement control system to test the PEC performance of the photoelectrodes. NOVA software was used as the interface to control and monitor voltammetry, chronoamperometry and impedance measurements.

Figure 2.10 shows the schematic illustration of electrochemical impedance spectroscopy (EIS) measurement set-up used to investigate the charge transfer resistance at photoelectrode/electrolyte interface. In EIS measurement, a sinusoidal potential perturbation, generated by frequency response analyser (FRA), is superimposed on the DC potential applied to the working electrode against reference electrode and the resulting current is measured. Then the current is analysed to determine the impedance of photoelectrodes. The fabrication and PEC measurements of GaN, InGaN/GaN MQW and InP photoelectrodes are discussed in detail in Chapters 4, 5 and 6.

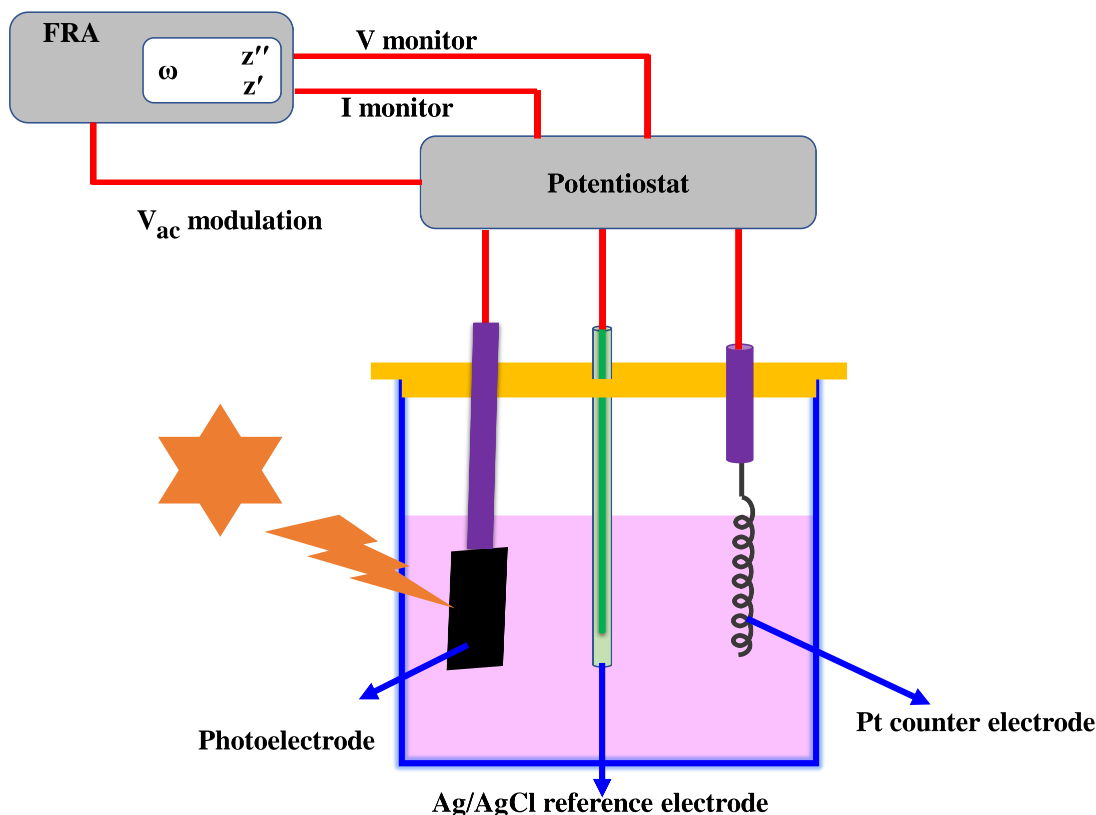

Figure 2.10: Schematic of electrochemical impedance spectroscopy measurement set-up.

2.7. Summary

To summarize, this chapter presents the experimental methods employed to accomplish the thesis. The experimental techniques involved in wafer growth, etch mask preparation, top-down NP fabrication, characterization of wafers and NPs and PEC testing of photoanodes are briefly discussed in this chapter. MOCVD was used for the growth of GaN and InGaN/GaN wafers. PECVD, EBL, RTA and RIE were used for preparing the etch mask to fabricate GaN alloy and InP NPs. ICP was employed to fabricate the GaN alloy and InP NPs. Microstructure and optical characterizations were carried out using SEM, μ-PL, TRPL and UV-Vis spectrophotometry. FDTD simulations were used to study the light interaction with GaN NP arrays. Finally, details of the PEC measurement unit used to test the GaN alloys and InP materials were discussed in this chapter.

2.8. References

[1] Karouta F, Vora K, Tian J and Jagadish C 2012 Structural, compositional and optical properties of PECVD silicon nitride layers *Journal of Physics D: Applied Physics* **45** 445301

[2] Iacona F, Ceriola G and La Via F 2001 Structural properties of SiO2 films prepared by plasma-enhanced chemical vapor deposition *Materials Science in Semiconductor Processing* **4** 43-6

[3] Chen Y 2015 Nanofabrication by electron beam lithography and its applications: A review *Microelectronic Engineering* **135** 57-72

[4] Hart M J and Evans A G R 1988 Rapid Thermal-Processing in Semiconductor Technology *Semiconductor Science and Technology* **3** 421-36

[5] Lin G-R, Kuo H-C, Lin H-S and Kao C-C 2006 Rapid self-assembly of Ni nanodots on Si substrate covered by a less-adhesive and heat-accumulated SiO_2 layers *Applied Physics Letters* **89** 073108

[6] Kim M J, Lee J S, Kim S K, Yeom G Y, Yoo J-B and Park C-Y 2005 Fabrication of Si nano-pillar array through Ni nano-dot mask using inductively coupled plasma *Thin Solid Films* **475** 41-4

[7] Huang H-W, Kao C-C, Hsueh T-H, Yu C-C, Lin C-F, Chu J-T, Kuo H-C and Wang S-C 2004 Fabrication of GaN-based nanorod light emitting diodes using self-assemble nickel nano-mask and inductively coupled plasma reactive ion etching *Materials Science and Engineering: B* **113** 125-9

[8] Homma Y, Finnie P, Ogino T, Noda H and Urisu T 1999 Aligned island formation using step-band networks on Si(111) *Journal of Applied Physics* **86** 3083-8

[9] Crouse D, Lo Y-H, Miller A E and Crouse M 2000 Self-ordered pore structure of anodized aluminum on silicon and pattern transfer *Applied Physics Letters* **76** 49-51

[10] Lieberman M A and Lichtenberg A J 2005 *Principles of Plasma Discharges and Materials Processing* (New York: John Wiley & Sons, Inc.)

[11] Fouad K 2014 A practical approach to reactive ion etching *Journal of Physics D: Applied Physics* **47** 233501

[12] Ameruddin A S 2015 Growth and Characterisation of Gold-seeded Indium Gallium Arsenide Nanowires for Optoelectronic Applications. (Canberra: The Australian National University) p 182

[13] Wang F, Gao Q, Peng K, Li Z, Li Z, Guo Y, Fu L, Smith L M, Tan H H and Jagadish C 2015 Spatially Resolved Doping Concentration and Nonradiative Lifetime Profiles in Single Si-Doped InP Nanowires Using Photoluminescence Mapping *Nano Lett* **15** 3017-23

Chapter 3

Fabrication of Ordered GaN Nanopillars Using Top-down Approach

3.1. Introduction

GaN nanostructures offer several advantages over their planar counterparts such as a large surface area, variable absorption and extraction of light, and non- and semi-polar planes for epitaxial growth to form core-shell device structures which increase the active junction area and mitigate polarization effects [1-3]. Exploiting these benefits, several optoelectronic devices based on GaN nanostructures such as LEDs [4-6], photodetectors [7-9] and solar cells [3, 10] have already been demonstrated. Fabrication of GaN NPs using a top-down process [11] can be the best approach for NPs of custom dimensions with controlled doping as it involves the etching of lithography-patterned epitaxial layers of high crystal quality grown using a well-matured technique such as MOCVD wherein doping and layer thickness are precisely controlled. On the other hand, bottom-up [12-14] approaches suffer from the lack of control over the NP dimensions with the doping concentration [15, 16]. Comprehensive studies are carried out to study the influence of etching parameters such as gas chemistry, ICP/RF power, chamber pressure and substrate temperature on the GaN NPs morphology, fabricated using inductively plasma etching (ICP) of pre-patterned GaN epitaxial layers in a top-down approach [11, 17]. Apart from the etching parameters, the spacing between the NPs, called array pitch, also have a significant influence on the NPs morphology and its optical properties. The optical properties of the NPs can be engineered by tailoring the NP dimensions such as pitch and diameter [18-20], which are critical for using them in any optoelectronic device application. In addition, the optical quality of the NPs also plays a crucial role in the performance of NP optoelectronic devices. In this chapter, we study the structural and optical/optoelectronic properties of GaN NPs fabricated using ICP etching of EBL-patterned epilayers. SEM was employed to study the influence of EBL pattern dimensions on the morphology of NPs. PL and FDTD simulations have been used to investigate the influence of NP dimensions on the optical properties and optical quality of the NPs.

This chapter focuses on the investigation of influence of array pitch on the morphology and optical properties of ordered GaN NPs fabricated using a top-down approach. Section 3.2

presents the processing steps involved in top-down fabrication of ordered GaN NPs. The top-down fabrication of GaN NPs involves the ICP etching of EBL-patterned GaN epilayers grown on sapphire using MOCVD. The array pitch of the EBL-patterned etch mask is varied from 400 to 800 nm while keeping a constant diameter of 100 nm. The influence of array pitch on the morphology was studied using SEM in Section 3.3. The effect of array pitch on the optical properties of the NPs is discussed in Section 3.4 using PL. NP arrays with 400 nm pitch and 100 nm diameter exhibited four-fold enhancement in PL intensity compared to their planar counterpart and the intensity decreased with increasing pitch. This enhancement in PL for NPs compared to the epilayer and influence of the array pitch on PL is explained in Section 3.5 with the support of FDTD simulations. The actual dimensions of top-down fabricated NPs is taken into consideration in FDTD simulation calculations of absorption, collection and extraction efficiency of GaN NP arrays. In Section 3.5, optical quality of the NPs is assessed using power dependent PL and FDTD simulations. Quantum efficiency of the GaN NPs is assessed by following the technique describe in ref. [21] through a combination of power dependent PL and FDTD simulations. At the end, section 3.6 summarizes the chapter.

3.2. Fabrication of ordered GaN NPs

The schematic representation of processing steps involved in top-down fabrication of GaN NPs is shown in Figure 3.1. GaN undoped epilayers of 2 µm thick grown on sapphire using MOCVD were used for the fabrication of GaN NPs. The top-down fabrication of GaN NPs was carried out by first depositing 500 nm SiO_2 at 300 ^{O}C using PECVD to create the SiO_2/Cr etch mask. SiO_2 was deposited at a chamber pressure of 650 mTorr with $SiH_4/N_2/N_2O$ flow rates of 9/161/710 sccm and 20 W RF power. Next, PMMA electron beam resist was spin-coated on these samples. The spin-coated samples were then loaded into EBL to write desired square lattice patterns of circles with a diameter of 100 nm and pitch ranging from 400 to 800 nm. These circles were transferred into the resist as circular holes after developing the exposed resist in methyl isobutyl ketone (MIBK) developer. A 100 nm Cr layer was then deposited on the sample using electron beam evaporation. Following lift-off in acetone, the sample had arrays of Cr nano-disks patterned on its surface. These Cr nano-disk patterns were transferred onto SiO_2 by etching the SiO_2 layer around the Cr using ICP to produce the SiO_2/Cr etch mask. In subsequent steps, the SiO_2/Cr etch mask was used for fabricating GaN NPs of desired dimensions using ICP. ICP etching of SiO_2 was carried out at room temperature under 10 mTorr operating pressure with a CHF_3 flow rate of 40 sccm and RF/ICP powers of 200/100

W. For ICP etching of GaN, the ICP sample chamber was maintained at a temperature of 60 ºC under an operating pressure of 4 mTorr and RF/ICP powers of 200/1000 W with $Cl_2/H_2/Ar$ flow rates of 25/2/5 sccm. The remaining Cr and SiO_2 was removed by Cr etchant and HF solutions, respectively. All of the NP arrays studied here were fabricated simultaneously on the same wafer to avoid variations in etch conditions between different etch runs.

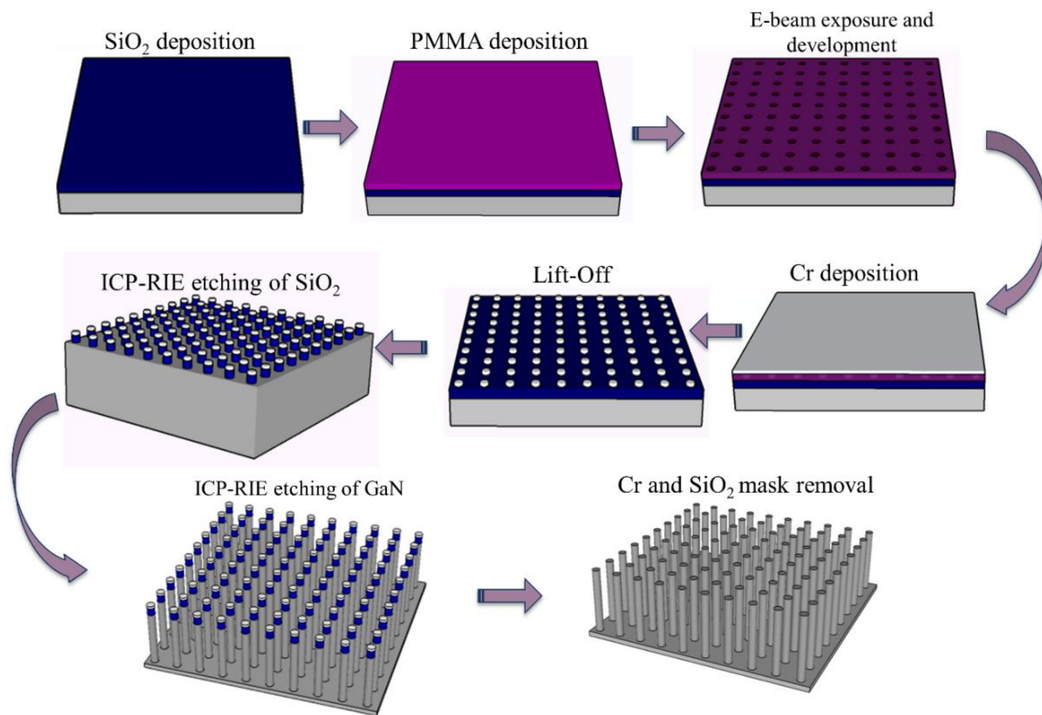

Figure 3.1: Flow chart of the processing steps involved in top-down fabrication of GaN NPs using ICP etching of EBL-patterned GaN epilayer.

3.3. Morphology of GaN NPs

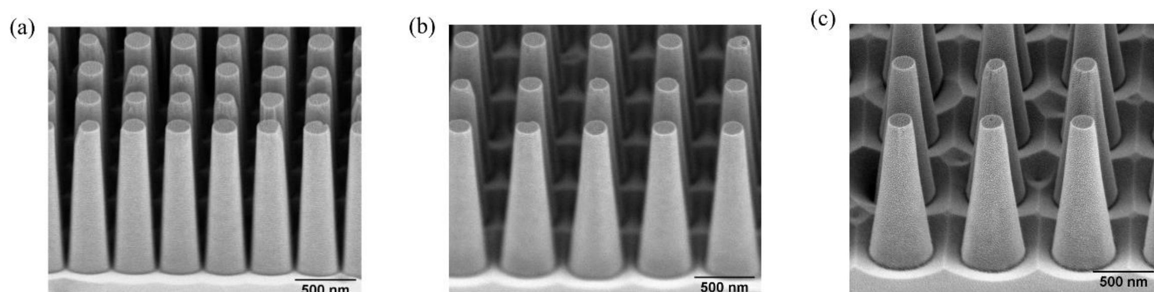

Figure 3.2: SEM images of GaN NP arrays with 100 nm diameter and a pitch of (a) 400 nm (b) 600 nm and (c) 800 nm taken at a 52º tilt angle.

Figure 3.2(a)-(c) shows SEM images of NP arrays with a diameter of 100 nm and pitch of 400, 600 and 800 nm. As shown in Figure 3.2, GaN NPs exhibit smooth sidewalls and a constant height of 1.3 μm irrespective of NP array pitch. The lag effect due to the variation of

array pitch is not observed for the fabrication conditions used in this study [22]. We observed variation in tapering (sloped sidewalls) of the NPs with the pitch of the array as shown in SEM images (Figure 3.2). The sidewall angle (α) of the NPs is defined as

$$\alpha = tan^{-1}\left(\frac{2h}{d_2 - d_1}\right) \quad \text{.....................3.1}$$

where h is the height and d_1 and d_2 are the top and bottom diameters of the NPs. The NP dimensions are illustrated in Figure 3.3(a). The sidewall angle reduces with increase in the pitch of the array as shown in Figure 3.3(b). The sidewall angle reduces from 87.5° for a pitch of 400 nm to 83.5° for a pitch of 800 nm. A sidewall angle of 90° represents perfectly vertical sidewalls and un-tapered NPs. Sloped sidewalls at higher pitches indicate that etching of GaN is dominated by the physical etching component also called the sputter-dominated regime [22]. The trenching observed at the bottom of the NPs at higher pitch can be a result of angular distributed ions, collected at the bottom of NPs upon colliding with a sidewall. The ions may have higher chances to collide at a glancing angle before reaching the bottom of the NPs when the sidewalls are tapered. With lowering pitch, ions hitting under angle have a higher chance of bouncing and hitting the surrounding NP sidewalls before reaching the bottom of the surface and as such contribute to the near vertical shape of the NPs. This results in reduced tapering of NPs with reducing pitch.

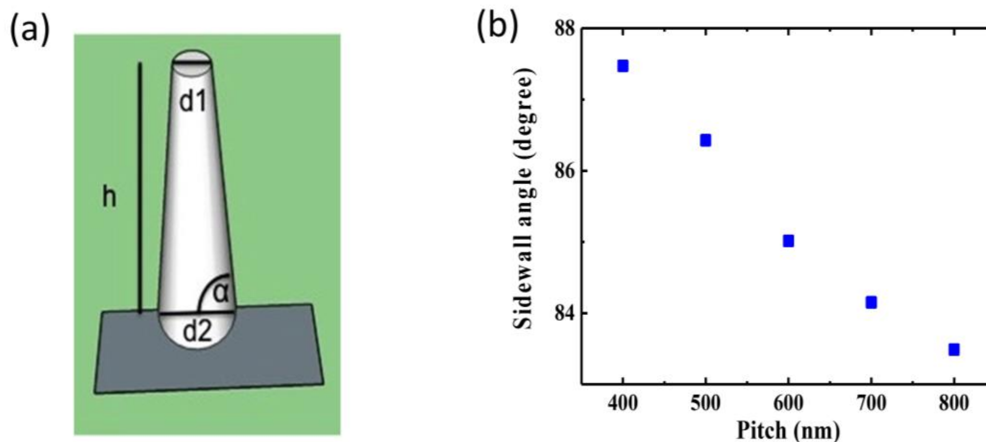

Figure 3.3: (a) NP dimensions used for calculating the sidewall angle, α and (b) variation of NP sidewall angle as a function of array pitch.

3.4. Optical characterization

Room temperature photoluminescence and power dependent photoluminescence measurements were employed to investigate the optical/optoelectronic quality of the NPs using μ-PL. The samples were optically excited with a continuous-wave 325 nm He-Cd laser and the emission from the samples was collected through a 36X (NA = 0.5) objective lens and detected

using a CCD detector. Details of the measurement set up is discussed in Section 2.4.2.1 of Chapter 2

3.4.1. Room temperature photoluminescence

Room temperature PL spectra of GaN NPs with varying pitch and its counterpart epilayer are shown in Figure 3.4(a). The PL peak intensity was normalized to one and the dependence of the peak intensity on NP pitch is also shown in Figure 3.4(b). The PL intensity of the NP array with 400 nm pitch is enhanced by four times than that of the epilayer under the same experimental excitation and collection conditions. The intensity of PL emissions from the NP arrays is higher than that from the epilayer for all pitches investigated. There is no significant contribution from the ~700 nm-thick epilayer, left underneath the NP arrays after etching, to the PL emissions from the arrays, as will be shown later in this chapter. The PL intensity from the NP arrays reduces with increasing pitch. The variation in emission intensity from the NPs could be a result of variation in the quantum efficiency of the NPs or variation in light absorption [23] and collection efficiency. Quantum efficiency is an indication of the material quality of the sample while the absorption/collection efficiency is a geometrical property of the array. Further, as shown in Figure 3.4(a), redshift in PL peak position is observed for NP arrays compared to the epilayer and it is independent of array pitch. This redshift could be because of partial strain relaxation in the NPs due to their smaller footprint sizes [17].

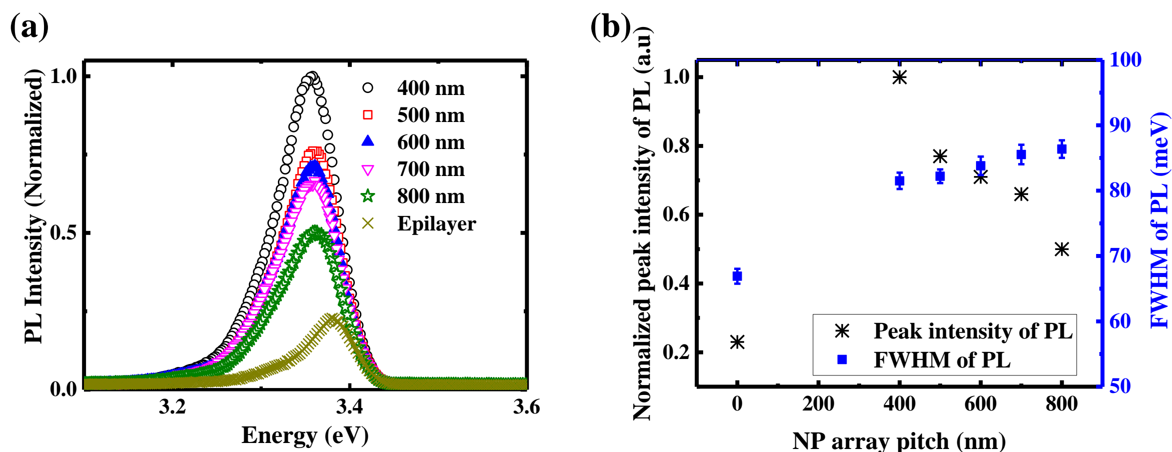

Figure 3.4: (a) Room temperature PL spectra from NP arrays with different pitch and (b) normalized peak intensity and full width at half maximum of the PL emission as a function of array pitch. Data for the GaN epilayer in (b) is also shown for comparison at pitch = 0.

Figure 3.4(b) also shows the influence of array pitch on the full width at half maximum (linewidth) of the PL spectra. The pitch at zero in the figure refers to the epilayer. The FWHM was deduced by fitting Gaussian functions with the experimental data in Figure 3.4(a). The PL linewidth for the NPs is slightly larger compared to the epilayer. This broadening could be attributed to the variation in strain relaxation along the NPs as the NPs are tapered. Furthermore, there is a slight trend of increasing linewidth by increasing the pitch of the NP arrays. As discussed earlier, tapering increases with increasing pitch and this may contribute to an increase in FWHM of PL emissions as a result of strain variation along the length of the NPs [17].

3.4.2. Power dependent photoluminescence

Power dependent measurements were carried out on the epilayer and the NP array with 400 nm pitch at room temperature. The excitation power was varied between 0.06 and 1.2 mW. The excitation power range was limited by the minimum power at which we were able to detect PL emissions and the maximum power emitted by the excitation laser. The measured variation in PL intensity from the epilayer and the NP array with excitation power at room temperature using a CW excitation at 325 nm is shown in Figure 3.5. The emission intensity from the NP array is higher than from the epilayer for the range of excitation powers investigated.

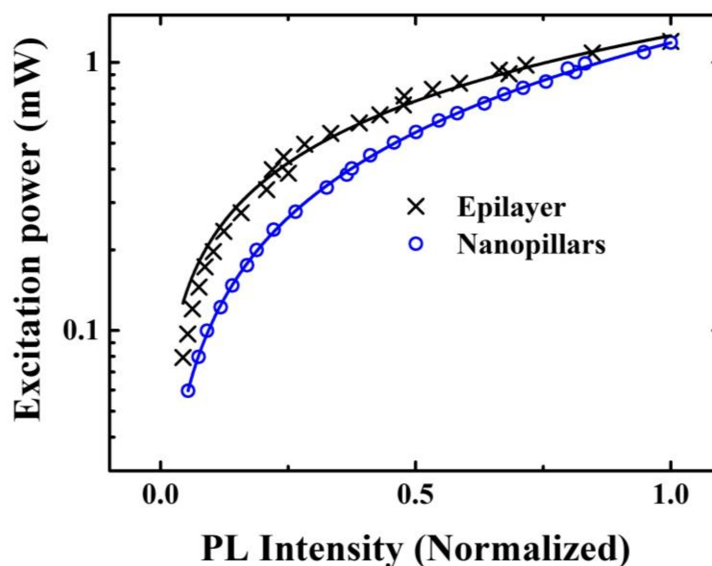

Figure 3.5: Power dependent PL of GaN epilayer and NP array with 400 nm pitch measured at room temperature using μ-PL.

3.5. FDTD simulations of optical properties

To explain the emission characteristics shown in Figure 3.4(a), we investigated the effect of array parameters on light absorption and emission characteristics using three dimensional FDTD simulations. NP arrays with infinite extension were simulated. Length, tapering and GaN epilayer left underneath the NP array were taken into consideration in simulations.

3.5.1. Absorption characteristics

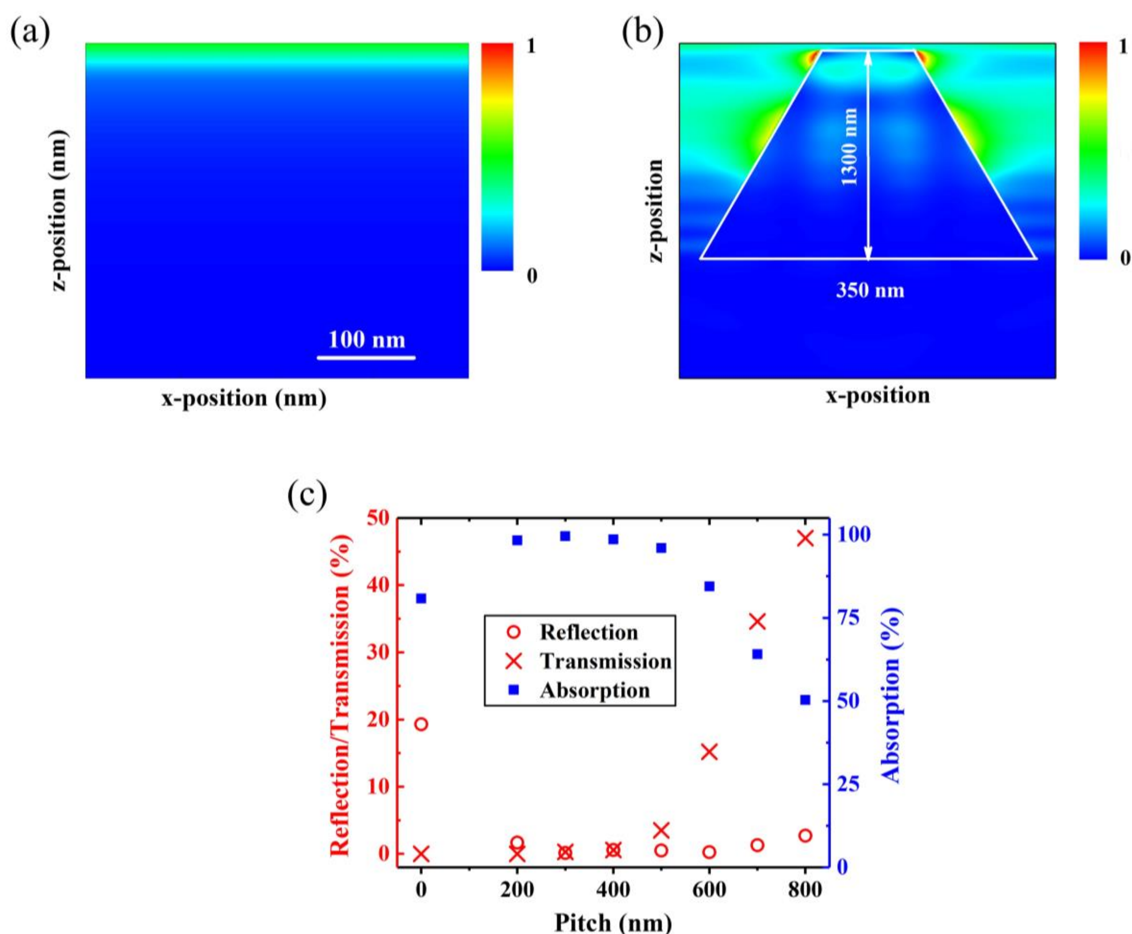

Figure 3.6: Electric field distribution of incident radiation in (a) epilayer, (b) NPs and (c) influence of array pitch on reflection, transmission and absorption properties calculated using FDTD simulations. The color bars on the right sides of figures (a) and (b) represent the normalized intensity of the electric field distribution of incident radiation from 0 to 1.

The absorption characteristics were determined by illuminating the sample with a plane wave source and recording the fraction of incident power which was reflected and transmitted through the sample at a wavelength of 325 nm. Figure 3.6(a) & (b) shows the electric field

intensity distribution across the epilayer and a NP in an array of 400 nm pitch. The field distributions show that incident light is strongly absorbed within few 10s of nm from the top surface of the epilayer and NP samples. This indicates that PL contribution from the GaN epilayer underneath the NP can be completely neglected because the incident light is completely absorbed within the top portion of the NP itself. Absorption of the sample was calculated by subtracting the sum of reflection and transmission from the incident power.

Figure 3.6(c) shows the variation in fraction of incident power reflected, transmitted and absorbed in the NP array as a function of pitch calculated using FDTD simulations. The data for the epilayer is referred as '0' array pitch in Figure 3.6(c). The NP arrays have geometry-dependent absorption characteristics that are very different to absorption in an epilayer. The absorption efficiency for the NP array with 400 nm pitch is 98.6%, which is 1.2 times larger than that of an epilayer (80.6%). The absorption efficiency reduces with increasing pitch and falls below that of an epilayer for pitch > 600 nm. This property is a consequence of the change in both the reflection and transmission properties of the NP arrays. The reflection losses for the NP arrays are significantly reduced (~25%) compared to the epilayer (19.3%). For NP arrays with dimensions much smaller than the wavelength of light, anti-reflection characteristics can be attributed to the lower effective index of the array compared to bulk material [24]. Effective medium theory is, however, not applicable to our NP arrays because of their wavelength-scale dimensions. We attribute lower reflection losses in our NP arrays to better in-coupling of incident light to the resonant modes supported in the array [24]. The transmission losses for the NP arrays are higher than in an epilayer because of reduced absorption volume. The transmission loss increases with increasing pitch and reaches 47% for a pitch of 800 nm. Therefore, we attribute the increase in absorption efficiency of NPs with 400 nm pitch to reduced reflection losses and subsequent lowering of absorption for larger pitches to an increase in transmission losses.

3.5.2. Emission characteristics

FDTD simulations were also performed on the epilayer and NPs samples to understand the influence of the NP array geometry on the emission characteristics of samples. Similar to the light absorption properties, the emission characteristics of NP arrays are also very different to that of an epilayer. The parameters of the array alter the angular distribution of emission from NPs. The angular distribution of emission determines the fraction of light emitted by the sample that is detected in our experiments, which is limited by the numerical aperture of the objective lens used. We placed dipole emitters inside the NPs at regions of maximum

absorption (shown in Figure 3.6(a) and (b)) and investigated their far-field emission characteristics. We then calculated the fraction of emitted light within a cone with a half angle of 30°, corresponding to the numerical aperture of the objective lens used in our experiments. Figure 3.7(a) and (b) show the far field emission properties of epilayer and NPs with discrete angular distributions. We calculated the fraction of emitted light within a cone with a half angle of 30°, corresponding to the numerical aperture of the objective lens used in our experiments. This data is represented as the collection efficiency in Figure 3.7(c) and is the average for three different polarisations of the dipole emitters. We observe two peaks in the collection efficiency data at 300 and 600 nm pitches, which is due to the first and second diffraction orders falling just below the collection angle in our experimental setup, respectively.

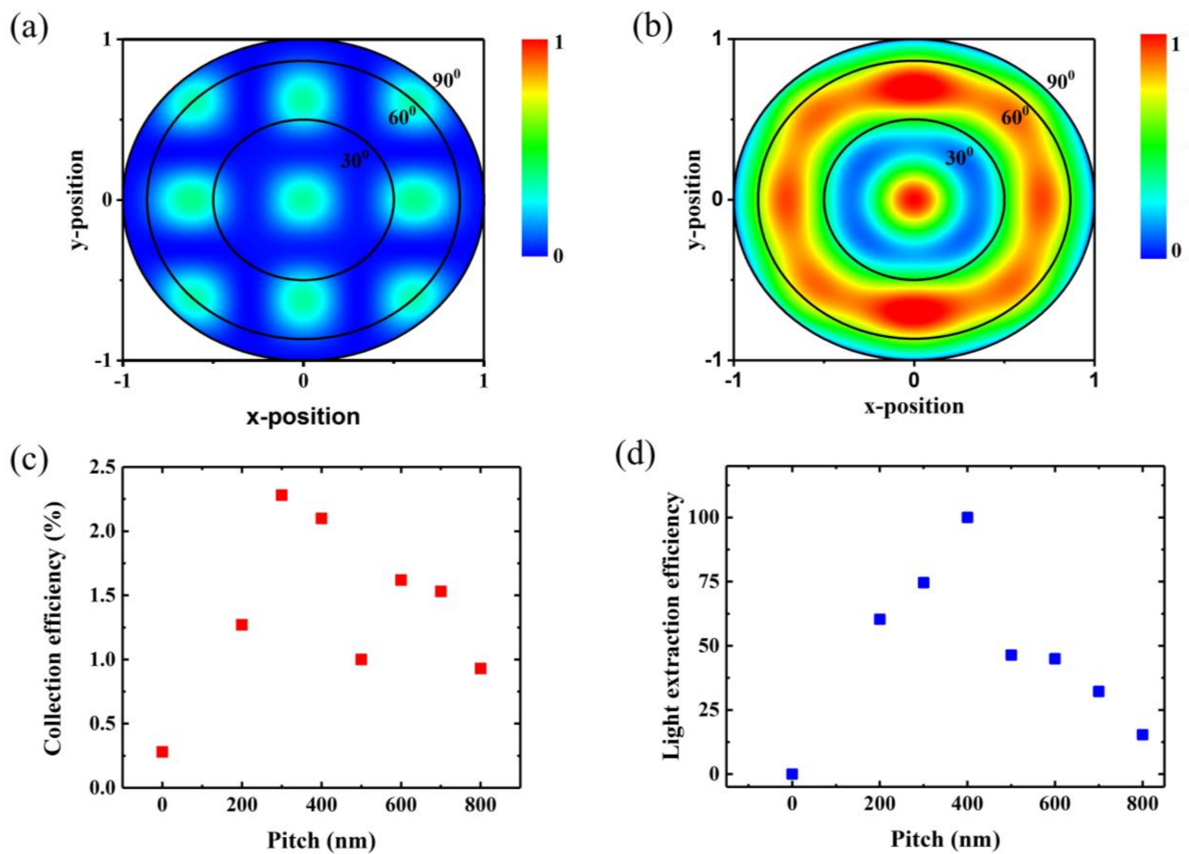

Figure 3.7: Far field emission patterns from (a) epilayer, (b) NPs in xy-plane and the influence of array pitch on (c) collection efficiency and (d) light extraction efficiency.

The ordered structure of the NP arrays also modifies the local density of optical states for the emitters and therefore alters their recombination rates [25]. This would affect the emission intensity from the sample. We determined the recombination rate enhancement for dipole emitters placed at regions of maximum absorption, with respect to an emitter in bulk

GaN, and studied the emission at 367 nm for an epilayer and at 370 nm for NPs which correspond to the respective peak positions shown in Figure 3.4(a). The PL emission intensity depends on the product of absorption and collection efficiencies and the emission rate enhancement, shown as light extraction efficiency in Figure 3.7(d). The light extraction efficiency follows the same trend observed in PL intensities (Figure 3.4(a)). Thus, it can be concluded that the change in PL emission intensities from the NP arrays is purely a geometrical effect.

3.5.3. Quantum efficiency of GaN nanopillars

Quantum efficiency (QE) is a measure of the optical quality of a material. QE is defined as the ratio of radiative recombination rate to the total recombination rate. We experimentally determined the QE of the GaN epilayer and the NPs using the approach outlined by Yoo et al. [21] in order to investigate the effect of the top-down fabrication method on the material quality. This model is based on the rate equation also called the 'ABC model', which defines relation between total recombination rate (G) to individual recombination rates such as Shockley-Read-Hall (SRH) nonradiative recombination, radiative recombination, and Auger nonradiative recombination

$$G = An + Bn^2 + Cn^3 \qquad \ldots\ldots\ldots\ldots\ldots\ldots\ldots 3.2$$

where, A, B and C are the Shockley-Read-Hall, radiative and Auger coefficients and n is carrier concentration. Quantum efficiency is defined as

$$QE = Bn^2/G \qquad \ldots\ldots\ldots\ldots\ldots\ldots\ldots 3.3$$

As the integrated PL intensity (I) is proportional to radiative recombination and G is linearly dependent on laser power (P), we have

$$I = a\,Bn^2 \qquad \ldots\ldots\ldots\ldots\ldots 3.4$$

$$G = xP \qquad \ldots\ldots\ldots\ldots\ldots 3.5$$

where a is determined by the excited active volume region and the total collection efficiency and x is a coefficient which is determined by the sample absorption. Equation 3.5 now can be expressed as

$$P = \frac{A}{x\sqrt{aB}}\sqrt{I} + \frac{1}{xa}I + \frac{C}{x(aB)^{3/2}}I^{3/2} \qquad \ldots\ldots\ldots\ldots\ldots\ldots 3.6$$

Equation 3.6 is simplified to the following equation by using the fitting parameters C1, C2, C3 for $\frac{A}{x\sqrt{aB}}$, $\frac{1}{xa}$ and $\frac{C}{x(aB)^{3/2}}$ respectively.

$$P = C_1 I^{1/2} + C_2 I + C_3 I^{3/2} \quad \ldots\ldots\ldots\ldots\ldots 3.7$$

Now the QE can be expressed as

$$QE = \frac{Bn^2}{G} = \frac{C_2 I}{P} \quad \ldots\ldots\ldots\ldots\ldots\ldots 3.8$$

The QE can be calculated by extracting C_2 from the fitted power dependent PL spectra (Figure 3.5) using Equation 3.7. Figure 3.8 shows the QE for an epilayer and a NP array with 400 nm pitch versus photo-generated carrier concentration. The photo-generated carrier concentration in the samples is calculated using the following expression

$$n = \frac{PA\tau}{E_g V} \quad \ldots\ldots\ldots\ldots\ldots\ldots 3.9$$

where P is excitation laser power, A is absorption, τ is effective carrier life time, E_g is band gap energy and V is the volume over which the carriers are generated. Absorption data calculated using FDTD simulations, as discussed in Section 3.5.1, is used in determination of absorption properties of the material. The absorption depth (Figure 3.6(a) & (b)) and spot size of the excitation laser are used in the calculation of volume, V. We used an effective carrier lifetime of 30 ps [26]. Figure3.8 shows that the QE of the epilayer increases with increasing carrier density, reaching a value of 0.6 at a carrier density of $1.58\text{x}10^{18}$ cm^{-3}. Variation of QE with carrier density suggests that QE is limited by Shockley-Read-Hall (SRH) recombination. With increasing carrier density, the radiative recombination rate increases and exceeds the monomolecular recombination rate leading to an increase in QE. On the other hand, the variation of QE of NPs with carrier density suggests that the carrier density in the NPs is in the region where Auger recombination becomes dominant and hence QE starts to decrease with increasing carrier concentration. The QE of the NPs is 0.71 at a carrier density of $3.11\text{x}10^{18}$ cm^{-3} and falls to 0.62 at a carrier density of $2.10\text{x}10^{19}$ cm^{-3}. The maximum and minimum power of the excitation source used in our experimental set-up limits the carrier concentration range in the epilayer and the NP array to the values shown in Figure 3.8. As a result, we were not able to determine the quantum efficiency for the epilayer and the NP array at the same carrier density.

We analytically calculated the QE with varying carrier concentration using the ABC model [21] by assuming the A, B and C coefficients are the same for the epilayer and the NPs and do not vary with carrier concentration. The solid green plot in Figure 3.8 shows the

analytically calculated QE variation with injected carrier density using the ABC model. The A, B and C coefficients determine the variation in monomolecular SRH recombination, radiative recombination and Auger recombination with carrier density, respectively. The data points for the epilayer for lower carrier densities and data points for the NP array for higher carrier densities are used in obtaining the quantum efficiency plot versus carrier density. The reasonably good fit of the ABC model with experimental data (Figure 3.8) results in A, B and C coefficient of $3.4x10^{7}$ s^{-1}, $4.5x10^{-11}$ cm^{3} s^{-1} and $2.5x10^{-30}$ cm^{6} s^{-1}, respectively. These coefficients are in good agreement with values reported earlier [27-29]. The fact that a single analytical curve fits both datasets indicates reasonably well that the material quality of the NPs is not degraded due to the etching process, and both the epilayer and NPs maintain similar optoelectronic quality.

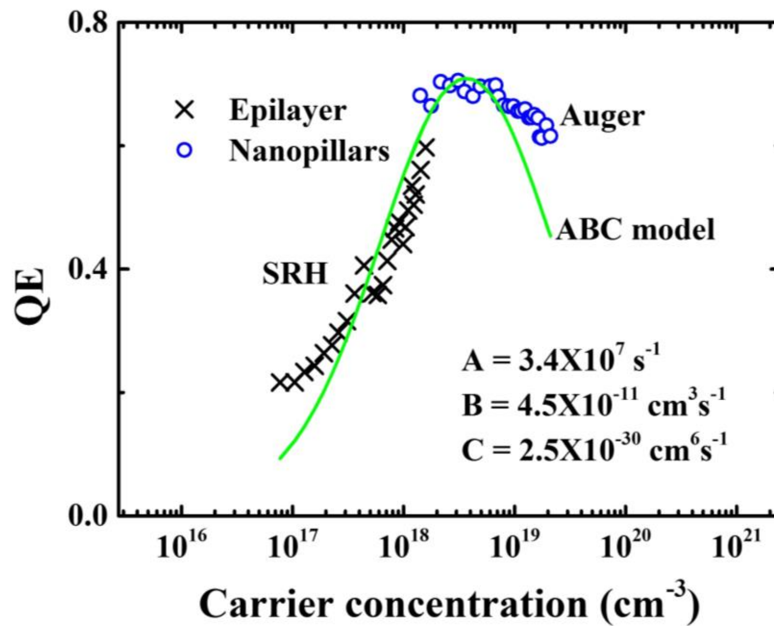

Figure 3.8: Dependence of quantum efficiency on photo-excited carrier concentration. The points are experimental data and the line is a fit to experimental data following the approach of Yoo et. al [21].

3.6. Summary

In this chapter, we studied the influence of array pitch on the microstructural evolution of GaN NPs fabricated using a top-down approach with ICP etching of EBL-masked GaN epilayers. The GaN NPs have smooth sidewalls and no lag effect is noticed for NP arrays irrespective of array pitch for the fabrication conditions considered in this study. The tapering of NPs increased, i.e., the sidewall angle decreased with increase in array pitch from 87.5° for

400 nm pitch to 83.5^{O} for 800 nm pitch arrays with a fixed diameter of 100 nm. NPs exhibit superior photoluminescence intensity compared to the epilayer despite having a smaller volume compared to the epilayer. About four times enhancement in PL intensity was observed for NPs with 400 nm pitch against the epilayer, which decreased with increasing array pitch. However, the PL spectra was slightly broadened for NPs with respect to the epilayer which could be due to variation in the partial relaxation along the NPs as they are tapered. Further, partial strain relaxation due to the small foot print size of NPs caused the redshift in PL peak position for NPs.

FDTD simulations confirm that the PL enhancement for NPs compared to their counter-part epilayer is a consequence of enhanced light absorption and light extraction efficiency in the NP arrays. FDTD simulation revealed that the variation in PL intensities of NP arrays was mainly due to the geometrical effect of NP array. The absorption characteristics of the GaN NP arrays were influenced by the NP array dimensions. Absorption was enhanced for NP arrays compared to the epilayer for high filling fraction values due to the dominating antireflection properties and fell below that of epilayer for low filling fraction due to the increased transmission losses. Further, we experimentally determined the quantum efficiency of the NPs and found it to be similar to that of the epilayer, indicating that the material quality of the NPs is not degraded by the top-down fabrication processes. The enhanced light absorption and extraction properties of the NPs compared to the epilayer makes them a promising candidate for solar energy conversion and solid-state lighting applications, respectively.

3.7. References

[1] Ryou J H, Yoder P D, Liu J P, Lochner Z, Kim H, Choi S, Kim H J and Dupuis R D 2009 Control of Quantum-Confined Stark Effect in InGaN-Based Quantum Wells *Ieee Journal of Selected Topics in Quantum Electronics* **15** 1080-91

[2] Chang J R, Chang S P, Li Y J, Cheng Y J, Sou K P, Huang J K, Kuo H C and Chang C Y 2012 Fabrication and luminescent properties of core-shell InGaN/GaN multiple quantum wells on GaN nanopillars *Applied Physics Letters* **100** 261103

[3] Wierer J J, Jr., Li Q, Koleske D D, Lee S R and Wang G T 2012 III-nitride core-shell nanowire arrayed solar cells *Nanotechnology* **23** 194007

[4] Wang C Y, Chen L Y, Chen C P, Cheng Y W, Ke M Y, Hsieh M Y, Wu H M, Peng L H and Huang J 2008 GaN nanorod light emitting diode arrays with a nearly constant electroluminescent peak wavelength *Optics express* **16** 10549-56

[5] Ra Y H, Navamathavan R, Park J H and Lee C R 2013 Coaxial In(x)Ga(1-x)N/GaN multiple quantum well nanowire arrays on Si(111) substrate for high-performance light-emitting diodes *Nano letters* **13** 3506-16

[6] Wang G T, Li Q, Wierer J J, Koleske D D and Figiel J J 2014 Top-down fabrication and characterization of axial and radial III-nitride nanowire LEDs *physica status solidi (a)* **211** 748-51

[7] Bugallo Ade L, Tchernycheva M, Jacopin G, Rigutti L, Julien F H, Chou S T, Lin Y T, Tseng P H and Tu L W 2010 Visible-blind photodetector based on p-i-n junction GaN nanowire ensembles *Nanotechnology* **21** 315201

[8] Babichev A V, Zhang H, Lavenus P, Julien F H, Egorov A Y, Lin Y T, Tu L W and Tchernycheva M 2013 GaN nanowire ultraviolet photodetector with a graphene transparent contact *Applied Physics Letters* **103** 201103

[9] Wang X, Zhang Y, Chen X, He M, Liu C, Yin Y, Zou X and Li S 2014 Ultrafast, superhigh gain visible-blind UV detector and optical logic gates based on nonpolar a-axial GaN nanowire *Nanoscale* **6** 12009-17

[10] Dong Y, Tian B, Kempa T J and Lieber C M 2009 Coaxial group III-nitride nanowire photovoltaics *Nano letters* **9** 2183-7

[11] Paramanik D, Motayed A, Aluri G S, Ha J-Y, Krylyuk S, Davydov A V, King M, McLaughlin S, Gupta S and Cramer H 2012 Formation of large-area GaN nanostructures with controlled geometry and morphology using top-down fabrication scheme *Journal of Vacuum Science & Technology B: Microelectronics and Nanometer Structures* **30** 052202

[12] Hersee S D, Sun X Y and Wang X 2006 The controlled growth of GaN nanowires *Nano Letters* **6** 1808-11

[13] Lin Y-T, Yeh T-W, Nakajima Y and Dapkus P D 2014 Catalyst-Free GaN Nanorods Synthesized by Selective Area Growth *Advanced Functional Materials* **24** 3162-71

[14] Qian F, Li Y, Gradecak S, Park H G, Dong Y, Ding Y, Wang Z L and Lieber C M 2008 Multi-quantum-well nanowire heterostructures for wavelength-controlled lasers *Nat Mater* **7** 701-6

[15] Tessarek C, Heilmann M, Butzen E, Haab A, Hardtdegen H, Dieker C, Spiecker E and Christiansen S 2014 The Role of Si during the Growth of GaN Micro- and Nanorods *Crystal Growth & Design* **14** 1486-92

[16] Yang P, Yan R and Fardy M 2010 Semiconductor nanowire: what's next? *Nano letters* **10** 1529-36

[17] Debnath R, Ha J-Y, Wen B, Paramanik D, Motayed A, King M R and Davydov A V 2014 Top-down fabrication of large-area GaN micro- and nanopillars *Journal of Vacuum Science & Technology B: Microelectronics and Nanometer Structures* **32** 021204

[18] Li K H and Choi H W 2011 Air-spaced GaN nanopillar photonic band gap structures patterned by nanosphere lithography *Journal of Applied Physics* **109** 023107

[19] Ng W N, Leung C H, Lai P T and Choi H W 2008 Nanostructuring GaN using microsphere lithography *Journal of Vacuum Science & Technology B: Microelectronics and Nanometer Structures* **26** 76

[20] Zhu J, Wang L, Zhang S, Wang H, Zhao D, Zhu J, Liu Z, Jiang D and Yang H 2010 The fabrication of GaN-based nanopillar light-emitting diodes *Journal of Applied Physics* **108** 074302

[21] Yoo Y-S, Roh T-M, Na J-H, Son S J and Cho Y-H 2013 Simple analysis method for determining internal quantum efficiency and relative recombination ratios in light emitting diodes *Applied Physics Letters* **102** 211107

[22] Rong B, Salemink H W M, Roeling E M, van der Heijden R, Karouta F and van der Drift E 2007 Fabrication of two dimensional GaN nanophotonic crystals (31) *Journal of Vacuum Science & Technology B: Microelectronics and Nanometer Structures* **25** 2632

[23] Zhu J, Yu Z, Burkhard G F, Hsu C M, Connor S T, Xu Y, Wang Q, McGehee M, Fan S and Cui Y 2009 Optical absorption enhancement in amorphous silicon nanowire and nanocone arrays *Nano letters* **9** 279-82

[24] Mokkapati S and Catchpole K R 2012 Nanophotonic light trapping in solar cells *Journal of Applied Physics* **112** 101101

[25] Purcell E M, Torrey H C and Pound R V 1946 Resonance Absorption by Nuclear Magnetic Moments in a Solid *Physical Review* **69** 37-8

[26] Kwon H K, Eiting C J, Lambert D J H, Wong M M, Dupuis R D, Liliental-Weber Z and Benamara M 2000 Observation of long photoluminescence decay times for high-quality GaN grown by metalorganic chemical vapor deposition *Applied Physics Letters* **77** 2503

[27] Dmitrieva A and Oruzheinikov A 1999 The rate of radiative recombination in the nitride semiconductors and alloys *Journal of Applied Physics* **86** 3241

[28] Bulashevich K A and Karpov S Y 2008 Is Auger recombination responsible for the efficiency rollover in III-nitride light-emitting diodes? *physica status solidi (c)* **5** 2066-9

[29] Kioupakis E, Rinke P, Delaney K T and Van de Walle C G 2011 Indirect Auger recombination as a cause of efficiency droop in nitride light-emitting diodes *Applied Physics Letters* **98** 161107

Chapter 4

Fabrication and Photoelectrochemical Studies of Random GaN Nanopillar Photoanodes

4.1. Introduction

GaN is considered one of the most promising materials for hydrogen generation via solar water splitting owing to its superior properties [1-5] and ability to straddle both oxidation and reduction potentials of water [6-14]. Moreover, nanopillars (NPs) offer enhanced light absorption, reduced carrier transfer lengths and large surface to facilitate efficient charge transfer at semiconductor/electrolyte interface over planar structures towards achieving efficient water splitting [15-20]. However, dimensions and carrier concentrations of NPs play a critical role in improving the PEC performance of NP photoanodes. Moreover, production of large area GaN NPs is essential for use in real world water splitting applications. Large area GaN NPs with controlled dimensions and carrier concentrations can be best achieved using a top-down approach as it allows for the use of quality GaN epilayers grown using well-matured planar growth technology wherein doping concentration is precisely controlled [21, 22]. On the other hand, the lack of NP dimension control during doping acts as a main setback for bottom-up growth methods [23, 24] and makes it difficult to understand the influence of carrier concentration on the PEC performance of NP photoanodes. In this chapter, we demonstrate the cost effective self-assembled random mask technique as an etch mask for the top-down fabrication of large area random GaN NPs and study the photoelectrochemical (PEC) performance of GaN NP photoanodes. Further, we investigate the influence of carrier concentration and NP dimensions on the PEC performance of GaN photoanodes.

In this chapter, we focus on the fabrication of large area GaN NPs using a top-down approach and understand their PEC properties using optical and electrochemical impedance spectra. Sections 4.2 and 4.3 present the fabrication of large area GaN NPs and their photoanodes, respectively. A self-assembled island random mask technique is adopted to create the etch mask for the fabrication of large area random GaN NPs. The morphology and optical properties of the planar and NP samples are discussed in Sections 4.4 and 4.5, respectively. Optical measurements reveal that NPs act as an anti-reflective coating below the GaN band

edge emission and it is NP dimension dependent. The determination of depletion layer thickness in n-GaN and its thickness variation as a function of carrier concentration is discussed in Section 4.6. The PEC properties of the GaN planar and NP photoanodes are examined and compared in Section 4.7. Substantial improvement in photocurrents is observed for NP photoanodes compared to their planar counterpart, tested using a three-electrode PEC testing station under one sun illumination. Further, the onset potentials of the NP photoanodes are slightly influenced by the carrier concentration and NP dimensions such as diameter and length. Section 4.8 deals with understanding the charge transfer resistance between semiconductors and electrolyte using electrochemical impedance spectra of NP photoanodes and GaN planar photoanodes with varying carrier concentration. A summary of the fabrication and PEC performance of the large area random GaN NP photoanodes is presented in Section 4.9.

4.2. Fabrication of random GaN nanopillars

GaN epitaxial layers (≈2 μm thick) with pre-defined carrier concentration grown on sapphire wafers using MOCVD were used for the fabrication of large area GaN NPs. Large area GaN NPs were fabricated by ICP etching of randomly masked GaN wafers. A self-assembled random mask technique was employed to create a large area nano etch mask for the fabrication of random GaN NPs using ICP etching. Rapid thermal annealing at high temperature and fast cooling of very thin metal film converts the film into random nano-islands, which can be used as a mask for ICP etching processes. The self-assembled random mask technique is a scalable and cost-effective technique for producing wafer scale NPs. To study the influence of carrier concentration on PEC performance, GaN NPs were fabricated from n-type GaN epilayers with four different carrier concentrations. The doping concentration of the GaN wafers was controlled by varying the silane flow during the MOCVD growth. The carrier concentration of the wafers was determined using Hall measurements. The carrier concentrations of GaN epilayers and assigned sample names are listed in Table 4.1. Figure 4.1 shows a schematic illustration of the top-down fabrication of GaN NPs using ICP etching of randomly masked GaN epilayers. Fabrication of GaN NPs was carried out by first depositing a 500 nm-thick SiO_2 using PECVD followed by the deposition of a very thin Ni film using e-beam evaporation. This Ni film was then converted into Ni nano-islands by RTA annealing at 900 ^{o}C in an argon atmosphere for 1 min. Figure 4.2(a) shows an SEM image of the Ni nano-islands formed from a 5 nm Ni film annealed at 900 ^{O}C. In the next step, the ICP etching of SiO_2 around the Ni particles created the SiO_2/Ni hard random mask. Figure 4.2(b) and (c) show SEM images of the SiO_2/Ni hard mask from top and side views, respectively. In the subsequent step, the

SiO_2/Ni mask was used as an etch mask for ICP etching of GaN for the fabrication of GaN NPs. After ICP etching, the fabricated GaN NPs were immersed in HF solution to remove the remainder of the SiO_2/Ni etch mask. The length and diameter of the NPs were controlled by varying the NP processing parameters such as ICP etching time and the thickness of the Ni film, respectively. The employed ICP etching parameters for both SiO_2 and GaN used for random GaN NPs are similar to those discussed in Chapter 3.

Table 4.1: Sample numbers and the corresponding n-type carrier concentrations.

Sample name	**Carrier concentration (cm^{-3})**
Sample 1 (S1)	Undoped
Sample 2 (S2)	1×10^{18}
Sample 3 (S3)	5×10^{18}
Sample 4 (S4)	1×10^{19}

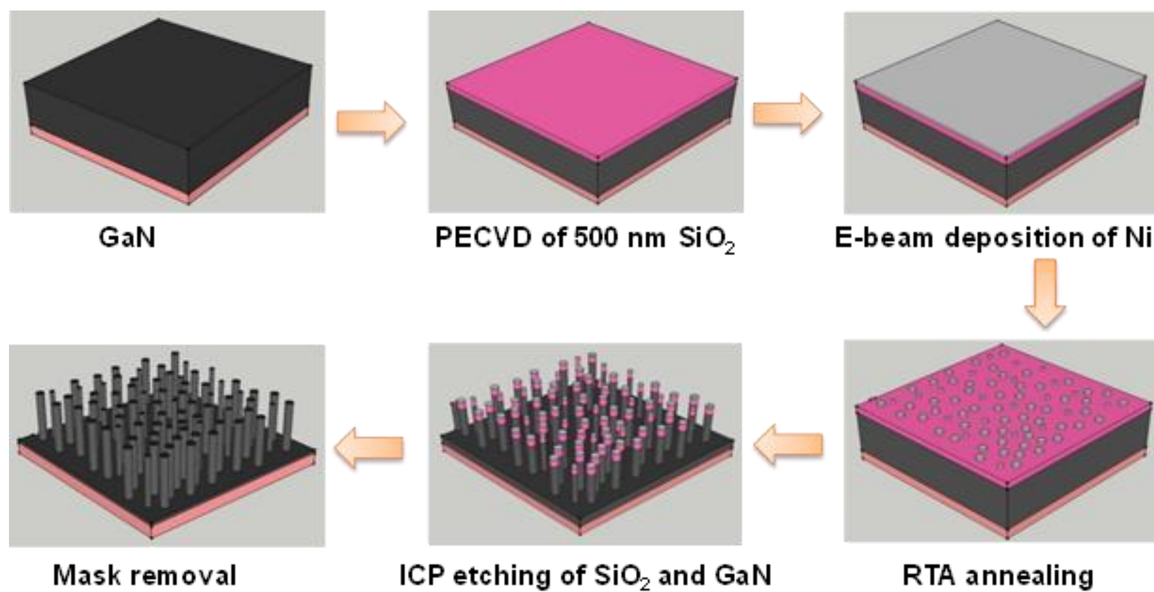

Figure 4.1: Illustration of the processing steps involved in the fabrication of random GaN NPs using a top-down approach.

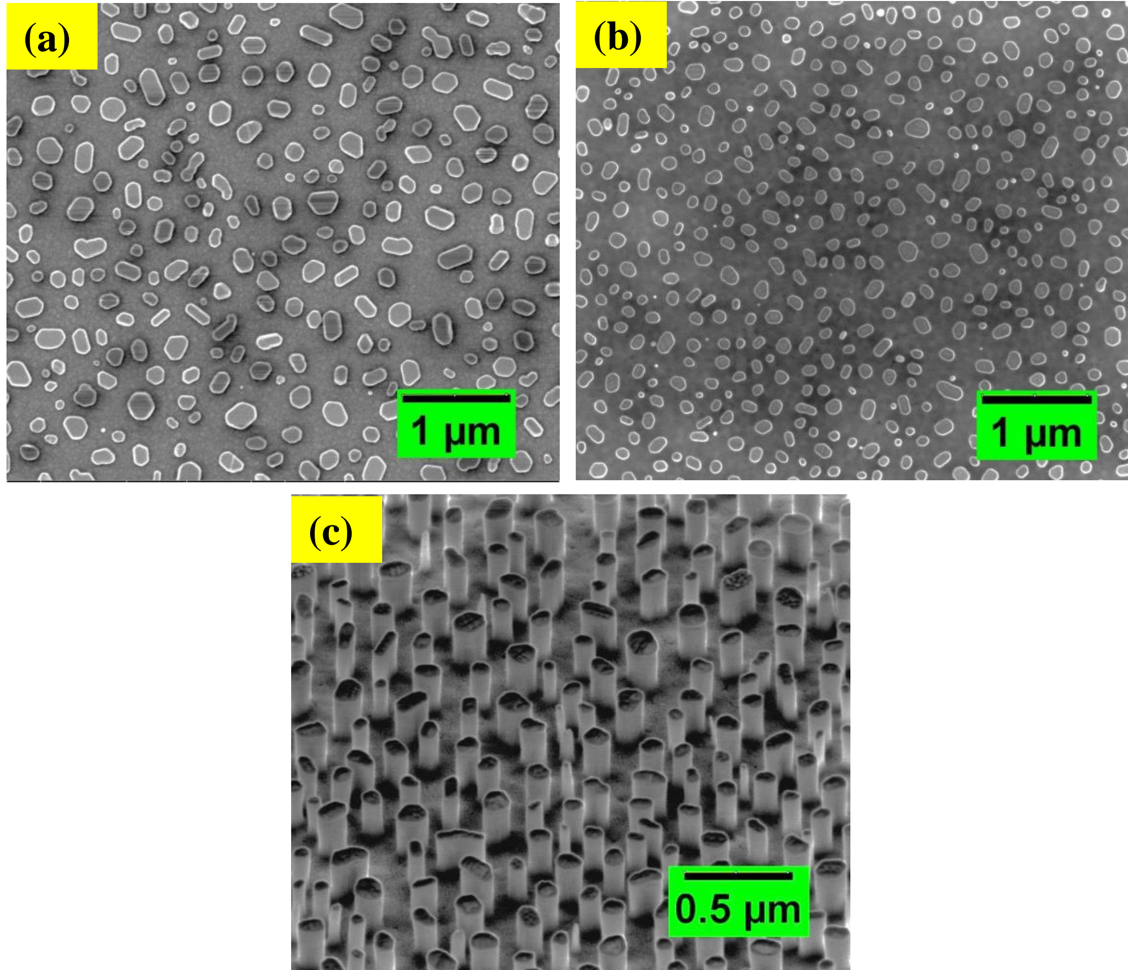

Figure 4.2: SEM images of (a) the Ni random mask formed by RTA annealing of 5 nm Ni at 900 ^{0}C in an Ar atmosphere, (b) the SiO_2/Ni random mask from the top and (c) the SiO_2/Ni hard mask taken at a 52^0 angle.

4.3. Fabrication of GaN photoanodes

Low resistance Ohmic contacts to the GaN photoanodes are crucial for measuring the PEC performance of GaN photoanodes. The Ohmic contacts to the planar and NPs photoanodes were formed by e-beam deposition of Ni/Au (30/150 nm) metal contacts. The contacts were then subjected to rapid thermal annealing at 400 °C in an argon atmosphere for 5 min. In this work, the contacts to the GaN photoanodes were made on the front side of the sample since GaN was grown on an insulating sapphire substrate. To achieve the top contacts, a portion of each sample was protected using a shadow mask while depositing the Ni mask film during the fabrication of GaN NPs. The metal contacts were made on this shadow masked area in the subsequent processing steps. Figure 4.3(a) shows a photographic image of a NP photoanode after metallization. To avoid carrier leakage from the metal contact to the electrolyte, a portion

of the metal contacts were painted with nail polish. Figure 4.3(b) shows a photograph of a GaN NP photoanode after painting.

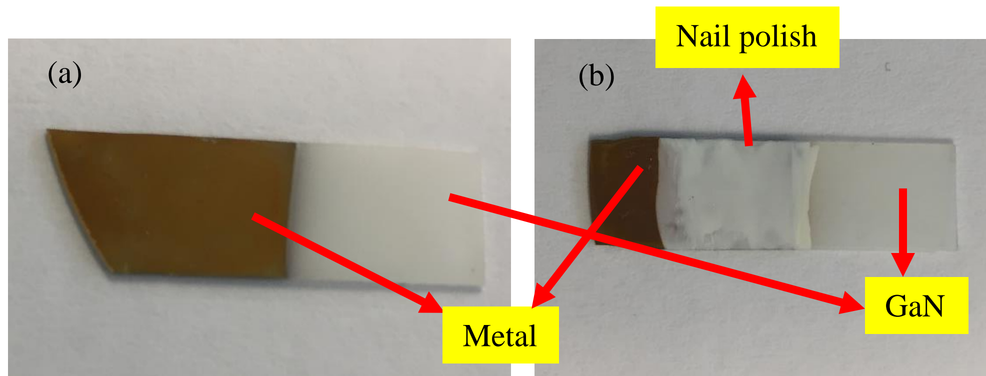

Figure 4.3: Photographs of (a) a NP photoanode with Ni/Au contacts and (b) a NP photoanode painted with nail polish to avoid carrier leakage into the electrolyte.

4.4. Morphology of the GaN NPs

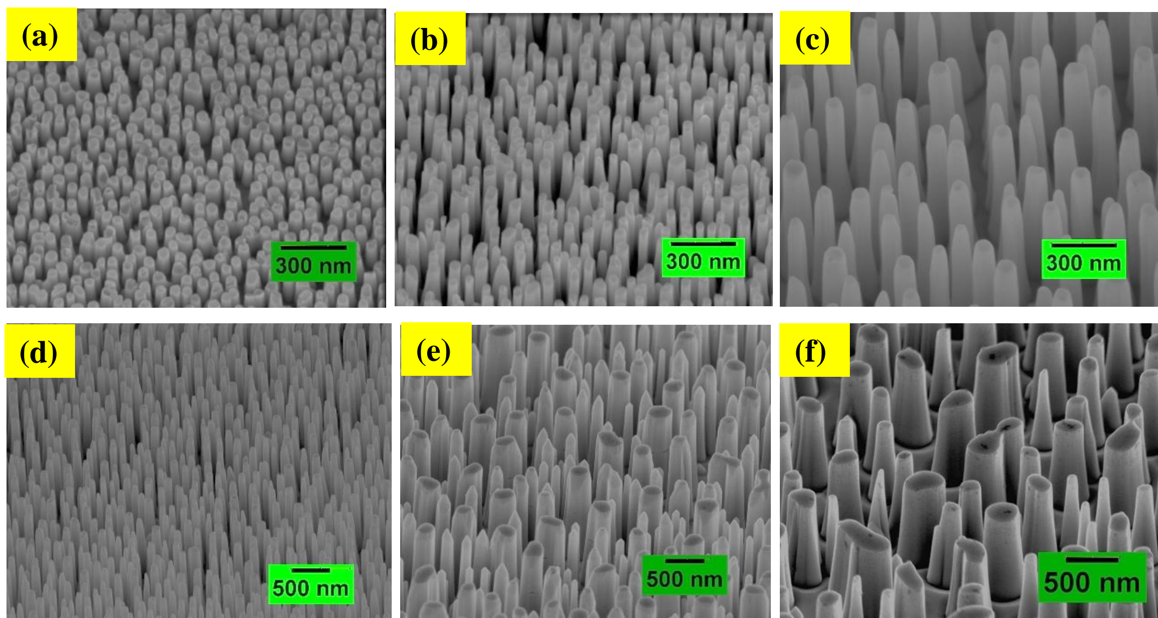

Figure 4.4: SEM images of (a) to (c) GaN NPs (images taken at a 30^0 tilt angle) with increasing lengths obtained from 5 nm Ni masked GaN sample by varying the ICP etch times from 60 to 120 s and (d) to (f) GaN NPs with increasing diameter (images taken at a 52^0 tilt angle) achieved by 120 s ICP etching of 5, 10 and 15 nm Ni masked GaN epilayers.

The microstructure of the large area random GaN NPs were examined using SEM. Figure 4.4 presents SEM images of the GaN NPs after removing the mask fabricated from Sample 2. The length and diameter of the NPs were determined by the etching time and Ni film

thickness, respectively. Figure 4.4(a)-(c) show SEM images of GaN NPs of lengths 200, 600 & 900 nm, etched for 60, 90 and 120 s respectively, from 5 nm Ni masked samples. While the etching time determines the length of the NPs, the diameter of the NPs is determined by the size of the Ni nano-islands. The size of the nano-islands in the self-assembled random mask technique depends on Ni film thickness and increases with increasing the film thickness. Figure 4.4(d)-(f) show NPs fabricated from etching for 120 s from 5, 10 and 15 nm Ni masked GaN samples, respectively. The diameter of the NPs increased with increasing the Ni thickness due to the increased size of Ni nano-islands. The diameters of the NP photoanodes were classified as a small (D1), medium (D2) and large (D3), fabricated from 5, 10 and 15 nm Ni masked samples, respectively. The diameter of the NPs is increased while the density is decreased with increasing Ni mask thickness under the same processing conditions as observed in Figure 4.4(d) - (f). From Figure 4.4(a)-(f), it can be noticed that all the NPs exhibit uniform height and smooth sidewalls irrespective of the etch time and Ni mask size. Figure 4.5(a)-(c) show histograms of diameter distribution of NPs fabricated from 5, 10 and 15 nm Ni masked samples, respectively. The diameter distribution becomes wider with increasing thickness of the Ni film. The average diameter of the NPs measured from the SEM images is 84, 144 and 202 nm for the 5, 10 and 15 nm Ni film masked samples, respectively.

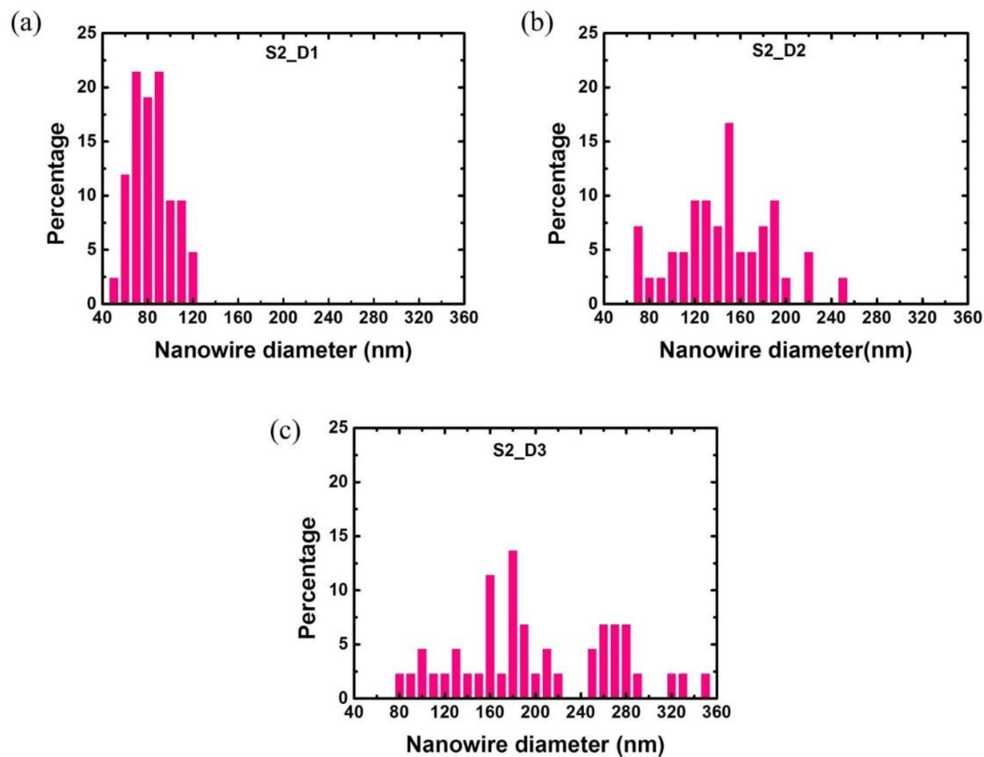

Figure 4.5: Diameter distribution of GaN NPs fabricated from ICP etching of (a) 5, (b) 10 and (c) 15 nm Ni masked GaN samples.

4.5. Optical properties of NPs

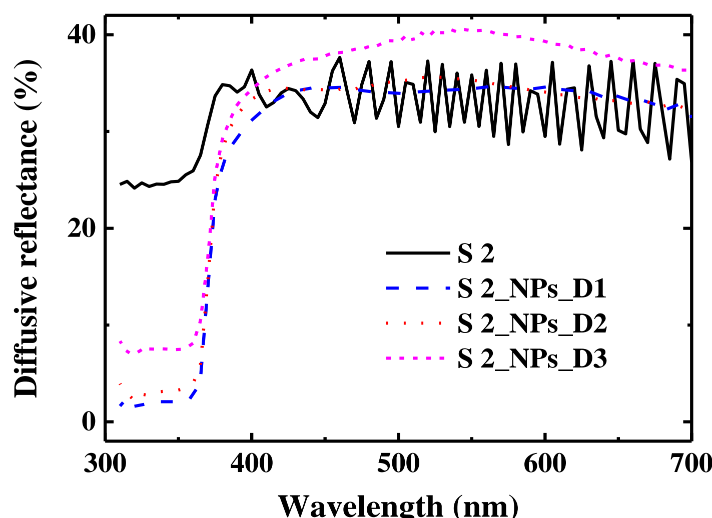

Figure 4.6: Diffuse reflectance spectra of planar and NP samples fabricated using 5, 10 and 15 nm thick Ni film mask.

To study the optical absorption of GaN NPs, diffuse reflectivity measurements were carried out on the epilayer and NPs using a UV-VIS spectrophotometer. The diffuse reflectance spectra of planar and NP photoanodes with varying diameters are shown in Figure 4.6. The fringes in the visible region of the diffuse reflectance spectra for the planar sample are attributed to Fabry-Perot interference. The NPs and planar samples used for these measurements were fabricated from Sample 2. From Figure 4.6, it can be observed that reflection for NPs is extremely small compared to the epilayers irrespective of the diameters of the NPs. Lower reflection losses lead to the enhanced light absorption by the NPs. Diffuse reflectivity of the small diameter NPs indicates that they absorb most of the light that is incident on the samples near the band edge of GaN. However, the anti-reflection properties of NPs decline with increasing diameter. On the other hand, the epilayer suffers from heavy reflection losses, which accounts for nearly 24% of the total incident light.

4.6. Depletion layer in n-GaN

The depletion layer is a space charge neutral region, which is formed due to band bending in doped semiconductors. Band bending leads to the migration of electrons and holes from higher to lower doping regions of semiconductors, which results in the formation of an ionic space charge neutral region called the depletion region. In the case of extrinsic semiconductors, Fermi level pinning at the surface leads to the formation of a depletion region near the semiconductor surface. The Fermi level pinning at the surface results in upward and

downward bending of the valence and conduction bands for n-type and p-type semiconductors, respectively. Figure 4.7 illustrate the formation of depletion region due to the band bending in n-type NPs. The upward (downward) band bending causes the electrons (holes) to flow into the bulk region and holes (electrons) into the surface region of the semiconductor. This results in a charge neutral region near the semiconductor surface. The width of the depletion region depends on the carrier concentration of the semiconductor. The depletion region width of GaN can be deduced using the following relation:

$$\text{Depletion layer width } (W) = \sqrt{\frac{\epsilon_0 \epsilon \Delta V}{e N_d}} \quad \ldots\ldots\ldots\ldots\ldots\ldots 4.1$$

where ϵ_0 = vacuum permittivity, ϵ = dielectric constant of GaN, ΔV = potential difference between GaN and the redox couple in the solution, e = elementary charge, and N_d = carrier concentration. Table 4.2 shows the calculated depletion layer thickness of the n-GaN epilayers for a given carrier concentration in this study. The calculated depletion layer width decreases with increasing carrier concentration of n-GaN.

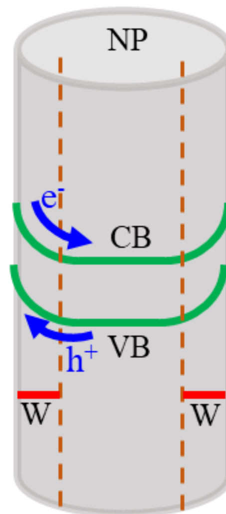

Figure 4.7: Schematic illustration of band bending in n-doped semiconductors NPs

Table 4.2: Estimated depletion layer width for different carrier concentrations in n-GaN epilayer.

Sample	**Carrier concentration (cm^{-3})**	**Depletion layer width (nm)**
S 2	$1X10^{18}$	24.5
S 3	$5X10^{18}$	11
S 4	$1X10^{19}$	7.7

4.7. Photoelectrochemical performance of GaN photoanodes

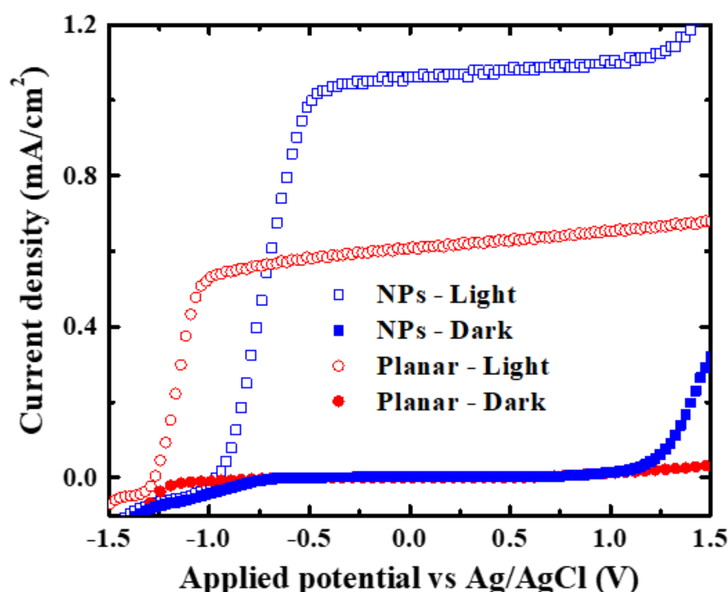

Figure 4.8: Linear sweep voltammetry of GaN planar and NP photoanodes measured in 1 M NaOH electrolyte using a three electrode configuration PEC setup under dark and sunlight illumination.

A three-electrode configuration PEC set-up as described in Section 2.6 of Chapter 2 was employed to carry out PEC measurements of the GaN photoanodes. PEC measurements were carried out in 1 M NaOH electrolyte solution in a quartz cell consisting of the GaN working electrode, a Pt counter electrode and anAg/AgCl reference electrode. The PEC performance of the photoanodes was evaluated under one sun illumination. Figure 4.8 shows the current density of planar and NP photoanodes measured under dark and sunlight illumination. The NPs used in this study were fabricated by ICP etching of 5 nm Ni masked Sample 2 for 120 s. Negligible dark currents are observed for both planar and NP photoanodes. As shown in Figure 4.8, a substantial improvement in saturation photocurrent is noticed for the NP photoanode compared to its planar counterpart. The enhancement for the NP photoanode is nearly 1.7 times that of the planar photoanode. The highest saturation photocurrent density of around 1.0 mA/cm^2 is measured for the NP photoanode. To our knowledge, this is the best reported current density in the literature for GaN NP photoanodes without the presence of InGaN quantum wells under one sun light illumination, which is also close to the theoretical limit [25, 26]. This enhancement can be attributed to the enhanced absorption by the NP photoanodes, as well as the increased semiconductor/electrolyte interface area. As discussed in Section 4.5 in this chapter, NPs absorb almost all the incident light while planar photoanodes incur a 24% absorption loss due to reflection from the flat surface (Figure 4.6). This

enhancement in absorption contributes to the generation of additional carriers in the NPs that participate in solar water splitting. Further, NPs offer massive semiconductor/interface areas compared to the planar structures that result in an enhanced depletion region around the semiconductor surface. This increased depletion region leads to enhancement in carrier separation and efficient transfer of holes to the semiconductor/electrolyte interface.

4.7.1. Influence of carrier concentration on PEC performance

The conductivity of the samples plays a critical role in the PEC performance of the photoanodes. In order to investigate the influence of conductivity on PEC performance, the photo-responses of the planar GaN and their respective NPs with different carrier concentrations were evaluated by applying them as a photoanode in a three-electrode configuration set-up as described in the previous section. The carrier concentrations of the planar samples and their respective NP photoanodes can be referred to in Table 4.1.

4.7.1.1. Planar photoanodes

Figure 4.9 shows the PEC performance of GaN planar photoanodes with varying carrier concentration. The dark currents for all the samples used in this study, irrespective of the carrier concentration, are insignificantly low. On the other hand, the photoresponse of the photoanodes shows a strong dependence on carrier concentration. The onset potential is the lowest for S1 and increases with increasing carrier concentration. However, the photocurrent of S1 increases gradually and reaches a plateau at a much higher potential, indicating that a large overpotential is needed for the undoped sample. The lowest overpotential to reach saturation currents is achieved for the photoanode S2 and it increases with increasing carrier concentration. This is attributed to the variation of depletion layer thickness with carrier concentration [27]. In general, the energy bands of the semiconductor are flat in bulk and bend at the surface. The band bending at the surface leads to the formation of a charge neutral region (depletion region) near the semiconductor surface. Photogenerated carriers within the depletion zone can be effectively separated due to band bending as compared to those generated in the bulk region due to the flat nature of the bands in the bulk region of the semiconductor. To avoid the inevitable carrier recombination and extract the photogenerated carriers outside the depletion region, a higher overpotential is required. Typically, the thickness of the depletion layer is close to 100 nm for undoped samples [28] and decreases with increasing carrier concentration (Table 4.2). It is noticeable that the overpotential increases with increasing carrier concentration for S2, S3 and S4. However, S1 exhibits the highest overpotential despite the lowest carrier

concentration. This is attributed to the poor conductivity of the undoped sample. On the other hand, the onset potential increases with increasing carrier concentration due to decreasing depletion layer width and the incorporation of structural defects in the epilayer with increasing doping content which may act as recombination centres for the photogenerated carriers [29]. It can be concluded that the lowest doped S2 photoanode has the optimum carrier concentration for lower carrier recombination and higher carrier separation efficiency.

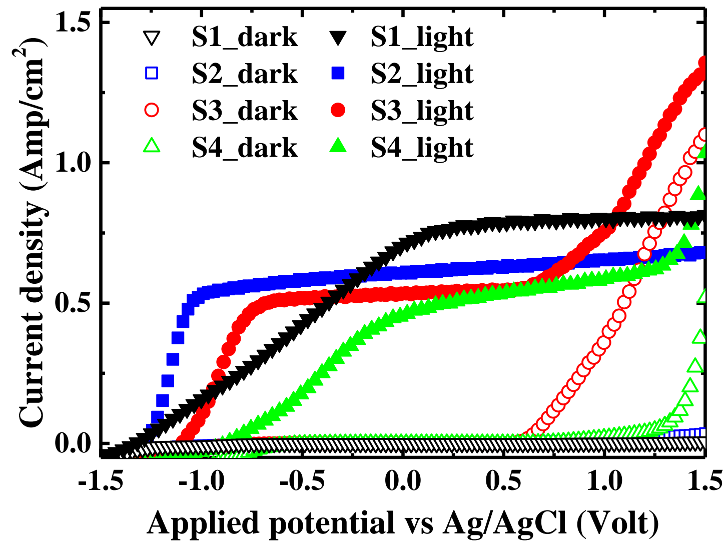

Figure 4.9: Linear sweep voltammetry of planar n-GaN photoanodes with varying carrier concentration.

4.7.1.2. GaN NP photoanodes

The PEC performance of GaN NP photoanodes with different carrier concentrations, fabricated for 120 s ICP-RIE etching of 5 nm Ni masked samples, is shown in Figure 4.10. The dark currents for all NPs photoanodes remain very low. Substantial improvement in the saturation photocurrent is noticed for all the doped NP photoanodes compared to the planar ones. The highest saturation current density of around 1.0 mA/cm^2 is measured for all the NP photoanodes. This enhancement can be attributed to the enhanced absorption by the NP photoanodes, as well as the increased semiconductor/electrolyte interface area. However, the onset and saturation potentials shift slightly towards higher potentials for all the NP photoanodes irrespective of the carrier concentration with respect to the planar photoanodes. This anodic shift is attributed to surface damage caused to the NP surface during plasma etching [30]. The surface defects act as traps for photogenerated charge carriers at the NP surface and therefore higher potentials are required to extract the photogenerated carriers that are trapped

in these defects. This leads to higher onset potentials for NP photoanodes compared to the planar photoanodes.

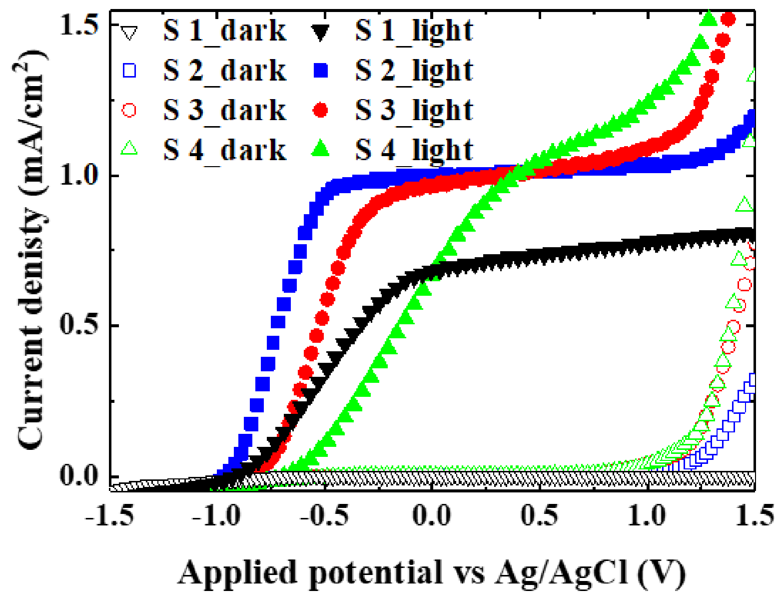

Figure 4.10: Linear sweep voltammetry of GaN NP photoanodes of fixed diameter and length with varying carrier concentration.

4.7.1.3. Applied Bias Photon-to-Current Conversion efficiency

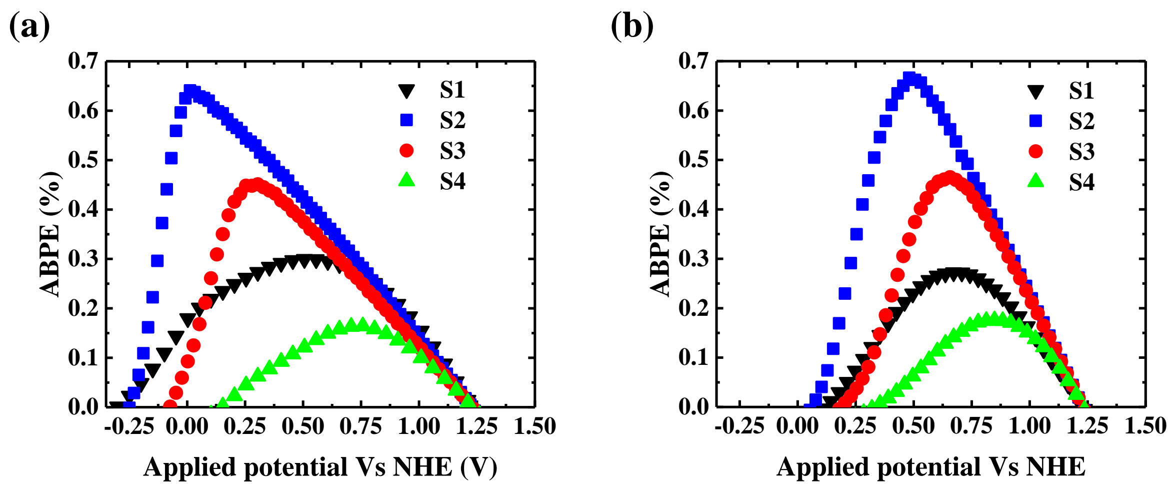

Figure 4.11: ABPE of (a) planar and (b) NP GaN photoanodes with varying carrier concentration.

To estimate the PEC performance of planar and NP photoanodes, the applied bias photon-to-current conversion efficiency (ABPE) is extracted from the J-V measurements of the planar and NP photoanodes. The following expression was used to calculate the ABPE of the photoanodes

$$ABPE = \frac{(1.23(V) - |V_{bias}|) \times J_{ph}\left[{}^{mA}/_{cm^2}\right]}{P_{incident}\left[{}^{mW}/_{cm^2}\right]} \times 100\% \quad \ldots\ldots\ldots\ldots\ldots 4.2$$

where V_{bias} is the applied potential versus the normal hydrogen electrode (NHE), J_{ph} is the photocurrent density and $P_{incident}$ is the power of illuminating light. The applied potential versus the Ag/AgCl reference electrode was converted into applied potential versus NHE using the following equation

$$V\ vs\ NHE = V\ vs\ Ag/AgCl + 0.059 \times pH + 0.198 \quad \ldots\ldots\ldots\ldots 4.3$$

Figure 4.11 shows the ABPE of planar and NP GaN photoanodes with varying carrier concentration. The GaN sample (S2) with a carrier concentration of 1×10^{18} cm^{-3} exhibited the maximum ABPE for both planar and NP photoanodes compared to other samples. However, unlike striking improvement in photocurrent (Figure 4.9 & Figure 4.10), only marginal improvement in ABPE is observed for NP photoanodes compared to their planar counterparts. NPs and planar GaN photoanodes with a carrier concentration of 1×10^{18} cm^{-3} exhibited ABPE of 0.67 and 0.64% respectively. Furthermore, the ABPE reached a maximum value at a higher applied potential of 0.5 V for NPs compared to 0 V for planar photoanodes. The anodic potential shift in onset potentials for NPs compared to the planar photoanodes in the J-V characteristics (Figure 4.8) may have contributed to the low ABPE and the higher applied potential versus NHE at which the maximum ABPE was achieved for NPs compared to the planar photoanodes.

4.7.2. Influence of NP dimensions on the PEC performance

To investigate the effect of diameter and length on the PEC performance of NP photoanodes, NPs with different diameters and lengths were fabricated using Sample 2. The thickness of the Ni film and ICP etching were varied to fabricate NPs with different diameters and lengths, as discussed above.

4.7.2.1. Influence of NP diameter

Figure 4.12 shows the influence of NP diameter on PEC performance of GaN NP photoanodes. The smallest diameter NP photoanodes exhibit the highest saturation photocurrent density, which decreases with increasing NP diameter. Increasing the diameter of the NPs results in the reduction of the total semiconductor/electrolyte interface area, which in turn contribute to the decreased saturation current density. Furthermore, as discussed in Section 4.5 of this chapter, the absorption by NPs decreases with increasing diameter due to the

increased reflection losses. This decrease in absorption with increasing NP diameter results in reduced photocarrier generation in the NP photoanodes. From Figure 4.12, it can also be observed that there is a slight change in onset potential with NP diameter. Due to the presence of surface band bending, the NPs could be either completely or partially depleted depending on the diameter of NPs for a given carrier concentration. The average diameters of the nanopillars are ~84, 144 and 202 nm for D1, D2 and D3 NP photoanodes, respectively. The estimated depletion layer width in one dimension is ~24.5 nm for $1x10^{18}$ cm^{-3} carrier concentration (Table 4.2) [31]. For a given carrier concentration, the width of the depletion region is constant. Therefore, the width of the flat band region increases with increasing NP diameter [32]. The deduced thicknesses of the flat band regions are ~35, 95 and 153 nm for D1, D2 and D3 NP photoanodes, respectively. As a consequence, recombination of the photogenerated carriers becomes more severe with increasing diameter of the NPs, which could in turn contribute to increased onset potentials with increasing NP diameter. However, the role of the depletion region may become insignificant compared to the flat band region beyond a certain NP diameter [32].

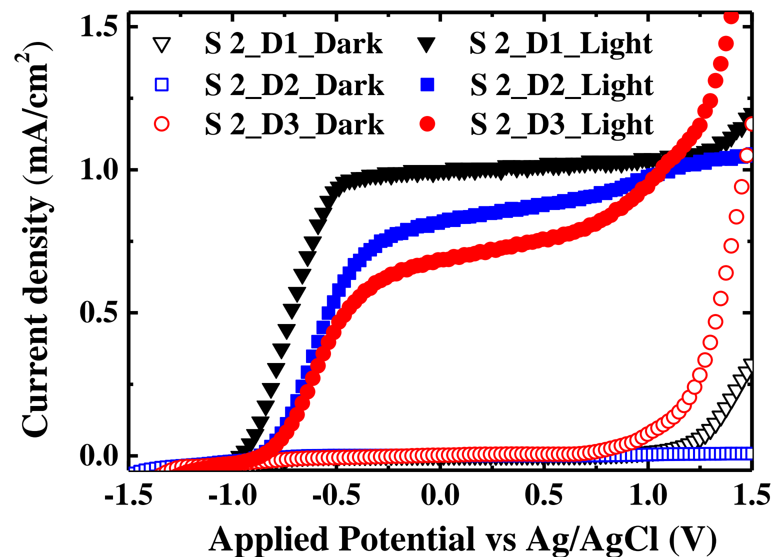

Figure 4.12: Linear sweep voltammetry of GaN NP photoanodes of varying diameter fabricated using ICP etching of 5, 10, 15 nm Ni film masked Sample 2 for 120 s. D1, D2 and D3 in the figure legend represent the NP samples fabricated using 5, 10 and 15 nm Ni film masks respectively.

4.7.2.2. Influence of length

Figure 4.13 shows the influence of NP length on the current density of NP photoanodes under dark and light illumination. NPs fabricated from 5 nm Ni masked Sample 2 were chosen for this study and the lengths of the NPs were 200, 500 and 900 nm and labelled as short (L1), medium (L2) and long (L3) NP photoanodes, respectively. Since the NP diameter is fixed while studying the influence of NP length on PEC performance, insignificant changes in onset potential are observed regardless of the NP length. The onset potential is dependent on the depletion layer width that varies only with the diameter and doping concentration. On the other hand, the saturation current is enhanced with increasing NP length. NP/electrolyte interface area is estimated to be linearly dependent on the length of the NPs, which contributes to increased depletion region volume with increasing NP length [31]. The increase in the depletion region volume leads to increased saturation photocurrent. It is also expected that a certain minimum length of NPs is necessary to mitigate the optical reflection losses [33]. This could be another possible reason for the reduction in photocurrent density with reducing length of the NPs.

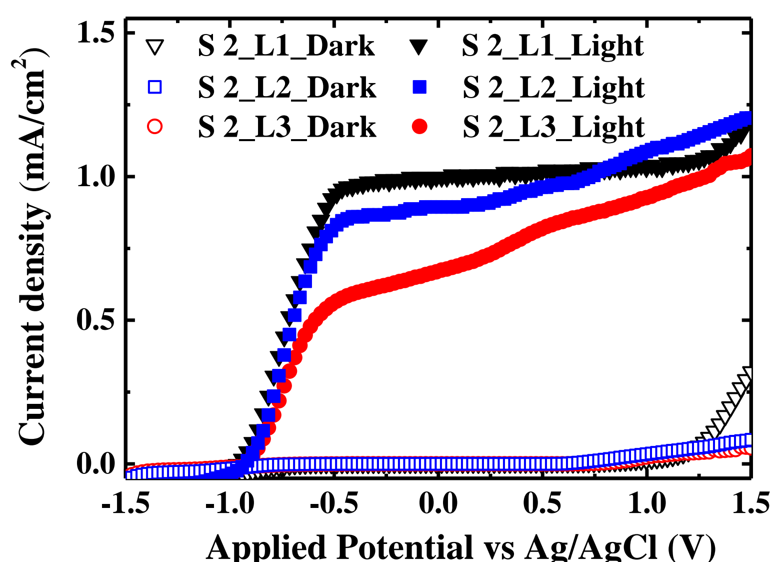

Figure 4.13: Linear sweep voltammetry of GaN NP photoanodes of varying lengths, where the ICP etching time was set to 30, 60 and 120 s to vary the length of NPs formed using the 5 nm Ni masked Sample 2. L1, L2 and L3 in the figure legend refers to the NP samples etched for 30, 60 and 120 s respectively.

4.8. Electrochemical impedance spectroscopy

Electrochemical impedance measurements were carried out to understand the charge transfer kinetics at the semiconductor and electrolyte interface as shown in Figure 4.14. The diameter of the half circles in the Nyquist plot is linked to the charge transfer resistance between semiconductor surface and electrolyte. In general, the half circle diameter of electrochemical impedance spectrum is proportional to the combination of electrolyte and photoelectrode/electrolyte charge transfer resistance. As a result, the smaller the diameter, the lower the charge transfer resistance. The Nyquist plot indicates that the charge transfer resistance is increased for NP photoanodes compared to the planar photoanodes. The increased charge transfer resistance could be due to plasma etching damage for NP photoanodes and contributes to anodic shift in the onset potential and overpotentials. Among the planar photoanodes, the GaN photoanode with $1x10^{18}$ cm^{-3} carrier concentration exhibits the lowest charge transfer resistance. Further increase in carrier concentration leads to structural defects in the epilayer due to the heavy doping and also decreased depletion region thickness for heavily doped n-GaN photoanodes. These two factors result in decreased charge transfer resistance between the semiconductor surface and electrolyte for planar photoanodes of carrier concentration above $1x10^{18}$ cm^{-3}.

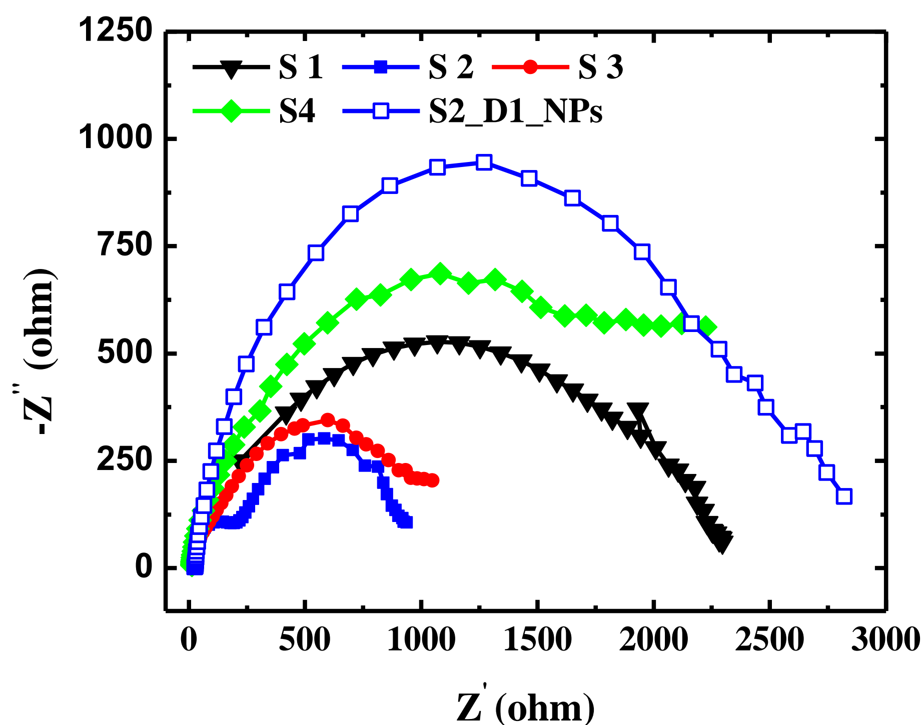

Figure 4.14: Nyquist plots of GaN planar photoanodes with varying carrier concentration and NPs fabricated from S2 using 5 nm Ni etch mask and 120 s ICP etching time.

4.9. Conclusions

To conclude, we have demonstrated the fabrication of large area random GaN NPs using a top-down approach with ICP etching in conjunction with a cost-effective and scalable self-assembled random mask technique. Large area GaN NPs are highly anti-reflective below the band gap of GaN, and the antireflective property decreased with increasing the diameter of the NPs. On the other hand, the planar samples suffer from high reflection losses (24%) compared to the NPs for all NP dimensions. The large area random NPs fabricated by following this approach exhibited substantial improvement in the PEC performance compared to their planar counterparts. The photocurrent of n-doped NP photoanodes could reach up to 1 mA/cm^2, which is close to the theoretical limit, owing to their enhanced optical absorption and increased semiconductor/electrolyte interface. This enhancement is found to be strongly influenced by the carrier concentration and NP dimensions. The decrease in depletion layer width with increasing carrier concentration leads to anodic potential shift for the NP photoanodes. Photocurrent density is reduced with increasing diameter and reducing length of the NPs. Reduction in optical absorption with increasing diameter and reducing length of the NPs contribute to the drop in the photocurrent density. Furthermore, increasing the diameter of the NP photoanodes for a given carrier concentration is found to cause an anodic shift of the onset potential due to the increased flat band region of the NPs. Carrier concentration of epilayer also plays a crucial in the charge transfer resistance between the semiconductor and electrolyte. Further, the NP photoanodes exhibit higher semiconductor/electrolyte interface charge transfer resistance compared to their planar counter parts possibly due to plasma etching damage.

4.10. References

[1] AlOtaibi B, Fan S, Vanka S, Kibria M G and Mi Z 2015 A Metal-Nitride Nanowire Dual-Photoelectrode Device for Unassisted Solar-to-Hydrogen Conversion under Parallel Illumination *Nano letters* **15** 6821-8

[2] Fan S, AlOtaibi B, Woo S Y, Wang Y, Botton G A and Mi Z 2015 High Efficiency Solar-to-Hydrogen Conversion on a Monolithically Integrated InGaN/GaN/Si Adaptive Tunnel Junction Photocathode *Nano letters* **15** 2721-6

[3] Zhao S, Nguyen H P T, Kibria M G and Mi Z 2015 III-Nitride nanowire optoelectronics *Progress in Quantum Electronics* **44** 14-68

[4] Kibria M G and Mi Z 2016 Artificial photosynthesis using metal/nonmetal-nitride semiconductors: current status, prospects, and challenges *Journal of Materials Chemistry A* **4** 2801-20

[5] Zakutayev A 2016 Design of nitride semiconductors for solar energy conversion *Journal of Materials Chemistry A* **4** 6742-54

[6] Moses P G and Van de Walle C G 2010 Band bowing and band alignment in InGaN alloys *Applied Physics Letters* **96** 021908

[7] Ebaid M, Kang J-H, Lim S-H, Ha J-S, Lee J K, Cho Y-H and Ryu S-W 2015 Enhanced solar hydrogen generation of high density, high aspect ratio, coaxial InGaN/GaN multi-quantum well nanowires *Nano Energy* **12** 215-23

[8] Caccamo L, Hartmann J, Fabrega C, Estrade S, Lilienkamp G, Prades J D, Hoffmann M W G, Ledig J, Wagner A, Wang X, Lopez-Conesa L, Peiro F, Rebled J M, Wehmann H H, Daum W, Shen H and Waag A 2014 Band Engineered Epitaxial 3D GaN-InGaN Core-Shell Rod Arrays as an Advanced Photoanode for Visible-Light-Driven Water Splitting *Acs Appl Mater Inter* **6** 2235-40

[9] AlOtaibi B, Nguyen H P, Zhao S, Kibria M G, Fan S and Mi Z 2013 Highly stable photoelectrochemical water splitting and hydrogen generation using a double-band InGaN/GaN core/shell nanowire photoanode *Nano letters* **13** 4356-61

[10] Ebaid M, Kang J-H, Lim S-H, Cho Y-H and Ryu S-W 2015 Towards highly efficient photoanodes: the role of carrier dynamics on the photoelectrochemical performance of InGaN/GaN multiple quantum well coaxial nanowires *RSC Advances* **5** 23303-10

[11] Kibria M G, Chowdhury F A, Zhao S, AlOtaibi B, Trudeau M L, Guo H and Mi Z 2015 Visible light-driven efficient overall water splitting using p-type metal-nitride nanowire arrays *Nature communications* **6** 6797

[12] Kibria M G, Zhao S, Chowdhury F A, Wang Q, Nguyen H P, Trudeau M L, Guo H and Mi Z 2014 Tuning the surface Fermi level on p-type gallium nitride nanowires for efficient overall water splitting *Nature communications* **5** 3825

[13] Wang D, Pierre A, Kibria M G, Cui K, Han X, Bevan K H, Guo H, Paradis S, Hakima A R and Mi Z 2011 Wafer-level photocatalytic water splitting on GaN nanowire arrays grown by molecular beam epitaxy *Nano letters* **11** 2353-7

[14] Phivilay S P, Roberts C A, Puretzky A A, Domen K and Wachs I E 2013 Fundamental Bulk/Surface Structure–Photoactivity Relationships of Supported (Rh2–yCryO3)/GaN Photocatalysts *The Journal of Physical Chemistry Letters* **4** 3719-24

[15] Reddy N P, Naureen S, Mokkapati S, Vora K, Shahid N, Karouta F, Tan H H and Jagadish C 2016 Enhanced luminescence from GaN nanopillar arrays fabricated using a top-down process *Nanotechnology* **27** 065304

[16] Spurgeon J M, Atwater H A and Lewis N S 2008 A comparison between the behavior of nanorod array and planar Cd(Se, Te) photoelectrodes *J Phys Chem C* **112** 6186-93

[17] Xiao F-X, Miao J, Tao H B, Hung S-F, Wang H-Y, Yang H B, Chen J, Chen R and Liu B 2015 One-Dimensional Hybrid Nanostructures for Heterogeneous Photocatalysis and Photoelectrocatalysis *Small* **11** 2115-31

[18] Chen H M, Chen C K, Liu R-S, Zhang L, Zhang J and Wilkinson D P 2012 Nano-architecture and material designs for water splitting photoelectrodes *Chemical Society Reviews* **41** 5654-71

[19] Jung H S, Hong Y J, Li Y, Cho J, Kim Y-J and Yi G-C 2008 Photocatalysis Using GaN Nanowires *ACS Nano* **2** 637-42

[20] Kato H, Asakura K and Kudo A 2003 Highly Efficient Water Splitting into H2 and O2 over Lanthanum-Doped NaTaO3 Photocatalysts with High Crystallinity and Surface Nanostructure *Journal of the American Chemical Society* **125** 3082-9

[21] Paramanik D, Motayed A, Aluri G S, Ha J-Y, Krylyuk S, Davydov A V, King M, McLaughlin S, Gupta S and Cramer H 2012 Formation of large-area GaN nanostructures with controlled geometry and morphology using top-down fabrication scheme *Journal of Vacuum Science & Technology B* **30** 052202

[22] Wang Y D, Chua S J, Tripathy S, Sander M S, Chen P and Fonstad C G 2005 High optical quality GaN nanopillar arrays *Applied Physics Letters* **86** 071917

[23] Tessarek C, Heilmann M, Butzen E, Haab A, Hardtdegen H, Dieker C, Spiecker E and Christiansen S 2014 The Role of Si during the Growth of GaN Micro- and Nanorods *Crystal Growth & Design* **14** 1486-92

[24] Zhu J, Wang L, Zhang S, Wang H, Zhao D, Zhu J, Liu Z, Jiang D and Yang H 2010 The fabrication of GaN-based nanopillar light-emitting diodes *Journal of Applied Physics* **108** 074302

[25] Zhebo Chen T G D, Huyen N. Dinh, Kazunari Domen, Keith Emery, Arnold J. Forman, Nicolas Gaillard, Roxanne Garland, Clemens Heske, Thomas F. Jaramillo, Alan Kleiman-Shwarsctein, Eric Miller , Kazuhiro Takanabe, John TurnerShow 2013 *Photoelectrochemical Water Splitting* ed H N D Zhebo Chen, Eric Miller Springer)

[26] Shockley W and Queisser H J 1961 Detailed Balance Limit of Efficiency of p-n Junction Solar Cells *Journal of Applied Physics* **32** 510-9

[27] Richter T, Meijers H L, Calarco R and Marso M 2008 Doping concentration of GaN nanowires determined by opto-electrical measurements *Nano letters* **8** 3056-9

[28] Iwaki Y, Ono M, Yamaguchi K, Kusakabe K, Fujii K and Ohkawa K 2008 Nitride photocatalyst to generate hydrogen gas from water *physica status solidi (c)* **5** 2349-51

[29] Kang J-H, Kim S H, Ebaid M, Lee J K and Ryu S-W 2014 Efficient photoelectrochemical water splitting by a doping-controlled GaN photoanode coated with NiO cocatalyst *Acta Materialia* **79** 188-93

[30] Tseng W-J, van Dorp D H, Lieten R R, Vereecken P M, Langer R and Borghs G 2014 Impact of Plasma-Induced Surface Damage on the Photoelectrochemical Properties of GaN Pillars Fabricated by Dry Etching *The Journal of Physical Chemistry C* **118** 11261-6

[31] Kornienko N, Gibson N A, Zhang H, Eaton S W, Yu Y, Aloni S, Leone S R and Yang P 2016 Growth and Photoelectrochemical Energy Conversion of Wurtzite Indium Phosphide Nanowire Arrays *ACS Nano* **10** 5525-35

[32] Calarco R, Marso M, Richter T, Aykanat A I, Meijers R, A V D H, Stoica T and Luth H 2005 Size-dependent photoconductivity in MBE-grown GaN-nanowires *Nano letters* **5** 981-4

[33] Jung J-Y, Um H-D, Jee S-W, Park K-T, Bang J H and Lee J-H 2013 Optimal design for antireflective Si nanowire solar cells *Solar Energy Materials and Solar Cells* **112** 84-90

Chapter 5

Band Gap Engineering and Photostability of GaN Photoanodes

5.1. Introduction

As discussed in Chapter 4, we achieved the maximum reported photoelectrochemical (PEC) performance of up to nearly 1 mA/cm^2 for GaN photoanodes, which is almost theoretically achievable limit for GaN. The wide band gap of GaN (3.4 eV) limits the PEC performance of GaN NP photoanodes because only a small portion of the solar spectrum is utilised at this band gap. The incorporation of In into GaN can vary the band gap from 3.4 eV (GaN) to 0.7 eV (InN) depending on the In concentration, which allows for band gap absorption tunability from UV to IR regions of the solar spectrum [1]. Moreover, InGaN alloy can straddle both water oxidation and reduction potentials up to 50% In composition, which makes it an ideal candidate for unassisted overall water splitting [2, 3].

In general, InGaN is grown in very thin layers (quantum wells) to mitigate the dislocation density which arises due to the lattice mismatch between InN and GaN. Further, the In rich regions form with in the quantum wells due to the difference in formation enthalpy between GaN and InN. The dislocation density and In segregation increases with increasing In concentration in InGaN. Nanostructures have the potential to accommodate higher In concentrations while maintaining good quality InGaN layers given that nanostructures can be made stress-free [3, 4]. Almost all studies, irrespective of growth method, are focused on improving the PEC performance of photoanodes by incorporating higher In concentration in InGaN in either planar [5-9] or nanostructured devices [3, 4, 10-16]. As a consequence, there are no reports on comparative studies of the influence of In concentration on the PEC performance of InGaN/GaN multiple quantum wells (MQWs) in planar and NP photoanodes. In order to carry out these studies, both planar and NP photoanodes require similar structural quality and In concentration in InGaN, which can be best achieved through top-down approach, since the fabrication of both NP and planar photoanodes makes use of the same epilayer. This is not possible with bottom-up growth methods, as the growth conditions are different for epilayers and nanostructures. Therefore, a top-down approach is ideal for studying the

influence of In on the PEC performance of InGaN/GaN MQW planar and NP photoelectrodes as they will retain similar crystal quality and In concentration.

In this chapter, we investigate the influence of In concentration in InGaN on the PEC performance of GaN photoanodes. Section 5.2 presents the architecture of the InGaN/GaN MQWs used in this study and morphology of the NPs. Section 5.3 deals with the optical properties of the InGaN/GaN MQW photoanodes. UV-VIS reflectance spectra and photoluminescence were used to determine the band edge emissions of the InGaN/GaN MQWs. PEC performance studies on planar and NP InGaN/GaN MQWs are described in Section 5.4. It was found that the In concentration in InGaN has negligible influence on the photocurrent density of planar InGaN/GaN MQWs, while it has an enormous influence on InGaN/GaN MQW photoanodes. In Section 5.5, the photon-to-current conversion efficiency measurements are presented to elucidate the contribution of In to the photocurrent density of planar and NP InGaN/GaN photoanodes. The applied bias photon-to-current efficiency of photoanodes is presented in Section 5.6. Section 5.7 focusses on the stability of the planar and NP photoanodes. The NP photoanodes are unstable in NaOH electrolyte compared to the planar photoanodes which are highly stable. A more stable performance of the NP photoanodes is achieved by decorating them with NiO or Co_3O_4 co-catalysts.

5.2. Design and fabrication of InGaN/GaN MQW NP photoanodes

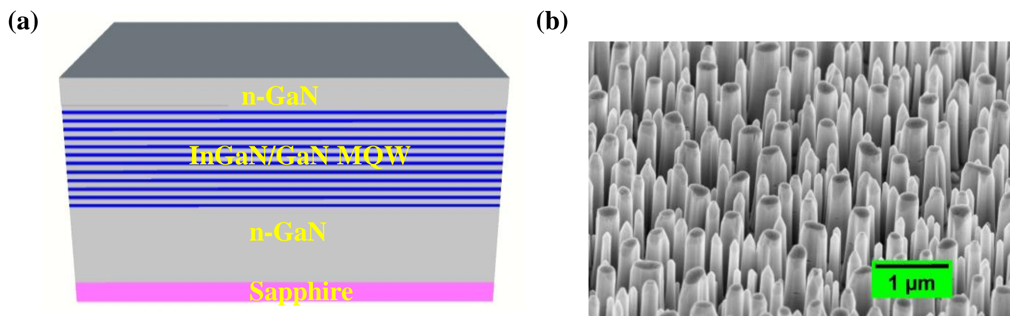

Figure 5.1. (a) Schematic of InGaN/GaN MQW epilayer structure and (b) SEM image of InGaN/GaN MQW NPs.

Figure 5.1(a) illustrates the schematic of the InGaN/GaN MQW wafers grown on sapphire using MOCVD. 10 pairs of InGaN (1.5 nm)/GaN (20 nm) MQWs were grown on 2 μm thick n-GaN, followed by 275 nm-thick n-GaN on top. The In concentrations in the InGaN/GaN MQWs were chosen to be 0, 20, 30 and 50% and are therefore labelled as Reference, 20%, 30% and 50% In samples, respectively, from here onwards. The carrier concentration of both the top and bottom n-GaN layers was ~5×10^{18} cm^{-3}. Figure 5.1(b) shows

an SEM image of the MQW NPs after removing the mask, fabricated using the top-down approach. The self-organized mask technique was used for the top-down fabrication of large area InGaN/GaN NPs using ICP. 10 nm Ni film deposited using e-beam evaporation was used as the mask for etching the InGaN/GaN MQW NPs. The mask preparation and NP fabrication conditions used for the fabrication of InGaN/GaN NPs were similar to those used for fabrication of GaN NPs in Section 4.2 of **Error! Reference source not found.** The NPs m aintain a uniform height (~1.2 μm) and exhibit smooth sidewalls. The diameters of the NPs range from 60 to 250 nm with an average diameter of ~144 nm as measured from the SEM image.

5.3. Optical properties of InGaN/GaN MQWs

A UV-Vis spectrometer and photoluminescence techniques were employed to investigate the optical absorption properties of planar and NP InGaN/GaN MQWs with varying In concentration.

5.3.1. Optical reflectivity of InGaN/GaN MQWs

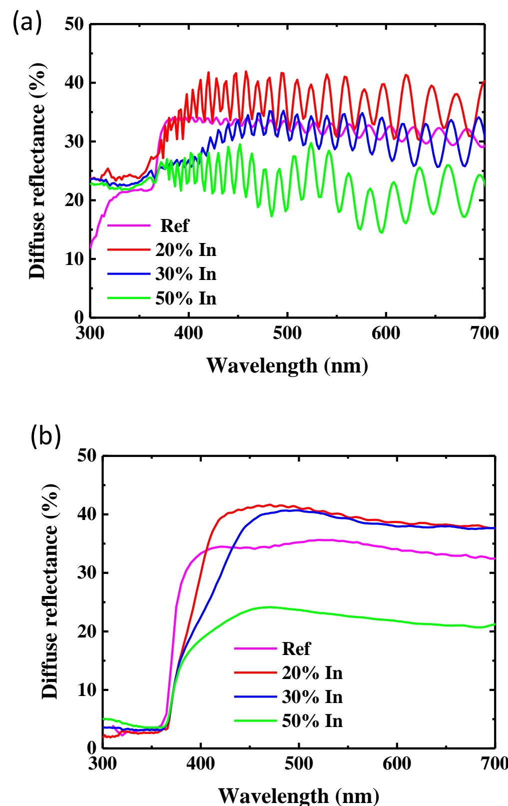

Figure 5.2. Diffuse reflectance spectra of (a) planar and (b) NP InGaN/GaN MQWs with varying In concentration. Ref, 20, 30 and 50% In legend indicate the InGaN/GaN samples with 0, 20, 30 and 50% In content in InGaN respectively.

Figure 5.2(a) shows the influence of In concentration on the diffuse reflectance of planar InGaN/GaN MQWs. There is a sharp fall in diffuse reflectance for all the planar samples below 370 nm, which corresponds to the band gap of GaN. The absorption by planar samples extends into the visible region with the incorporation of In into InGaN layers due to the lower band gap of InGaN. This extension of the absorption range increases with increasing In concentration, reaching up to 450 nm for the 30% In sample. However, further increasing the In concentration (50% In) leads to broad absorption of light in the visible region. Segregation of InN micro clusters typically associated with high In concentrations could be the reason for the broad absorption in the visible region of the 50% In sample [17]. The fringes beyond 400 nm are generated by Fabry-Perot interference. As shown in Figure 5.2(b), the NP samples exhibit a huge enhancement in absorption within the given absorption region of the planar samples. This enhancement can be ascribed to the improved total internal reflection of the incident light as a result of the NPs [18, 19].

5.3.2. Photoluminescence of InGaN/GaN MQWs

Micro-photoluminescence measurements were carried out at room temperature. A 325 nm He-Cd laser was used to excite the samples, with the emitted light collected through a 36X (NA = 0.5) objective lens and detected using a Si charge-coupled device (CCD). PL spectra of the InGaN/GaN MQW planar and NP samples with varying In concentration are shown in Figure 5.3. PL intensities are normalised with respect to the peak at 365 nm for all samples. Figure 5.3(a) shows the PL spectra of the planar samples. All the planar samples irrespective of In concentration feature a strong peak at 365 nm corresponding to emission from bulk GaN. A broad defect-related peak, which commonly appears in MOCVD-grown GaN, is also observed around 620 nm [28]. PL emissions corresponding to InGaN are noticed only for the 20% In sample, centred at 420 nm, with no InGaN emissions from the 30% or 50% In samples. The incorporation of high concentrations of In into InGaN can create threading dislocations and InN micro clusters in the InGaN layers due to the large lattice mismatch and miscibility gap between InN and GaN [20-22]. These defects act as non-radiative recombination centres for photo-generated carriers and thus annihilate the PL emission from InGaN. The defect density and micro cluster formation in InGaN increases rapidly beyond 20% In [20]. This could conceivably be the reason for the absence of InGaN PL peaks in the visible region of the 30% and 50% In planar samples (Figure 5.3(a)).

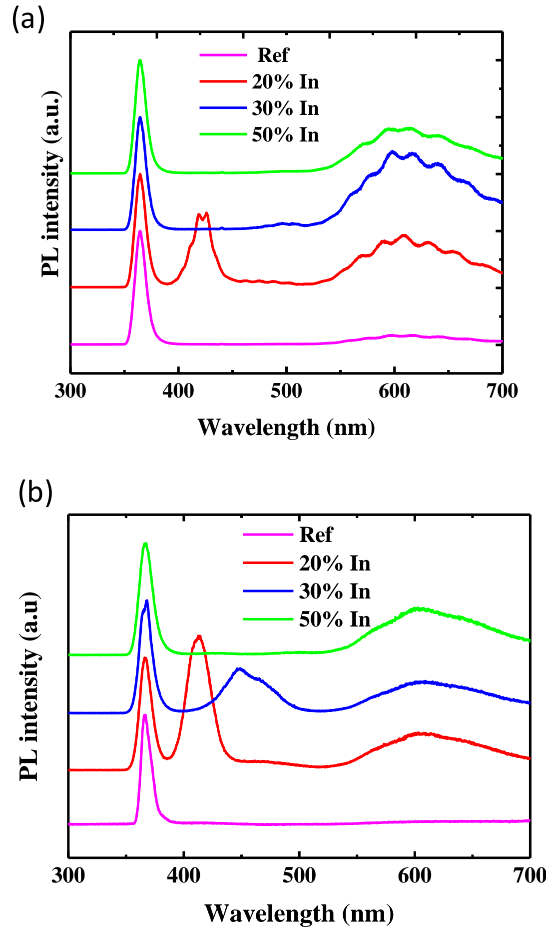

Figure 5.3. Room temperature photoluminescence spectra of InGaN/GaN MQW (a) planar and (b) NP samples. Ref, 20, 30 and 50% In in the legend represent the 0, 20, 30 and 50% In content in the InGaN/GaN samples respectively.

Figure 5.3(b) shows the PL spectra of InGaN/GaN MQW NPs. Similar to the planar samples, the PL spectra of all NP samples show a strong emission peak corresponding to GaN. In the case of PL emission corresponding to InGaN, unlike the planar samples, the PL peak is noticed for NPs up to 30% In concentration. As shown in Figure 5.3(b), the InGaN PL peak at ~ 450 nm is clearly visible for the 30% In NP sample, in addition to the increased emission intensity from the 20% In NP sample compared to its planar counterpart. However, PL is still not observed for the 50% In NP sample. Furthermore, the InGaN PL peak of the 20% In NPs is shifted towards shorter wavelengths by 10 nm compared to those of planar structures. Strain relaxation in the NPs might be the reason behind this observed blue shift. The small foot print of NPs helps in reducing the defect density compared to the planar structures and leads to enhanced radiative recombination of photo-generated carriers, which results in the observation of PL emissions from the 30% In NP MQWs. Further, enhanced absorption and emission by

the NPs compared to the planar structures augment the PL of the NP samples [18]. These two factors aid the surge and enrichment of the InGaN peak for the 30% and 20% In NP samples respectively (Figure 5.3(b)). However, in the case of the 50% In NP sample, defect density and phase segregation may be above the threshold to produce any PL emissions from the MQWs. Overall, diffuse reflectance and PL spectra reveal that the 20% and 30% In samples can capture sunlight up to 420 and 450 nm, respectively, and that there is a greater enhancement in absorption by the NPs compared to their corresponding planar samples.

5.4. PEC performance of InGaN/GaN MQW photoanodes

The PEC performance of the InGaN/GaN MQW planar and NP photoanodes was measured in NaOH electrolyte under one sun illumination. The experiments were carried out using three electrodes set up with InGaN/GaN MQWs as photoanodes. The Ti/Au contacts were made to the bottom n-GaN layer of the InGaN/GaN MQW photoanodes. ICP was used to etch the top n-GaN layer and MQWs to expose the bottom n-GaN layer of the MQW structure. The details of the contact preparation of the photoanodes and PEC measurements are discussed in Chapter 2 and Chapter 4.

5.4.1. PEC performance of planar photoanodes

Figure 5.4 shows the PEC performance of the planar photoanodes measured under dark and one sun illumination. The planar photoanodes with all In concentrations show negligible dark currents. The reference photoanode (without MQWs) generates a photocurrent density of ~0.48 mA/cm^2, which is slightly higher than the MQW photoanodes. Photoanodes with 20% and 30% In show similar saturation photocurrent densities of ~0.44 mA/cm^2, but the 50% In photoanode witnessed a slightly lower photocurrent density of ~0.4 mA/cm^2. This indicates that the InGaN MQWs do contribute to the PEC performance of MQW planar photoanodes. The slight drop in the photocurrent of the InGaN photoanodes can be attributed to the relatively lower quality of the top n-GaN layer of the InGaN MQWs compared to the reference photoanode, as discussed below. Further, a slight positive shift in onset potentials, the potential at which photocurrent onset occurs, is observed for the MQW photoanodes compared to the reference photoanode. The photocurrent onset occurs at ~ -1.1 V for the reference photoanode and at -1.0 V for the 50% photoanode. The drop in photocurrent density and anodic shift in onset potential for the InGaN photoanodes can be attributed to the relatively low quality of the top n-GaN layer. This is because the top n-GaN layer of the InGaN MQW samples were grown at a lower temperature than the reference to avoid diffusion of In from the InGaN MQW layers.

The depletion layer effect on the PEC performance of planar photoanodes can be eliminated since the reference and InGaN planar anodes have the same carrier concentration ($5x10^{18}$ cm^{-3}). The depletion layer thickness for this carrier concentration can be less than 100 nm [23, 24, 19]. InGaN MQWs in our photoanodes are placed 275 nm (thickness of top n-GaN layer) below the semiconductor/electrolyte interface. Therefore, the depletion region does not influence the PEC performance of InGaN photoanodes.

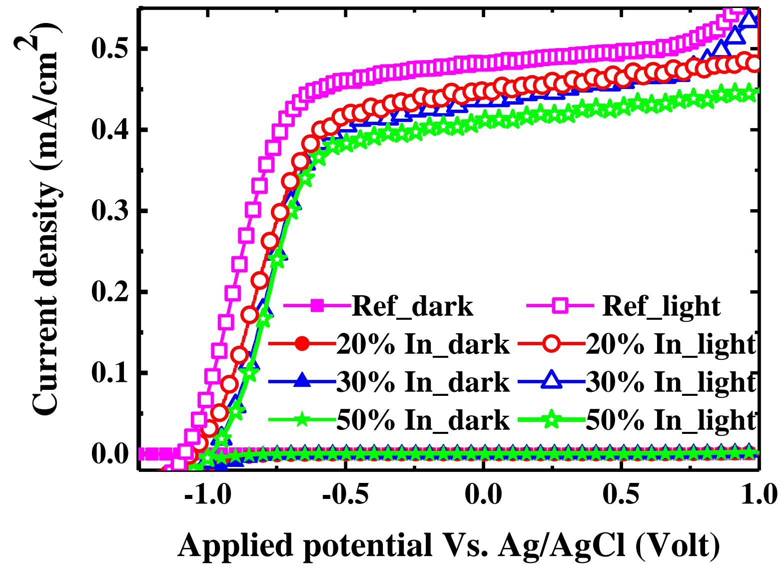

Figure 5.4: J-V characteristics of InGaN/GaN MQW planar photoanodes measured under dark and sunlight illumination using a three terminal PEC set up.

5.4.2. PEC performance of NP photoanodes

Figure 5.5 shows the influence of In concentration on the current density of InGaN MQW NP photoanodes under dark and sunlight illumination. The current density for NPs under dark remains zero irrespective of the In concentration. As shown in Figure 5.5, the NPs in comparison with the planar photoanodes exhibit vastly different J-V characteristics and generate much greater photocurrent densities. Almost 100% improvement is observed in the photocurrent density for the reference NP photoanode compared to the planar reference photoanode. For the 30% In NP sample, the photocurrent density reaches ~1.6 mA/cm^2, which is almost four times that of the corresponding planar photoanode and 1.8 times that of the reference NP photoanode. This indicates that the InGaN MQWs play a significant role in the PEC performance of the NP photoanodes, unlike the planar photoanodes. The vast increase in the semiconductor/electrolyte interface area and enhanced absorption by the NPs (Figure 5.3(b)) can be attributed to this huge improvement in the photocurrent density. The NP

geometry brings the InGaN MQWs into direct contact with the electrolyte. Therefore, photo-generated carriers in InGaN under sunlight illumination can participate in water splitting and thus contribute to the enhanced photocurrent density of InGaN NPs compared to the reference NP photoanode. The photocurrent density of the InGaN NP photoanodes improves with increasing In concentration up to 30% In, which can be attributed to absorption extended into the visible part of the spectrum by the InGaN NPs, as observed in Figure 5.2(b) and Figure 5.3(b). Further increasing the In concentration leads to severe defect formation which results in inferior performance of the InGaN NP photoanodes, as shown for the 50% In NP photoanodes. From Figure 5.5, it can also be observed that the NP photoanodes exhibit higher onset and saturation potentials compared to their counterpart planar photoanodes. This could be due to surface damage sustained during NP fabrication. Furthermore, similar to the planar photoanodes, there is a slight positive shift in the onset potential of the NP InGaN/GaN MQW photoanodes with respect to the reference electrode. However, this shift is not as apparent as for the planar MQWs. This may be due to dominating surface damage effect on the onset potentials of the MQW NPs.

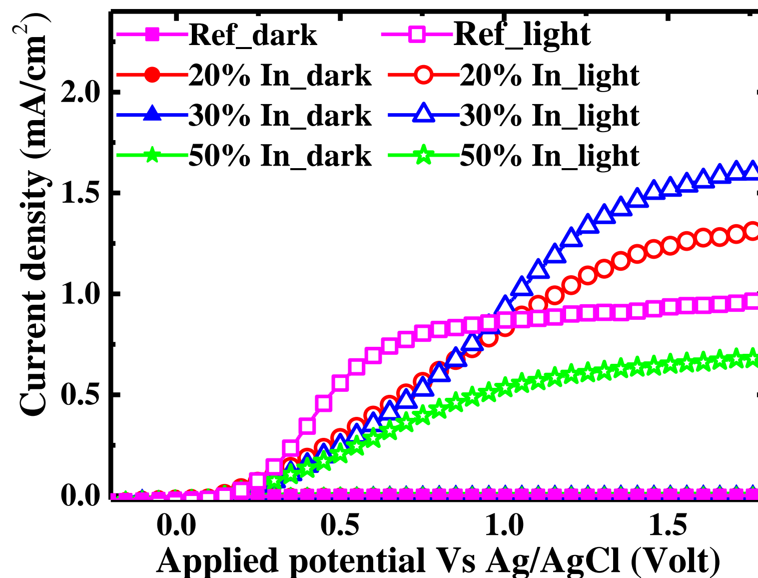

Figure 5.5. J-V characteristics of InGaN/GaN MQW NP photoanodes measured under dark and sunlight illumination using a three terminal PEC set up.

To further understand the influence of InGaN on the PEC performance of InGaN/GaN MQW photoelectrodes, the fill factor (FF) was extracted from J-V characteristics of planar (Figure 5.4) and NP (Figure 5.5) photoanodes and listed in Table 5.1 by following the methodology described by Wang et al. [25]. The FF was estimated using the following relation

$$FF = \frac{P_{max}}{|V_{Onset} - V_{RHE}| \times J_{RHE}} \qquad \text{………………5.1}$$

where P_{max} is the maximum power obtained by the photoelectrode, V_{onset} is the potential at which the photoelectrode current passes zero, V_{RHE} is the potential of the reversible hydrogen photoelectrode and J_{RHE} is the current density at V_{RHE}. The fill factors for the planar photoanodes irrespective of the In concentration are nearly the same. This indicates that only the top GaN layer is contributing to the PEC performance and InGaN is not supplementing the PEC performance. On the other hand, a significant drop in FF is noticed for the reference and InGaN NP photoanodes. The drop in FF for reference NP photoanode compared to the reference planar sample could be due to the surface damage caused to the NPs during fabrication. A further drop in FF for the 20% and 30% In NPs implies that InGaN is involved in the PEC performance of these photoanodes. However, the FF for the 50% NP photoanode is increased compared to the 20% and 30% In NP photoanodes, but still lower than the reference NP photoanode. This implies that InGaN is not contributing to the PEC performance and due to the inferior crystal quality of the 50% In NPs compared to the reference photoanode the 50% exhibits lower FF compared to the reference NP photoanode.

Table 5.1. Fill factor calculated for PEC performance of planar and NP photoanodes.

Planar photoanodes		**NP photoanodes**	
% In	FF (%)	% In	FF (%)
0	60.9	0	46.27
20	57.6	20	23.6
30	58.44	30	19.20
50	59.53	50	30.0

5.5. Incident photon-to-current conversion efficiency

To further elucidate the influence of In on the PEC performance of InGaN MQW photoanodes, incident photon-to-current efficiency (IPCE) was measured for the reference and 30% In planar and NP photoanodes and illustrated in Figure 5.6. The IPCE was determined using the following equation

$$IPCE(\%) = \frac{|J_{ph}(mA/cm^2)| \times 1239.8}{P_{mono}(mW/cm^2) \times \lambda(nm)} \times 100\% \qquad \text{……….. 5.2}$$

where λ is wavelength, J_{ph} is the photocurrent density and P_{mono} is the incident light power at a given wavelength. The IPCE was measured at zero applied potential versus the Ag/AgCl

reference electrode. As shown in Figure 5.6, the IPCE of each planar photoanode and the reference NP photoanode drops to negligible values beyond 370 nm, which is slightly below the band gap of GaN. In contrast, there is a great enhancement in the IPCE for the 30% In NP photoanode near the band edge of GaN. Moreover, the IPCE of the 30% NP sample extends into the visible region up to 440 nm, which is slightly below the band gap of the MQWs observed from diffuse reflectance (Figure 5.2 (b)) and PL (Figure 5.3(b)). This confirms that InGaN participates in water splitting for the NP photoanodes but does not contribute in planar photoanodes, which agrees with observations of the photocurrent densities for planar and NP photoelectrodes (Figure 5.4 and Figure 5.5). The IPCE confirms that InGaN plays a crucial role in the PEC performance of NP photoanodes but has little impact on the performance of planar photoanodes.

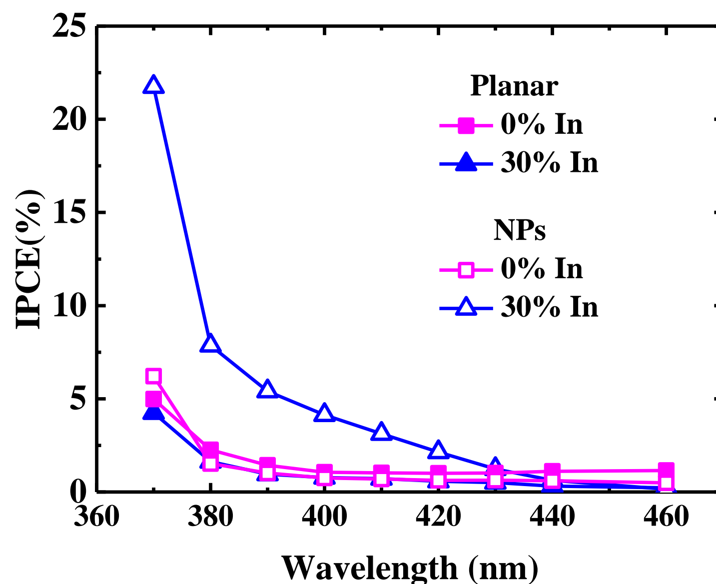

Figure 5.6. Incident photon-to-current efficiency (IPCE) of the reference and 30% In planar and NP photoanodes measured at zero applied potential versus the Ag/AgCl reference electrode.

5.6. Applied Bias Photon-to-Current Conversion efficiency

Figure 5.7 shows the ABPE efficiency of InGaN/GaN planar and NP photoanodes, determined from their J-V measurements (Figure 5.4 & Figure 5.5) by following Equations 4.2 and 4.3. The ABPE of the reference NP photoanode is slightly improved compared to the planar photoanode. On the other hand, a marginal drop in ABPE is observed for NP photoanodes with 20% and 30% In compared to their planar counterparts while a significant drop is observed for the 50% In sample. Moreover, all InGaN/GaN MQW planar photoanodes exhibited lower ABPEs compared to reference planar photoanodes. Relatively inferior quality of the top GaN

and non-participation of the InGaN layers in the water splitting reaction (Figure 5.6) may have contributed to low ABPEs for InGaN/GaN planar photoanodes compared to the reference photoanode. The increase in onset and saturation potentials due to ion surface damage and increased defect densities in InGaN layers can be attributed to the lower ABPEs of InGaN/GaN MQW NP photoanodes compared to their planar counterparts and reference NP photoanode.

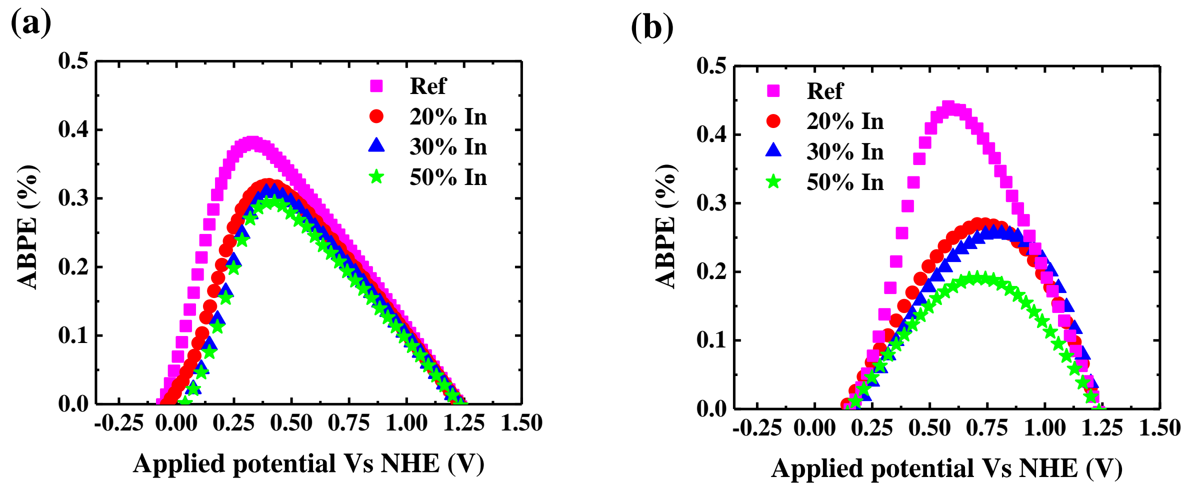

Figure 5.7: ABPE of InGaN/GaN MQW (a) planar and (b) NP photoanodes with different In content in InGaN layers.

5.7. Stability of GaN photoanodes

Figure 5.8 (a) shows the transient current density of planar and NP GaN photoanodes against time measured at bias voltage of 0 V versus Ag/AgCl in 1 M NaOH under one sun illumination. Transient currents were measured by closing and opening the shutter of the solar simulator while measuring the current density of the photoanodes. From Figure 5.8(a), it can be observed that the NP photoanode is unstable in electrolyte as the photocurrent density of the NP photoanode decreased gradually over time, while the photocurrent density of the planar photoanode remained stable. The photocurrent density of the NP photoanode dropped to below that of the planar photoanode after five minutes. The degradation of the NPs further confirms that photo-chemical reaction is not contributing to the PEC performance of the NP photoanodes. It is well known that the c-plane of GaN is chemically stable compared to the r and m-planes. [26, 27] When the planar photoanodes are dipped in the electrolyte, only the c-plane is exposed to the electrolyte and hence the planar photoelectrodes exhibit stable performance. On the other hand, for NP photoanodes, the m- and r-planes are exposed to the electrolyte, resulting in photocurrent degradation with time.

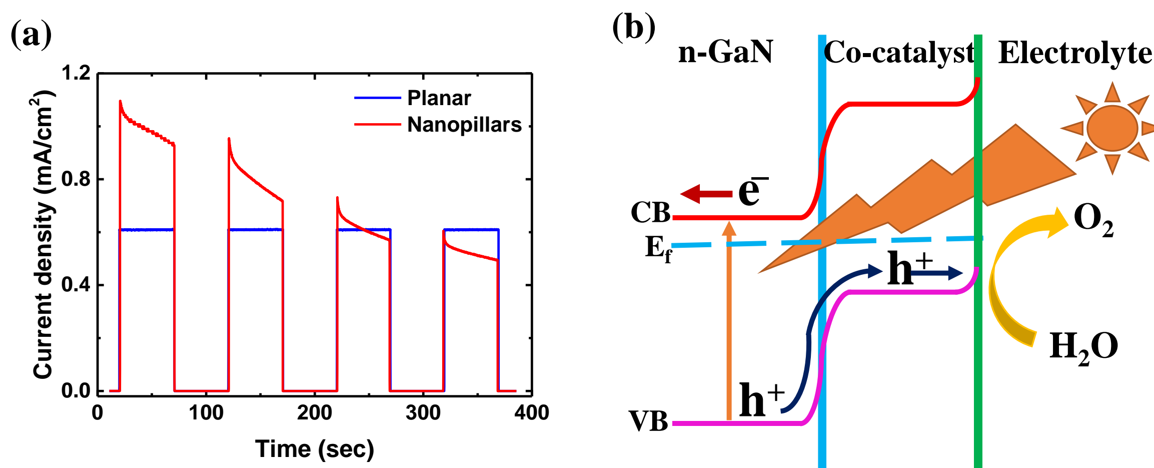

Figure 5.8. (a) Photostability of planar and NP GaN reference photoanodes under AM1.5 light illumination at 0 V vs. Ag/AgCl in 1 M NaOH electrolyte and (b) schematic energy band diagram of GaN/co-catalyst/electrolyte and electron and hole transfer at the material interfaces (CB: conduction band, VB: valence band and E_f: Fermi level).

5.7.1. Transition metal oxide co-catalysts for stability of NP photoanodes

NiO and Co_3O_4 co-catalysts were employed to improve the stability of the NP photoanodes. A schematic band diagram of the GaN/NiO/electrolyte interface is illustrated in Figure 5.8(b). Co-catalyst energy band positions are located at a higher energy relative to the GaN energy bands. As a consequence, the migration/extraction of photogenerated holes from GaN to the co-catalyst is enhanced, thereby significantly reducing the number of holes accumulated at the NP/electrolyte interface. The reduced number of accumulated holes at the interface thus leads to reduced oxidative etching of the NPs surface. This results in the improved photostability of the GaN NP photoanodes.

5.7.2. NiO co-catalyst for the stabilization of NP photoanodes

GaN NPs with a carrier concentration of $1x10^{18}$ cm^{-3} fabricated using a 5 nm thick Ni mask were employed in studying the stability of the photoanodes. NiO nanoparticle co-catalyst decoration on the surface of the GaN NPs was achieved by depositing a 5 nm Ni film on the GaN NPs using e-beam evaporation. The Ni film-coated NPs were furnace annealed at 550 ^{o}C in air for 30 min to convert the Ni film into NiO nano-islands. Figure 5.9 shows an SEM image of the GaN NPs with the NiO co-catalyst. From the SEM image, it can be observed that the NiO nanoparticles are uniformly decorated over the NPs.

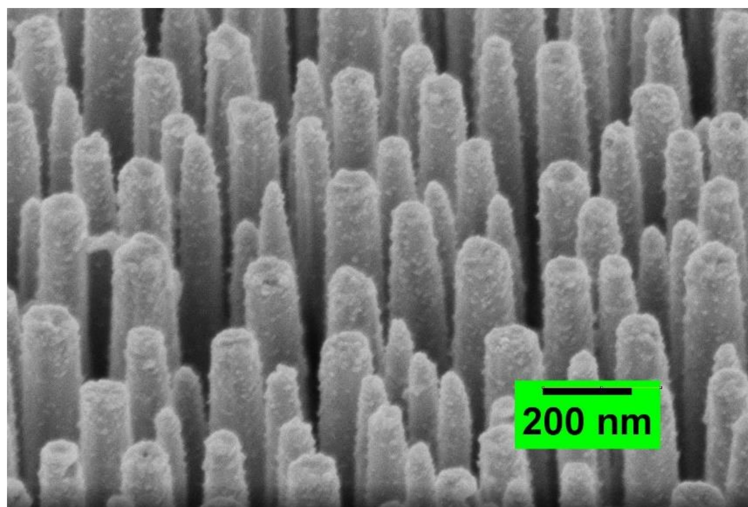

Figure 5.9. SEM image of GaN NPs decorated with a NiO co-catalyst taken at a 52° tilt angle.

Transient photocurrent curves for the NP photoanodes with the NiO co-catalyst are shown in Figure 5.10(a). The photocurrent density became stable after NiO coating. The improved stability can be attributed to discontinuities in the bands between GaN and NiO [28, 29]. The long-term stability of the NiO coated NP photoanodes is shown in Figure 5.10(b). Only a slight drop in the photocurrent density is noticed after 2 hr of illumination. Figure 5.10(c) shows linear sweep voltammetry of the NP photoanodes with and without the NiO co-catalyst under solar illumination. A small drop in the photocurrent density is observed for the NiO-coated NP photoanodes which could be due to parasitic light absorption by the NiO nanoparticles. Further, a sharp rise in photocurrent density is observed for the NiO-coated GaN NP photoanodes beyond 0.5 V. This voltage is close to the reported OER potential of the NiO co-catalyst [30] and hence the sharp rise in the photocurrent density beyond this value can be attributed to the electrochemical catalytic activity of NiO.

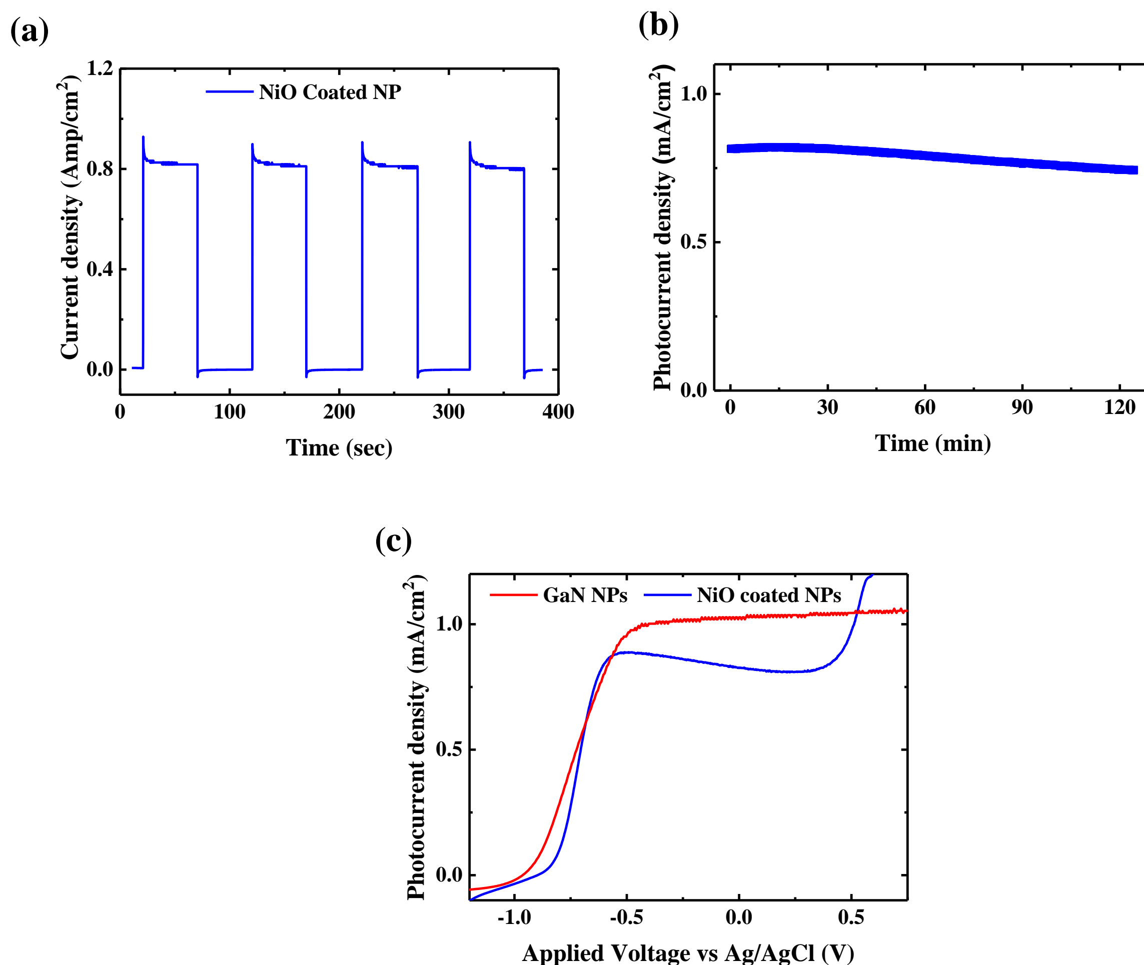

Figure 5.10: (a) Current density-time plots of NP photoanodes with the NiO co-catalyst, (b) long term photostability of NiO-coated NP photoanodes under AM1.5 light illumination at 0 V vs. Ag/AgCl in 1 M NaOH electrolyte and (c) variation of photocurrent density with applied bias for GaN NP photoanodes with and without NiO co-catalyst.

5.7.3. Co_3O_4 co-catalyst for the stabilization of NP photoanodes

GaN NPs fabricated using a 10 nm Ni film were used for the investigation of the photostability of GaN NPs. Sub-monolayers of cobalt oxide nanoparticles were deposited on the GaN NPs by flame spray pyrolysis of solutions containing cobalt (III) acetylacetonate. The Co_3O_4-coated GaN NP samples were prepared by 5 s deposition of Co_3O_4 sub-monolayers followed by calcination at 550 ^{o}C for 1 hr. Combustible liquid solutions containing a total Co-atom concentration of 0.1 M were prepared by dissolving cobalt(III) acetylacetonate in toluene. This combustible solution was fed through a custom-built nozzle at a rate of 3 mL/min and atomized with an oxygen flow of 5 L/min (COREGAS grade 2.5) at a set pressure drop of 5

bar. The resulting spray was ignited with a surrounding annular set of premixed methane/oxygen flame ($CH_{4\text{-flamlet}}$ = 1.2 L/min, $O_{2\text{-flamlet}}$ = 2 L/min, COREGAS grade 4.5).

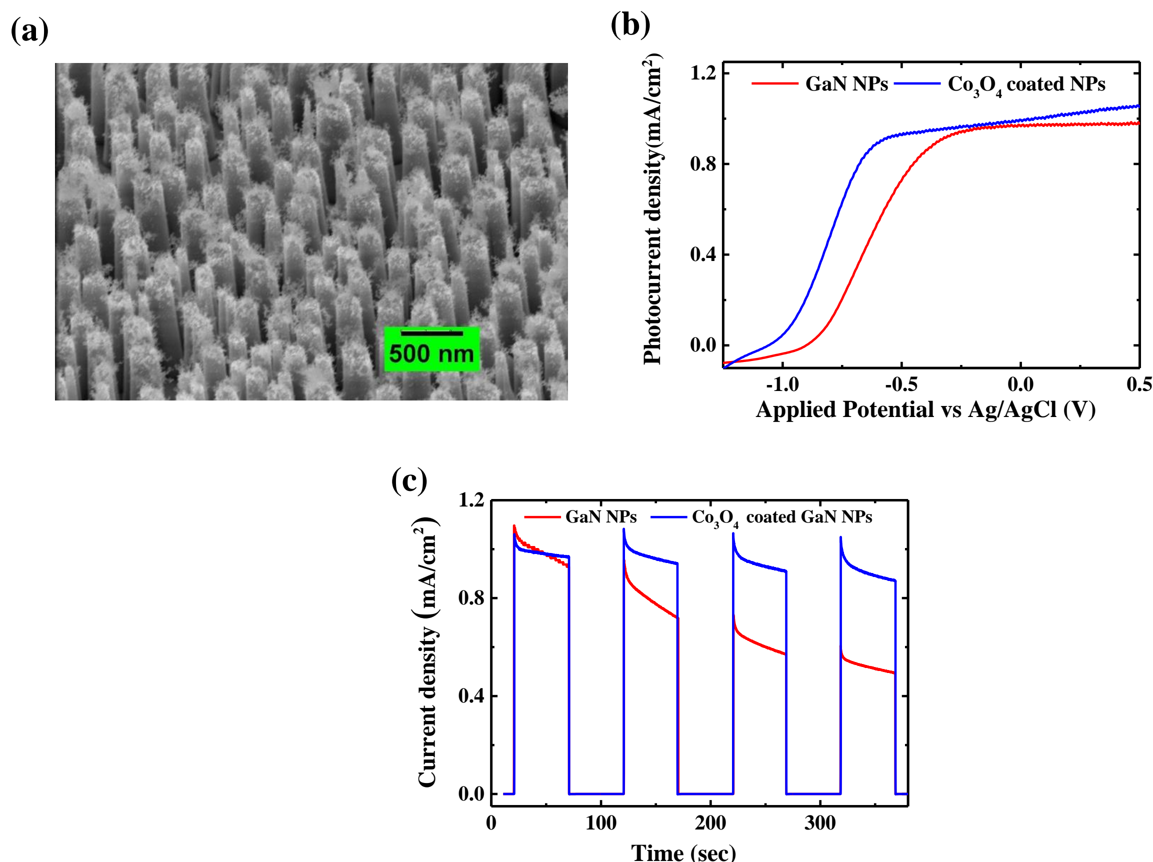

Figure 5.11: (a) SEM image of GaN NPs coated with Co_3O_4 nanoparticles using flame spray synthesis, (b) linear sweep voltammetry of NP photoanodes with and without Co_3O_4 under one sun illumination and (c) photostability of the NP photoanodes in 1 M NaOH electrolyte with and without Co_3O_4.

An SEM image of the GaN NPs decorated with the Co_3O_4 co-catalyst is shown in Figure 5.11(a). It is seen that the NPs are partially covered by Co_3O_4 where the top part of the NPs is loaded with Co_3O_4 but the bottom of the NPs is not fully covered. Figure 5.11(b) shows the dependence of the photocurrent density on applied bias versus Ag/AgCl measured under one sun illumination in NaOH electrolyte for GaN NP photoanodes with and without Co_3O_4. A cathodic shift in the onset potential of ≈ 100 mV is noticed for the Co_3O_4-coated NP samples compared with bare NPs. The efficient collection of the photogenerated holes and negligible parasitic absorption by Co_3O_4 can be attributed to the improved PEC performance of the Co_3O_4-coated NP photoanodes. The favourable band bending at the GaN/Co_3O_4 interface assists the separation of photo-generated carriers, allowing holes to diffuse from GaN into Co_3O_4 even at lower applied potentials (Figure 5.11(b)). This contributes to the improvement in the onset

potential for Co_3O_4-coated GaN NPs compared to the bare GaN NPs. The photostability of the NP photoanodes with and without Co_3O_4 tested at 0 V versus Ag/AgCl under one sun illumination is shown in Figure 5.11(c). A considerable improvement in stability is observed for GaN NP photoanodes with the Co_3O_4 co-catalyst compared to the bare NP photoanodes.

5.7.4. Electrochemical impedance spectroscopy

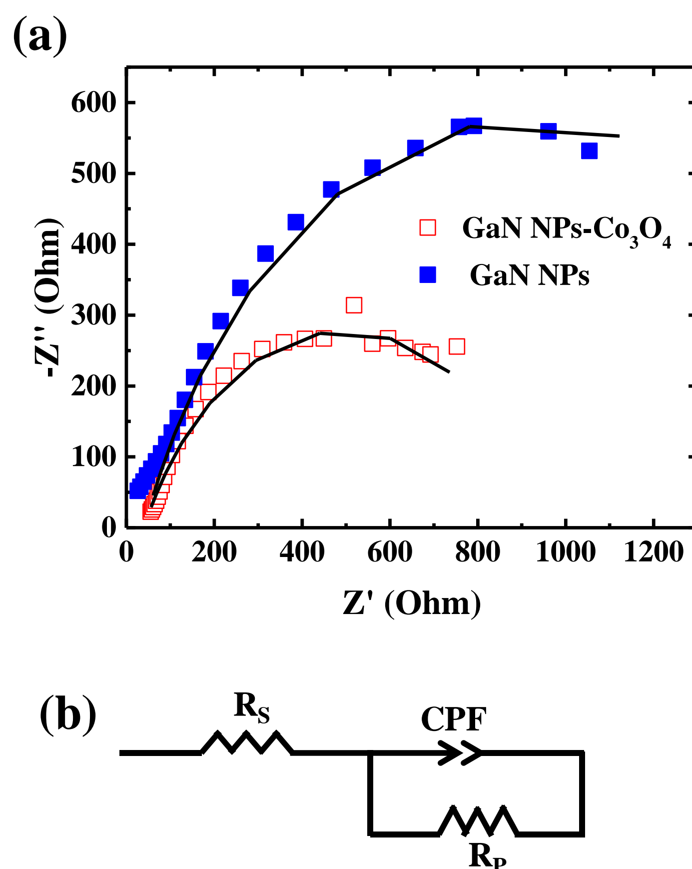

Figure 5.12: (a) Nyquist plots of bare (open squares) and Co_3O_4-decorated GaN NP photoanodes (solid squares) fitted with an equivalent circuit impedance and (b) the equivalent circuit used to model the photoelectrode/electrolyte interface. In figure (a), the solid black line is the fitted curve from the equivalent circuit model.

Electrochemical impedance measurements were carried out under one sun illumination in open circuit mode. Nyquist plots of Co_3O_4-coated and bare GaN NP photoanodes are shown in Figure 5.12(a). In general, a smaller arc diameter of a Nyquist plot means the charge transfer resistance between the semiconductor and electrolyte is lower. The diameter of the Nyquist plot for GaN after Co_3O_4 coating is decreased compared to the bare GaN. This indicates that the deposition of Co_3O_4 reduces the charge transfer resistance and improves the charge transfer

kinetics at the interface between GaN and electrolyte. This contributes to the improved PEC performance of GaN NPs after Co_3O_4 deposition as discussed above.

The Randles circuit or equivalent electrical circuit is designed to further investigate the photoelectrode/electrolyte interface and it is shown in Figure 5.12(b). The equivalent circuit consists of series resistance R_s in series with a parallel combination of parallel resistance R_p and a constant phase element (CPE). R_s and R_p of the equivalent circuit represent the electrolyte resistance and the charge transfer resistance between the photoelectrode and electrolyte, while the CPE is associated with the diffusion capacitance of the double layer formed at photoelectrode/electrolyte interface. The equivalent circuit model (solid black line) fitted to the GaN NP Nyquist plots in Figure 5.12(a) revealed that the R_p value decreased from 1750 to 915 Ω for GaN NPs after being coated with Co_3O_4, while there is no change in the R_s of 40 Ω. This confirms that the Co_3O_4 decoration of GaN NPs has significantly reduced the charge transfer resistance for photogenerated carriers at the photoelectrode/electrolyte interface there by contributed to the improved PEC performance of Co_3O_4-coated NPs.

5.8. Summary

In summary, band gap engineering of GaN has been investigated by incorporating InGaN/GaN MQWs into GaN to capture an extended range of the solar spectrum. The optical properties of the InGaN/GaN MQW planar and NP structures reveal that the optical absorption wavelength of InGaN/GaN MQWs is extended into visible spectrum with increasing In concentration and reaches up to 450 nm for the 30% In sample. However, extended absorption by InGaN is not noticed for the 50% In sample, possibly due to the large defect density in the MQWs. The PEC studies of these samples reveal that the In content has little effect on the planar MQW photoanodes because the MQWs are not directly in contact with the electrolyte and far from the semiconductor/electrolyte interface. The MQW NPs, on the other hand, generate much greater photocurrent densities that display a very strong dependence on the In content. This dependence arises from the direct exposure of the InGaN MQWs to the electrolyte, which allows holes to escape with far greater ease. Out of the four NP photoanodes with In contents ranging from 0%, to 50%, the 30% In NPs generated the largest photocurrent densities of 1.6 mA/cm^2 respectively, as compared to 0.44 mA/cm^2 generated by their planar counterparts and 0.9 mA/cm^2 generated by the reference NPs. Photostability studies of the NP photoanodes were carried out using NiO and Co_3O_4 co-catalysts. NPs coated with NiO exhibited a long-term stable PEC performance under one sun illumination. The Co_3O_4 co-catalyst improved the PEC performance and photostability of the NPs. Optimisation of the In

concentration, the absorption effects, and the right choice of co-catalyst could make it possible to achieve a stable and improved PEC performance for InGaN/GaN NP photoanodes.

5.9. References

[1] Morkoc H 2013 *Nitride Semiconductor Devices: Fundamentals and Applications*: Wiley-VCH Verlag GmbH & Co. KGaA

[2] Vijay Parameshwaran; Chad Gallinat; Ryan W. Enck; Anand V. Sampath; Paul H. Shen; Tevye Kuykendall; Shaul Aloni; Michael Wraback; Bruce M. Clemens, 2012, III-V nitride semiconductors for solar hydrogen production. In: *SPIE Defense, Security, and Sensing*: SPIE, p 83770B

[3] Kibria M G, Chowdhury F A, Zhao S, AlOtaibi B, Trudeau M L, Guo H and Mi Z 2015 Visible light-driven efficient overall water splitting using p-type metal-nitride nanowire arrays *Nat Commun* **6** 6797

[4] Pendyala C, Jasinski J B, Kim J H, Vendra V K, Lisenkov S, Menon M and Sunkara M K 2012 Nanowires as semi-rigid substrates for growth of thick, $In_xGa_{1-x}N$ ($x > 0.4$) epi-layers without phase segregation for photoelectrochemical water splitting *Nanoscale* **4** 6269-75

[5] Theuwis A, Strubbe K, Depestel L M and Gomes W P 2002 A Photoelectrochemical Study of $In_xGa_{1-x}N$ Films *Journal of The Electrochemical Society* **149** E173

[6] Fujii K, Kusakabe K and Ohkawa K 2005 Photoelectrochemical Properties of InGaN for H2Generation from Aqueous Water *Japanese Journal of Applied Physics* **44** 7433-5

[7] Aryal K, Pantha B N, Li J, Lin J Y and Jiang H X 2010 Hydrogen generation by solar water splitting using p-InGaN photoelectrochemical cells *Applied Physics Letters* **96** 052110

[8] Luo W, Liu B, Li Z, Xie Z, Chen D, Zou Z and Zhang R 2008 Stable response to visible light of InGaN photoelectrodes *Applied Physics Letters* **92** 262110

[9] Fujii K, Nakamura S, Yokojima S, Goto T, Yao T, Sugiyama M and Nakano Y 2011 Photoelectrochemical Properties of $In_xGa_{1-x}N$/GaN Multiquantum Well Structures in Depletion Layers *The Journal of Physical Chemistry C* **115** 25165-9

[10] AlOtaibi B, Nguyen H P, Zhao S, Kibria M G, Fan S and Mi Z 2013 Highly stable photoelectrochemical water splitting and hydrogen generation using a double-band InGaN/GaN core/shell nanowire photoanode *Nano letters* **13** 4356-61

[11] Kibria M G, Zhao S, Chowdhury F A, Wang Q, Nguyen H P, Trudeau M L, Guo H and Mi Z 2014 Tuning the surface Fermi level on p-type gallium nitride nanowires for efficient overall water splitting *Nature communications* **5** 3825

[12] Kamimura J, Bogdanoff P, Lahnemann J, Hauswald C, Geelhaar L, Fiechter S and Riechert H 2013 Photoelectrochemical properties of (In,Ga)N nanowires for water splitting investigated by in situ electrochemical mass spectroscopy *J Am Chem Soc* **135** 10242-5

[13] Fan S, AlOtaibi B, Woo S Y, Wang Y, Botton G A and Mi Z 2015 High efficiency solar-to-hydrogen conversion on a monolithically integrated InGaN/GaN/Si adaptive tunnel junction photocathode *Nano letters* **15** 2721-6

[14] Ebaid M, Kang J-H, Lim S-H, Ha J-S, Lee J K, Cho Y-H and Ryu S-W 2015 Enhanced solar hydrogen generation of high density, high aspect ratio, coaxial InGaN/GaN multi-quantum well nanowires *Nano Energy* **12** 215-23

[15] Caccamo L, Hartmann J, Fabrega C, Estrade S, Lilienkamp G, Prades J D, Hoffmann M W, Ledig J, Wagner A, Wang X, Lopez-Conesa L, Peiro F, Rebled J M, Wehmann H H, Daum W, Shen H and Waag A 2014 Band engineered epitaxial 3D GaN-InGaN core-shell rod arrays as an advanced photoanode for visible-light-driven water splitting *ACS Appl Mater Interfaces* **6** 2235-40

[16] Kibria M G, Nguyen H P T, Cui K, Zhao S, Liu D, Guo H, Trudeau M L, Paradis S, Hakima A-R and Mi Z 2013 One-Step Overall Water Splitting under Visible Light Using Multiband InGaN/GaN Nanowire Heterostructures *ACS Nano* **7** 7886-93

[17] Holec D, Zhang Y, Rao D V S, Kappers M J, McAleese C and Humphreys C J 2008 Equilibrium critical thickness for misfit dislocations in III-nitrides *Journal of Applied Physics* **104** 123514-20

[18] Reddy N P, Naureen S, Mokkapati S, Vora K, Shahid N, Karouta F, Tan H H and Jagadish C 2016 Enhanced luminescence from GaN nanopillar arrays fabricated using a top-down process *Nanotechnology* **27** 065304

[19] Narangari P R, Karuturi S K, Lysevych M, Hoe Tan H and Jagadish C 2017 Improved photoelectrochemical performance of GaN nanopillar photoanodes *Nanotechnology* **28** 154001

[20] Cai X-m, Zeng S-w and Zhang B-p 2009 Fabrication and characterization of InGaN p-i-n homojunction solar cell *Applied Physics Letters* **95** 173504

[21] Holec D, Zhang Y, Rao D V S, Kappers M J, McAleese C and Humphreys C J 2008 Equilibrium critical thickness for misfit dislocations in III-nitrides *Journal of Applied Physics* **104**

[22] Ho I h and Stringfellow G B 1996 Solid phase immiscibility in GaInN *Applied Physics Letters* **69** 2701-3

[23] Calarco R, Marso M, Richter T, Aykanat A I, Meijers R, A V D H, Stoica T and Luth H 2005 Size-dependent photoconductivity in MBE-grown GaN-nanowires *Nano letters* **5** 981-4

[24] Richter T, Meijers H L, Calarco R and Marso M 2008 Doping concentration of GaN nanowires determined by opto-electrical measurements *Nano letters* **8** 3056-9

[25] Wang H P, Sun K, Noh S Y, Kargar A, Tsai M L, Huang M Y, Wang D and He J H 2015 High-Performance a-Si/c-Si Heterojunction Photoelectrodes for Photoelectrochemical Oxygen and Hydrogen Evolution *Nano letters* **15** 2817-24

[26] Lai Y-Y, Hsu S-C, Chang H-S, Wu Y S, Chen C-H, Chen L-Y and Cheng Y-J 2016 The study of wet etching on GaN surface by potassium hydroxide solution *Research on Chemical Intermediates* 1-10

[27] Li Q, Westlake K R, Crawford M H, Lee S R, Koleske D D, Figiel J J, Cross K C, Fathololoumi S, Mi Z and Wang G T 2011 Optical performance of top-down fabricated InGaN/GaN nanorod light emitting diode arrays *Opt. Express* **19** 25528-34

[28] Benton J, Bai J and Wang T 2013 Significantly enhanced performance of an InGaN/GaN nanostructure based photo-electrode for solar power hydrogen generation *Applied Physics Letters* **103** 133904

[29] Waki I, Cohen D, Lal R, Mishra U, DenBaars S P and Nakamura S 2007 Direct water photoelectrolysis with patterned n-GaN *Applied Physics Letters* **91** 093519

[30] Bernicke M, Eckhardt B, Lippitz A, Ortel E, Bernsmeier D, Schmack R and Kraehnert R 2016 Synthesis and OER activity of NiO coatings with micelle-templated mesopore structure *ChemistrySelect* **1** 482-9

Chapter 6

Fabrication and Photoelectrochemical Studies of InP Nanopillars

6.1. Introduction

Light harvesting via tandem semiconductor absorbers is considered one of the most promising approaches for efficient overall photoelectrochemical (PEC) water splitting to generate hydrogen fuel, where both electrodes are made of photoactive materials with complementary band gaps [1]. Gallium nitride (GaN) based alloys and indium phosphide (InP) have the potential to be a perfect combination of photoelectrodes for PEC tandem cells given their direct and complementary band gaps and favourable band edge positions for PEC water splitting. As noted in Chapters 4 and 5, we demonstrated GaN based nanopillars (NPs) as excellent photoanodes with PEC performances reaching close to the theoretical limit. The incorporation of InGaN/GaN multiple quantum wells (MQWs) into GaN further improved PEC performance through the band gap engineering of GaN. This chapter discusses the development of photocathodes with a complementary energy band gap and favourable conduction band with respect to the water reduction potential for high efficiency PEC tandem cells. Although the band gap of GaN alloys can be engineered to 0.7 eV (InN), it is extremely difficult to achieve defect free growth of InGaN layers beyond 30% In concentration and to make low resistance Ohmic contacts to p-type GaN [2, 3].

On the other hand, InP possesses all the essential attributes to be a highly efficient photocathode such as optimum and direct band gap (1.35 eV) for water splitting, high absorption coefficient and perfect conduction band alignment with the water reduction potential [4, 5]. InP can capture sunlight up to the infrared region (IR) due to its low band gap and allows the usage of thin-film material given its high absorption coefficient, where a few microns of InP is enough to capture nearly all the incident light. Most importantly, InP can serve as an ideal complementary low band gap photocathode material for photoanodes with band gaps of 1.6 to 1.7 eV in a PEC tandem cell configuration to achieve very high efficiency overall water splitting [1]. The enhanced absorption and increased semiconductor/electrolyte interface area of nanostructures can further improve the performance of InP photocathodes. Among the III-V semiconductors, InP attained considerable research interest as a photocathode

for PEC water splitting applications [6-14, 5, 4]. Gao *et al.* reported the highest ever photocathodic efficiency of 15.8% for InP photocathodes in 1 M $HClO_4$ electrolyte under one sun illumination [9] by incorporating a buried junction and periodic array of NPs at the top of photoelectrode. The photovoltage of the photocathodes was controlled by the buried junction instead of the semiconductor/electrolyte junction and the absorption properties of the photocathodes were manipulated by the periodic array of NPs fabricated using a top-down approach. Lee *et al.* achieved approximately 14% cathodic efficiency for InP NP photocathodes fabricated using a top-down approach [14]. So far, all the reported NP photocathodes fabricated using a top-down approach used an extensive and cumbersome approach to remove plasma damage. Further, long-term stability of the photocathodes, irrespective of the NP synthesis technique, was achieved by deposition of a protection layer, typically TiO_2 [9, 14, 10-12, 8]. To avoid multi-step processing, in this work, we propose the wet chemical treatment of NPs in sulfur dissolved oleylamine (S-OA) for simultaneous plasma damage removal and protection against photocorrosion for long-term stability of photocathodes to develop highly efficient InP photocathodes in a simple and cost-effective approach.

This chapter presents the fabrication of large area InP NPs using a cost-effective top-down approach, plasma damage removal using a wet chemical treatment and a study of their PEC performance. Section 6.2 deals with the top-down fabrication of large area InP NPs using inductively coupled plasma etching (ICP) of InP wafers, masked using a self-organized random mask technique. However, as-fabricated NPs are severely damaged by high energy plasma ion impingement, which causes the formation of defect states at the semiconductor surface. These defects act as traps for photogenerated carriers, thereby reducing the PEC performance of NP photocathodes. Section 6.3 deals with the plasma damage removal of NPs using S-OA solution and studying their morphology and optical properties. Photoluminescence (PL) and time resolved photoluminescence (TRPL) techniques were employed to characterise the optical quality of the NPs after removing plasma damage. The absorption properties of the InP planar and NP structures are discussed in Section 6.4. Section 6.5 is focussed on PEC studies of InP planar and NP photocathodes. The S-OA treated InP NP photocathodes exhibited a huge improvement in PEC performance compared to the planar and as-fabricated NP photocathodes. The influence of the S-OA treatment on charge transfer resistance for photogenerated carriers at the semiconductor/electrolyte interface is discussed in Section 6.6. Section 6.7 presents the long-term stability of NP photocathodes followed by Section 6.8 which concludes Chapter 6.

6.2. Fabrication of InP NPs

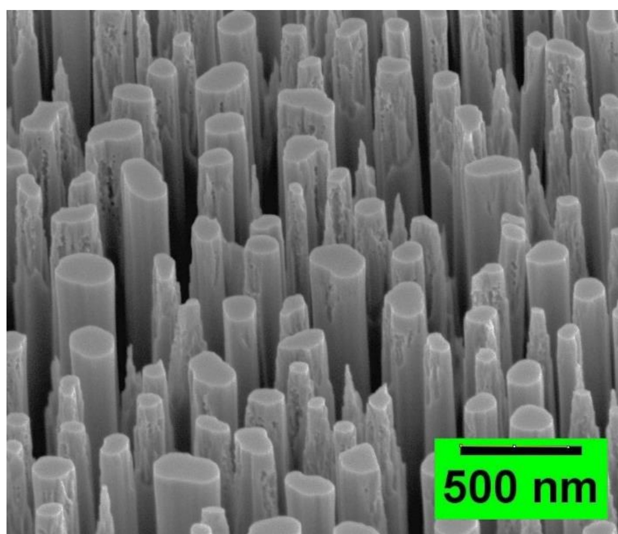

Figure 6.1: SEM image of InP NPs fabricated using ICP etching of self-organised randomly masked p-InP wafers. The image was taken at a 52° tilt angle and the scale bar is 500 nm.

In this work, we employed p-type InP (100) wafers with carrier concentrations of 2–5 x 10^{17} cm^{-3} for the fabrication of NPs using a top-down approach. A self-assembled random mask technique was employed to make an etch mask for ICP fabrication of NPs in a top-down approach [15-18]. Au/SiO_2 was used as a mask for the fabrication of InP NPs. The mask preparation methodology used for the fabrication of large area InP NPs is similar to the mask preparation for the fabrication of GaN NPs as discussed in Section 4.2 of Chapter 4 and also discussed in Chapter 2. Instead of a Ni mask as for the fabrication of GaN NPs, Au was used as a metal mask for the top-down fabrication of InP NPs because InP is unstable at higher temperatures compared to GaN and Au can form nano-islands at lower temperatures. Further, a 500 nm SiO_2 film was deposited on the rear side of the InP wafer to protect the wafer from decomposition during RTA annealing while converting the Au film into nano-islands. The Au film was converted into nano-island particles by RTA annealing at 500 ^{O}C in an Ar atmosphere for 1 min. Reactive ion etching (RIE) was then used to etch the SiO_2 around the Au nano-island particles to produce an Au/SiO_2 etch mask. The SiO_2 etching was carried out at room temperature and 200 W RF power. CHF_3 gas was injected at a flow rate of 25 sccm while maintaining the chamber pressure at 30 mTorr. After mask production, a SAMCO ICP system was employed to fabricate InP NPs using Cl_2/Ar gas chemistry. NP fabrication was carried out at an electrode temperature of 200 ^{O}C and a chamber pressure of 2.3 mTorr. The plasma was generated by flowing 25/1.5 sccm of Cl_2/Ar and applying 50/200 W RF/ICP power. Cr coated

sapphire was used as a carrier wafer to load the InP wafers into the ICP reactor. After NP fabrication, the samples were immersed in buffered HF to remove the left-over mask and rear side SiO_2 deposited during the mask preparation stage. Figure 6.1 shows SEM images of as-fabricated InP NPs after removing the mask. From Figure 6.1, the NPs fabricated using the random mask exhibit uniform height and very high density. The average diameter and length of the NPs were measured from the SEM image to be ~200 nm and ~900 nm, respectively. However, plasma caused severe damage to the NP surface as can be seen from the surface of NPs (Figure 6.1).

6.3. Plasma surface damage removal

As discussed above in Section 6.2, InP NPs fabricated using plasma etching techniques experience severe surface damage due to high energy ion impingement. These defects from surface damage can be detrimental to the PEC performance of InP NPs since they act as traps for photogenerated carriers. Therefore, eradication of surface damage is critical to reap the advantages of NPs for PEC water splitting applications. So far, the digital etching technique, which involves the self-limiting oxidation and subsequent removal of the oxide layer, is the most commonly used technique for removing the plasma damage at nanoscale levels [19, 20]. However, this technique is cumbersome for etching relatively thick layers as it requires a large number of repetitive oxidation and removal cycles. To avoid this difficulty, in this work, the sulfur dissolved oleylamine solution was employed to remove the surface damage of InP NPs through a monolayer controlled etching process [21]. Furthermore, S-OA treatment is also found to provide simultaneous surface passivation and stabilisation of InP NPs [21-23]. From here onwards, the oleylamine contained sulfur solution is referred as S-OA. The NPs were wet treated in S-OA to remove the plasma damage.

6.3.1. Morphology of NPs

To eliminate the surface damage from the InP NPs, wet treatment was carried out using 5% S-OA solution. The 5% S-OA solution was prepared by dissolution of 5 g of sulfur in 100 ml oleylamine solution at 98 ºC for a prolonged time (>24 hours). The reaction of sulfur with oleylamine forms alkyl ammonium polysulfides in solution. Next, the InP NP samples were immersed in S-OA solution while maintaining the temperature at 98 ºC. The morphology of the NPs before and after the wet treatment in S-OA is shown in Figure 6.2. From Figure 6.2, it can be observed that the sidewalls of the NPs become smooth after wet treatment compared to the as-fabricated NPs. This suggests that the surface damage is eliminated during wet treatment

of NPs in S-OA. Further, the increase in etching time from 60 to 90 min led to variation in the morphology at the top of the NPs. F. Maeda *et al.* [22] and S. Naureen *et al.* [21] proposed an etching model to explain the controlled sculpting of InP in S-OA. According to them, the polysulfides in S-OA solution adsorb to the InP surface and sulfur atoms bond to either In or P. The bonded sulfur then invades the In-P bonds to form soluble $InPS_4$. The dissolution of $InPS_4$ results in etching of an InP layer and the etching continues by attacking the underneath InP layers. The S-OA wet treatment of InP is an anisotropic etching process and the etch rate depends on the crystal orientation of the material. This anisotropic etching process leads to the change in the morphology of NPs with increasing wet treatment time because the differences in etching rates of InP in different crystallographic planes may become prominent after a longer etching time. The anisotropic etching behaviour of NPs in S-OA can be attributed to the variation in the morphology of NP tips as observed from Figure 6.2(b)-(c) when increasing the etch time from 60 to 90 min.

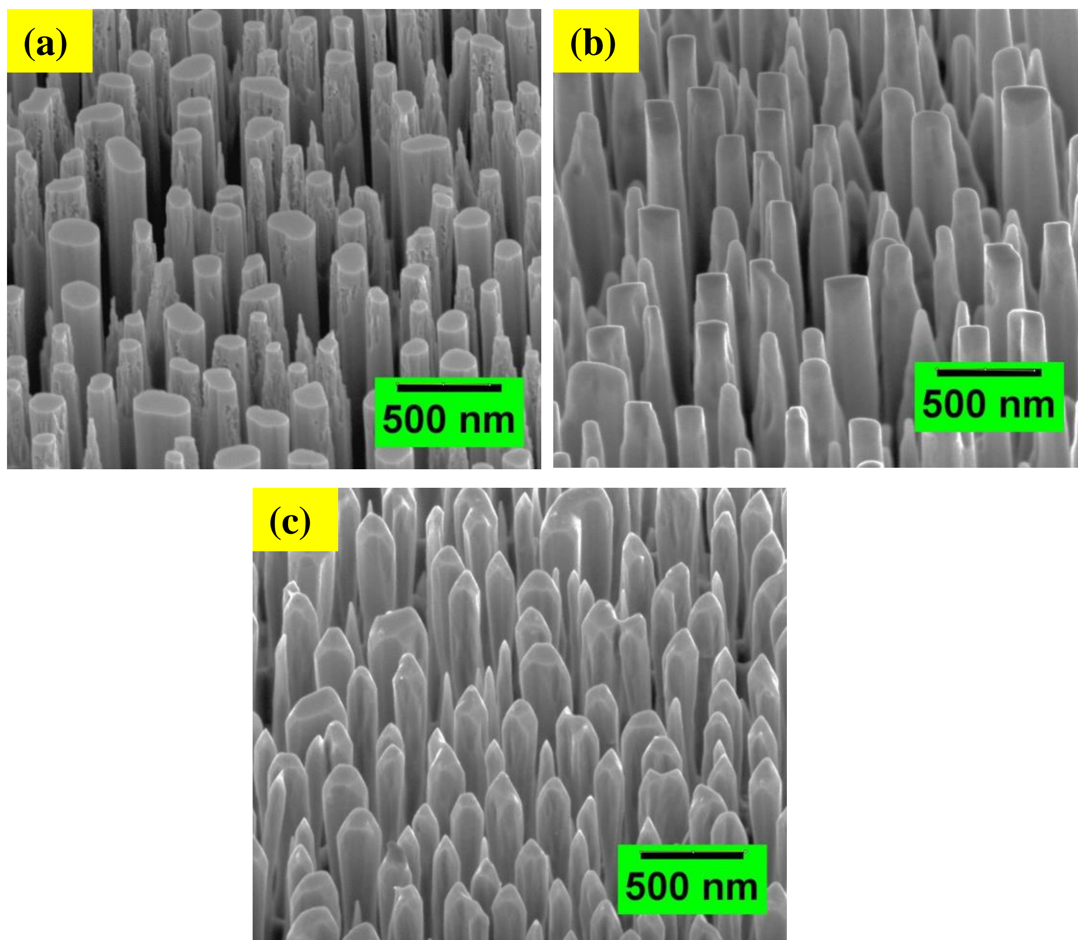

Figure 6.2: SEM images of (a) as-fabricated large area InP NPs and S-OA trim etched NPs for (b) 60 min and (c) 90 min. SEM images were taken at a 52° tilt angle and scale the bar is 500 nm.

6.3.2. Optical characterization of NPs

To study the effect of plasma damage and wet treatment on the optical quality of InP NPs, time resolved photoluminescence (TRPL) and micro-photoluminescence (μ-PL) techniques were employed for the optical characterization of InP NPs. Details of the TRPL and PL set-ups are discussed in Section 2.4.2 of Chapter 2. The TRPL and PL measurements were carried out on NPs, along with the wafers from which the NPs were fabricated. A 522 nm wavelength green laser was used to excite the samples for both TRPL and PL measurements. The luminescence results of the planar samples were used as a reference to estimate the influence of plasma damage and S-OA treatment on NP surface.

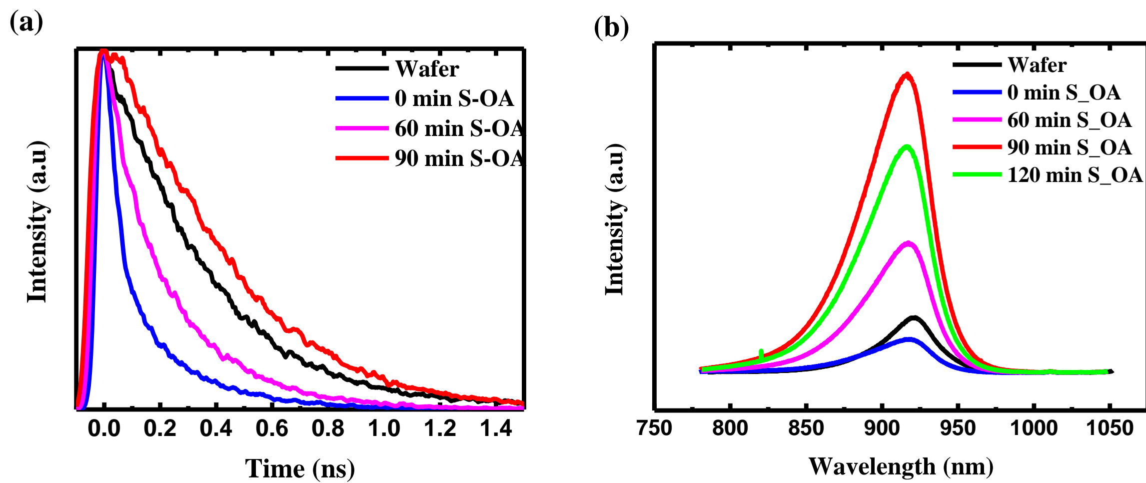

Figure 6.3: (a) TRPL decay curves and (b) PL spectra of the InP wafer and NPs with and without wet treatment in S-OA solution measured by exciting the samples with a green laser.

TRPL was employed to measure the minority carrier lifetime of NPs. Figure 6.3(a) shows the TRPL decay curves of a planar sample (bare wafer) and NPs with and without S-OA trim etching. The minority carrier lifetime is a measure of material quality, where a longer minority carrier lifetime means a lower defect density. The minority carrier lifetime is defined as the average time taken for the photoexcited carriers to recombine either radiatively or non-radiatively. The minority carrier lifetime is expressed as $\frac{1}{\tau_{mc}} = \frac{1}{\tau_r} + \frac{1}{\tau_{nr}}$, where τ_{mc} is minority carrier lifetime and τ_r and τ_{nr} are the radiative and non-radiative recombination lifetimes of the carriers, respectively. The minority carrier lifetime can be extracted by fitting the TRPL decay curve with an exponential decay function. The minority carrier lifetimes for the InP wafer and NPs were extracted by fitting the TRPL decay curves in Figure 6.3(a) with mono-exponential decay functions and the deduced results are tabulated in Table 6.1. The 0 min S-OA in Figure 6.3 and Table 6.1 refers to the as-fabricated NPs after removing the etch mask, i.e. NPs without

wet treatment in S-OA solution. As observed from Figure 6.3(a) and Table 6.1, the minority carrier lifetime of as-fabricated NPs drops by around 67% compared to the wafers. As-fabricated NPs show a minority carrier lifetime of 119 ps against 363 ps for the wafer. The degradation of the carrier lifetime indicates that the top-down fabrication process causes severe damage to the NP surface. The plasma damage creates defects, thereby annihilating the photogenerated carriers through non-radiative recombination. On the other hand, the S-OA treatment of NPs shows substantial improvement in the minority carrier lifetime of the NPs compared to the as-fabricated NPs. The minority carrier lifetime of the NPs is increased with increasing wet treatment time. Moreover, the minority carrier lifetime for the NPs exceeds the value of the wafer from which the NPs were fabricated after 90 min of wet treatment. The minority carrier lifetime of the InP NPs reached 425 ps after S-OA treatment. The improvement in the optical quality of the NPs after S-OA treatment indicates that it successfully eliminated the surface damage of the NPs through the layer-by-layer etching of InP. Furthermore, the improved carrier lifetime of 90 min S-OA treated NPs in comparison to the bare wafer suggests that S-OA not only removes the plasma damage but also passivates the InP surface. The passivation of the NPs can be attributed to the formation of a sulfide layer around the NPs during the S-OA treatment [24, 25]. It was reported that the optical quality of InP was improved after sulfur treatment due to the formation of a sulfide layer on the InP surface [21, 26].

Table 6.1: Minority carrier lifetime of the InP wafer and NPs with and without S-OA treatment extracted by fitting the TRPL decay curves with exponential decay functions.

Sample	**Lifetime (ps)**
Wafer	363
0 min S-OA	119
60 min S-OA	222
90 min S-OA	425

PL measurements were carried out to further investigate the optical quality of the InP planar and NP samples and the results are presented in Figure 6.3(b). Although the comparison of PL intensity of planar and NP samples does not provide any insights into the optical quality of the materials given the difference in absorption and emission properties of NPs and planar samples, the relative variation in the PL intensity of NPs can be used to analyse the optical quality of the NPs before and after S-OA treatment. As shown in Figure 6.3(b), the PL intensity

of as-fabricated NPs is reduced considerably compared to the wafer near the band edge emission of the NPs due to the plasma induced surface damage of the NPs. The PL intensity of the NPs is recovered after S-OA treatment and shown a marked improvement in PL intensity with increasing wet treatment time. The remarkable improvement in PL intensity after S-OA treatment demonstrates the successful elimination of surface damage of the NPs after S-OA treatment.

6.4. Absorption properties of NPs

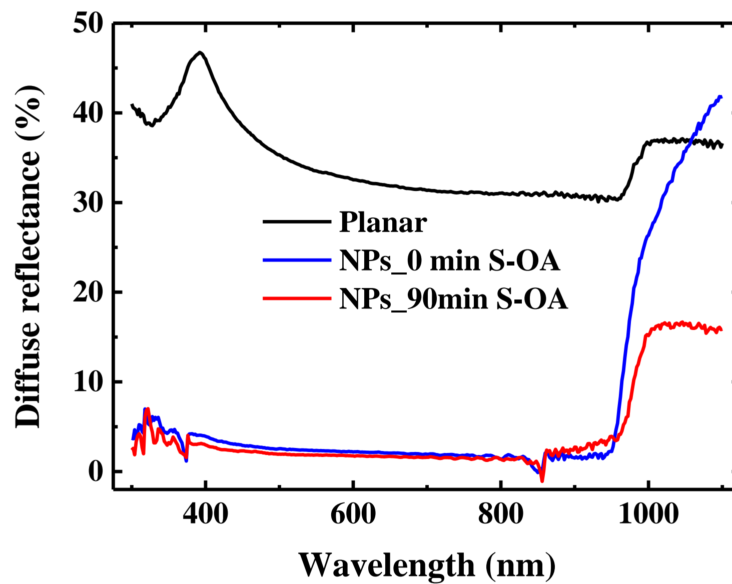

Figure 6.4: Diffuse reflectance spectra of InP planar and NPs before and after S-OA wet etching.

To study the absorption behaviour of NPs with and without S-OA treatment, diffuse specular reflectance measurements were carried out using a spectrophotometer. Figure 6.4 shows the diffuse reflectance spectra of planar, as-fabricated NPs and 90 min S-OA treated NPs. From Figure 6.4, it can be seen that the planar sample reflects more than 30% of the incident light above the band gap of InP (~920 nm). Fabrication of NPs reduces reflection losses to insignificant values. This means that almost all the incident light is absorbed by NPs as the transmission losses for InP NPs can be neglected since the absorption length of light for InP is less than 1 μm based on the bulk absorption coefficient. The striking improvement in absorption properties of NPs can be attributed to the suppressed Fresnel reflection losses [27, 28]. Moreover, the S-OA shows no influence on absorption properties of NPs. This could be due to the fact that the removed damaged layer (due to plasma etching) of the NPs after S-OA treatment is not thick enough to affect the absorption properties of the NPs. As shown in Figure

6.4, the diffuse reflectance spectrum of the S-OA treated NPs follows a trend similar to that of the untreated NP samples. The improved absorption leads to enhanced photo-excited carrier generation thereby contributing to the enhanced photocurrent of the NPs compared to the planar structures.

6.5. PEC studies of InP photocathodes

The PEC performance of the InP planar and NP photocathodes was evaluated using a PEC cell consisting of three electrodes. The details of the PEC testing station are discussed in Section 2.6 of Chapter 2. The PEC measurements were performed in 1 M HCl electrolyte under simulated one sun illumination using InP planar/NP structures as a working photocathode, Pt as a counter electrode and Ag/AgCl as a reference electrode. In this work, voltammetry measurements are reported with applied potential versus RHE. The following relation was used to convert the applied potential versus Ag/AgCl into applied potential versus RHE

$$V\ vs.RHE = V\ vs.Ag/AgCl + 0.197 + 0.059 * pH \quad \text{..............} \ 6.1$$

Since the pH value for 1 M HCl electrolyte, used in this study, is zero, eq 1 becomes

$$V\ vs.RHE = V\ vs.AgAgCl + 0.197 \quad \text{..................} 6.2$$

6.5.1. Fabrication of InP photocathodes

To test the PEC performance of InP planar and NP photocathodes, Zn/Au ohmic contacts were made to the rear side of the InP samples. The wet treatment of NPs was carried out after preparing the contacts to the samples. Back contacts to the InP photocathodes were made by DC sputtering of 20/100 nm thick Zn/Au films followed by annealing in forming gas (H_2 (5%) +N_2) at 400 ^{O}C for 40 mins. Before depositing the back-contacts, the samples were dipped in buffered HF for one minute to remove the native oxide. After making contacts, 2 nm platinum was deposited as a catalyst on top of the InP samples using electron beam evaporation. The active area of each photocathode was then defined by painting with non-transparent nail-polish. Finally, the fabrication of photocathodes was accomplished by applying white paint to the back of the photocathodes to prevent the corrosion of metal contact and block carrier leakage from the metal contacts.

6.5.2. PEC performance of NP photocathodes

The PEC performance of the InP planar and as-fabricated NP photocathodes is shown in Figure 6.5. The dark currents for both planar and NP photocathodes were insignificant.

Ironically, both photocathodes exhibited merely similar saturation current densities even under sunlight illumination despite striking enhancement in light absorption by the NPs compared to the planar structure as discussed in Section 6.4 of this chapter. Planar and NP photocathodes show similar saturation photocurrent densities of over 20 mA/cm^2 despite more than 30% improvement in light absorption by the NPs compared to their counterpart. Further, a 100 mV negative shift in onset potential is noticed for NPs compared to the planar photocathode. The onset of photocurrent occurs at 500 mV vs RHE for the NP photocathode compared to 600 mV for the planar photocathode. The decline in the PEC performance of the as-fabricated NPs can be attributed to the severe damage caused to the NP surface during plasma etching. As discussed in Section 6.3.2 of this chapter, the carrier lifetime of as-fabricated NPs is degraded by more than 60% compared to the planar structure. The plasma damage creates defect states at the NP surface which traps photogenerated carriers and prevents them from participating in PEC water splitting. Additional potential is required to extract these trapped photogenerated carriers out of the defect traps compared to the planar structures and thus results in a reduced onset potential for the NP photocathode. Despite this, it may not be possible to extract all the photogenerated carriers due to the severe surface damage sustained by the NPs. This may be a possible reason for the unimproved photocurrent density of as-fabricated NPs despite an improvement in light absorption by the NPs compared to the planar sample.

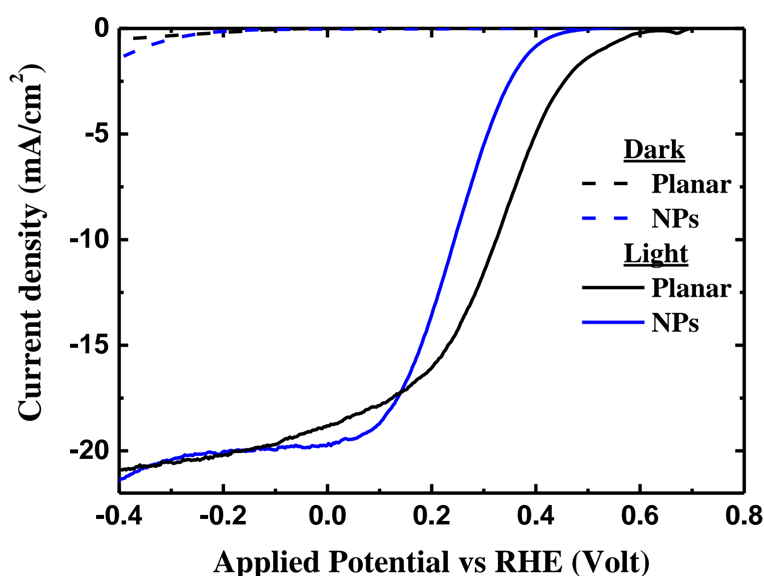

Figure 6.5: Linear-sweep voltammetry of planar and as-fabricated InP NP photocathodes under one sun illumination in 1 M HCl electrolyte.

6.5.3. Influence of S-OA treatment on PEC performance of NP photocathodes

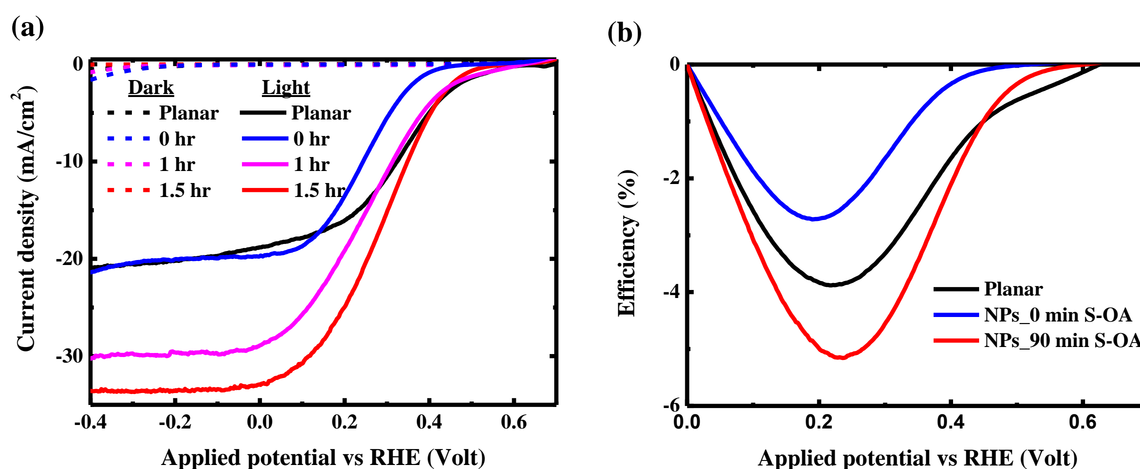

Figure 6.6: Influence of wet treatment on (a) PEC performance and (b) ABPE of NPs tested in 1 M HCl electrolyte.

As discussed above, as-fabricated NPs exhibit slightly reduced PEC performance compared to the planar photocathodes due to severe plasma damage to the NPs. To overcome the plasma damage, the NPs were wet treated in S-OA solution and their PEC performance was tested. Figure 6.6(a) shows the linear sweep voltammetry measurements of InP planar and NP photocathodes with and without S-OA treatment. NPs exhibit exceptional PEC performance after S-OA treatment compared to the planar and as-fabricated NPs. InP NP photocathodes generate a remarkable saturation photocurrent density of nearly 34 mA/cm^2 after 90 min wet treatment in S-OA, which is the highest ever reported value for InP photocathodes in HCl electrolyte under one sun illumination. The saturation photocurrent density of NP photocathodes increased by 67% compared to the planar and as-fabricated NP photocathodes. Most importantly, the photocurrent density of NPs after 90 min S-OA treatment reaches very close to the theoretically achievable limit for InP photocathodes (~34 mA/cm^2) given the band gap of the material. The saturation photocurrent density of NP photocathodes is dependent on wet treatment time and increases with increasing wet etching time. Moreover, the onset potential of NPs is shifted towards higher positive values after S-OA treatment compared to the as-fabricated NPs and returns to the onset potential of the planar photocathode. The rise of the photocurrent density and retrieved onset potential after S-OA treatment is consistent with the TRPL and PL results (Figure 6.3). S-OA removal of plasma damage eliminates the traps of photogenerated carriers and thereby contribute to the improved PEC performance of wet treated NPs. Further, plasma damage removal also helps improve the onset potential because no additional energy is required to extract the photogenerated carriers from plasma defect traps,

as is the case with untreated NPs. In addition to the elimination of plasma damage, remarkable improvement in photo-absorption properties and increased electrolyte/semiconductor interface also contribute to the striking improvement in the photocurrent density of wet treated NPs compared to the planar photocathode.

To compare the quantitative PEC performance of InP planar and NP photocathodes, the photocathodic conversion efficiency (η) of each cathode was determined using the following relation [9, 29, 30]

$$\eta = \frac{V_{app} j_p}{P_{in}} \quad \text{...............6.3}$$

where V_{app} is the applied potential versus RHE, P_{in} is the optical power density of incident light and j_p is the measured photocurrent density. The η of the InP photocathodes is evaluated from the PEC voltammetry measurements presented in Figure 6.6(a). Figure 6.6(b) shows the η of the planar and NP photocathodes under one sun light conditions calculated using Equation 6.3. The η of S-OA treated NP photocathodes after 90 min reaches ~5.2% at an applied voltage of 0.23 V versus RHE, which is highest for InP nanostructure photocathodes without either buried junctions or heterojunctions. The η of S-OA treated NP photocathodes exceeds their planar counterpart by 32%, where the planar photocathode recorded an η of ~3.9%. On the other hand, as-fabricated NPs exhibited inferior performance compared to the planar photocathodes due to the severe damage caused to the NP surface as observed in lifetime measurements (Figure 6.3(a) and Table 6.1). The improved onset potential and currents after removing the surface damage in S-OA treatment contribute to the excellent η of NPs compared to the planar and as-fabricated NPs.

6.6. Electrochemical impedance of NP photocathodes

Electrochemical impedance measurements were performed at open circuit conditions to investigate the influence of S-OA treatment on the charge transfer resistance between the semiconductor and electrolyte interface. Figure 6.7(a) shows Nyquist plots of InP NP photocathodes with and without S-OA treatment. The half-circle radius of the Nyquist plot refers to the charge transfer impedance at the semiconductor/electrolyte interface, where a smaller diameter means a lower interface charge transfer resistance. As shown in Figure 6.7(a), the radius of the Nyquist plot for InP NPs is reduced substantially after 90 min of S-OA treatment compared to the untreated NPs. This indicates that the resistance is significantly reduced for the photo-excited carriers to reach the electrolyte from the semiconductor and participate in water splitting. The elimination of defect states at the NP surface using S-OA

treatment, which act as traps for photogenerated carriers (Figure 6.3(a)), help to reduce the interface resistance of NPs after S-OA treatment. The reduced charge transfer resistance is also one of the key contributors for the excellent PEC performance of the S-OA treated NP photocathodes compared to the as-fabricated NPs (Figure 6.6). To further investigate the impact of S-OA treatment on the photoelectrode/electrolyte interface, the equivalent circuit model was designed to extract the charge transfer resistance at the interface. The Randles circuit model shown in Figure 6.7(b) fitted to the measured data, as shown in Figure 6.7(a), confirms the drop in charge transfer resistance for S-OA treated NPs compared to the as-fabricated NPs. The parallel resistance R_p, which represents charge transfer resistance at the interface, dropped from 400 Ω for as-fabricated NPs to 240 Ω for S-OA treated NP samples.

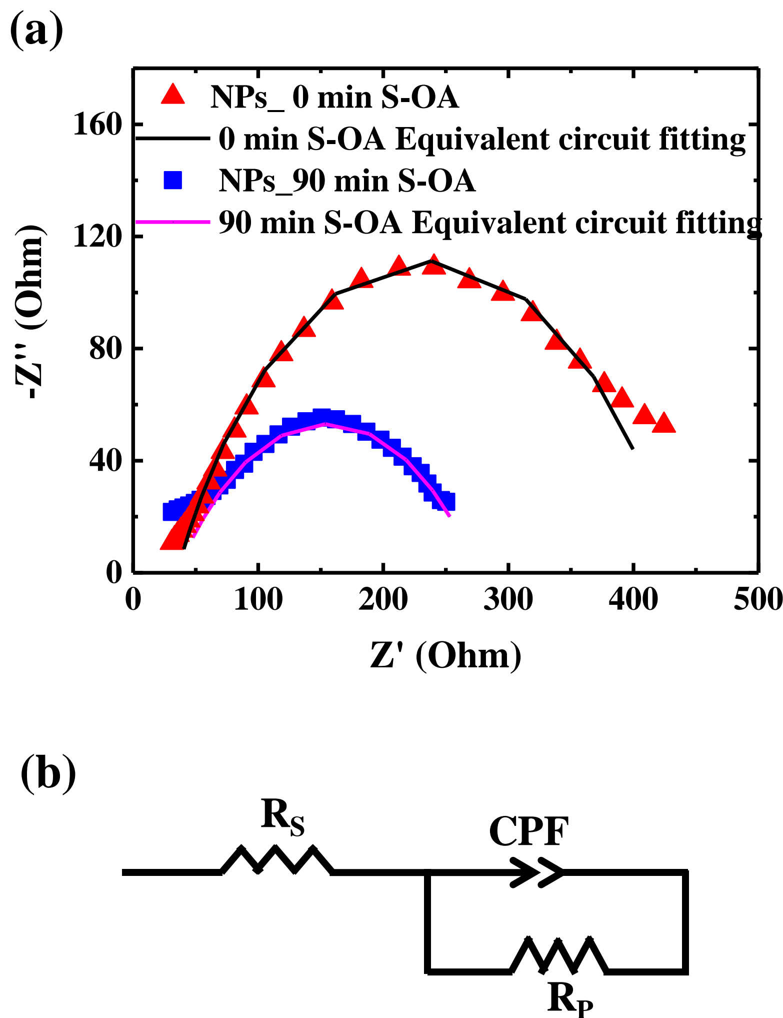

Figure 6.7: (a) Nyquist plots of NP photocathodes measured before and after S-OA treatment and fitted to the Randles circuit and (b) Equivalent electrical circuit.

6.7. Stability of NP photocathodes

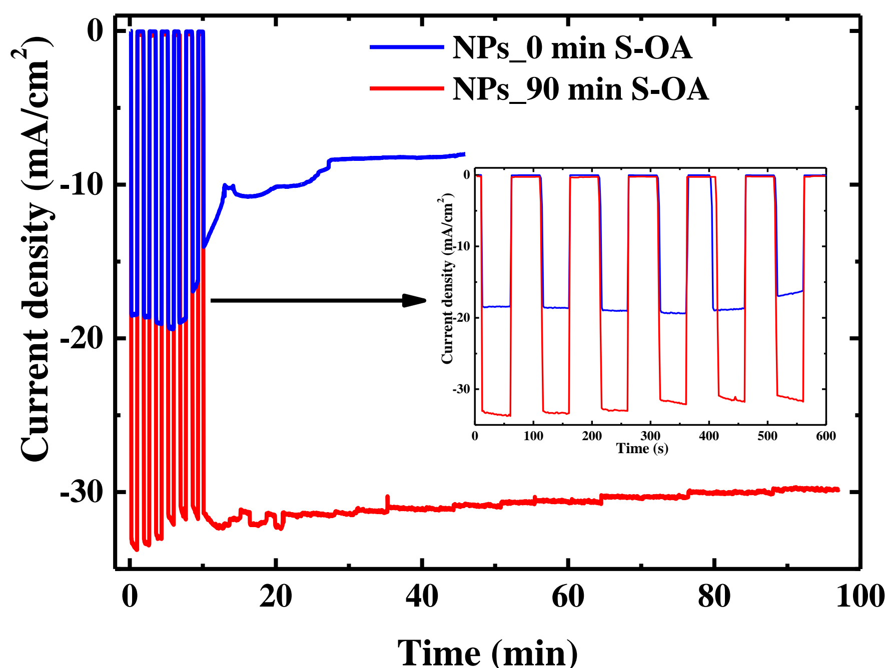

Figure 6.8: Amperometric J-t curves of the InP NP photocathodes at 0 V vs. RHE under simulated one sun illumination in 1 M HCl electrolyte with and without S-OA treatment. The inset shows the transient J-t plots of InP NP photocathodes.

Long-term stability is a prerequisite for any photoelectrode before being employed in practical PEC applications. Therefore, we tested the long-term stability of NP photocathodes in 1 M HCl electrolyte before and after S-OA treatment under continuous one sun illumination at an applied voltage of 0 V versus RHE and the results are presented in Figure 6.8. For 10 min at the beginning of each stability measurement, the transient J-t response was measured for each NP photocathode and presented in the inset of Figure 6.8. As shown in the inset of Figure 6.8, irrespective of the wet treatment, the rise and drop of the current during on and off cycles of light exposure is observed for both photocathodes. This indicates that the PEC performance of the NP photocathodes stems from the photoresponse and is not due to chemical reaction with the electrolyte. However, the untreated NPs experienced a severe degradation in PEC performance as shown in Figure 6.8, where the photocurrent dropped by 50% within 20 min of commencing the stability measurement. The decomposition of the InP in the electrolyte is a plausible reason for the reduced PEC performance of the untreated NPs. It was reported that InP decomposes into oxides and phosphates in acidic solution, even in the presence of catalyst. The stability of the NP photocathode is improved significantly after wet treatment in S-OA. A drop in the photocurrent of less than 10% is registered for the NP photocathode after 100 min

of sunlight exposure, with the largest drop occurring within the first 10 min of the test. The improved stability of the S-OA treated NP photocathodes can be attributed to the presence of a sulfide layer, which is relatively stable in acidic electrolyte, around the InP NPs. The S-OA treatment of InP was reported to form a sulfide layer at the InP surface and reduce the oxides dramatically [22-24]. This indicates that the stable PEC performance for InP NPs can be achieved without any wide band gap transition oxide protection layer, such as widely studied TiO_2. The S-OA treatment of InP NPs not only removes the plasma damage but also provides protection against the photocorrosion of NPs.

6.8. Conclusions

In summary, we demonstrated a cost-effective approach for the fabrication of InP NPs, proposed a new approach for simultaneous plasma damage removal and protection of InP NPs against photocorrosion and studied their PEC performance. A simple, cost-effective and scalable gold nano-island mask was developed by short time RTA annealing of a thin Au film to fabricate very high density and uniform height InP NPs using a top-down approach. However, the top-down fabrication of NPs creates severe damage to the NP surface due to high energy plasma ion impingement, which is confirmed through the morphology and TRPL measurements of NPs. The wet treatment of NPs in S-OA was employed to improve the optical quality of the NPs. The controlled etching of InP in S-OA removes the plasma damage, thereby reducing non-radiative traps for photo-excited carriers. The minority carrier lifetime of the NPs is improved with increasing S-OA treatment time and even surpasses the minority carrier lifetime of the planar wafer after 90 min of wet treatment. The improved carrier lifetime of the NPs after S-OA treatment can be attributed to the simultaneous etching and passivation of the NPs.

The InP NPs exhibit exceptional PEC performance as a photocathode after S-OA treatment, where the PEC measurements were carried out using a three-electrode set-up in 1 M HCl. The saturation photocurrent density and photocathodic efficiency of the S-OA treated NPs is improved by 60% and 32% respectively, compared to their planar counterparts. On the other hand, as-fabricated NPs exhibit inferior PEC performance compared to the planar structure due to severe surface damage caused by the plasma etching. The record photocurrent density of close to 34 mA/cm^2 was achieved after 90 min of wet treatment, which is very close to the theoretical limit for InP given the band gap of the material. The record PEC photocurrent density of the S-OA treated NPs can be ascribed to the improved absorption, enhanced semiconductor/electrolyte interface area and improved optical quality of the NPs. Further, S-

OA treatment of the NPs helps to reduce charge transfer resistance at semiconductor/electrolyte interface, measured from electrochemical impedance, compared to the as-fabricated NPs due to the elimination of surface damage. Moreover, long term PEC stability is achieved for the NPs without any protection layer after S-OA treatment, which is attributed to the formation of a sulfide layer around the NPs. Relatively stable and record PEC performance of NP photocathodes after S-OA treatment make them a promising photocathode if the onset potentials are improved further as it involves cost-effective and scalable fabrication of InP NPs.

6.9. References

[1] Zhang K, Ma M, Li P, Wang D H and Park J H 2016 Water Splitting Progress in Tandem Devices: Moving Photolysis beyond Electrolysis *Advanced Energy Materials* **6** 1600602

[2] Holec D, Zhang Y, Rao D V S, Kappers M J, McAleese C and Humphreys C J 2008 Equilibrium critical thickness for misfit dislocations in III-nitrides *Journal of Applied Physics* **104** 123514-20

[3] Chin-An C, Tzu-Yu T, Pen-Hsiu C, Nie-Chuan C and Chi-Te L 2007 Magnesium Doping of In-rich InGaN *Japanese Journal of Applied Physics* **46** 2840

[4] Heller A and Vadimsky R G 1981 Efficient Solar to Chemical Conversion: 12% Efficient Photoassisted Electrolysis in the [p-type InP(Ru)]/HCl-KCl/Pt(Rh) Cell *Physical Review Letters* **46** 1153

[5] Heller E A S a A 1982 Efficient p - InP (Rh - H alloy) and p - InP (Re - H alloy) Hydrogen Evolving Photocathodes *The Electrochemical Society* **129** 2865

[6] Li Q, Zheng M, Zhong M, Ma L, Wang F, Ma L and Shen W 2016 Engineering MoS_x/Ti/InP Hybrid Photocathode for Improved Solar Hydrogen Production *Scientific Reports* **6** 29738

[7] Li Q, Zheng M, Zhang B, Zhu C, Wang F, Song J, Zhong M, Ma L and Shen W 2016 InP nanopore arrays for photoelectrochemical hydrogen generation *Nanotechnology* **27** 075704

[8] Kornienko N, Gibson N A, Zhang H, Eaton S W, Yu Y, Aloni S, Leone S R and Yang P 2016 Growth and Photoelectrochemical Energy Conversion of Wurtzite Indium Phosphide Nanowire Arrays *ACS Nano* **10** 5525-35

[9] Gao L, Cui Y, Vervuurt R H J, van Dam D, van Veldhoven R P J, Hofmann J P, Bol A A, Haverkort J E M, Notten P H L, Bakkers E P A M and Hensen E J M 2016 High-

Efficiency InP-Based Photocathode for Hydrogen Production by Interface Energetics Design and Photon Management *Advanced Functional Materials* **26** 679-86

[10] Lin Y, Kapadia R, Yang J, Zheng M, Chen K, Hettick M, Yin X, Battaglia C, Sharp I D, Ager J W and Javey A 2015 Role of TiO2Surface Passivation on Improving the Performance of p-InP Photocathodes *The Journal of Physical Chemistry C* **119** 2308-13

[11] Hettick M, Zheng M, Lin Y, Sutter-Fella C M, Ager J W and Javey A 2015 Nonepitaxial Thin-Film InP for Scalable and Efficient Photocathodes *J Phys Chem Lett* **6** 2177-82

[12] Gao L, Cui Y, Wang J, Cavalli A, Standing A, Vu T T, Verheijen M A, Haverkort J E, Bakkers E P and Notten P H 2014 Photoelectrochemical hydrogen production on InP nanowire arrays with molybdenum sulfide electrocatalysts *Nano Lett* **14** 3715-9

[13] Munoz A G, Heine C, Lublow M, Klemm H W, Szabo N, Hannappel T and Lewerenz H J 2013 Photoelectrochemical Conditioning of MOVPE p-InP Films for Light-Induced Hydrogen Evolution: Chemical, Electronic and Optical Properties *ECS Journal of Solid State Science and Technology* **2** Q51-Q8

[14] Lee M H, Takei K, Zhang J, Kapadia R, Zheng M, Chen Y Z, Nah J, Matthews T S, Chueh Y L, Ager J W and Javey A 2012 p-Type InP nanopillar photocathodes for efficient solar-driven hydrogen production *Angew Chem Int Ed Engl* **51** 10760-4

[15] Narangari P R, Karuturi S K, Lysevych M, Hoe Tan H and Jagadish C 2017 Improved photoelectrochemical performance of GaN nanopillar photoanodes *Nanotechnology* **28** 154001

[16] Tseng W J, van Dorp D H, Lieten R R, Mehta B, Vereecken P M and Borghs G 2013 Enhanced Photocatalytic Activity of Nanoroughened GaN by Dry Etching *ECS Electrochemistry Letters* **2** H51-H3

[17] Benton J, Bai J and Wang T 2013 Significantly enhanced performance of an InGaN/GaN nanostructure based photo-electrode for solar power hydrogen generation *Applied Physics Letters* **103** 133904

[18] Joshua B, Parvathala Reddy N, Siva Krishna K, Rowena Y, Mykhaylo L, Hark Hoe T and Chennupati J 2018 Photoelectrochemical studies of InGaN/GaN MQW photoanodes *Nanotechnology* **29** 045403

[19] Cui Y, van Dam D, Mann S A, van Hoof N J, van Veldhoven P J, Garnett E C, Bakkers E P and Haverkort J E 2016 Boosting Solar Cell Photovoltage via Nanophotonic Engineering *Nano Lett* **16** 6467-71

[20] Cao X and Thayne I 2003 Novel high uniformity highly reproducible non-selective wet digital gate recess etch process for InP HEMTs *Microelectronic Engineering* **67-68** 333-7

[21] Naureen S, Shahid N, Sanatinia R and Anand S 2013 Top-Down Fabrication of High Quality III-V Nanostructures by Monolayer Controlled Sculpting and Simultaneous Passivation *Advanced Functional Materials* **23** 1620-7

[22] Maeda F, Watanabe Y and Oshima M 1993 Surface chemical bonding of (NH4)2Sx-treated InP(001) *Applied Physics Letters* **62** 297-9

[23] Anderson G W, Hanf M C, Norton P R, Lu Z H and Graham M J 1994 Thermal stability of sulfur passivated InP(100)-(1×1) *Applied Physics Letters* **65** 171-3

[24] Thomson J W, Nagashima K, Macdonald P M and Ozin G A 2011 From sulfur-amine solutions to metal sulfide nanocrystals: peering into the oleylamine-sulfur black box *J Am Chem Soc* **133** 5036-41

[25] Bessolov V N and Lebedev M V 1998 Chalcogenide passivation of III–V semiconductor surfaces *Semiconductors* **32** 1141-56

[26] van Vugt L K, Veen S J, Bakkers E P, Roest A L and Vanmaekelbergh D 2005 Increase of the photoluminescence intensity of InP nanowires by photoassisted surface passivation *J Am Chem Soc* **127** 12357-62

[27] Mokkapati S and Catchpole K R 2012 Nanophotonic light trapping in solar cells *Journal of Applied Physics* **112** 101101

[28] Clapham P B and Hutley M C 1973 Reduction of Lens Reflexion by the “Moth Eye” Principle *Nature* **244** 281

[29] Coridan R H, Nielander A C, Francis S A, McDowell M T, Dix V, Chatman S M and Lewis N S 2015 Methods for comparing the performance of energy-conversion systems for use in solar fuels and solar electricity generation *Energy & Environmental Science* **8** 2886-901

[30] Varghese O K and Grimes C A 2008 Appropriate strategies for determining the photoconversion efficiency of water photoelectrolysis cells: A review with examples using titania nanotube array photoanodes *Solar Energy Materials and Solar Cells* **92** 374-84

Chapter 7

Conclusions and Future Scope

7.1. Conclusions

This dissertation presents investigations of top-down fabrication techniques using inductively coupled plasma (ICP) etching for fabrication of gallium nitride (GaN) and indium phosphide (InP) nanopillar (NP) photoelectrodes for photoelectrochemical (PEC) hydrogen generation.

Investigations on the influence of GaN NP dimensions, fabricated using a top-down approach, on their optical properties such as photoluminescence and absorption properties are presented in Chapter 3. Ordered GaN NPs with controlled dimensions and smooth side walls were fabricated by ICP etching of EBL patterned GaN epitaxial wafers. Variation in NP array pitch or spacing between the NPs, showed a strong influence on morphology and optical properties of the NPs for a constant NP diameter. The tapering, referring to the side wall angle of the NPs, increased with increasing array pitch. Significant change in optical properties was observed for GaN NPs compared to their planar counterpart. The PL intensity was improved by four times for NP arrays with a 400 nm pitch and 100 nm diameter compared to the planar structures and then decreased with increasing pitch. Finite-difference time-domain (FDTD) simulation studies were carried out to understand the influence of NP dimensions on the PL intensity of GaN NPs. FDTD simulations revealed that the absorption characteristics of the NPs were greatly influenced by NP dimensions. Reduced reflection losses contributed to enhanced absorption by the NPs at smaller array pitch compared to the epilayer. This enhanced light absorption together with light extraction efficiency contributed to the improved PL intensity of the NPs compared to the planar structures. Moreover, the quantum efficiency of the NPs revealed that as-fabricated NPs maintain reasonable optical quality compared to that of the epilayer from which they were fabricated.

Chapter 4 presented a cost-effective and scalable top-down approach to fabricate large area GaN NPs for PEC water splitting applications. This chapter also presented investigation of the influence of carrier concentration and NP dimensions on their PEC performance. The simple and cost-effective self-assembled random mask technique was introduced to produce

an etch mask for top-down fabrication of GaN NPs. Using this mask technique, a Ni random metal mask was produced by RTA annealing of a very thin Ni film for a short time in an Ar atmosphere. Large area random GaN NPs fabricated by ICP etching of Ni random masked n-GaN wafers exhibited smooth side walls and uniform height. The GaN NP dimensions were well controlled by varying metal film thickness and ICP etch time. Absorption properties of NPs were improved substantially compared to the epilayer and then deteriorated with increasing diameter of the NPs due to increasing reflection losses. The PEC performances of the GaN planar and NP photoanodes with varying carrier concentration and NP dimensions were evaluated using a set up consisting of three electrodes in 1 M NaOH electrolyte under simulated one sun illumination. NP photoanodes performed exceptionally well compared to their planar counterpart due to enhanced absorption properties and increased semiconductor/electrolyte interface area for NPs. GaN NP photoanodes achieved the highest ever reported photocurrent density of 1 mA/cm^2, which is very close to the theoretical limit for GaN materials. The PEC performance of the NPs was shown to be dependent on NP dimensions and doping concentration. The PEC performance of the NPs decreased with increasing diameter and decreasing length of the NPs due to reduced optical absorption. Increasing the carrier concentration of the NPs caused anodic shift in the onset potential because of decreased depletion region width

Chapter 5 focussed on the band gap engineering of GaN to further improve the PEC performance of GaN NPs and their photo-stability. To improve the PEC performance of GaN photoanodes, the band gap of GaN was modulated by incorporating InGaN/GaN multi-quantum well (MQW) structures into GaN. The band gap of GaN was reduced by incorporating In concentrations of 20, 30 and 50% into the MQWs to extend absorption from the ultraviolet into the visible region of the solar spectrum. Large area MQW NP photoanodes were fabricated by ICP etching of Ni random masked MQW wafers. The optical absorption of the MQW NP structures was extended up to 450 nm for 30% In concentration. However, further increase in In concentration did not show PL signal for InGaN, which could be due to the formation of high defect densities in the InGaN layers. The PEC performance of MQW NPs exhibited a strong dependence on In concentration, while no significant influence of In was noticed for their planar counterparts. This is because the direct exposure of InGaN to the electrolyte makes it easy for photogenerated carriers to participate in water splitting for NP, unlike planar structures where InGaN are isolated from the electrolyte. MQW NPs with 30% In generated the highest photocurrent density of 1.6 mA/cm^2, which is 1.8 times greater than that of the NP photoanode without MQWs and 4 times greater than that of their planar counterpart. Moreover,

long-term stability of the NP photoanodes was demonstrated by decorating the NPs with transition metal oxide co-catalysts such as NiO and Co_3O_4. Co-catalysts loaded on to NPs extract the photogenerated holes from NPs due to their favourable band gap and act as active sites in place of NP surface sites for water oxidation reaction. As a result, NPs alienated from oxidation process thereby protected from the photocorrosion.

Chapter 6 discussed the development of stable and highly efficient InP NP photocathodes using a top-down approach for PEC water splitting applications. A Au random mask was produced using a self-assembled random mask technique for fabrication of large area InP NPs. Au was chosen as a metal mask instead of Ni to avoid thermal decomposition of InP at high temperatures (>800 °C) needed to form Ni random mask. As-fabricated NPs exhibited extraordinary anti-reflection properties above the band gap of the material. However, NPs suffered from severe surface damage due to plasma ion impingement. This damage was removed by wet treatment of InP NPs in sulfur dissolved oleylamine (S-OA) solution. The S-OA treatment of NPs provided simultaneous plasma damage removal and passivation. The optical quality of the NPs was improved with increasing wet treatment time and exceeded the optical quality of the epilayer after 90 min S-OA treatment. The PEC performance of the InP NPs was tested under one sun illumination in 1 M HCl electrolyte. S-OA treated NP photocathodes exhibited exceptional PEC performance owing to the extraordinary absorption, increased surface area and improved optical quality of the NPs. The photocurrent density of NP photocathodes reached nearly 34 mA/cm^2 after 90 min of S-OA treatment, which is very close to the theoretical limit for InP given the band gap of the material. The S-OA treated NPs showed a 32% improvement in photocathodic efficiency compared to the planar photocathodes. S-OA treatment also reduced the charge transfer impedance of NPs at the semiconductor/electrolyte interface due to the elimination of surface defects. In addition to the elimination of surface damage, S-OA treatment also helped to improve the photostability of the InP NPs, possibility due to formation of a stable sulphide protection layer around NPs.

7.2. Future scope

This dissertation has made considerable progress in demonstrating highly efficient and stable III-V semiconductor photoelectrodes such as GaN and InP NP fabricated using a top-down approach for PEC solar water splitting applications. However, there are still many challenges which need to be addressed before using them for practical applications. Possible directions to address some of the key challenges are presented here to improve the PEC performance of III-V semiconductor photoelectrodes.

7.2.1. Improving the PEC performance of InGaN/GaN MQW photoanodes

As discussed in this thesis, GaN NP photoanodes achieved close to the theoretically maximum achievable photocurrent density for GaN. To further improve the PEC performance of GaN NP photoanodes, we introduced low band gap InGaN/GaN MQWs into GaN to capture sunlight in the visible portion of the solar spectrum. Although the MQW NP photoanodes with 30% In concentration generated 1.8 times higher photocurrent than the bare GaN NPs, the PEC performance of the NPs was not up to the expected level for InGaN with 30% In. The substandard PEC performance of the MQW photoanodes can be attributed to the very small active area of the InGaN/GaN MQWs given the small footprint size of the NPs and insufficient InGaN thickness to capture all the incident light within the band gap of the material [1]. These difficulties can be resolved if the MQWs are regrown epitaxially around GaN NPs using metal organic vapour phase epitaxy (MOVPE) in the form of core-shell structures [2, 3]. The core-shell growth of MQWs provides InGaN along the length of the NPs to completely absorb the incident light compared to the very thin InGaN layers in axial MQWs. Further, the number of MQW structures can also be reduced for core-shall structures compared to the axial structures because of the increased area of the InGaN for light absorption. This can help to minimize the energy required to extract the photogenerated carriers from the quantum wells thereby contributing to improved onset potential of core-shell MQW NP photoelectrodes. The enhanced absorption and improved onset potential together can contribute to enrich the PEC performance of MQW NP photoanodes to the expected levels if the MQWs are grown in core-shell structures.

7.2.2. Engineering the onset potential of InP photocathodes

This thesis demonstrated a remarkable photocurrent density achieved for InP NP photocathodes after removing the plasma damage. However, the photocathodic efficiency of InP photocathodes did not improve on a similar scale as that of the photocurrent density. This is mainly caused by the NP photocathodes exhibiting low onset potentials and poor fill factors. Therefore, improving the onset potential and fill factor is critical to exploit the remarkable photocurrent density and demonstrate record efficiency for NP photocathodes. The onset potential of InP photocathodes was reported to be greater than 0.8 V versus RHE, with an impressive fill factor, with the formation of a buried junction [4, 5]. This strategy can be adopted to improve the onset potential of InP NPs and thereby improve upon the photocathodic efficiency of the InP NP photocathodes demonstrated in this thesis. Buried junction InP NP

photocathodes can be fabricated in two possible ways using a top-down approach. One of them is the growth of a thick and heavily doped n-layer on top of the p-InP wafer to form a p-n junction followed by the top-down fabrication of NPs, where NPs are confined to only the n-doped layer. The second approach is the epitaxial regrowth of a heavily n-doped layer around the top-down fabricated p-InP NPs in a core-shell structure using MOVPE. Both approaches have the potential to improve the onset potential and fill factor and therefore the photocathodic efficiency of InP photocathodes through the modifications of the band energies at the semiconductor/electrolyte interface. The onset potential depends on the alignment of the energy bands at semiconductor/electrolyte interface. A schematic of the semiconductor/electrolyte interface energetics with and without a buried junction is shown in Figure 7.1 [4]. The maximum extracted theoretical onset potential (E_{max}) of the photocathode is determined by subtracting the water reduction potential ($eU_{H2/H2O}$) from the flat band potential of the semiconductor (eU_{fb}) in the electrolyte. The onset potential of the photocathodes can be tuned by engineering the semiconductor/electrolyte interface. This can be achieved through the formation of a buried junction by growing heavily n-doped (n^+) layers on top of p-InP. As shown in Figure 7.1(b), a heavily doped n-type layer makes an Ohmic contact with the electrolyte and n-p junction with p-type InP. The heavily doped n-layer in the case of buried junction n^+-p InP forms favourable band alignments with the electrolyte to minimize the energy loss of photogenerated carriers compared to the bare p-InP, thereby improving the onset potential of the photocathode. Further, the fill factor of the photocathode is also determined by the quality of the p-n junction as the energetics of the photoelectrode is controlled by the p-n junction rather than the semiconductor/electrolyte interface.

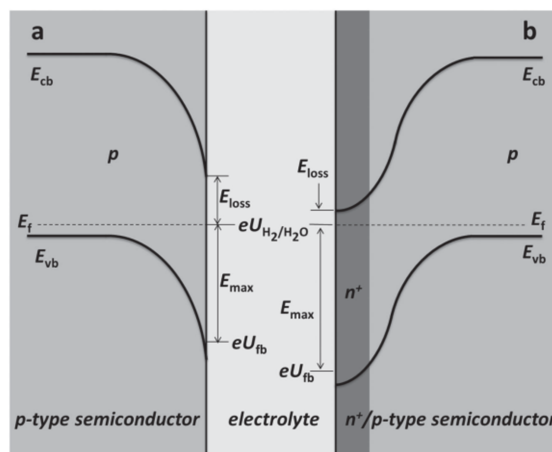

Figure7.1: Schematic of the semiconductor/electrolyte interface energetics in electrolyte for (a) p and (b) n^+-p InP photocathodes [4].

7.2.3. Cost effective strategies for III-V semiconductor photoelectrodes

Although III-V semiconductor photoelectrodes have achieved record solar-to-hydrogen conversion efficiencies, they still suffer from heavy material cost which makes them not viable for generation of hydrogen fuel. The substrate wafers used for the epitaxial growth of III-V layers are the main contributor to the hefty price of photoelectrodes as they are ~300 µm thick, which is 100 times more than required for a photocathode. Due to very high absorption coefficient of III-V semiconductors, very thin III-V films (few microns) are sufficient to capture all the incident light. Therefore, eliminating substrate wafers from the fabrication of photoelectrodes reduces the material usage without compromising light absorption, which can minimize the cost of photoelectrodes. This can be best achieved using a variety of thin film transfer technologies such as epitaxial lift-off [6, 7], spalling [8] or selective etching [9], successfully demonstrated for electronic and optoelectronic device applications. Although the working principles vary, all these techniques involve removal of the epitaxial films from the expensive III-V substrates and transfer onto inexpensive rigid substrates. These thin-film transfer techniques allow the expensive substrates to be reused for the growth of fresh epitaxial films and help to overcome the cost related obstacles of III-V semiconductor devices.

The cost of the photoelectrodes can be lowered further using direct growth of III-V semiconductor materials on cost friendly foreign substrates as it does not use either expensive III-V substrates or additional processes like thin-film transfer technology for transferring epitaxial films. The thin-film vapour-liquid-solid (TF-VLS) growth technique was shown to be capable of producing InP polycrystalline thin films with very large lateral grain size up to 1 mm [10]. The optical quality of any material depends on the grain size in the film; larger the grain size means better is the quality of material [10]. TF-VLS growth of III-V semiconductor films has great potential for the fabrication of price worthy photoelectrodes as it can produce high quality III-V films. Formation of NPs can further enhance the PEC performance of these photoelectrodes due to enhanced absorption and surface area. Moreover, fabrication of NPs helps to avoid the loss of photogenerated carriers at grain boundaries in lateral directions due to the small diameter of NPs compared to grain size. This means all the photo-excited carriers in the semiconductor can contribute to PEC performance of NP photoelectrodes.

7.3. References

[1] Tu D-H, Wang H-C, Wang P-S, Cheng W-C, Chen K-H, Wu C-I, Chattopadhyay S and Chen L-C 2013 Improved corrosion resistance of GaN electrodes in NaCl electrolyte for photoelectrochemical hydrogen generation *International Journal of Hydrogen Energy* **38** 14433-9

[2] Jonathan J W, Jr., Qiming L, Daniel D K, Stephen R L and George T W 2012 III-nitride core–shell nanowire arrayed solar cells *Nanotechnology* **23** 194007

[3] Chang J R, Chang S P, Li Y J, Cheng Y J, Sou K P, Huang J K, Kuo H C and Chang C Y 2012 Fabrication and luminescent properties of core-shell InGaN/GaN multiple quantum wells on GaN nanopillars *Applied Physics Letters* **100** 261103-7

[4] Gao L, Cui Y, Vervuurt R H J, van Dam D, van Veldhoven R P J, Hofmann J P, Bol A A, Haverkort J E M, Notten P H L, Bakkers E P A M and Hensen E J M 2016 High-Efficiency InP-Based Photocathode for Hydrogen Production by Interface Energetics Design and Photon Management *Advanced Functional Materials* **26** 679-86

[5] Lin Y, Kapadia R, Yang J, Zheng M, Chen K, Hettick M, Yin X, Battaglia C, Sharp I D, Ager J W and Javey A 2015 Role of TiO2Surface Passivation on Improving the Performance of p-InP Photocathodes *The Journal of Physical Chemistry C* **119** 2308-13

[6] Demeester P, Pollentier I, Dobbelaere P D, Brys C and Daele P V 1993 Epitaxial lift-off and its applications *Semiconductor Science and Technology* **8** 1124

[7] Cheng C-W, Shiu K-T, Li N, Han S-J, Shi L and Sadana D K 2013 Epitaxial lift-off process for gallium arsenide substrate reuse and flexible electronics *Nature Communications* **4** 1577

[8] Shahrjerdi D, Bedell S W, Ebert C, Bayram C, Hekmatshoar B, Fogel K, Lauro P, Gaynes M, Gokmen T, Ott J A and Sadana D K 2012 High-efficiency thin-film InGaP/InGaAs/Ge tandem solar cells enabled by controlled spalling technology *Applied Physics Letters* **100** 053901

[9] Young J L, Steiner M A, Döscher H, France R M, Turner J A and Deutsch Todd G 2017 Direct solar-to-hydrogen conversion via inverted metamorphic multi-junction semiconductor architectures *Nature Energy* **2** 17028

[10] Kapadia R, Yu Z, Wang H-H H, Zheng M, Battaglia C, Hettick M, Kiriya D, Takei K, Lobaccaro P, Beeman J W, Ager J W, Maboudian R, Chrzan D C and Javey A 2013 A

direct thin-film path towards low-cost large-area III-V photovoltaics *Scientific Reports* **3** 2275